UNIVERSITY OF CALIFORNIA
RIVERSIDE

Iron Biogeochemical Cycle Throughout Earth History

A Dissertation submitted in partial satisfaction
of the requirements for the degree of

Doctor of Philosophy

in

Geological Sciences

by

Bridget Kenlee

March 2021

Dissertation Committee:
Dr. Timothy Lyons, Chairperson
Dr. Andrey Bekker
Dr. Gordon Love

The Dissertation of Bridget Kenlee is approved:

_____

_____

_____

Committee Chairperson

University of California, Riverside

Acknowledgements

I am grateful for the opportunity to formally express my thanks to so many people for their guidance and support throughout the years I spent in the University of California, Riverside. First of all, would like to start by thanking my committee Tim Lyons, Andrey Bekker and Gordon Love for all of the scientific guidance and knowledge you have provided throughout this journey. Tim, thank you for the education in science that you have bestowed upon me as your student. You are an expert at thinking about the big picture and set very high standards for the quality of work. I can assure that your guidance and support were essential to keep me moving forward at many points during this process and I am tremendously grateful to you for your trust and encouragement of my interests inside as well as outside of the lab. I cannot forget those who have significantly impacted my career through their inspiration and mentorship in my most formative years –in particular Jeremy Owens, Rob Raiswell, Mary Droser and Pete Sadler.

The Lyons Lab is an environment rich with intellect, research experience, and friendship and I am fortunate to have been a part of this group. In particular, Steve Bates has been incredibly helpful in teaching me how to carryout geochemical analysis and discuss the environmental sequence data in the context of my project. I also appreciate those who I have worked closely with or who have provided essential role in supporting the work of and creating community within the Lyons Lab including Dalton Hardisty, Charles Diamond, Konstantin Choumilline and Maria Figueroa.

My family has been a constant source of comfort, joy, and adventure in my graduate years. I especially thank my two sons, Jonathan and Steve, for embarking in this ride with curiosity. You have always been the driving force for my successes and will continue through life. Love you.

ABSTRACT OF THE DISSERTATION

Iron Biogeochemical Cycle Throughout Earth History

by

Bridget Kenlee

Doctor of Philosophy, Graduate Program in Geological Sciences
University of California, Riverside, March 2021
Dr. Timothy W. Lyons, Chairperson

Iron (Fe) is present over a wide range of redox states and is one of most the important nutrients for phytoplankton growth in the oceans. In a marine environment, Fe composition in the sediments is intimately linked to the chemistry of the waters from which they precipitate. Particularly, the elemental and isotopic signature of Fe recorded in sediments provide clues about the nature of the redox state and the biogeochemical cycling of bio-essential metals, both of which are associated to primary productivity, carbon cycling, and the evolution of Earth through time.

In this work, I begin by evaluating Fe, a fundamental regulator of ocean primary productivity and the global carbon cycle and a limiting micronutrient for phytoplankton growth, to draw connections between wind-borne bioavailable Fe distribution and its potential impact on Fe-based climate feedbacks over the last 120,000 years. Our results from sediments in the North Atlantic suggest that atmospheric processing of Saharan dust enhances the solubility and hence bioavailability of dust-borne iron independent of grain size, and this transport-dependent processing scales with atmospheric residence time and

thus, transport distance. These observations and inferred processes may extend to many other regions beyond the North Atlantic and thus inform our understanding of the global distribution of primary productivity today and in the past.

A second study defines natural variations in water column redox in the Dove and Pirie basins of the southern Scotia Sea based on scientific drilling of sedimentary records during Expedition 382 of the International Ocean Discovery Program (IODP). The distinct trends in the pore water and sedimentary concentrations from the two basins reveal nonsteady-state diagenetic signals, coupled with a quantitative understanding of the biogeochemical cycles of Fe, C, and S and their relationships to microbial communities.

Lastly, I examine the redox state of the late-Archean and Paleoproterozoic using black shales and Banded Iron Formations (BIFs) from the San Francisco Craton, Brazil, to reconstruct O_2 evolution based on redox changes of Earth's ocean. These two studies capture a local accumulation of oxygen in the Quadrilátero Ferrífero-Minas basin. The evolution of atmospheric and marine O_2 was more complex than a simple abrupt event and demands further investigation addressing local versus global controls and records of the rise of atmospheric oxygen.

Table of Contents

List of Figures

List of Tables

CHAPTER 1

Introduction and Motivation

Life and its environments have coevolved through Earth history with changes in the environment occurring in parallel with evolutionary innovation. One of the most complex relationships is between life and oxygen. The oxygenation of the atmosphere and oceans is a milestone in the evolution of the biosphere and geochemical cycles of elements (Bekker et al., 2004; Lyons et al., 2014).

Iron (Fe) is a vital component of the chemical architecture of the biosphere. Iron (Fe), the fourth most abundant element in the Earth's crust, exists over a very wide range of redox conditions. It is extremely efficient scavenger of other elements and, through formation of minerals rich in both reduced and oxidized Fe, effectively archives chemical information about the fluids from which they form (Berner, 1981) - including ancient seawater. Depending on the environmental conditions, Fe can form stable compounds in both the divalent and trivalent state (Schwertmann and Fitzpatrick, 1993), playing an important role in redox processes within the environment. Fe (II), ferrous iron, forms minerals such as siderite, vivianite, and iron sulfide in anoxic habitats under weakly acidic to neutral conditions. In the presence of oxygen, Fe(II) is rapidly oxidized to Fe(III) (ferric iron), forming minerals that are widespread in both oxic and anoxic habitats. The redox-dependent speciation of Fe is accompanied by isotope fractionation processes (Johnson et al., 2008) that can allow us to reconstruct the ancient marine redox-state (Rouxel et al., 2005). The separation of anoxic Fe(II)-rich deep waters with a homogeneous isotopic composition and an oxic surface layer, where Fe(II) is oxidized, causes large isotopic gradients at the chemocline (Busigny et al., 2014). The Fe composition of sediments deposited along such chemoclines, thus, provide records of the geochemical

history of their formation, in both modern and ancient waters, that are linked to primary productivity, carbon cycling, and ultimately the evolution of Earth's surface environments through time.

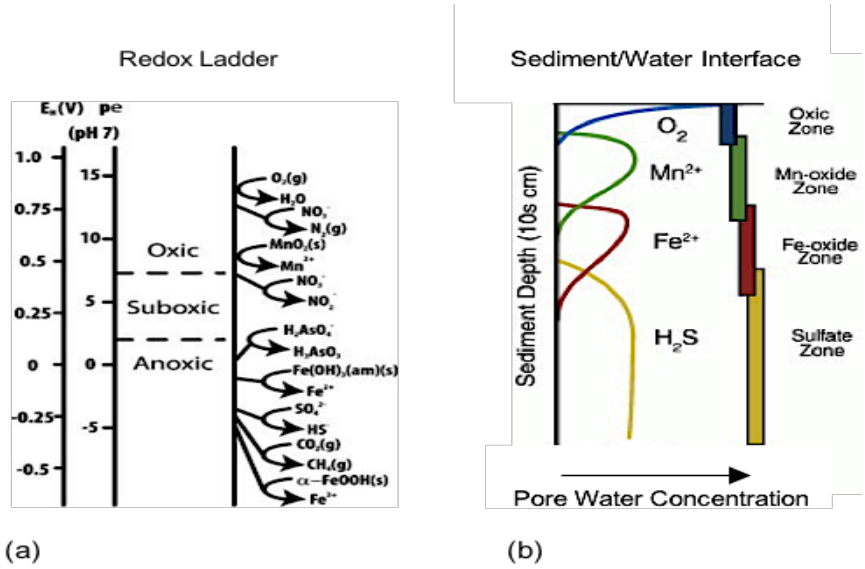

Figure 1.1: (a) Redox Ladder: The redox- couples are shown on each stair-step, where the most energy is gained at the top step and the least at the bottom step. Gibb's free energy becomes more positive going down the step (Barcelona and Holm, 1991; Kappler et al., 2005; Weber et al., 2006). (b) Oxidant zonation in non-euxinic sediments (Canfield and Thamdrup, 2009; Scott and Lyons, 2012).

The biogeochemical cycling of Fe has controlled major nutrient cycles throughout Earth history. Iron, an essential micronutrient, is one of the most important transition metals for nearly all life on Earth. Iron is fundamental in many key enzyme systems for chlorophyll synthesis multiply (Geider and La Roche, 1994; Peers et al., 2005), nitrate utilization (Mark Moore et al., 2009; Mills et al., 2004), and redox systems (Lyons and Severmann, 2006; Reinhard et al., 2013), which are involved in the biochemical processes of photosynthesis and carbon fixation (De Baar and La Roche, 2003; McKay et al., 2005).

In today's oceans, for example, it is estimated that in about 40% of the world's oceans primary productivity by low availability of micronutrient Fe (Martin, 1990; Moore et al., 2013; Moore and Braucher, 2007). These Fe-limited regions are often referred to as having high nutrient/low chlorophyll (HNLC) because macronutrients are underutilized compared to other oceanic regions. The low Fe concentrations in HNLC regions result from both low Fe input and low solubility of the metal under oxic conditions (Liu and Millero, 2002) can be scavenged onto particle surfaces predominantly via the formation of colloidal nanoparticles that subsequently aggregate onto larger sinking particles (Honeyman and Santschi, 1989; Rose and Waite, 2007). As a result, Fe has a very short residence time in the oceans compared to macronutrients and some other trace elements (Boyd and Ellwood, 2010). Thus, Fe, plays a critical role in carbon cycling, and changes in its supply to the surface ocean may have had a significant effect on atmospheric carbon dioxide (CO_2) concentrations (Martin, 1990; Sigman and Boyle, 2000; Watson et al., 2000) throughout geological time.

This dissertation explores Fe biogeochemistry to provide information pertaining to Earth's redox and biogeochemical evolution from before the Great Oxidation Event (GOE) to more recent events occurring up to and into Cenozoic Era. This goal is accomplished specifically through a focus on the spatiotemporal distribution of Fe and its role in governing changes of atmospheric CO_2 during the last glacial period in chapter 2 and chapter 3, and the Archean-Proterozoic transition, an evolutionary milestone marked by a rise in oxygen (O_2) in Earth's atmosphere at the GOE (Lyons et al., 2014) in chapter 4 and chapter 5.

REFERENCES

Barcelona, M. J., and Holm, T. R., 1991, Oxidation-reduction capacities of aquifer solids: Environmental Science & Technology, v. 25, no. 9, p. 1565-1572.

Bekker, A., Holland, H., Wang, P.-L., Rumble, D., Stein, H., Hannah, J., Coetzee, L., and Beukes, N., 2004, Dating the rise of atmospheric oxygen: Nature, v. 427, no. 6970, p. 117-120.

Canfield, D. E., and Thamdrup, B., 2009, Towards a consistent classification scheme for geochemical environments, or, why we wish the term 'suboxic'would go away: Geobiology, v. 7, no. 4, p. 385-392.

De Baar, H., and La Roche, J., 2003, Trace metals in the oceans: evolution, biology and global change, Marine science frontiers for Europe, Springer, p. 79-105.

Geider, R. J., and La Roche, J., 1994, The role of iron in phytoplankton photosynthesis, and the potential for iron-limitation of primary productivity in the sea: Photosynthesis research, v. 39, no. 3, p. 275-301.

Johnson, C. M., Beard, B. L., and Roden, E. E., 2008, The iron isotope fingerprints of redox and biogeochemical cycling in modern and ancient Earth: Annu. Rev. Earth Planet. Sci., v. 36, p. 457-493.

Kappler, A., Pasquero, C., Konhauser, K. O., and Newman, D. K., 2005, Deposition of banded iron formations by anoxygenic phototrophic Fe (II)-oxidizing bacteria: Geology, v. 33, no. 11, p. 865-868.

Lyons, T. W., Reinhard, C. T., and Planavsky, N. J., 2014, The rise of oxygen in Earth's early ocean and atmosphere: Nature, v. 506, no. 7488, p. 307-315.

Lyons, T. W., and Severmann, S., 2006, A critical look at iron paleoredox proxies: New insights from modern euxinic marine basins: Geochimica Et Cosmochimica Acta, v. 70, no. 23, p. 5698-5722.

Mark Moore, C., Mills, M. M., Achterberg, E. P., Geider, R. J., LaRoche, J., Lucas, M. I., McDonagh, E. L., Pan, X., Poulton, A. J., Rijkenberg, M. J. A., Suggett, D. J., Ussher, S. J., and Woodward, E. M. S., 2009, Large-scale distribution of Atlantic nitrogen fixation controlled by iron availability: Nature Geoscience, v. 2, no. 12, p. 867-871.

Martin, J. H., 1990, Glacial-Interglacial Co2 Change: The Iron Hypothesis: Paleoceanography, v. 5, no. 1, p. 1-13.

McKay, R., Wilhelm, S., Hall, J., Hutchins, D., Al-Rshaidat, M., Mioni, C., Pickmere, S., Porta, D., and Boyd, P., 2005, Impact of phytoplankton on the biogeochemical cycling of iron in subantarctic waters southeast of New Zealand during FeCycle: Global Biogeochemical Cycles, v. 19, no. 4.

Mills, M. M., Ridame, C., Davey, M., La Roche, J., and Geider, R. J., 2004, Iron and phosphorus co-limit nitrogen fixation in the eastern tropical North Atlantic: Nature, v. 429, no. 6989, p. 292-294.

Peers, G., Quesnel, S. A., and Price, N. M., 2005, Copper requirements for iron acquisition and growth of coastal and oceanic diatoms: Limnology and oceanography, v. 50, no. 4, p. 1149-1158.

Reinhard, C. T., Planavsky, N. J., Robbins, L. J., Partin, C. A., Gill, B. C., Lalonde, S. V., Bekker, A., Konhauser, K. O., and Lyons, T. W., 2013, Proterozoic ocean redox and biogeochemical stasis: Proceedings of the National Academy of Sciences of the United States of America, v. 110, no. 14, p. 5357-5362.

Rouxel, O. J., Bekker, A., and Edwards, K. J., 2005, Iron isotope constraints on the Archean and Paleoproterozoic ocean redox state: Science, v. 307, no. 5712, p. 1088-1091.

Schwertmann, U., and Fitzpatrick, R. W., 1993, Iron minerals in surface environments: Catena Supplement, v. 21, p. 7-7.

Scott, C., and Lyons, T. W., 2012, Contrasting molybdenum cycling and isotopic properties in euxinic versus non-euxinic sediments and sedimentary rocks: Refining the paleoproxies: Chemical Geology, v. 324, p. 19-27.

Sigman, D. M., and Boyle, E. A., 2000, Glacial/interglacial variations in atmospheric carbon dioxide: Nature, v. 407, no. 6806, p. 859.

Watson, A., Bakker, D., Ridgwell, A., Boyd, P., and Law, C., 2000, Effect of iron supply on Southern Ocean CO2 uptake and implications for glacial atmospheric CO2: Nature, v. 407, no. 6805, p. 730-733.

Weber, K. A., Urrutia, M. M., Churchill, P. F., Kukkadapu, R. K., and Roden, E. E., 2006, Anaerobic redox cycling of iron by freshwater sediment microorganisms: Environmental Microbiology, v. 8, no. 1, p. 100-113.

CHAPTER 2

Long-range transport of North African dust enhances oceanic iron bioavailability

ABSTRACT

Wind-borne dust supply of iron (Fe) to the oceans plays a crucial role in Earth's biogeochemical cycles. Iron, a limiting micronutrient for phytoplankton growth, is a fundamental regulator of ocean primary productivity and the global carbon cycle. The flux of bioavailable Fe to the open ocean affects oscillations in atmospheric CO_2 due to its control on inorganic carbon fixation into organic matter that is subsequently exported to the deep ocean. However, the nature of dust-delivered Fe to the ocean and controls on its bioavailability remain poorly constrained. Here, we examine sediments from four North Atlantic localities that document a proximal to distal transect relative to Saharan dust inputs to evaluate the wind-borne bioavailable Fe supply and its potential impact on Fe-based climate feedbacks over the last 120,000 years. Bulk δ^{56}Fe isotope compositions (average = -0.05‰) and Fe_T/Al ratios suggest crustal values, thus pointing to a dominant dust origin for the sediments at all four sites. We observed no variability in grain size distribution (GSD) and in bioavailable Fe supply at individual sites as a function of glacial versus interglacial deposition. Importantly, there is no correlation between sediment grain size and Fe bioavailability. Spatial trends do, however, suggest increasing Fe bioavailability with increasing distance of atmospheric transport, and our sediments also indicate the loss of this Fe once deposited in the ocean. This study draws connections between the loss of bioavailable Fe, as recorded in the sedimentary record, to enhanced biological activity at sites far from the source region.

SIGNIFICANCE STATEMENT

Dust-bound bioavailable iron, its chemical processing in the atmosphere, and its impacts on global climate remain essential research themes. Iron is a limiting micronutrient for phytoplankton growth and a central regulator of marine primary productivity and the global carbon cycle. Our results from sediments in the North Atlantic suggest that atmospheric processing of Saharan dust enhances the solubility and hence bioavailability of dust-borne iron independent of grain size, and this transport-dependent processing scales with atmospheric residence time and thus transport distance. Our data reveal the loss of bioavailable iron from dust in distal oceans, which could have supported productivity at those locations. These observations and inferred processes may extend to many other regions beyond the North Atlantic.

INTRODUCTION

Wind-borne (aeolian) dust is an integral part of Earth's climate system. Aeolian dust is the dominant source of iron (Fe) to the open oceans (Fung et al., 2000). As an essential micronutrient, iron plays an important role in regulating the oceanic biological pump due to its limited bioavailability for phytoplankton in large regions of the ocean (Jickells et al., 2005b; Martin and Fitzwater, 1988). Consequently, Fe bioavailability exerts a strong control on levels of atmospheric carbon dioxide (CO_2) and climate on global scales (Baker et al., 2003; Boyd and Ellwood, 2010; Joos et al., 1991). One of the primary sources of dust to Earth's atmosphere, where it is subsequently deposited in the oceans and on continents, is North African dust (Engelstaedter et al., 2006). Downwind from North Africa, dust-driven fertilization may enhance long-term productivity in Amazon rain forests and Bahamian and Caribbean coral reefs (Bristow et al., 2010; Muhs et al., 2007; Prospero and Mayol-Bracero, 2013; Shinn et al., 2000; Swart et al., 2014; Yu et al., 2015). More generally, transport-dependent enhancement of iron bioavailability may have been a factor in determining the loci of primary productivity in the oceans through Earth history.

Importantly, not all dust-borne Fe is bioavailable in the ocean, and the processes that enhance Fe bioavailability are not well understood. Atmospheric deposition of Fe in the open ocean is predominantly via fine-grained iron (oxyhydr)oxide (mostly as grain coatings) and silicate minerals (Raiswell and Canfield, 2012a). Previous studies have suggested that the chemical properties of Fe in atmospheric dust are often grain size-dependent (Baker and Jickells, 2006; Hand et al., 2004; Ooki et al., 2009). Furthermore,

with longer transport times in the atmosphere, Fe solubility (and consequently Fe bioavalibility) should increase via atmospheric processing, principally involving acid production via photochemistry (Hand et al., 2004). The signatures of these processes, however, are yet to be explored systematically in modern sediments using carefully calibrated iron extraction techniques. Instead, past studies have often characterized potentially soluble iron (Fe_{Sol}) as bioavailable Fe, emphasizing reactive minerals such as ferrihydrite (Fan et al., 2006; Wells et al., 1983). However, ferrihydrite is thermodynamically unstable and will transform into more stable phases on diagenetic timescales, including (oxyhydr)oxides such as goethite, hematite, and magnetite, or other secondary phases such as pyrite and Fe-carbonates. The critical implication is that measured values for the residual, most reactive phases in sediment cores may underestimate the total original reactive Fe pool (Schwertmann et al., 2004).

Here, we have adopted a scheme for iron speciation that is more inclusive of Fe phases that may have been bioavailable prior to transformations in seawater and during burial. We define a broader array of Fe mineral pools as being highly reactive (Fe_{HR}) because their precursors may have initially been bioavailable. These mineral phases consist of (a) carbonate Fe (plus weakly bound, surface Fe); (b) amorphous and crystalline Fe oxides and (oxyhydr)oxides such as ferrihydrite, goethite, and hematite; (c) magnetite Fe; and (d) pyrite (Poulton and Canfield, 2005). We normalize Fe_{HR} to total Fe (Fe_T) to identify relative enrichments or deficiencies in the Fe_{HR} pool. These Fe_{HR}/Fe_T ratios are insensitive to the potential artifacts of dilution (e.g., by carbonate or biogenic silica) that can otherwise lead to ambiguous or spurious interpretations of absolute concentrations. Importantly,

substantial portions of all these phases may have formed by mineral transformation of soluble bioavailable precursor phases following deposition (Benner et al., 2002). Thus, Fe_{HR} effectively functions as a proxy for the upper limit of the residual concentration of initial potentially bioavailable Fe. While we recognize that this Fe will be an overestimation of the original bioavailable pool, because of detrital magnetite inputs for example, it nevertheless provides a comprehensive background against which enrichments and depletions in formerly bioavailable forms can be assessed. This approach is conservative, in terms of percentages, because percent loss from Fe_{HR} would be low relative to the loss from the smaller amount of the most soluble original Fe (Fe_{Sol}). However, little to none of those original phases will be present in cores, given expected rapid diagenetic transformations, which may potentially contribute to any of the pools of Fe_{HR}.

Several recent studies have addressed the controls and distribution of aeolian bioavailable Fe in the oceans and subsequent climate feedbacks (Lis et al., 2015; Shoenfelt et al., 2018; Thöle et al., 2019), including grain size controls on aerosol Fe solubility (Baker and Jickells, 2006; Mackie et al., 2006; Trapp et al., 2010), but none has focused on characterization, spatial trends, and grain size relationships as preserved in marine sediments. To isolate trends in aeolian bioavailable iron in marine sediments, four sample locations that preserve marine sedimentary records of African dust export were strategically selected from International Ocean Discovery Program (IODP) sites to provide a wide spatial distribution in the Northern Atlantic Ocean (Fig. 1) from the last glacial period to present (about the last 120,000 years). We use bulk Fe isotopes to identify the

potential end-member inputs to these sites. We then examine grain size characteristics, and finally, we quantify the Fe pools present to assess controls on bioavailable Fe distribution. We show that dust-borne Fe at distal sites experiences enhanced atmospheric processing, leading to an increase in Fe_{Sol}, which was readily available to primary producers (Borchardt et al., 2019; Hassler et al., 2011). Instantaneous consumption of Fe_{Sol} could have simulated primary productivity that increase the overall impact farther from the Saharan source.

MATERIAL AND METHODS

Study Sites

The four locations are sites 658 (21°N, 19°W) and 659 (18°N, 21°W) from ODP expedition 108, located on top of the Cape Verde Plateau near the northwest African continental margin, and sites 1062 (28°N, 74°W) and 1063 (33°N, 57°W) from the sediment drifts of the western North Atlantic Ocean as part of ODP Leg 172. The sites were selected because they span a wide portion of the Northern Atlantic Ocean (Figure 1). The marine sedimentary records of North African dust export offer the advantage of continuous sedimentation (Giosan et al., 2002; Tiedemann et al., 1989). These sites range from proximal to distal relative to the Sahara Dust Corridor source region. The average time resolution of the four records is about 4 kyr/sample covering the last glacial period to present (over the last 120,000 years) (Supporting Information, Table S6).

Dust deposition average

Calculations of dust deposition (g m^{-2} y^{-1}) were obtained from the average of three

models (Ginoux et al., 2001; Jickells et al., 2005a; Mahowald et al., 1999) (Table S6) to represent our best approximations of dust delivery.

Grain Size Analysis

The GSD in marine sediments is often used as a measure of dust delivery (Baker et al., 2006; Blott and Pye, 2001; Harrison et al., 2001; Ooki et al., 2009). Samples were dried at 80ºC. Dry sieving was carried out for 15 minutes using a tapping sieve shaker (RO-TAP) equipped with a set of stainless-steel sieves. Short sieving times prevented the formation of aggregates due to electrostatic interactions and interparticle cohesion. Each fraction was weighed and recorded. Particle size distribution is represented graphically using a cumulative distribution curve and the D value method (Blott and Pye, 2001) from GRADISTAT (Blott, 2000). Samples were divided into >45μm (bulk), 45 to 20μm, and <20μm size fractions.

Iron Speciation and Iron Isotope Analysis

We used a state-of-the-art sequential Fe extraction procedure modified from Poulton and Canfield (Poulton and Canfield, 2005) to characterize the Fe phases present ($Fe_{Na\text{-}Ac}$, $Fe_{Dith,}$ and Fe_{Ox}), including minerals that might have formed diagenetically from initially bioavailable Fe. All Fe extracts were analyzed by inductively coupled plasma-mass spectrometry (ICP-MS; Agilent 7500ce) using H_2 and He in the collision cell diluted with trace-metal grade 2% HNO_3.

A multi-acid digest was performed to determine total solid-phase iron (Fe_T) and aluminum (Al) concentrations. Dried samples were ashed at 550°C, and a standard three-

step digestion performed using trace metal grade HF, HNO_3, and HCl at 140ºC. This way, the potential bioreactivity of the Fe can be expressed as a fraction of the total Fe pool. Final concentrations were determined using the same ICP-MS. Reference standards SDO-1 (Devonian Ohio Shale) and SCO-1 (Cody Shale) were digested and analyzed in parallel with the sample extractions and yielded errors of less than <4%.

Splits from the multi-acid digest were used to measure the Fe isotope composition of the bulk sample ($\delta^{56}Fe_T$). Samples were purified using anion exchange resin and a standard ion chromatography protocol for Fe separation to eliminate matrix effects (Arnold et al., 2004; Skulan et al., 2002). Column yields were carefully monitored by the Ferrozine colorimetric method with UV-Vis spectrophotometry (λ = 562 nm) (Viollier et al., 2000) before and after chromatographic purification. Only samples with yields ≥95% were used for isotopic analysis. Isotopic compositions were measured on a Neptune Thermo Scientific MC-ICP-MS (Multiple Collector-Inductively Coupled Plasma-Mass Spectrometer) at Rutgers University, applying the method of Arnold et al. (2004) (Arnold et al., 2004). Samples were introduced as a 1 ppm solution using a cyclonic spray chamber. Mass bias during the analysis was corrected by applying a Cu elemental spike. Standard reference material IRMM-014 was used as a bracketing standard between each sample for accurate mass bias correction. The iron isotopic composition ($\delta^{56}Fe$) is defined as follows:

$$\delta^{56}Fe_{‰} = \left[\frac{(^{56}Fe/^{54}Fe)_{sample}}{(^{56}Fe/^{54}Fe)_{IRMM-14}}\right] \text{-1 x } 10^3 \text{ ,}$$

where the $\delta^{56}Fe$ is reported relative to IRMM-014 reference material. The measured Fe isotope composition of IRMM-014 is $\delta^{56}Fe_T$ =-0.09‰ on this scale with an internal precision of ±0.06‰ (2σ).

Carbon concentrations

Sedimentary total carbon (TC) was analyzed by combustion using an Eltra CS-500 carbon-sulfur analyzer. Total inorganic carbon (TIC) was determined by acidification of a split of the sample. Total organic carbon (TOC) content was calculated as the difference between TC and TIC. The geostandards AR4007 and AR4011 were analyzed routinely, with values falling within reported ranges and deviating less than <5%. Calcium carbonate concentrations ($CaCO_3$), as weight percent, were calculated from the measured IC content assuming that all evolved CO_2 was derived from dissolution of $CaCO_3$:

$$CaCO_3 \text{ (wt\%)} = IC \times 8.33 \text{(wt\%)}$$

Standard $CaCO_3$ (>99.9% calcium carbonate, Fisher Scientific) was used during individual batches of analyses to confirm accuracy and instrument performance before, during, and after each run (target reproducibility better than 3%). No correction was made for the presence of other carbonate minerals.

Statistical Analysis

The analysis of variance (ANOVA), the F-test, and t-tests were conducted to determine whether there is a significant difference of bioavailable Fe distribution between proximal and distal sites and in terms of dependence of Fe_{HR}/Fe_T with grain size (Haynes, 2013;

Montgomery et al., 2009). The 95% confidence interval was used in all analyses (see supplementary information for grouping rationale and sensitivity analyses).

Aerosols Optical Properties

Aerosol optical depth (AOD) data from MIRS – Multi-angle Imaging SpectroRadiometer (https://misr.jpl.nasa.gov/getData/accessData/). We averaged concentration of AOD between 2009-2019 over the North Atlantic Ocean to observe the atmospheric deposition of African dust in the North Atlantic Ocean.

The ecoGEnIE model

To model the relationship between Fe flux and primary productivity dynamics, we used the ecoGEnIE model, an extension of cGEnIE—a carbon-centric, Grid Enabled Integrated Earth system model featuring comprehensive marine biogeochemical uptake (Ward et al., 2018). EcoGEnIE incorporates a new scheme for plankton ecology (ECOGEM) with a size-dependent control on the plankton biogeochemical function (Ward et al., 2018). This addition allows for a better representation of biodiversity, including ecosystem shifts in response to environmental forcing. EcoGEnIE provides dynamic simulations of nutrient usage in response to availability. For our purposes, we used cGEnIE/ecoGEnIE default configurations (Ridgwell and Hargreaves, 2007).

RESULTS AND DISCUSSION

Iron supply from the North African dust to the North Atlantic Ocean

Iron isotopes ($\delta^{56}Fe$) can be a powerful way to constrain the Fe sources to the ocean (Beard et al., 2003a; Owens et al., 2012; Waeles et al., 2007). The average bulk $\delta^{56}Fe$ values for samples from all four sites (-0.05±0.02‰; 2-standard deviations) is consistent with continentally derived dust (Figure 1, Table S1) given the similarity to the $\delta^{56}Fe$ composition of most silicate rocks (Beard et al., 2003b; Conway and John, 2014; Dauphas and Rouxel, 2006; Waeles et al., 2007). The Fe_T/Al ratio of 0.55±0.02 also overlaps with the mean Fe_T/Al ratio for terrigenous sediments and average continental crust (0.55±0.11) (Martinez et al., 2007), suggesting no significant hydrothermal contribution, which typically has Fe_T/Al >2.00 (Clarkson et al., 2014; Raiswell et al., 2018a). Our average Al/Ti ratio of 18.9±0.78 is also consistent with an aeolian origin for our samples (Yarincik et al., 2000).

The potential Fe bioavailability can be explored by speciation studies, which are broadly linked to Fe phases in the sample (Shi et al., 2009). Concentrations of Fe extracted using sodium acetate ($Fe_{Na\text{-}Ac}$) comprised 0.5-2.9wt% of Fe_T (Table S2a-d, S3a-d). Although Poulton and Canfield (19) used $Fe_{Na\text{-}Ac}$ to remove carbonate-bound Fe, their data show that small concentrations are also removed from iron-bearing silicates. We confirmed this possibility by extracting a range of Fe-bearing silicates with sodium acetate (Table S4), suggesting that acetate removes a minor fraction of Fe from such minerals—potentially from weakly bound surface sites (Heron et al., 1994; Raiswell et al., 2018b). This pool has been documented to be readily bioavailable (Shoenfelt et al., 2017), where the Fe(II)-rich

silicate minerals enhanced diatom growth as well as photosynthetic efficiency. However, this Fe-bound silicate fraction is very small relative to the other potentially bioavailable pools we now discuss. A dithionite Fe extraction (Fe_{Dith}), dominantly representing Fe (oxyhydr)oxide minerals, removed 8.6 to 21.6wt% of Fe_T (Table S2a-d, S3a-d). Previous studies have considered Fe_{Dith} to be an effective measure of potentially bioavailable iron from aeolian dust particles (Baker and Croot, 2010; Fan et al., 2006). An oxalate Fe extraction (Fe_{Ox}) mainly targets Fe in magnetite and ranges from 5.4-12.1wt% of Fe_T (Table S2a-d, S3a-d). If delivered unaltered to the ocean, rather than forming during diagenesis, magnetite would likely represent refractory (insoluble) iron in surface seawaters.

On the broadest scales, an overall increase in atmospheric dust deposition occurs during glacial intervals due to an expansion in the source areas (Mahowald et al., 1999) and stronger winds (McGee et al., 2010) that consequently influence the supply of bioavailable Fe to the open ocean. However, at low latitudes, there is no significant glacial-interglacial trend in dust input (Maher et al., 2010). Iron bioavailability in marine systems is linked to complexation with prokaryotic-released organic compounds, such as siderophores, polycarboxylate ligands (Barbeau, 2006; Shaked and Lis, 2012), and saccharides (Hassler et al., 2011). Thus, a fraction of this delivered Fe pool should be bioavailable. Our analyses of Fe_T, Fe_{HR}/Fe_T, and total organic carbon (TOC) at all four sites show no statistically relevant variation over the last glacial period to the present ($p>0.05$) (Figure 2, Table S10a-d). Further, the TOC contents argue against enhanced productivity for one interval over the other. This combination, therefore, tells us little about the

importance of iron limitation at low latitudes over this interval. Importantly, however, other downwind locations may be impacted biologically by the enhanced solubility of delivered Fe, such as the Bahamas and Amazon region (Bristow et al., 2010; Muhs et al., 2007; Muhs et al., 2012; Prospero and Mayol-Bracero, 2013; Shinn et al., 2000; Swart et al., 2014; Yu et al., 2015). More generally, our data document a transport-dependent process that would be relevant to other regions and time intervals that are characterized by Fe limitation. Further, atmospheric pathways of enhanced reactivity seem relatively constant, at least at low latitude, under glacial versus interglacial global climatic regimes. The glacial-interglacial uniformity we observe implies consistency in sourcing and transport despite temporal differences in weathering relationships in the source regions and wind patterns, among other varying controls (McGee et al., 2013). This surprising result is certain to influence future climate models for this region and beyond.

Grain size distribution

The bioavailable Fe supply in sediments as a function of grain size distribution (GSD) during glacial-interglacial periods could have important impacts on marine primary productivity (Mahowald et al., 2014). Therefore, we determined the GSD at all four sites by dry sieving (Figure S1, Table S5). To test the variability of GSD during glacial and interglacial periods, a statistical one sample t-Test was carried out for all four sites (n=128) (Figure 2 and Table S9). The p-values for proximal sites 658 and 659 are 0.88 and 0.76, respectively, and 0.72 and 0.19 for distal sites 1062 and 1063, respectively. The end member p-valus suggest the variability in GSD over glacial-interglacial timescale is not

statistically significant for any of the four sites, consistent with previous findings that the flux of low-latitude Saharan dust does not vary significantly over these timescales (Maher et al., 2010; Skonieczny et al., 2019).

Previous work has suggested that Fe bioavailability is grain size-dependent, primarily due to the greater surface-area-to-volume relationship of small grains of atmospheric dust (Mahowald et al., 2018). Greater relative surface areas for small-sized particles could support proportionally larger surface alteration during transport and associated coatings of soluble Fe. To test for statistically significant differences of bioavailable Fe distribution for GSD in the drill-core sediments, Fe_{HR}/Fe_T (n=394) were compared using an analysis of variance (ANOVA) and a t-test (see Supplementary Information for grain size rationale and sensitivity analyses). We found no statistically significant differences in Fe_{HR}/Fe_T with grain size at a given location (Table S8a-d). For example, the ANOVA for site 658 shows no significant dependence ($p<0.05$), with an f-critical value of $2.80e^{-4}$ and a p-value of 1.0 between grain sizes. The ANOVA data for site 659 have an f-critical value of 1.13 and a p-value of 0.33, which is also not significant at $p<0.05$. Sites 1062 and 1063 also show no significant dependence at $p<0.05$, with an f-critical value of 1.12 and p-value of 0.33 for site 1062 and f-critical value of 0.99 and p-value of 0.37 for site 1063. The negligible variability in potentially bioavailable Fe distribution as a function of GSD in these sediments from each site is likely due, at least in part, to the particles having experienced many series of aggregation and disaggregation as they settled through the water column (Bacon et al., 1985)—thus larger particles are mostly aggregates of finer original materials. In this case, the Fe_{HR}/Fe_T ratio of larger grains should

be similar to that of smaller particles, as they dominantly represent large aggregates of the smaller particles (Figure S3) (Anderson et al., 2016).

Spatial trends in potentially bioavailable Fe distribution

North African dust is carried to great distances over thousands of kilometers. Because atmospheric transport is a size-selective process (Pye, 1989), proximal and distal Fe dust can be distinguished by the grain-size distributions related to distance from the source, whereby dust particle size decreases with increasing distance (Mahowald et al., 2014). Average particle size distributions for our samples show a decrease of ~20% in grain size (Table S5) and a corresponding increase of ~30% in surface area (Table S6) from proximal to distal sites. Small particles have a longer lifetime in the atmosphere and thus experience enhanced atmospheric processing (chemical and/or photochemical), likely leading to an increase in the solubility (Fe_{Sol}) of Fe_{HR} (Desboeufs et al., 2001; Shi et al., 2009; Spokes et al., 1994).

Our measurements show a systematic decrease in Fe_{HR}/Fe_T from proximal to distal sites (Figure 3a) between proximal and distal sites. More detailed insight into Fe behavior is provided by our Fe_{Dith} data, which shows the greatest decrease, from 21.5wt% and 15.5wt% of Fe_T at proximal sites 658 and 659, respectively, to 9wt% at both distal sites (1062 and 1063; Table S2a-d and S3a-d). We argue that our Fe_{HR}/Fe_T ratios decrease with increasing transport caused enhanced Fe solubility via atmospheric reactions (Oakes et al., 2012) followed by dissolution in seawater and uptake of the bioavailable Fe by the primary producers in the surface ocean at the distal sites, which has been observed in this general

region (29). However, quantifying the loss of soluble Fe will require more information about the North African dust source region (Huneeus et al., 2011; McGee et al., 2013), the post-depositional processing of the Fe (Bressac and Guieu, 2013; Meskhidze et al., 2019), biogeochemical conditions of the surface seawater (Boyd and Ellwood, 2010), and atmospheric processes (Baker and Croot, 2010).

It is important to consider alternative interpretations of our data. For example, the Fe content of analyzed dust samples could decrease downwind of North Africa, as described by Zhang et al. (Zhang et al., 2015), due to selective, progressive loss of heavier hematite-rich grains through gravitational settling during transport in the atmosphere. In truth, many of our observations are consistent with this possibility, and it may play a role, but there are other observations that are less consistent. First, it is not clear that the trend seen in Fig. 5e of Zhang et al. is an expression of hematite availability. Other Fe phases, in particular Fe (oxyhydr)oxides, are likely a substantial part of the Fe pool in the dust—both as original constitutes from the source region and as products of atmospheric reactions. Importantly, these phases are roughy half as dense as crystalline hematite and would be decidedly less vulnerable to differential settling effects during transport. Moreover, soil hematite, the likely source of dust, would also be less dense than well-crystallized hematite, and these Fe phases are likely to be only a small part of the total grain mass (discrete Fe oxide grains are rare) (Poulton and Raiswell, 2005). Further, hematite and other Fe(III) phases are often present as coatings on aluminosilicate grains that tend, if anything, to have lower densities than other silicates.

Our detailed speciation provides additional insight. Specifically, we see the same distal trends in our data from the acetate extraction, which does not target hematite but instead extracts more reactive, less dense Fe (oxyhydr)oxide phases. Finally, we also do not observe a difference in Fe chemistry as a function of grain size, in contrast to expected transport-related physical sorting that is controlled by grain size and/or density. These observations do not preclude other important processes, but they do leave us with our interpretation as the most parsimonious explantion of the full range of observations.

Implications for ocean primary productivity

The potential effects of iron fertilization via dust delivery likely scale (although perhaps not linearly) with the total dust input and the proportion of bioavailable (soluble) Fe present. Our results show that while dust fluxes decrease with transport distance, the solubility/bioavailability of the associated iron increases downwind as a consequence of greater transport distance and thus greater time of exposure to atmospheric photochemical reactions that favor transformation to more soluble Fe(III) phases. The decrease in Fe_{HR}/Fe_T ratios in downwind sediments fingerprints a loss of bioavailable Fe upon deposition due to dissolution of the Fe phases. Despite lower dust fluxes compared to upwind sites (Figure 4a), our data are consistent with the idea of downwind loci of productivity stimulated by elevated bioavailability of the iron (Figure 4b). The enhancement of reactivity, we suggest, would surpass the consequences of more abundant inputs of less-soluble Fe upwind. Previous suggestions of enhanced biological activity related to these Fe patterns include microbial response in the surface layers, nitrogen

fixation of the North Atlantic Ocean (Moore et al., 2009), carbonate production in Bahamas (Swart et al., 2014), growth of the coral reefs in the Caribbean (Prospero and Mayol-Bracero, 2013), and the fertilization of Amazon region (Bristow et al., 2010). For example, Swart et al. 2014 argued for dust-related stimulation of Fe-limited nitrogen-fixing cyanobacteria with a concomitant local drawdown of CO_2 that triggers carbonate precipitation in the Bahamas. Importantly, suggestions of lower total Fe concentrations at proximal sites (Figure 3b) mostly reflect higher carbonate dilution at those locations.

CONCLUSION

In summary, distal sites would be characterized by lower dust fluxes and thus total Fe delivery. The key point, however, is that reactivity of the distal site is elevated beyond that found proximally. In other words, the 'reactive' Fe pool in proximal locations would be dominated by relatively insoluble phases, so that even high total dust fluxes would result in relatively low delivery of bioavailable Fe. In contrast, the distal sites receive less dust, but the Fe is highly soluble and bioavailable because of distance-dependent transport processing in the atmosphere. This Fe, we argue, is lost upon deposition in the ocean, which results in the lower residual ratio of reactive to total iron in the sedimentary record compared to the sediments of the proximal sites. Beyond impacts in the recent North Atlantic, our data suggest that distal enhancement of Fe bioavailability in Fe-limited regions could help explain patterns of biological activity and organic accumulation relative to dust source in other regions throughout Earth history (Sardar Abadi et al., 2019).

REFERENCES

Anderson, R., Cheng, H., Edwards, R., Fleisher, M., Hayes, C., Huang, K.-F., Kadko, D., Lam, P., Landing, W., and Lao, Y., 2016, How well can we quantify dust deposition to the ocean?: Philosophical Transactions of the Royal Society A: Mathematical, Physical and Engineering Sciences, v. 374, no. 2081, p. 20150285.

Arnold, G. L., Weyer, S., and Anbar, A., 2004, Fe isotope variations in natural materials measured using high mass resolution multiple collector ICPMS: Analytical Chemistry, v. 76, no. 2, p. 322-327.

Bacon, M. P., Huh, C.-A., Fleer, A. P., and Deuser, W. G., 1985, Seasonality in the flux of natural radionuclides and plutonium in the deep Sargasso Sea: Deep Sea Research Part A. Oceanographic Research Papers, v. 32, no. 3, p. 273-286.

Baker, A. R., and Croot, P. L., 2010, Atmospheric and marine controls on aerosol iron solubility in seawater: Marine Chemistry, v. 120, no. 1-4, p. 4-13.

Baker, A. R., and Jickells, T. D., 2006, Mineral particle size as a control on aerosol iron solubility: Geophysical Research Letters, v. 33, no. 17.

Baker, A. R., Jickells, T. D., Witt, M., and Linge, K. L., 2006, Trends in the solubility of iron, aluminium, manganese and phosphorus in aerosol collected over the Atlantic Ocean: Marine Chemistry, v. 98, no. 1, p. 43-58.

Baker, A. R., Kelly, S. D., Biswas, K. F., Witt, M., and Jickells, T. D., 2003, Atmospheric deposition of nutrients to the Atlantic Ocean: Geophysical Research Letters, v. 30, no. 24.
Barbeau, K., 2006, Photochemistry of organic iron(III) complexing ligands in oceanic systems: Photochemistry and Photobiology, v. 82, no. 6, p. 1505-1516.

Beard, B. L., Johnson, C. M., Skulan, J. L., Nealson, K. H., Cox, L., and Sun, H., 2003a, Application of Fe isotopes to tracing the geochemical and biological cycling of Fe: Chemical Geology, v. 195, no. 1, p. 87-117.

Beard, B. L., Johnson, C. M., Von Damm, K. L., and Poulson, R. L., 2003b, Iron isotope constraints on Fe cycling and mass balance in oxygenated Earth oceans: Geology, v. 31, no. 7, p. 629-632.

Benner, S. G., Hansel, C. M., Wielinga, B. W., Barber, T. M., and Fendorf, S., 2002, Reductive dissolution and biomineralization of iron hydroxide under dynamic flow conditions: Environmental Science & Technology, v. 36, no. 8, p. 1705-1711.

Blott, S., 2000, Grain size distribution and statistics package for the analysis of unconsolidated sediments by sieving or by laser granulometer: Grandistat, p. 1-6.

Blott, S. J., and Pye, K., 2001, GRADISTAT: A grain size distribution and statistics package for the analysis of unconsolidated sediments: Earth Surface Processes and Landforms, v. 26, no. 11, p. 1237-1248.

Borchardt, T., Fisher, K. V., Ebling, A. M., Westrich, J. R., Xian, P., Holmes, C. D., Landing, W. M., Lipp, E. K., Wetz, M. S., and Ottesen, E. A., 2019, Saharan dust deposition initiates successional patterns among marine microbes in the Western Atlantic: Limnology and Oceanography.

Boyd, P., and Ellwood, M., 2010, The biogeochemical cycle of iron in the ocean: Nature Geoscience, v. 3, no. 10, p. 675.

Bressac, M., and Guieu, C., 2013, Post-depositional processes: What really happens to new atmospheric iron in the ocean's surface?: Global biogeochemical cycles, v. 27, no. 3, p. 859-870.

Bristow, C. S., Hudson-Edwards, K. A., and Chappell, A., 2010, Fertilizing the Amazon and equatorial Atlantic with West African dust: Geophysical Research Letters, v. 37, no. 14.

Clarkson, M., Poulton, S., Guilbaud, R., and Wood, R., 2014, Assessing the utility of Fe/Al and Fe-speciation to record water column redox conditions in carbonate-rich sediments: Chemical Geology, v. 382, p. 111-122.
Conway, T. M., and John, S. G., 2014, Quantification of dissolved iron sources to the North Atlantic Ocean: Nature, v. 511, no. 7508, p. 212-+.

Dauphas, N., and Rouxel, O., 2006, Mass spectrometry and natural variations of iron isotopes: Mass Spectrometry Reviews, v. 25, no. 4, p. 515-550.

Desboeufs, K., Losno, R., and Colin, J.-L., 2001, Factors influencing aerosol solubility during cloud processes: Atmospheric environment, v. 35, no. 20, p. 3529-3537.

Engelstaedter, S., Tegen, I., and Washington, R., 2006, North African dust emissions and transport: Earth-Science Reviews, v. 79, no. 1-2, p. 73-100.

Fan, S.-M., Moxim, W. J., and Levy, H., 2006, Aeolian input of bioavailable iron to the ocean: Geophysical Research Letters, v. 33, no. 7.

Fung, I. Y., Meyn, S. K., Tegen, I., Doney, S. C., John, J., and Bishop, J., 2000, Iron supply and demand in the upper ocean (vol 14, pg 281, 2000): Global Biogeochemical Cycles, v. 14, no. 2, p. 697-700.

Ginoux, P., Chin, M., Tegen, I., Prospero, J., Holben, B., Dubovik, O., and Lin, S., 2001, Global simulation of dust in the troposphere: Model description and assessment: J. Geophys. Res, v. 106, no. 20, p. 255-220.

Giosan, L., Flood, R. D., Grützner, J., and Mudie, P., 2002, Paleoceanographic significance of sediment color on western North Atlantic drifts: II. Late Pliocene–Pleistocene sedimentation: Marine Geology, v. 189, no. 1-2, p. 43-61.

Hand, J. L., Mahowald, N. M., Chen, Y., Siefert, R. L., Luo, C., Subramaniam, A., and Fung, I., 2004, Estimates of atmospheric-processed soluble iron from observations and a global mineral aerosol model: Biogeochemical implications: Journal of Geophysical Research-Atmospheres, v. 109, no. D17.

Harrison, S. P., Kohfeld, K. E., Roelandt, C., and Claquin, T., 2001, The role of dust in climate changes today, at the last glacial maximum and in the future: Earth-Science Reviews, v. 54, no. 1–3, p. 43-80.

Hassler, C. S., Schoemann, V., Nichols, C. M., Butler, E. C. V., and Boyd, P. W., 2011, Saccharides enhance iron bioavailability to Southern Ocean phytoplankton: Proceedings of the National Academy of Sciences of the United States of America, v. 108, no. 3, p. 1076-1081.

Haynes, W., 2013, Student's t-test, Encyclopedia of Systems Biology, Springer, p. 2023-2025.

Heron, G., Crouzet, C., Bourg, A. C., and Christensen, T. H., 1994, Speciation of Fe (II) and Fe (III) in contaminated aquifer sediments using chemical extraction techniques: Environmental science & technology, v. 28, no. 9, p. 1698-1705.

Huneeus, N., Schulz, M., Balkanski, Y., Griesfeller, J., Prospero, M., Kinne, S., Bauer, S., Boucher, O., Chin, M., and Dentener, F., 2011, Global dust model intercomparison in AeroCom phase I: Atmospheric Chemistry and Physics, v. 11, p. 7781-7816.

Jickells, T., An, Z., Andersen, K. K., Baker, A., Bergametti, G., Brooks, N., Cao, J., Boyd, P., Duce, R., and Hunter, K., 2005a, Global iron connections between desert dust, ocean biogeochemistry, and climate: science, v. 308, no. 5718, p. 67-71.

Jickells, T. D., An, Z. S., Andersen, K. K., Baker, A. R., Bergametti, G., Brooks, N., Cao, J. J., Boyd, P. W., Duce, R. A., Hunter, K. A., Kawahata, H., Kubilay, N., laRoche, J., Liss, P. S., Mahowald, N., Prospero, J. M., Ridgwell, A. J., Tegen, I., and Torres, R., 2005b, Global Iron Connections Between Desert Dust, Ocean Biogeochemistry, and Climate: Science, v. 308, no. 5718, p. 67–71.

Joos, F., Sarmiento, J. L., and Siegenthaler, U., 1991, Estimates of the effect of Southern Ocean iron fertilization on atmospheric CO2 concentrations: Nature, v. 349, no. 6312, p. 772.

Lis, H., Shaked, Y., Kranzler, C., Keren, N., and Morel, F. M., 2015, Iron bioavailability to phytoplankton: an empirical approach: The ISME journal, v. 9, no. 4, p. 1003.

Mackie, D., Peat, J., McTainsh, G., Boyd, P., and Hunter, K., 2006, Soil abrasion and eolian dust production: Implications for iron partitioning and solubility: Geochemistry, Geophysics, Geosystems, v. 7, no. 12.

Maher, B., Prospero, J., Mackie, D., Gaiero, D., Hesse, P. P., and Balkanski, Y., 2010, Global connections between aeolian dust, climate and ocean biogeochemistry at the present day and at the last glacial maximum: Earth-Science Reviews, v. 99, no. 1, p. 61-97.

Mahowald, N., Albani, S., Kok, J. F., Engelstaeder, S., Scanza, R., Ward, D. S., and Flanner, M. G., 2014, The size distribution of desert dust aerosols and its impact on the Earth system: Aeolian Research, v. 15, p. 53-71.

Mahowald, N., Kohfeld, K., Hansson, M., Balkanski, Y., Harrison, S. P., Prentice, I. C., Schulz, M., and Rodhe, H., 1999, Dust sources and deposition during the last glacial maximum and current climate: A comparison of model results with paleodata from ice cores and marine sediments: Journal of Geophysical Research-Atmospheres, v. 104, no. D13, p. 15895-15916.

Mahowald, N. M., Hamilton, D. S., Mackey, K. R., Moore, J. K., Baker, A. R., Scanza, R. A., and Zhang, Y., 2018, Aerosol trace metal leaching and impacts on marine microorganisms: Nature communications, v. 9, no. 1, p. 1-15.

Martin, J. H., and Fitzwater, S. E., 1988, Iron deficiency limits phytoplankton growth in the north-east Pacific subarctic: Nature, v. 331, no. 6154, p. 341.

Martinez, N. C., Murray, R., Thunell, R. C., Peterson, L. C., Muller-Karger, F., Astor, Y., and Varela, R., 2007, Modern climate forcing of terrigenous deposition in the tropics (Cariaco Basin, Venezuela): Earth and Planetary Science Letters, v. 264, no. 3-4, p. 438-451.

McGee, D., Broecker, W. S., and Winckler, G., 2010, Gustiness: The driver of glacial dustiness?: Quaternary Science Reviews, v. 29, no. 17-18, p. 2340-2350.

McGee, D., deMenocal, P. B., Winckler, G., Stuut, J. B. W., and Bradtmiller, L. I., 2013, The magnitude, timing and abruptness of changes in North African dust deposition over the last 20,000yr: Earth and Planetary Science Letters, v. 371-372, p. 163-176.

Meskhidze, N., Völker, C., Al-Abadleh, H. A., Barbeau, K., Bressac, M., Buck, C., Bundy, R. M., Croot, P., Feng, Y., and Ito, A., 2019, Perspective on identifying and characterizing the processes controlling iron speciation and residence time at the atmosphere-ocean interface: Marine Chemistry, p. 103704.

Montgomery, D. C., Runger, G. C., and Hubele, N. F., 2009, Engineering statistics, John Wiley & Sons.

Moore, C. M., Mills, M. M., Achterberg, E. P., Geider, R. J., LaRoche, J., Lucas, M. I., McDonagh, E. L., Pan, X., Poulton, A. J., Rijkenberg, M. J. A., Suggett, D. J., Ussher, S. J., and Woodward, E. M. S., 2009, Large-scale distribution of Atlantic nitrogen fixation controlled by iron availability: Nature Geoscience, v. 2, no. 12, p. 867-871.

Muhs, D. R., Budahn, J. R., Prospero, J. M., and Carey, S. N., 2007, Geochemical evidence for African dust inputs to soils of western Atlantic islands: Barbados, the Bahamas, and Florida: Journal of Geophysical Research, v. 112, no. F2.

Muhs, D. R., Budahn, J. R., Prospero, J. M., Skipp, G., and Herwitz, S. R., 2012, Soil genesis on the island of Bermuda in the Quaternary: The importance of African dust transport and deposition: Journal of Geophysical Research: Earth Surface, v. 117, no. F3, p. n/a-n/a.

Oakes, M., Ingall, E., Lai, B., Shafer, M., Hays, M., Liu, Z., Russell, A., and Weber, R., 2012, Iron solubility related to particle sulfur content in source emission and ambient fine particles: Environmental science & technology, v. 46, no. 12, p. 6637-6644.

Ooki, A., Nishioka, J., Ono, T., and Noriki, S., 2009, Size dependence of iron solubility of Asian mineral dust particles: Journal of Geophysical Research-Atmospheres, v. 114.

Owens, J. D., Lyons, T. W., Li, X. N., Macleod, K. G., Gordon, G., Kuypers, M. M. M., Anbar, A., Kuhnt, W., and Severmann, S., 2012, Iron isotope and trace metal records of iron cycling in the proto-North Atlantic during the Cenomanian-Turonian oceanic anoxic event (OAE-2): Paleoceanography, v. 27.

Poulton, S. W., and Canfield, D. E., 2005, Development of a sequential extraction procedure for iron: implications for iron partitioning in continentally derived particulates: Chemical Geology, v. 214, no. 3-4, p. 209-221.

Poulton, S. W., and Raiswell, R., 2005, Chemical and physical characteristics of iron oxides in riverine and glacial meltwater sediments: Chemical Geology, v. 218, no. 3-4, p. 203-221.

Prospero, J. M., and Mayol-Bracero, O. L., 2013, Understanding the Transport and Impact of African Dust on the Caribbean Basin: Bulletin of the American Meteorological Society, v. 94, no. 9, p. 1329-1337.

Pye, K., 1989, Processes of fine particle formation, dust source regions, and climatic changes, Paleoclimatology and Paleometeorology: Modern and Past Patterns of Global Atmospheric Transport, Springer, p. 3-30.

Raiswell, R., and Canfield, D. E., 2012, The Iron Biogeochemical Cycle Past and Present: Geochemical Perspectives, v. 1, no. 1, p. 1-220.

Raiswell, R., Hardisty, D. S., Lyons, T. W., Canfield, D. E., Owens, J. D., Planavsky, N. J., Poulton, S. W., and Reinhard, C. T., 2018a, The iron paleoredox proxies: A guide to the pitfalls, problems and proper practice: American Journal of Science, v. 318, no. 5, p. 491-526.

Raiswell, R., Hawkings, J., Elsenousy, A., Death, R., Tranter, M., and Wadham, J., 2018b, Iron in Glacial Systems: Speciation, Reactivity, Freezing Behaviour and Alteration during Transport: Frontiers in Earth Science, v. 6, p. 222.

Ridgwell, A., and Hargreaves, J., 2007, Regulation of atmospheric CO2 by deep-sea sediments in an Earth system model: Global Biogeochemical Cycles, v. 21, no. 2.

Sardar Abadi, M., Owens, J. D., Liu, X., Them, T. R., Cui, X., Heavens, N. G., and Soreghan, G. S., 2019, Atmospheric dust stimulated marine primary productivity during Earth's penultimate icehouse: Geology.

Schwertmann, U., Stanjek, H., and Becher, H.-H., 2004, Long-term in vitro transformation of 2-line ferrihydrite to goethite/hematite at 4, 10, 15 and 25 C: Clay Minerals, v. 39, no. 4, p. 433-438.

Shaked, Y., and Lis, H., 2012, Disassembling iron availability to phytoplankton: Frontiers in microbiology, v. 3.

Shi, Z. B., Krom, M. D., Bonneville, S., Baker, A. R., Jickells, T. D., and Benning, L. G., 2009, Formation of Iron Nanoparticles and Increase in Iron Reactivity in Mineral Dust during Simulated Cloud Processing: Environmental Science & Technology, v. 43, no. 17, p. 6592-6596.

Shinn, E. A., Smith, G. W., Prospero, J. M., Betzer, P., Hayes, M. L., Garrison, V., and Barber, R. T., 2000, African dust and the demise of Caribbean coral reefs: Geophysical Research Letters, v. 27, no. 19, p. 3029-3032.

Shoenfelt, E. M., Sun, J., Winckler, G., Kaplan, M. R., Borunda, A. L., Farrell, K. R., Moreno, P. I., Gaiero, D. M., Recasens, C., and Sambrotto, R. N., 2017, High particulate iron (II) content in glacially sourced dusts enhances productivity of a model diatom: Science advances, v. 3, no. 6, p. e1700314.

Shoenfelt, E. M., Winckler, G., Lamy, F., Anderson, R. F., and Bostick, B. C., 2018, Highly bioavailable dust-borne iron delivered to the Southern Ocean during glacial periods: Proceedings of the National Academy of Sciences, v. 115, no. 44, p. 11180-11185.

Skonieczny, C., McGee, D., Winckler, G., Bory, A., Bradtmiller, L., Kinsley, C., Polissar, P., De Pol-Holz, R., Rossignol, L., and Malaizé, B., 2019, Monsoon-driven Saharan dust variability over the past 240,000 years: Science advances, v. 5, no. 1, p. eaav1887.

Skulan, J. L., Beard, B. L., and Johnson, C. M., 2002, Kinetic and equilibrium Fe isotope fractionation between aqueous Fe(III) and hematite: Geochimica et Cosmochimica Acta, v. 66, no. 17, p. 2995–3015.

Spokes, L. J., Jickells, T. D., and Lim, B., 1994, Solubilisation of aerosol trace metals by cloud processing: A laboratory study: Geochimica et Cosmochimica Acta, v. 58, no. 15, p. 3281-3287.

Swart, P. K., Oehlert, A., Mackenzie, G., Eberli, G. P., and Reijmer, J., 2014, The fertilization of the Bahamas by Saharan dust: A trigger for carbonate precipitation?: Geology, v. 42, no. 8, p. 671-674.

Thöle, L. M., Amsler, H. E., Moretti, S., Auderset, A., Gilgannon, J., Lippold, J., Vogel, H., Crosta, X., Mazaud, A., and Michel, E., 2019, Glacial-interglacial dust and export production records from the Southern Indian Ocean: Earth and planetary science letters, v. 525, p. 115716.

Tiedemann, R., Sarnthein, M., and Stein, R., Climatic changes in the western Sahara: Aeolo-marine sediment record of the last 8 million years (sites 657-661), *in* Proceedings Proceedings of the ocean drilling program, scientific results1989, Volume 108, p. 241-277.

Trapp, J. M., Millero, F. J., and Prospero, J. M., 2010, Trends in the solubility of iron in dust-dominated aerosols in the equatorial Atlantic trade winds: Importance of iron speciation and sources: Geochemistry, Geophysics, Geosystems, v. 11, no. 3.

Viollier, E., Inglett, P., Hunter, K., Roychoudhury, A., and Van Cappellen, P., 2000, The ferrozine method revisited: Fe (II)/Fe (III) determination in natural waters: Applied geochemistry, v. 15, no. 6, p. 785-790.

Waeles, M., Baker, A. R., Jickells, T., and Hoogewerff, J., 2007, Global dust teleconnections: aerosol iron solubility and stable isotope composition: Environmental Chemistry, v. 4, no. 4, p. 233-237.

Ward, B. A., Wilson, J. D., Death, R. M., Monteiro, F. M., Yool, A., and Ridgwell, A., 2018, EcoGEnIE 1.0: plankton ecology in the cGEnIE Earth system model: Geoscientific Model Development, v. 11, no. 10, p. 4241-4267.

Wells, M. L., Zorkin, N. G., and Lewis, A., 1983, The role of colloid chemistry in providing a source of iron to phytoplankton: Journal of Marine Research, v. 41, no. 4, p. 731-746.

Yarincik, K., Murray, R., and Peterson, L., 2000, Climatically sensitive eolian and hemipelagic deposition in the Cariaco Basin, Venezuela, over the past 578,000 years: Results from Al/Ti and K/Al: Paleoceanography, v. 15, no. 2, p. 210-228.

Yu, H., Chin, M., Yuan, T., Bian, H., Remer, L. A., Prospero, J. M., Omar, A., Winker, D., Yang, Y., and Zhang, Y., 2015, The fertilizing role of African dust in the Amazon rainforest: A first multiyear assessment based on data from Cloud-Aerosol Lidar and Infrared Pathfinder Satellite Observations: Geophysical Research Letters, v. 42, no. 6, p. 1984-1991.

Zhang, Y., Mahowald, N., Scanza, R., Journet, E., Desboeufs, K., Albani, S., Kok, J., Zhuang, G., Chen, Y., and Cohen, D., 2015, Modeling the global emission, transport and deposition of trace elements associated with mineral dust.

FIGURES

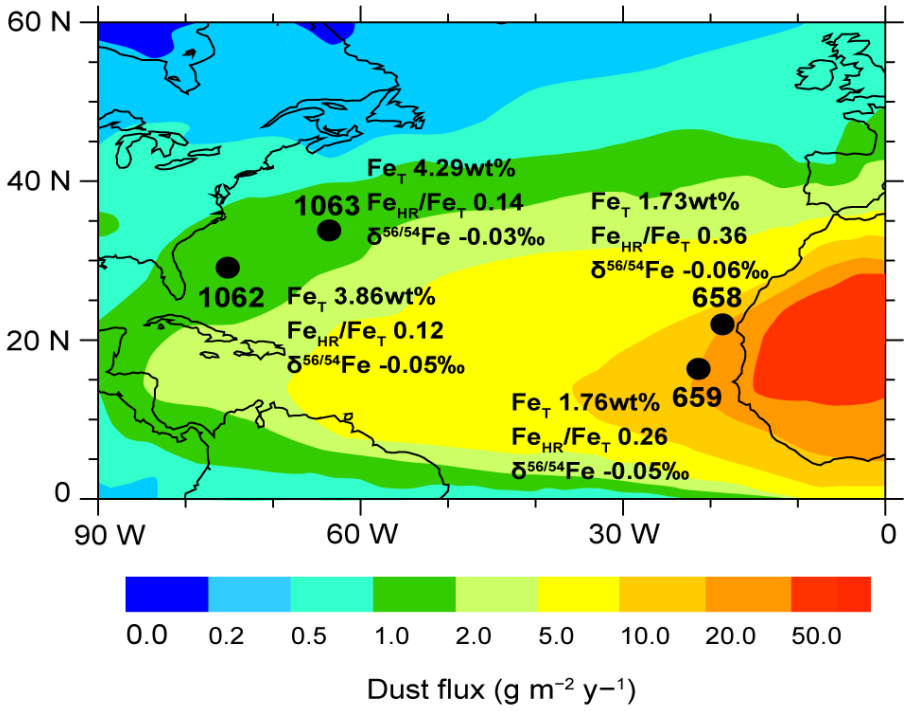

Figure 2.1: Locations of IODP sites 658, 659, 1062 and 1063 with Fe data. Base map shows estimates for dust deposition (g m^{-2} y^{-1}) — specifically transport of African dust across the surface ocean. Dust flux data are from Jickells et al. (2005), Mahowald et al. (1999), and Ginoux et al. (2001); all other data are from this study. Highly reactive Fe (Fe_{HR}) for each site is normalized to total Fe (Fe_T) to distinguish relative enrichments or deficiencies in the Fe_{HR} pool. Also shown are the Fe isotope compositions ($\delta^{56}Fe$) to constrain different sources of Fe.

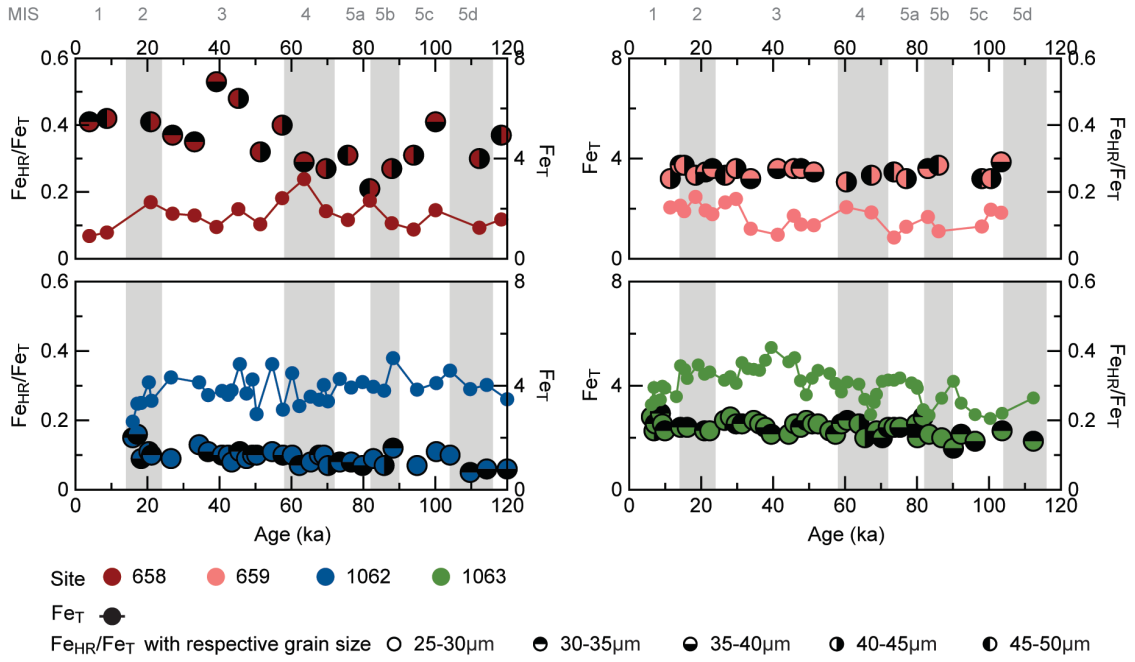

Figure 2.2: Age profiles for iron (Fe) in IODP cores 658 (red), 659 (orange), 1062 (blue), and 1063 (green) showing glacial-interglacial relationships. Gray bars indicate climatic events of importance for the Last Glacial Period (extending back ~ 120,000 years) as recorded in polar ice cores. MIS refers to marine isotope stages. Total Fe (Fe_T) is shown as filled, connected circles for each site. Highly reactive (Fe_{HR}) consists of (a) carbonate Fe (plus weakly bound surface Fe); (b) amorphous and crystalline Fe oxides and (oxyhydr)oxides such as ferrihydrite, goethite, and hematite; and (c) magnetite Fe. Fe_{HR} data are normalized to total Fe (Fe_T) to distinguish relative enrichments or deficiencies in the Fe_{HR} pool. Fe_{HR}/Fe_T ratios are expressed in terms of grain size populations.

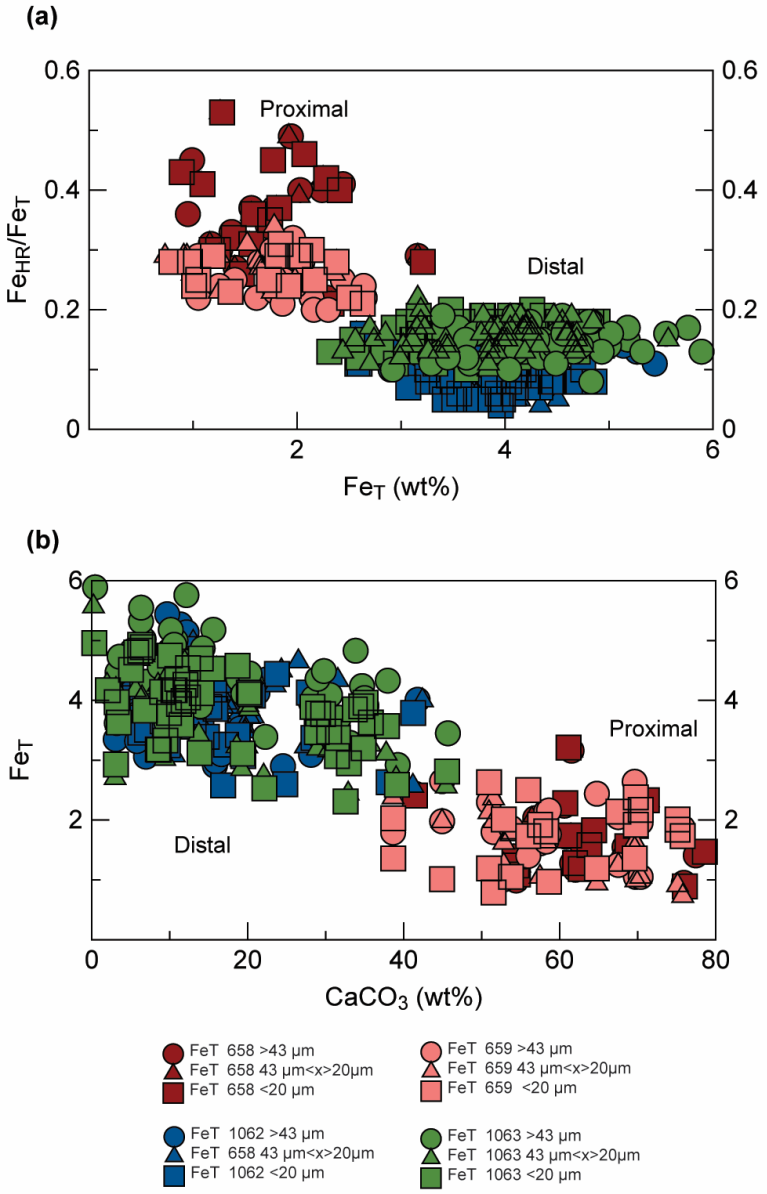

Figure 2.3: (a) Fe_{HR}/Fe_T versus Fe_T for proximal (658-red and 659-orange) and distal (1062-blue and 1063-green) sites. Note the systematic decrease in Fe_{HR}/Fe_T from proximal to distal sites. (b) Fe_T versus $CaCO_3$ for proximal and distal sites. The effects of carbonate dilution on Fe_T are confirmed by a steep inverse relationship between Fe_T and $CaCO_3$ content across all sites and in all size fractions. Samples with grain size >45µm (bulk), 45 to 20µm, and <20µm are shown as a circles, triangles, and squares, respectively. There is no significant difference in Fe_{HR}/Fe_T among the grain size populations from a given site.

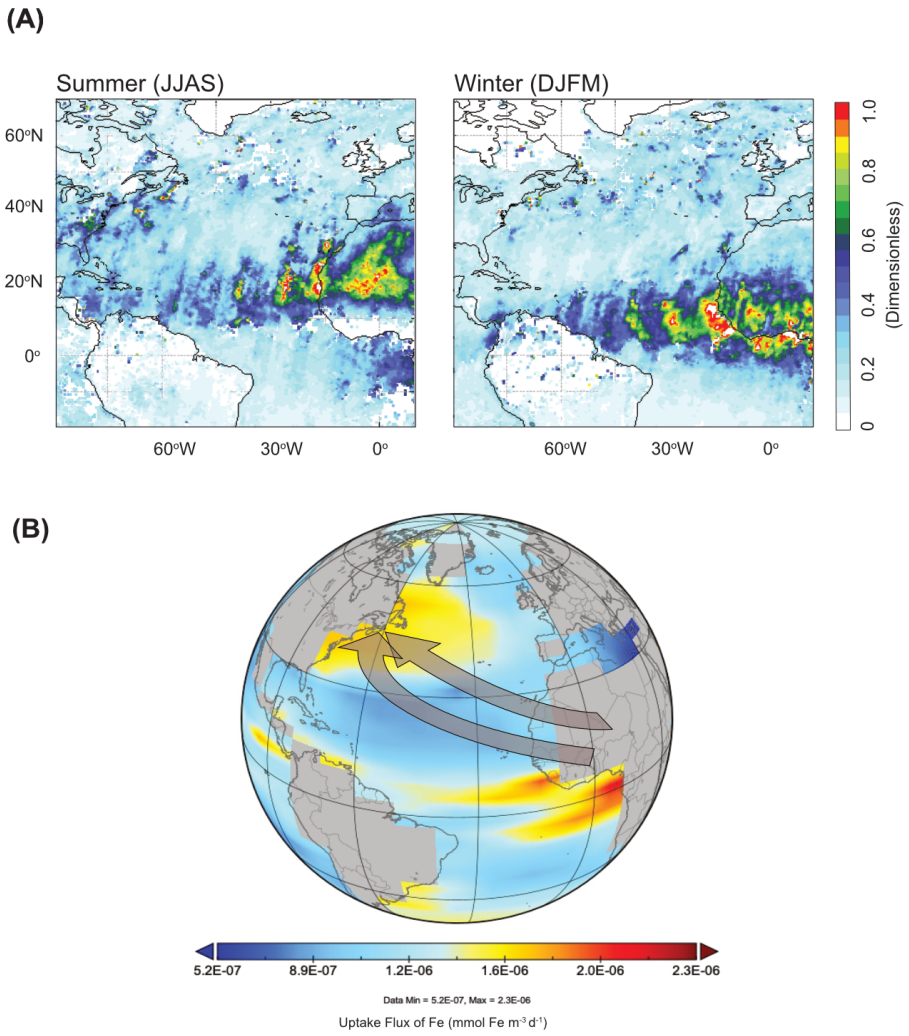

Figure 2.4: (A) Modern dust transport over the North Atlantic Ocean. Map of dust aerosol optical depth (AOD) over the North Atlantic showing the transport of African dust across the North Atlantic Ocean during the boreal summer [June-July-August-September (JJAS)] and boreal winter [December-January-February-March (DJFM)]. AOD is a measure of the extinction of the solar beam by dust and haze. It is a dimensionless number that is related to the amount of aerosol in the vertical column of atmosphere over the observation location. (B) Uptake of Fe flux modeled using ecoGEnIE. Gray arrow indicates the African dust that are carried from Northern Africa across the Atlantic Ocean.

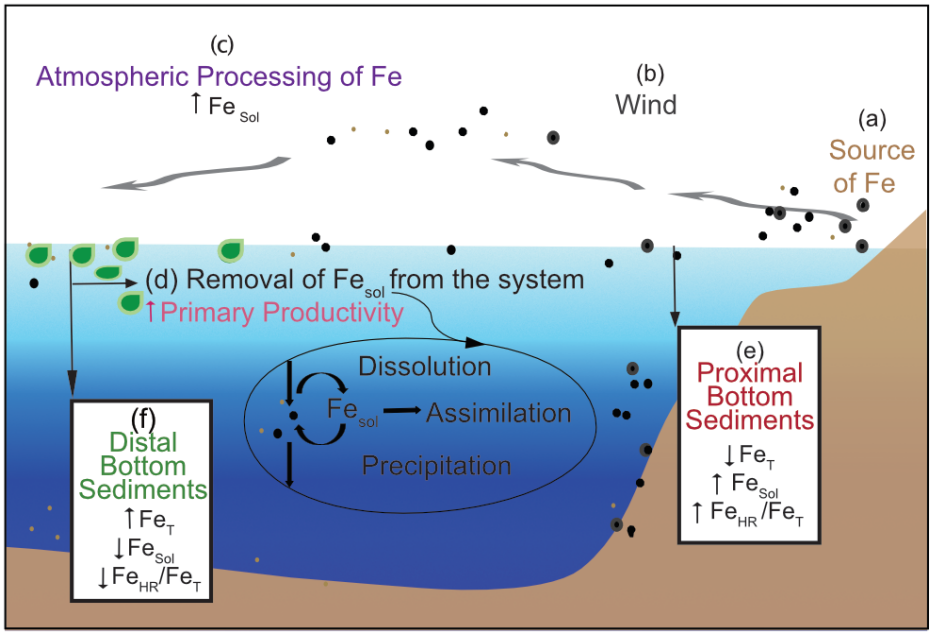

Figure 2.5: Generalized schematic of the iron biogeochemical cycle. The major source of Fe in the open ocean is dust delivered by the atmosphere. Fe_T: total, Fe_{HR}: highly reactive Fe (at least partly bioavailable Fe at the time of deposition), and FeSol : soluble Fe (bioavailable Fe that is readily used for primary productivity). (a) Source of dust is from the Sahara Desert. (b) Wind eroding soils containing Fe oxides and silicates leads to transport of the dust seaward. Coarse particles will sink rapidly, while smaller particles will travel further in the atmosphere and remain in the surface ocean longer. (c) Atmospheric processing can increase Fe solubility and bioavailability. (d) In the ocean, FeSol is removed from the system via dissolution and is assimilated by the phytoplankton. The dissolved Fe does not remain in solution in oxic seawater since oxidation to Fe(III) is rapid, and seawater is close to saturation with iron(oxyhydr)oxides. (e) Sediments of proximal sites show relatively low values for Fe_T due to carbonate dissolution and relatively high Fe_{Sol} and Fe_{HR}/Fe_T. (f) Sediments at distal sites show decreases of FeSol due to its dissolution and removal by primary producers in the surface ocean, leading to low values for FeSol and Fe_{HR}/Fe_T in the underlying sediments.

APPENDIX – Supplement

Site	Fe_T (wt%)	Fe_{HR} (wt%)	Fe_{HR}/Fe_T	Fe_T/Al	$CaCO_3$ (wt%)	TOC (wt%)	Al/Ti	$\delta^{56/54}Fe$ (‰)
658	1.73	0.61	0.36	0.58	62.78	0.64	18.45	-0.06
659	1.76	0.44	0.26	0.52	59.44	0.14	18.16	-0.05
1062	3.86	0.44	0.12	0.54	16.38	0.41	19.24	-0.05
1063	4.29	0.62	0.14	0.56	18.22	0.17	19.56	-0.03

Table 2. S1: Mean values for all the Fe data at all four sites.

Fe speciation
Fe-extractions from each site are presented in wt%.

658 (n=54)	$Fe_{Na\text{-}Ac}$ (wt%)	Fe_{Dith} (wt%)	Fe_{Ox} (wt%)
>45µm	0.05	0.37	0.20
45µm<x>20µm	0.04	0.37	0.21
<20µm	0.04	0.37	0.20

Table 2. S2a: Eighteen samples were analyzed for each grain size (total 54 samples).

659 (n=66)	$Fe_{Na\text{-}Ac}$ (wt%)	Fe_{Dith} (wt%)	Fe_{Ox} (wt%)
>45µm	0.04	0.27	0.14
45µm<x>20µm	0.03	0.26	0.14
<20µm	0.03	0.27	0.15

Table 2. S2b: Twenty-two samples were analyzed for each grain size (total 66 samples).

1062 (n=105)	$Fe_{Na\text{-}Ac}$ (wt%)	Fe_{Dith} (wt%)	Fe_{Ox} (wt%)
>45µm	0.02	0.26	0.17
45µm<x>20µm	0.02	0.26	0.15
<20µm	0.02	0.26	0.15

Table 2. S2c: Thirty-five samples were analyzed for each grain size (total 105 samples).

1063 (n=159)	$Fe_{Na\text{-}Ac}$ (wt%)	Fe_{Dith} (wt%)	Fe_{Ox} (wt%)
>45µm	0.02	0.38	0.24
45µm<x>20µm	0.02	0.38	0.23
<20µm	0.02	0.37	0.23

Table 2. S2d: Fifty-three samples were analyzed for each grain size (total 159 samples).

Fe extraction pools in relation to total iron (Fe_T)

658 (n=54)	$Fe_{Na\text{-}Ac}$ % of Fe_T	Fe_{Dith} % of Fe_T	Fe_{Ox} % of Fe_T
>45µm	2.9	21.4	11.6
45µm<x>20µm	2.3	21.6	12.1
<20µm	2.3	21.4	11.3

Table 2. S3a: Percentage of Fe extracted from Fe_T.

659 (n=66)	$Fe_{Na\text{-}Ac}$ % of Fe_T	Fe_{Dith} % of Fe_T	Fe_{Ox} % of Fe_T
>45µm	2.2	14.8	7.7
45µm<x>20µm	1.6	14.9	7.8
<20µm	2.0	15.8	8.5

Table 2. S3b: Percentage of Fe extracted from Fe_T.

1062 (n=105)	$Fe_{Na\text{-}Ac}$ % of Fe_T	Fe_{Dith} % of Fe_T	Fe_{Ox} % of Fe_T
>45µm	0.5	8.7	5.4
45µm<x>20µm	0.5	8.8	5.3
<20µm	0.6	8.9	5.5

Table 2. S3c: Percentage of Fe extracted from Fe_T.

1063 (n=159)	$Fe_{Na\text{-}Ac}$ % of Fe_T	Fe_{Dith} % of Fe_T	Fe_{Ox} % of Fe_T
>45µm	0.5	8.6	5.4
45µm<x>20µm	0.6	9.1	5.9
<20µm	0.6	9.6	6.0

Table 2. S3d: Percentage of Fe extracted from Fe_T.

Sodium acetate extraction experiment

Sample	$Fe_{Na\text{-}Ac}$ (wt%)	$Fe_{Na\text{-}Ac}$ (%) of Fe_T
Biotite 1	0.15	0.09
Biotite 2	0.17	0.09
Chlorite 1	0.07	0.48
Chlorite 2	0.07	0.52
Fayalite 1	0.10	0.64
Fayalite 2	0.11	0.63
Hornblende 1	0.04	0.23
Hornblende2	0.04	0.20

Table 2. S4: Percentage of Fe extracted from different minerals by the sodium acetate step. The data indicate that only a very small amount of Fe bound in silicate phases is removed.

Grain Size Distribution (GSD)

METHOD OF MOMENTS		658 (n=18)	659 (n=22)	1062 (n=35)	1063 (n=53)
Arithmetic (µm)	MEAN ($\bar{x}_a$)	41.89	41.43	33.70	32.72
	SKEWNES (Sk_a)	2.04	0.99	1.08	0.97
	KURTOSIS (K_a)	12.67	5.60	5.33	5.04
Geometric (µm)	MEAN ($\bar{x}_g$)	37.49	37.09	29.90	28.76
	SKEWNES (Sk_g)	-0.45	-0.50	-0.23	-0.24
	KURTOSIS (K_g)	3.866	3.32	3.55	3.04

	SIEVING ERROR (%)	8.7	6.3	6.0	7.3

Table 2. S5: Average GSD (grain size distribution) for all four sites based on dry sieving. Sieving error calculated based on sample loss and comparison with wet sieving.

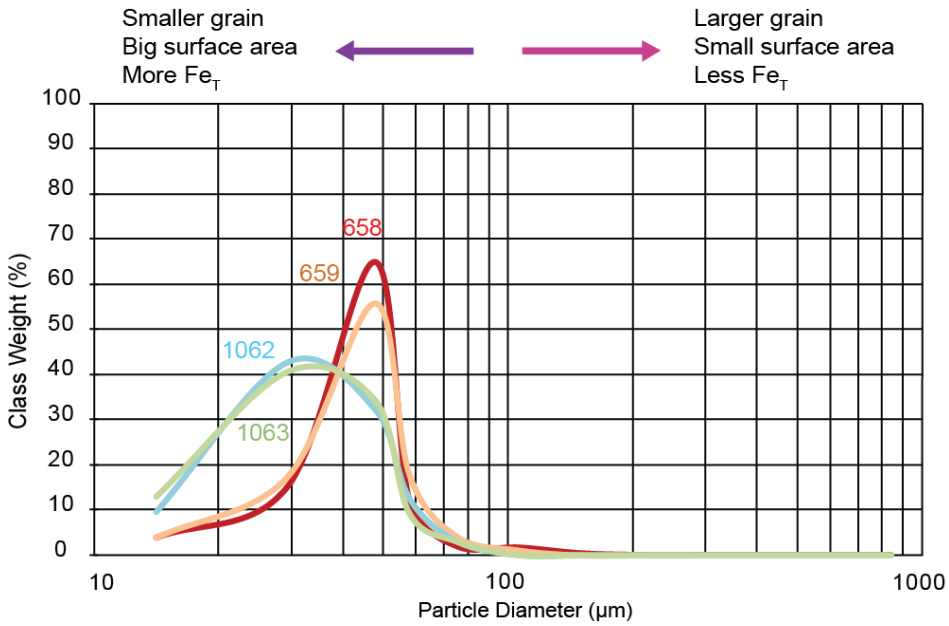

Figure 2. S1: Plot of grain size data for representative samples from ODP drill cores based on dry sieving.

Export of dust particles in the water column

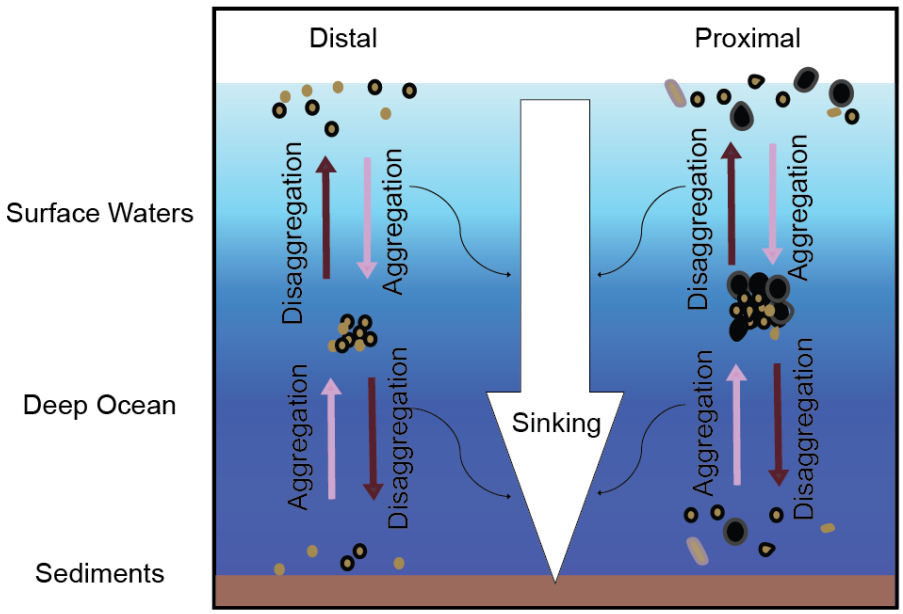

Figure 2. S2: Schematic representation of hypothesized export of dust particles in the water column. Dust particles can be aggregated into larger, sinking particles, which can sink and be removed from the water column or disaggregate back to slowly settling particles. Dust particles undergo many cycles of aggregation and disaggregation in the water column (49-50), making the chemical composition of large aggregates similar to the smaller particles (see text).

Surface area analysis

For a given weight and total volume of a particular material, the surface activity and adsorption volume can vary as a function of the grain size and thus surface area. Surface area is important in our study in terms of reactions during transport that enhance Fe bioavailability.

Surface area can be calculated from the grain size distribution by dividing the size distribution into a finite number of bins and assuming equivalent spherical diameters of particles that correspond to the mean size of each bin (Cepuritis et al., 2017) and using the following relation (Ersahin et al., 2006):

$$SA = \frac{6000}{\rho D}, \qquad \text{(Baron and Willeke, 2001)}$$

where ρ is the material density, and D the size of the particle. We assume a density of 1.49 g/cm^3 for dust (Parnell Jr et al., 1986).

	658	**659**	**1062**	**1063**
Arithmetic surface area (m^2/kg)	96.13	97.20	119.49	123.07
Geometric surface area (m^2/kg)	107.41	108.57	134.68	140.02

Table 2. S6: Surface area calculations based on mean grain size distributions.

Location, average dust deposition fluxes, and age models

Core	Location	Water Depth (m)	Our Estimated Eolian Flux (g m^{-2} y^{-1})	Eolian flux (g m^{-2} y^{-1})	Eolian flux Reference	Age Model Reference
ODP Leg 108 Site 658	21°N, 19°W	2263	20.1	19.2	Adkins et al. (2006); deMenocal et al. (2000)	Tiedemann et al. (1989b)
ODP Leg 108 Site 659	18°N, 21°W	3070	19.5	14.7	Tiedemann et al. (1994)	Tiedemann et al. (1994)
ODP Leg 172 Site 1062	28°N, 74°W	4765	1.5	1.3	Arimoto et al. (2003)	Franz and Tiedemann, (2002); Gruetzner et al (2002)
ODP Leg 172 Site 1063	33°N, 57°W	4585	1.4	1.6	Muhs et al. (2012)	Channell et al. (2012); Gruetzner et al. (2002)

Table 2. S7: Desert dust deposition ($g/m^2/y$) estimated from the average of three models (Jickells et al., 2005c; Mahowald et al., 2008; Mahowald et al., 1999) representing our best estimate of dust deposition.

Statistical analyses of iron geochemical data for different grain size populations

The normality of the data in each sample was verified by comparing the ANOVA and t-test. The analyses with low p-values (< 0.05) can be considered to have a skewed or non-normal distribution.

The ANOVA test for independent measures is designed to compare the means of three or more independent samples simultaneously of grain size.

SS: Sums of Squares

df: Degree of freedom

MS: Means of squares

The test statistic for testing H_0: $\mu_1 = \mu_2 = ... = \mu_k$ is:

$$F = \frac{\sum N_j(\ \overline{X_j} - \overline{X}\ )\ /\ (k-1)}{\sum\ (X - \overline{X_j}\ )^2\ /(N-k)}$$

The **t test statistic** is used to determine if there is a significant difference between the means of two groups and to determine if they come from the same population.

$$t = \frac{\overline{X_1} - \overline{X_2}}{\sqrt{\left(\frac{(N_1-1)S_1^2 + (N_2-1)S_2^2}{N_1 + N_2 - 2}\right)\left(\frac{1}{N_1} + \frac{1}{N_2}\right)}}$$

Statistical analyses of the Fe_{HR}/Fe_T data for each site

Site 658

	Site 658			
	>45µm	45µm<x>20µm	<20µm	Total
N	18	18	18	54
∑X	6.42	6.42	6.43	19.27
Mean	0.3567	0.3567	0.3572	0.357
$\sum X^2$	2.4	2.4038	2.4149	7.2187
Std.Dev.	0.0805	0.0819	0.0833	0.0803

ANOVA test

Site 658	***SS***	***df***	***MS***	
Between grain sizes	0	2	0	F = 0.00028
Within grain sizes	0.3422	51	0.0067	
Total	0.3422	53		

The *f*-ratio value is 0.00028. The *p*-value is .999724. The result is *not* significant at $p < .05$.

Student´s **T-test (**two-tailed)

	Site 658		
	>45µm vs 45µm<x>20µm	>45µm vs <20µm	45µm<x>20µm vs <20µm
t-value	0	-0.02018	0.02035
p-value	1	0.984019	0.983887
Significance at $p < 0.05$	*not* significant	*not* significant	*not* significant

Table 2. S8a: Results of statistical analysis. ANOVA and T-test for site 658 that are significant at the P< 0.05 level are colored in black and are not significant when red.

Site 659

	Site 659			
	>45µm	45µm<x>20µm	<20µm	Total
N	22	22	22	66
∑X	5.43	5.43	5.8	16.66
Mean	0.2468	0.2468	0.2636	0.252
$\sum X^2$	1.3621	1.4161	1.547	4.3252
Std.Dev.	0.0323	0.0601	0.0292	0.0429

ANOVA test

Site 659	***SS***	***df***	***MS***	
Between grain sizes	0.0041	2	0.0021	F = 1.1298
Within grain sizes	0.1157	63	0.0018	
Total	0.1198	65		

The *f*-ratio value is 1.1298. The *p*-value is .329554. The result is *not* significant at $p < .05$.

Student´s **T-test** (two-tailed)

	Site 659		
	>45µm vs 45µm<x>20µm	>45µm vs <20µm	45µm<x>20µm vs <20µm
t-value	0	-1.81231	-1.1804
p-value	1	0.077091	0.244482
Significance at $p < 0.05$	*not* significant	*not* significant	*not* significant

Table 2. S8b: Results of statistical analysis. ANOVA and T-test for site 659 that are significant at the P< 0.05 level are colored in black and are not significant when red.

Site 1062

	Site 1062			
	>45µm	45µm<x>20µm	<20µm	Total
N	35	35	35	105
∑X	4.09	3.78	4.21	12.08
Mean	0.1169	0.108	0.1203	0.115
$\sum X^2$	0.5139	0.448	0.5583	1.5202
Std.Dev.	0.0325	0.0342	0.0391	0.0354

ANOVA test

Site 1062	***SS***	***df***	***MS***	
Between grain sizes	0.0028	2	0.0014	F = 1.12435
Within grain sizes	0.1276	102	0.0013	
Total	0.1304	104		

The *f*-ratio value is 1.12435. The *p*-value is .328856. The result is *not* significant at $p < .05$.

Student´s **T-test (**two-tailed)

	Site 1062		
	>45µm vs 45µm<x>20µm	>45µm vs <20µm	45µm<x>20µm vs <20µm
t-value	1.1104	-0.39904	-1.39988
p-value	0.270739	0.691117	0.083048
Significance at $p < 0.05$	*not* significant	*not* significant	*not* significant

Table 2. S8c: Results of statistical analysis. ANOVA and T-test for site 1062 that are significant at the P< 0.05 level are colored in black and are not significant when red.

Site 1063

	Site 1063			
	>45µm	45µm<x>20µm	<20µm	Total
N	53	53	53	159
∑X	7.67	7.63	7.99	23.29
Mean	0.1447	0.144	0.1508	0.146
$\sum X^2$	1.1435	1.1355	1.2499	3.5289
Std.Dev.	0.0254	0.0267	0.0295	0.0273

ANOVA test

Site1063	***SS***	***df***	***MS***	
Between grain sizes	0.0015	2	0.0007	F = 0.98825
Within grain sizes	0.116	156	0.0007	
Total	0.1174	158		

The *f*-ratio value is 0.98825. The *p*-value is .374545. The result is *not* significant at $p < .05$.

Student´s **T-test** (two-tailed)

	Site 1063		
	>45µm vs 45µm<x>20µm	>45µm vs <20µm	45µm<x>20µm vs <20µm
t-value	0.14913	-1.1285	-1.24195
p-value	0.881742	0.261706	0.217049
Significance at $p < 0.05$	*not* significant	*not* significant	*not* significant

Table 2. S8d: Results of statistical analysis. ANOVA and T-test for site 1063 that are significant at the P< 0.05 level are colored in black and not significant in red.

Statistical analyses of GDS during glacial-interglacial periods

The one sample *t*-Test is used to determine the difference between a sample mean and a known value of the mean in the population to check for the variability of grain size distribution during glacial-interglacial time periods.

The null hypothesis is:

H_o: M-μ = 0, where M is the sample mean and μis the population mean or hypothesized mean.

$$t = \frac{M - \mu}{\sqrt{\left(\frac{\sum X^2 - ((\sum X)^2/N)}{(N-1)(N)}\right)}}$$

T-test	658 (n=18)	659 (n=22)	1062 (n=35)	1063 (n=53)
t-value	-0.15	-0.30	-0.35	-1.33
p-value	0.88	0.76	0.72	0.19
Significance at $p < 0.05$	*not* significant	*not* significant	*not* significant	*not* significant

Table 2. S9: Results of statistical analysis of GDS during glacial-interglacial periods. T-test for all four sites that are significant at the $p < 0.05$ level are colored in black and are not significant when red.

Geochemical analysis T- test during glacial-interglacial periods

We used a single sample t-test to determine whether our samples show significant variations of Fe distribution during glacial and interglacial periods.

Site 658	*t*-value	p-value	significance at $p < .05$
Fe_T	-0.037	0.970	*not* significant
Fe_{HR}/Fe_T	-0.176	0.863	*not* significant
TOC	0.089	0.930	*not* significant

Table 2. S10a: Results of statistical analysis for site 658.

Site 659	*t*-value	p-value	significance at $p < .05$
Fe_T	0.009	0.993	*not* significant
Fe_{HR}/Fe_T	0.462	0.649	*not* significant
TOC	0.162	0. 873	*not* significant

Table 2. S10b: Results of statistical analysis for site 659.

Site 1062	*t*-value	p-value	significance at $p < .05$
Fe_T	0.013	0.980	*not* significant
Fe_{HR}/Fe_T	-0.572	0.571	*not* significant
TOC	0.049	0.962	*not* significant

Table 2. S10c: Results of statistical analysis for site 1062.

Site 1063	*t*-value	p-value	significance at $p < .05$
Fe_T	2.714	0.009	significant
Fe_{HR}/Fe_T	1.353	0.182	*not* significant
TOC	-0.107	0.182	*not* significant

Table 2. S10d: Results of statistical analysis for site 1063.

Daily Aerosol Optical Depth

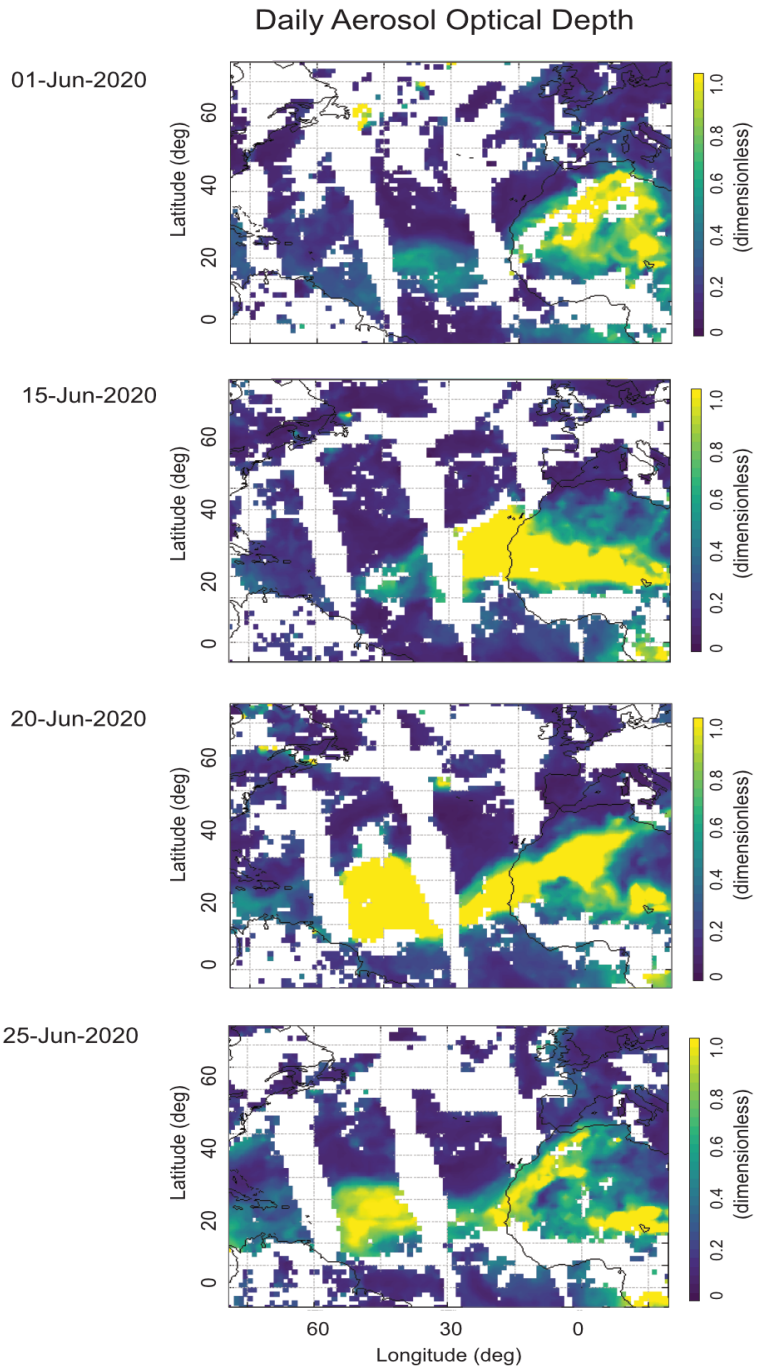

Figure 2. S3: Daily Aerosol Optical Depth from VIIRS - Visible Infrared Imaging Radiometer Suite (https://earthdata.nasa.gov/earth-observation-data/near-real-time/download-nrt-data/viirs-nrt)

Modern Seasonal Distribution of Aerosol Optical Depth and Chlorophyll Concentration

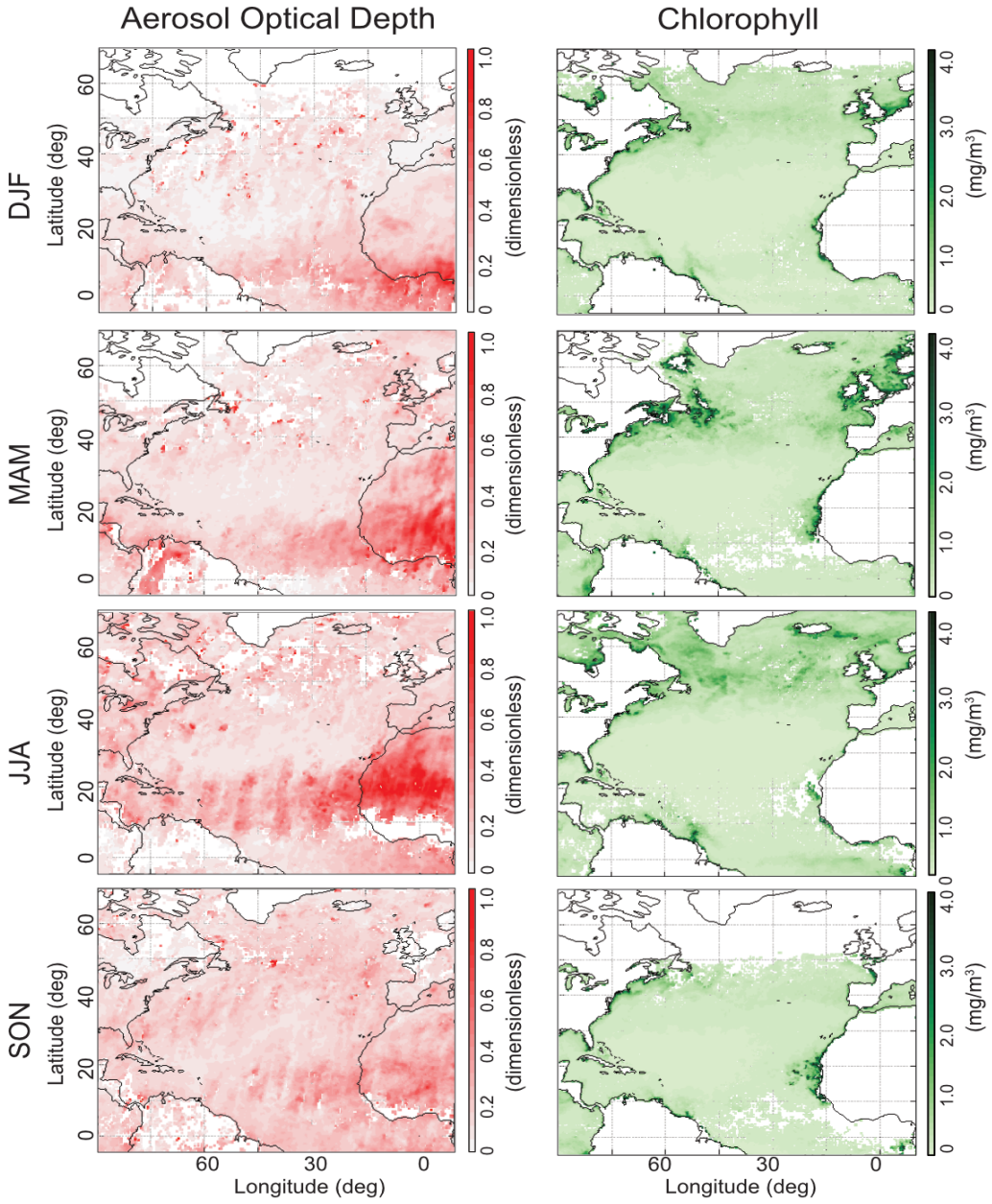

Figure 2. S4: Seasonal (DJF, MAM, JJA and SON) aerosol optical depth (550nm) and Chlorophyll average concentration between 2009-2019 over the North Atlantic Ocean. Aerosol optical depth data source is from MIRS – Multi-angle Imaging SpectroRadiometer (https://misr.jpl.nasa.gov/getData/accessData/). Chlorophyll data source is from MODIS – Moderate Resolution Imaging Spectrometer (https://modis.gsfc.nasa.gov/data/).

Linear Regression Analysis Model

For hypothesis testing of the variability of spatial Fe distribution we use linear regression model. Our goal is to explore the relationship between p-values and confidence intervals for linear regression parameters. The Fit output is used to estimate p-values using the tcdf function and confidence intervals using the tinv function.

In relationship to distance

The distance is an approximate estimate calculated based on longitude and latitude points using the Longitude/latitude distance calculator from NOAA (https://www.nhc.noaa.gov/gccalc.shtml) and is expressed in kilometers (km).

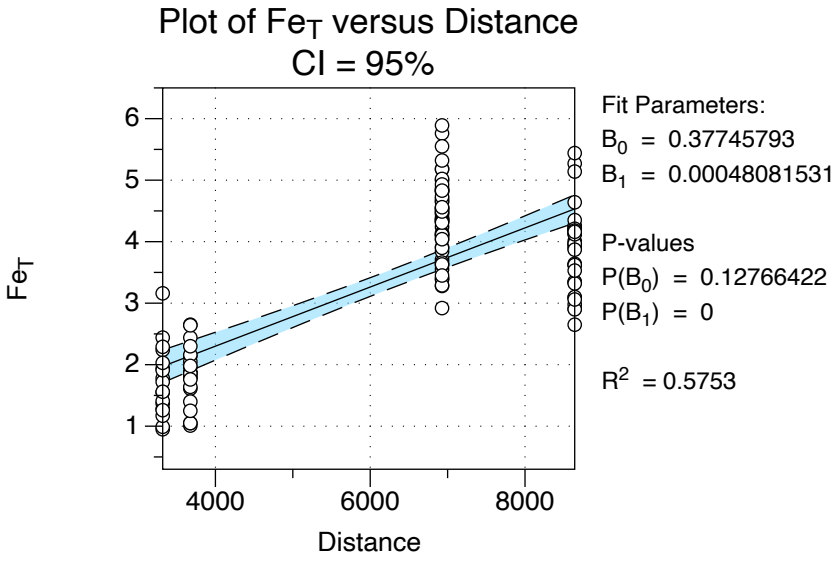

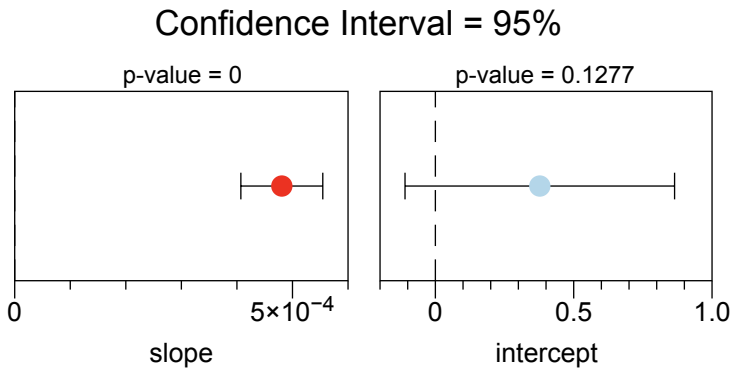

Figure 2. S5a: Fe_T versus Distance

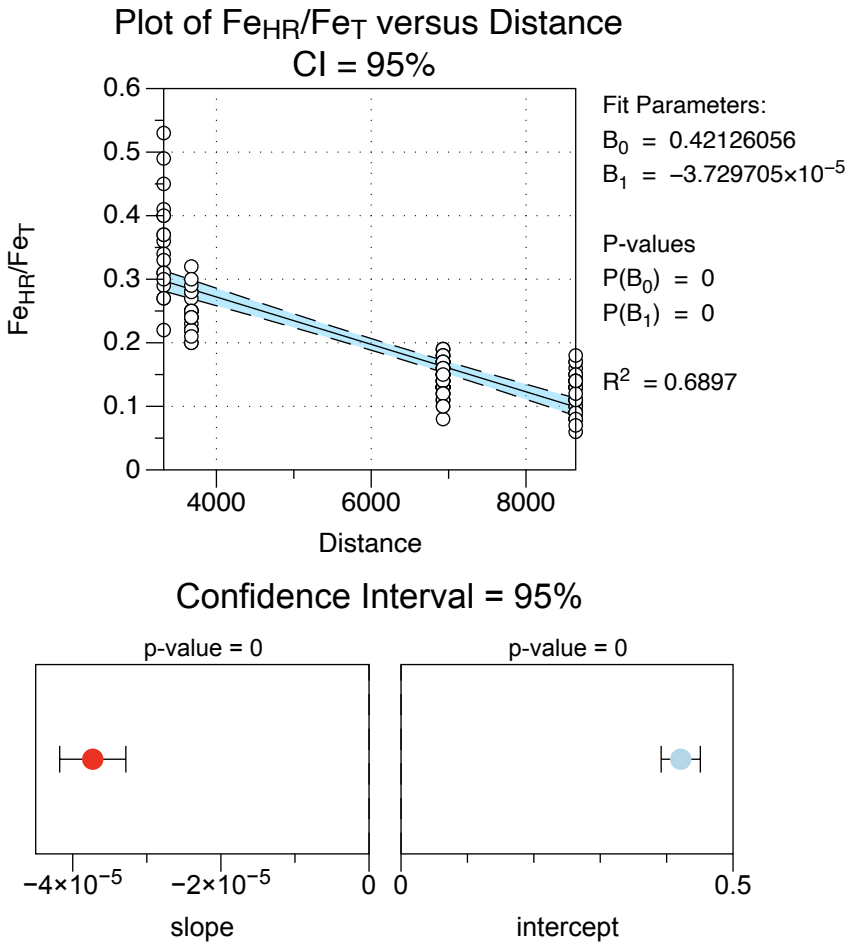

Figure 2. S5b: Linear regression of Fe_{HR}/Fe_T versus Distance

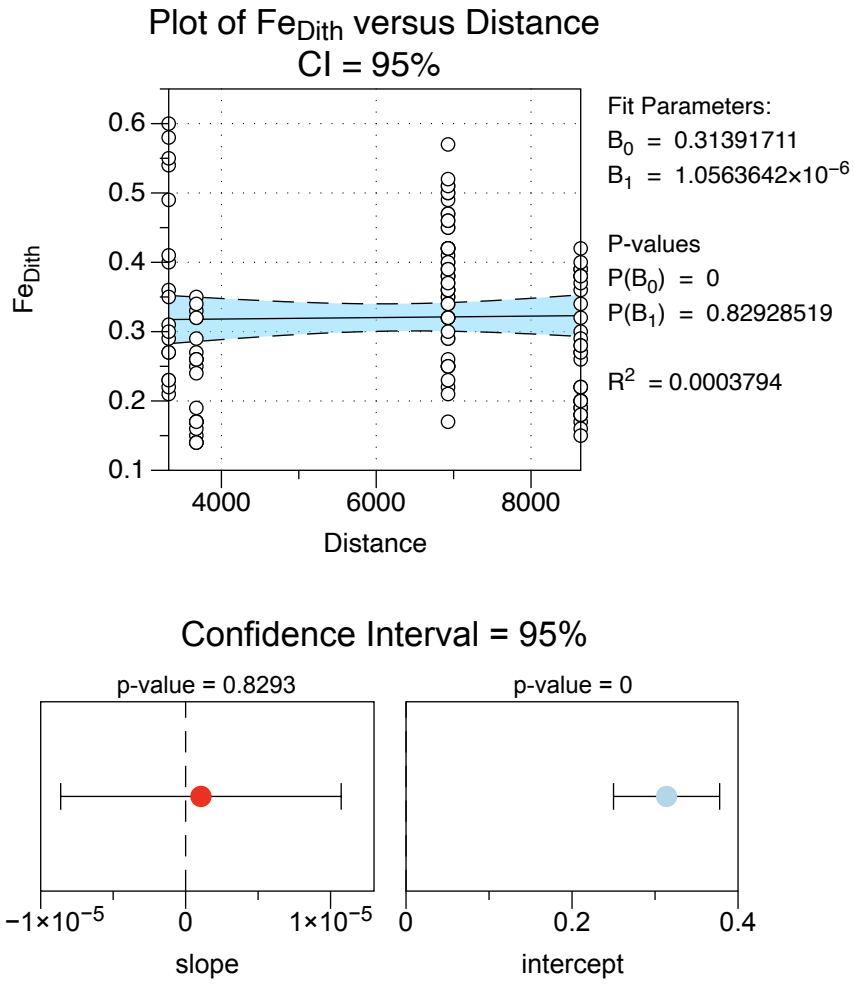

Figure 2. S5c: Linear regression of Fe_{Dith} versus Distance

In relationship to $CaCO_3$

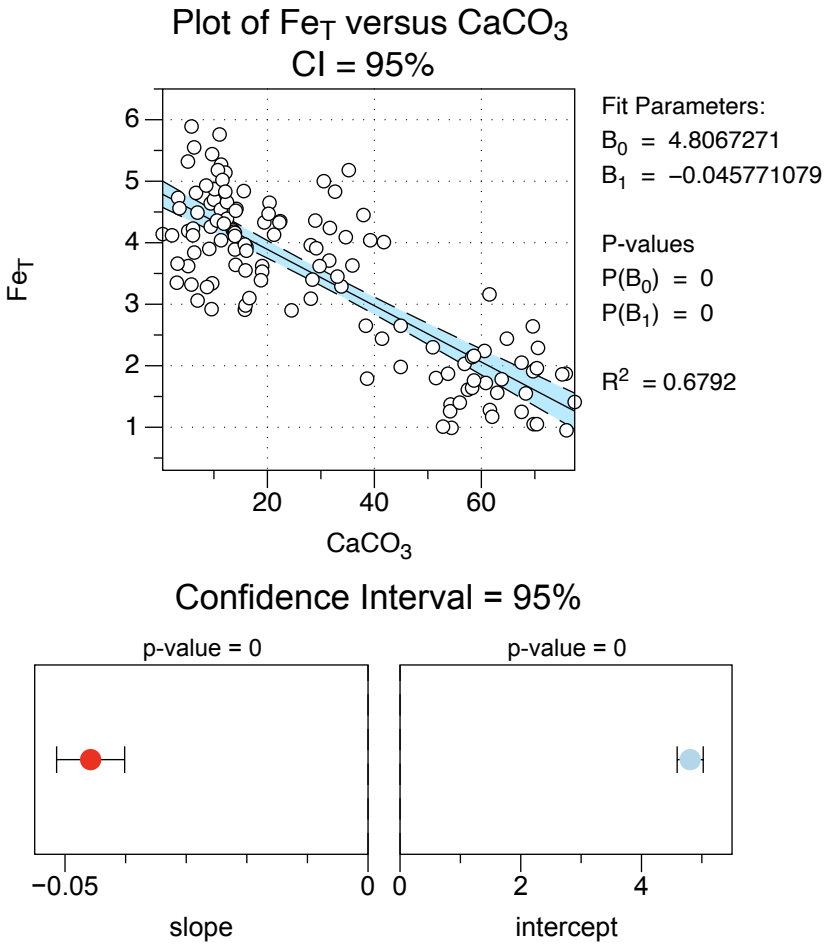

Figure 2. S6a: Linear regression of Fe_T versus $CaCO_3$

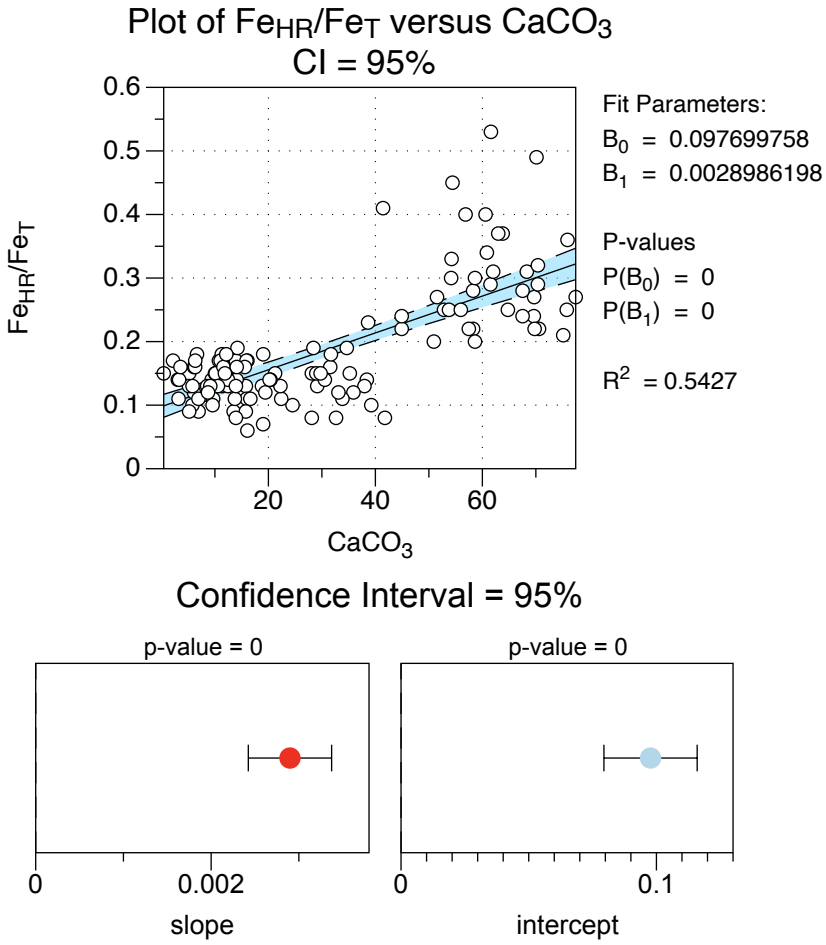

Figure 2. S6b: Linear regression of Fe_{HR}/Fe_T versus $CaCO_3$

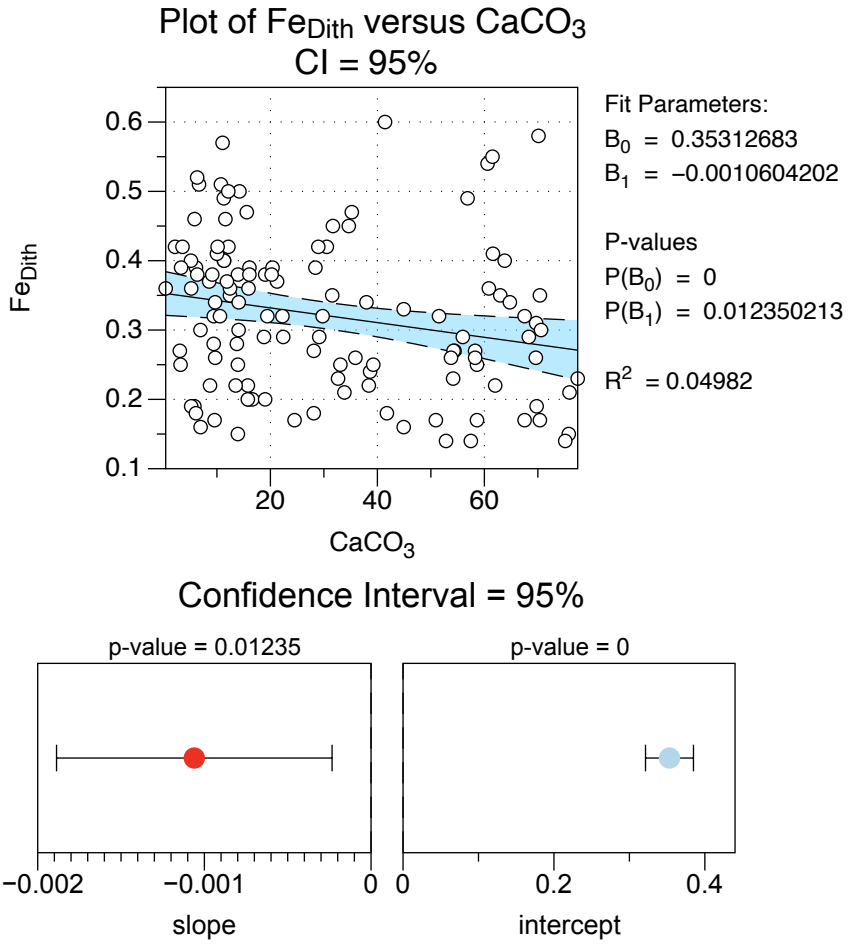

Figure 2. S6c: Linear regression of Fe_{Dith} versus $CaCO_3$

References

Baron, P. A., and Willeke, K., 2001, Aerosol measurement: principles, techniques, and applications.

Cepuritis, R., Garboczi, E. J., Ferraris, C. F., Jacobsen, S., and Sørensen, B. E., 2017, Measurement of particle size distribution and specific surface area for crushed concrete aggregate fines: Advanced Powder Technology, v. 28, no. 3, p. 706-720.

Ersahin, S., Gunal, H., Kutlu, T., Yetgin, B., and Coban, S., 2006, Estimating specific surface area and cation exchange capacity in soils using fractal dimension of particle-size distribution: Geoderma, v. 136, no. 3-4, p. 588-597.

Jickells, T. D., An, Z. S., Andersen, K. K., Baker, A. R., Bergametti, G., Brooks, N., Cao, J. J., Boyd, P. W., Duce, R. A., Hunter, K. A., Kawahata, H., Kubilay, N., laRoche, J., Liss, P. S., Mahowald, N., Prospero, J. M., Ridgwell, A. J., Tegen, I., and Torres, R., 2005, Global iron connections between desert dust, ocean biogeochemistry, and climate: Science, v. 308, no. 5718, p. 67-71.

Mahowald, N., Jickells, T. D., Baker, A. R., Artaxo, P., Benitez-Nelson, C. R., Bergametti, G., Bond, T. C., Chen, Y., Cohen, D. D., Herut, B., Kubilay, N., Losno, R., Luo, C., Maenhaut, W., McGee, K. A., Okin, G. S., Siefert, R. L., and Tsukuda, S., 2008, Global distribution of atmospheric phosphorus sources, concentrations and deposition rates, and anthropogenic impacts: Global Biogeochemical Cycles, v. 22, no. 4.

Mahowald, N., Kohfeld, K., Hansson, M., Balkanski, Y., Harrison, S. P., Prentice, I. C., Schulz, M., and Rodhe, H., 1999, Dust sources and deposition during the last glacial maximum and current climate: A comparison of model results with paleodata from ice cores and marine sediments: Journal of Geophysical Research-Atmospheres, v. 104, no. D13, p. 15895-15916.

Parnell Jr, C. B., Jones, D. D., Rutherford, R. D., and Goforth, K. J., 1986, Physical properties of five grain dust types: Environmental Health Perspectives, v. 66, p. 183-188.

CHAPTER 3

Iron-Sulfur interactions recorded in the southern Scotia Sea

ABSTRACT

The Southern Ocean is known to be a high nutrient-low chlorophyll (HNLC) region where primary production is limited by the availability of bioavailable iron. Consequently, the recycling of trace metals in the sediments and their subsequent release into the water column could be an important source of bioavailable iron to the Southern Ocean as has been proposed in previous studies. The two investigated sites have different depositional histories but have in common that reactive iron phases are abundant close to the surface but decrease down core. Our results reveal differences in the concentrations of dissolved iron and manganese in pore-waters, the concentration of solid-phase iron and sulfur species, and sulfur isotopes between Site U1537 and Site U1538. Varying inputs of reactive iron (oxyhydr)oxides to the sediment likely dictated the oxidative pathways of the sedimentary sulfur cycle and related biogeochemical signals. Our study provides evidence for a prominent anerobic oxidation of methane (AOM) driven sulfate reduction.

INTRODUCTION

The microbially mediated mineralization of organic material control redox conditions and therefore the cycling of trace metals and nutrients in marine sediments (Elderfield, 1985; Meyer et al., 2016). Since the oxidation of carbon is coupled to the reactivity and availability of electron acceptors, like O_2, nitrate, Mn(IV), Fe(III), and sulfate, their presence or absence in pore waters provides valuable information on redox conditions and evolution in the sediment (Beck et al., 2008; Canfield et al., 1993; Hardisty et al., 2018). Redox-sensitive trace metals (Fe, Mn, V, Mo, U, Re) and nutrients (NO^-, NH^+, PO^{3-}) have therefore been successfully used to decipher the redox state and biogeochemical processes in a wide range of coastal marine and deep-sea settings of the North Atlantic, the North Pacific, the North Sea, and off Peru (Canfield et al., 1993; Froelich et al., 1979; Morford et al., 2005; Scholz et al., 2013; Shaw et al., 1990)—among many other locations.

Iron occurs in ferrous Fe(II) and ferric Fe(III) forms and is bound to a variety of minerals with a wide range in stabilities, surface areas, adsorption capacities, and chemical reactivities (Cornell and Schwertmann, 2003; Raiswell, 2011). The transportation and distribution of iron is strongly affected by pH, Eh (redox potential), and the presence of dissolved compounds that can form dissolved complexes, colloids, and poorly soluble mineral phases (Raiswell and Canfield, 2012). Redox conditions have a great impact on the behavior of iron because Fe(II) and Fe(III) have different chemical bonding affinities and thus form different mineral phases (Kendall et al., 2012). Trivalent iron bonds readily with OH^- ion (hydroxyl ion) under oxic, high Eh conditions, which leads to a variety of poorly soluble hydrated Fe(III) oxyhydroxides (Kendall et al., 2012; Michel et al., 2010;

Michel et al., 2007). Bivalent iron can be bound to sulfides as well as to phosphates and carbonates, forming siderite and vivianite if there is an excess of Fe(II) over HS^- (Berner, 1981; Kappler and Newman, 2004; Krom and Berner, 1980).

Iron bound to oxyhydroxides goes through a series of diagenetic changes when it enters an aquatic environment. These poorly crystalline nanosized particles 'age' during transportation, which causes increase in the crystal lattice. Transformation into more strongly crystalline phases decreases surface area, which makes the minerals more stable and less reactive chemically and also less available for biological processes (Raiswell, 2011). The first iron oxyhydroxide to precipitate under oxidizing and hydrolyzing conditions is ferrihydrite [$(Fe^{3+}_{10}O_{14}(OH)_{12}$] (Hansel et al., 2004; van der Zee et al., 2003). It is the least stable and most reactive hydroxide (Cornell and Schneider, 1989; Raiswell, 2011; van der Zee et al., 2003).

Iron sulfides are important sinks for both iron and sulfur, and they are formed when dissolved sulfide reacts with either dissolved iron or iron bearing minerals that are reactive towards sulfur (Berner, 1970; Raiswell and Canfield, 1998). For example, iron oxides such as ferrihydrite, goethite, hematite, and lepidochrosite are reactive (Canfield, 1989a; Raiswell and Canfield, 1998). Also, iron-bearing silicates can be reactive but significantly less so compared to iron oxides. Reactivity towards sulfur has been studied by determining half-lives of sedimentary iron minerals when reacting with dissolved sulfide. The half-life of ferrihydrite, for example, is 2.8 hours, but for sheet silicates it can be 89000 years (Canfield et al., 1992). Pyrite formation is therefore largely controlled by the burial of iron oxides into sediments. Dissolved sulfide for the reaction is produced in the sediment by

microbial reduction of sulfate and decomposition of organic sulfur compounds (Berner, 1970; Canfield, 1989a; Canfield et al., 1992). The first precipitates are usually amorphous iron sulfides, such as mackinawite (FeS). Mackinawite is an unstable phase that transforms rapidly into more crystalline phases pyrrhotite ($Fe_{1-x}S$) and greigite (Fe_3S_4). Pyrite (FeS_2) is the end-product of the process. The transformation of monosulfide into pyrite requires an electron acceptor to oxidize sulfur. There are three pathways for pyrite formation:

1. The 'polysulfide pathway' where pyrite is formed by addition of zero-valent sulfur (S^0), which acts as electron acceptor (Berner, 1970, 1984; Luther III, 1991).

$$FeS + S^0 \rightarrow FeS_2$$

2. The 'H_2S pathway,' which has been shown to be the fastest as well as dominant pyrite forming pathway in anoxic systems (Rickard, 1997), although this assertion is not universally accepted. This pathway provides reducing equivalents in the form of H_2 that could be coupled to the reduction of CO_2 to CH_4 or more complex organic matter (Holmkvist et al., 2011; Jørgensen et al., 2019a).

$$FeS + H_2S \rightarrow FeS_2 + H_2 \quad (2)$$

3. The 'iron-loss pathway' by which pyrite is formed through the loss of iron (Wilkin and Barnes, 1996).

$$2FeS + 2H^+ \rightarrow FeS^2 + Fe^{2+} + H_2 \quad (3)$$

Marine sediments are the main sink for seawater sulfate, which demonstrates that the sedimentary sulfur cycle is a major component of the global sulfur cycle. The most important mechanisms for removing sulfate from the oceans to the sediments are (1) the bacterial reduction of sulfate to hydrogen sulfide, which subsequently reacts with iron to form sulfide minerals, particularly pyrite (FeS_2); (2) the formation of organic sulfur, i.e. the incorporation of sulfur into sedimentary organic matter during early diagenesis; and (3) the precipitation of calcium sulfate minerals in evaporites (Hardie, 1991; Vandieken et al., 2006). The biogeochemical transformations of sulfur in marine sediments represent important components of the global sulfur cycle. These processes include the microbial reduction of sulfate coupled to the oxidation of organic matter and methane (Deusner et al., 2014; Egger et al., 2015; Froelich et al., 1979; Jørgensen, 1982; Riedinger et al., 2014), with organoclastic sulfate reduction as the dominant terminal electron accepting pathway in anoxic marine sediments (Jørgensen, 1982; Jørgensen et al., 2019a; Sivan et al., 2014).

It has been suggested that iron oxides may play a role in the anaerobic oxidation of methane (CH_4) (AOM) in marine and freshwater sediments (Cai et al., 2018; Rooze et al., 2016; Sivan et al., 2011; Sivan et al., 2014). Methane is produced in the sediment below the sulfate-reducing zone by splitting of acetate and reduction of CO_2 by hydrogen (Jørgensen and Kasten, 2006). As methane diffuses upward, the majority is consumed at the Sulfate-Methane Transition (SMT), where methane is anaerobically oxidized by in combination with microbial sulfate reduction (Brunner et al., 2016; Jørgensen et al., 2019b; Jørgensen and Kasten, 2006). Below the SMT where sulfate is depleted, solid-phase iron oxides have been shown to act as alternative electron acceptors for this process (Riedinger

et al., 2017). Iron and manganese oxides are abundant in the sediments below the SMT, but their bioavailability may be the limiting factor to iron-dependent AOM (Beal et al., 2009; Egger et al., 2015; Ettwig et al., 2016). Even if only a fraction of iron influx participates in AOM, it may act as a major methane sink, as both elements can be oxidized and reduced up to 300 times before final burial in the sediment (Beal et al., 2009; Canfield et al., 1993). Previous studies have shown that Fe-dependent AOM occurs at much slower rates than sulfate dependent AOM even though Fe oxides are energetically more favorable electron acceptors (Beal et al., 2009; He et al., 2018; van Grinsven et al., 2020). This relationship may be because iron is bound to solids, which makes them less accessible than dissolved sulfate (Sivan et al., 2011). In this study, we investigate the iron-sulfur interactions and biogeochemical cycling of sulfur in the sediments of Iceberg-Alley with focus the controlling factors of early diagenetic processes and redox conditions in the Southern Ocean. These processes are responsible for recycling of trace metals in Antarctic shelf sediments and the subsequent release of the Fe into the water column, which helps regulate the bioavailable iron to the Southern Ocean.

MATERIAL AND METHODS

Reginal setting

The formation of the Scotia Sea is linked to the opening of the Drake Passage since the Eocene. The formation and evolution Drake Passage-Scotia Sea gateways allowed for the establishment and subsequent history of the Antarctic Circumpolar Current (ACC). The onset of the ACC influenced the thermal isolation of Antarctica, that together with

atmospheric CO_2 decline, enabled growth of the Antarctic Ice Sheet sheets (Barker and Burrell, 1977; Barker and Thomas, 2004; DeConto and Pollard, 2003; Kennett, 1977; Martinson, 2012). The Drake Passage is proposed to be the final stage in the Gondwana breakup, and it has since been a crucial area for exchange of water masses between the Pacific Ocean, the Atlantic Ocean, and the Weddell Sea (Dalziel et al., 2013; Eagles and Jokat, 2014; Scher and Martin, 2006).

The Dove and Pirie basins are two of several oceanic basins in the southern Scotia Sea with thick contourite deposits formed by the influence of the eastward flowing Antarctic Circumpolar Current (ACC); the northward flowing Weddell Sea Deep Water (WSBW); and, on long timescales, by regional tectonics (Maldonado et al., 2006; Pérez et al., 2014; Pérez et al., 2017) (figure). The Scotia Sea constitutes a back-arc system where the active spreading center at the East Scotia Ridge leads to regional compression along the southern Scotia Sea basins (Pérez et al., 2021). These two basins lie beneath an export pathway for Antarctic icebergs, named 'Iceberg Alley' (Anderson and Andrews, 1999). Icebergs are calved from all sectors of Antarctica and predominantly travel counterclockwise around the continent in the Antarctic Coastal Current until they reach the Weddell Sea Gyre (Collares et al., 2018). Here, they travel north and, ultimately, reach the warmer Antarctic Circumpolar Current where they melt and shed their terrigenous load (Budge and Long, 2018). The sediments of 'Iceberg Alley' provides an outstanding opportunity to investigate iceberg-dust-climate interactions as well as to help evaluate the role of dust in iron fertilization in the Southern Ocean.

Sampling and Sample Processing

The samples analyzed in the present study are from first deep scientific drilling of the Scotia Sea sedimentary record during International Ocean Discovery Program (IODP) Expedition 382 in two of the southern Scotia Sea basins, Dove and Pirie (Fig. 1) (Weber et al., 2019). The two drill sites described here for U1537 are located 265 km northwest of the South Orkney Islands at 59°6.65′S, 40°54.37′W in the abyssal plain of Dove Basin at 3220 and 3713 m water depth. Piston cores from Holes U1537A and U1537D provided near-continuous stratigraphic coverage to 264 and 354 mbsf, respectively. Site U1538 is located 365 km north-northeast of the South Orkney Islands at 57°26.52′S, 43°21.47′W and was drilled in the northern part of Pirie Basin at 3131 m water depth and recovered sediment to 676 mbsf.

Samples from both sites, U1537 and U1538, collected for shipboard determination of salinity, alkalinity (TA), pH, phosphate, and ammonia, as well as major and trace elemental concentrations, were processed by squeezing 5-20 cm whole-round sections cut from cores immediately after core retrieval. Whole-round samples were typically collected at a frequency of one sample per core (<100 m mbsf) or every third core (>100 m mbsf) until the bottom of the site except for Site U1538 or until extraction produced <6 mL of IW after 2.0 h of squeezing. As for Site U1538, we collected samples at a frequency of one sample per core at depths of <222 m mbsf, every second core (222-300 m mbsf), and every third core (>300 m mbsf) to the bottom of the hole. The resulting ‘squeeze cakes’ (formed from sediment intervals cut from the core) were sealed in N_2-flushed bags onboard the ship immediately following collection and stored frozen prior to analysis to minimize oxidation

of redox sensitive Fe minerals important for this study. Sediment analyses took place at the University of California-Riverside. Fresh material was used exclusively for each analysis described below; sediments showing signs of oxidation (gray or brown colors formed from the formerly black iron monosulfides) were scraped away.

Solid Phase Analyses

Contents of total carbon (C) and inorganic carbon (TIC) were measured using an ELTRA CS 500 carbon and sulfur analyzer equipped with acidification and furnace modules. Total C were determined through combustion of samples at 1350°C, with quantification of evolved gasses by infrared absorption. TIC was measured by online acidification with quantification of liberated CO_2 by infrared absorption. Total organic carbon (TOC) was calculated as the difference between total carbon and TIC. The accuracy was ±4% and ±5%, respectively.

A multi-acid digest procedure was used for determination of bulk sediment metal concentrations. Dry samples were ashed at 450-650°C and digested using trace metal grade HF:HNO_3:HCl, with the metals solubilized at the end in 0.24 M HNO_3 acid. Total digests were measured for major elements (Al, Fe, Mn) via an Agilent 7900 quadrupole ICP-MS using a multi-element standard solution in a 0.24 M HNO_3 matrix. Total digest geostandards (NIST 2702, USGS SCO-1, and USGS SGR-1) were routinely compared for accuracy, with all elements analyzed deviating by <5% from the reported values.

Sequential extractions were carried out using freeze-dried sediment samples to characterize the Fe pools present. Ascorbate, dithionite, and oxalate steps were applied on

ca. 100-150 mg sample to determine the fractions present as adsorbed ferrous iron and highly reactive and bioavailable ferric iron (Fe_{bio}); crystalline Fe oxides such as goethite and hematite (Fe_{oxide}); and magnetite (Fe_{mag}), respectively (Ferdelman, 1988; Kostka and Luther III, 1994; Poulton and Canfield, 2005). All solutions were freshly prepared and flushed with N_2 for >20 minutes prior to extraction, and reagent blanks were taken. The iron concentration was analyzed by inductively coupled plasma-mass spectrometry (ICP-MS; Agilent 7500ce) after dilution in trace-metal grade 2% HNO_3. Replicate sample extractions yielded reproducibility within 9%, and all iron concentrations of reagent blanks were below detection limit. Highly reactive iron (Fe_{HR}) was defined according to Raiswell and Canfield (Raiswell and Canfield, 1998) as the sum of Fe_{bio} , Fe_{oxide}, Fe_{mag} , Fe_{AVS} , and Fe_{CRS} .

Analysis of HCl-extractable Fe (Fe_{HCl}) was performed via the method of Berner (1970) and Raiswell et al. (1988) to determine degree of pyritization (DOP), an estimate of the Fe remaining for reaction with dissolved sulfide (Berner, 1970; Raiswell et al., 1988). 100 mg of sample was treated with 5 mL of 12 M HCl, then immediately heated to boil for 1 minute. Following heating, 2 mL of DI water were added to quench the reaction, and the solution was then transferred quantitatively to a 50 mL volumetric flask. After the particles settled, the solution was diluted 10-fold using DI H_2O. Prior to analysis, 1 mL of a buffered ferrozine solution was added to allow for full color development. Iron concentrations were measured spectrophotometrically (λ = 562nm). The degree of pyritization (DOP) was calculated as follows:

$$DOP = (Fe_{CRS} / [Fe_{CRS} + Fe_{HCl}]).$$

A classic method was applied to determine the concentrations of acid volatile sulfide (AVS; mainly iron monosulfides – 'FeS') and chromium reducible sulfur (CRS, corresponding mainly to pyrite, Fe_2S) (Berner et al., 1979; Lyons, 1997; Morse and Cornwell, 1987). Concentrations of both CRS and AVS were measured via the methylene blue method using a spectrophotometer at wavelength of 660 nm (Cline, 1969). Assuming negligible concentrations of [S^0], pyritic sulfur was determined by subtracting the AVS from CRS. Reproducibility was better than 8% based on an in-house standard. All solid-phase data are reported in dry weight units. Sulfur isotope analyses were performed using a Costech Elemental Analyzer (EA) coupled to a Thermo Finnegan Delta V Plus gas-source isotope-ratio mass-spectrometer (IRMS) via a ConFlo III open-split interface. The S^{34}/S^{32} ratios of samples were calibrated using three international reference standards (IAEA-S1, IAEA-S2, and IAEA-S3), deviations among all the repeat sample standard analyses were better than 0.2‰. Results are reported in standard per-mil notation relative to Vienna-Canyon Diablo Troilite (V-CDT).

RESULTS

Volatile hydrocarbons and Interstitial water chemistry

The volatile hydrocarbons and interstitials waters chemistry were analyzed as part of IODP Expedition 382 and are described in detail in the expedition report (Weber et al., 2019). We use these data to complement our corresponding sedimentary data. At Site U1537, headspace methane concentrations were low (1.9-3.2 ppmv) throughout the sedimentary sequence, and ethane, propane, and other higher molecular weight

hydrocarbons were below detection limit. Site U1537 exhibits generally reducing sedimentary conditions as indicated by the disappearance of dissolved sulfate concentrations at ~85 mbsf, yet Site U1537 is not methanogenic at any depth in the observed sedimentary column. Dissolved sulfate concentrations increase again below 160 mbsf and remain constant at 5.5 mM until the bottom of hole.

Dissolved Mn concentrations are highest at 9 mbsf (45 uM) and generally elevated in the upper 40 mbsf. Below this depth, Mn concentrations are low throughout most of the interval recovered and elevated again below 260 mbsf. Dissolved Fe is slightly enriched in the uppermost sampled depth at 9 mbsf (6.5 uM), otherwise it is below or close to the detection limit (Figure 2). Together, the interstitial water Fe and Mn concentration patterns suggest that sedimentary reductive processes do not lead to generally elevated dissolved Fe and Mn, at least not at the resolution we sampled, apart from elevated Mn levels in the topmost 30 mbsf.

At Site U1538, methane is the dominant hydrocarbon present in low concentrations (2.0-5.4 ppmv) throughout. The reducing sedimentary conditions at Site U1538 result in systematic diagenetic profiles for the interstitial water profiles of several species measured during shipboard analyses, including alkalinity, Ca, Mn, Fe, PO_4, NH_4, and Mn (see EXP 382 preliminary reports) (Weber et al., 2019). Sulfate decreases from 22 mM at 6 mbsf to near zero at 52 mbsf. Minor dissolved sulfate concentrations were detected below 500 mbsf (SO_4<1.5 M) (Figure 2).

Dissolved Mn enrichment is observable in the uppermost 32 mbsf at Site U1538, followed by Fe enrichment below this depth, suggesting Mn and Fe oxide mobilization in

the upper 260 mbsf. Iron concentrations in the sulfate reduction zone average ~1.2 μM, rising up to 6.7 μM between the interval from 52 mbsf to 260 mbsf. The presence of detectable dissolved Mn concentrations seen at every depth at Site U1538 suggests that burial rates of reactive iron and manganese oxides exceed microbial reduction of these metals. In turn, relatively elevated dissolved Mn levels, as high as 22.7 μM in the sulfate reduction zone, suggest partial Mn oxide dissolution at shallow depth.

Solid Phase

The total organic carbon (TOC) and calcium carbonate ($CaCO_3$) from Site U1537 show relatively low contents (TOC: 0.15–0.7 wt %, $CaCO_3$: 0.24-0.92 wt%). The consistent TOC/TN ratio averaging 6.4 via shipboard solid phase analysis (Weber et al., 2019) at Site U1537 indicates a predominance of marine organic material. At Site U1538, the total organic carbon (TOC) concentrations vary from 0.16 to 3.42 wt %, while calcium carbonate ($CaCO_3$) concentration fluctuates between 0.45 wt % and 3.02 wt %, with values in most samples below 1 wt %. The shipboard solid phase analysis of TOC/TN ratios show values lower than 10, suggesting a marine origin of sedimentary organic matter. The one exception is a sample at 503.9 mbsf with a significantly high value of 152 that suggests some at least brief input of appreciable terrestrial organic matter.

The Fe/Al ratios at both Sites U1537 and U1538 stay constant throughout the sediment column, with an average value of 0.5, similar to the average value for upper continental crust (Taylor and McLennan, 1985). Contents of iron extracted in the Fe_{bio} fraction are invariant for both Sites U1537and U1538, with averages of 0.4 wt% and 0.5

wt%, respectively. Variations in Fe_{oxide} are observed in both sites, with higher Fe_{oxide} values occurring particularly in the upper parts of the section. The iron oxide phases (Fe_{oxide}) at the Site U1537 are in the range of 0.05 wt% to 0.25 wt%, with an average of 0.11 wt%. In the upper 8.5 mbsf we see an increase of up to 0.25 wt%, followed by a slight increase at 192 mbsf. The concentration profile for iron in magnetite (Fe_{mag}) at Site U1537 averages 0.21 wt%, followed by a pronounced decrease at the 294.9 mbsf to 0.08 wt% (Figure 3). At site 1538, Fe_{oxide} averages 0.08 wt%, with values ranging from 0.03 wt % to 0.27 wt% (with an outlier of 0.47 wt% 279.6 mbsf). The Fe_{mag} contents from Site U1538 scatter between 0.19 wt% to 0.45 wt%, with the highest values occurring above and below the sulfidic zone, followed by a decrease in the lower interval (Figure 3). There is a strong difference in DOP values between Sites U1537 and U1538 despite similar averages of 0.27 and 0.29, respectively. However, at site 1537, the DOP ranges from 0.11 to 0.43 (with one outlier of 0.02 at 352.4 mbsf) and displays higher ratios of up to 0.43 in the sulfidic zone. At site 1538, the DOP ratio ranges from 0.10 to 0.63, with higher ratios of up to 0.47 at the sulfidic zone, followed by a decrease and subsequent peak at 613.6 mbsf. In contrast, in the uppermost zone, pyrite contents remain below 0.5 wt% (Figure 3).

Pyrite contents (CRS) at Site U1537 are elevated within the sulfidic zone, reaching values of up to 1.09 wt%. The stable sulfur isotope composition of pyrite (δ^{34}S-CRS) shows a trend similar to the CRS profile, starting with values of -50.5‰ at the surface and showing the highest enrichment in ^{34}S (-1.83‰) at 84.5 mbsf - just below the SMT (Figure 4). Below the sulfidic zone, δ^{34}S-CRS shows a considerable depletion from -22.6 to -50.6‰ in the lowermost sediment layer. In contrast to pyrite, the contents of iron

monosulfide phases (AVS) at Site U1537 are low (average 0.005 wt.%) in the upper 132 mbsf and increase below the sulfidic zone to a maximum of 0.019 wt.% at 247 mbsf (Figure 4). The contents of S^0 show similar trends to CRS, with highest contents below the sulfidic zone. At Site U1538, pyrite content in the sulfidic zone ranges up to 1.33 wt.%, while below and above this zone, the pyrite contents show an average of 0.63 wt.% with a dramatic increase to 2.05 wt% at 613.6 msbf, followed by a decrease to 0.22 down core (Figure 4). The δ^{34}S-CRS data display a positive excursion in the sulfidic zone, reaching +31.13‰. Above and below the sulfidic zone, δ^{34}S-CRS data stay below -20‰, with an exception at 279.6 mbsf, where a second excursion occurs with δ^{34}S-CRS of -2.37‰. The amounts of AVS are low, with values ranging from 0.001 to 0.016wt% (Figure 4).

DISCUSSION

Evidence of Anaerobic methane oxidation (AOM)

The pore water sulfate concentration profile by bacterial sulfate reduction is controlled by the availability of labile organic matter, diffusive/advective methane flux, and depositional conditions (Hensen et al., 2003; Niewöhner et al., 1998; Treude et al., 2014). To determine the relative contribution of AOM and/or organoclastic sulfate reduction (OSR) degradation toward alkalinity we used $(\Delta TA + \Delta Ca + \Delta Mg)/ \Delta SO_4^{2-}$ ratios of pore water (Burdige and Komada, 2011; Hensen et al., 2003; Kastner et al., 2008; Malinverno and Pohlman, 2011; Mazumdar et al., 2012; Peketi et al., 2020). ΔTA, ΔCa^{2+}, ΔMg^{2+}, and ΔSO_4^{2}values at each depth interval were calculated by taking the difference between the seawater concentration and pore water concertation at that depth interval of individual parameter respectively. The

concentrations of TA, Ca^{2+}, $Mg^{2+,}$ and SO_4^{2-} of seawater are 2.3 mM, 10.3 mM, 53 mM, and 28 mM respectively. An AOM driven sulfate reduction process results in $\Delta(TA + Ca^{2+} + Mg^{2+})/ \Delta SO_4^2$ ratio of 1:1, whereas this ratio is ~2:1 where OSR is the driver for sulfate reduction. An AOM driven sulfide reduction processes occur in both Site U1537and Site U1538 (Figure 5). Except at the lower depth (586-680) from Site U1538 where it suggests dual influence of AOM and OSR with intermediate values (average 1.2) (Figure 5) (Kastner et al., 2008).

Pyritization influenced by AOM Induced Sulfite Reduction

Upon deposition in the marine environment, ferric Fe phases are involved in reactions to form iron monosulfide phases that continue to react with sulfide to form pyrite (Lyons et al., 2003; Morse and Cornwell, 1987; Schoonen and Barnes, 1991). The observed concentration profiles of the various iron sulfide phases reflect the ongoing alteration of iron oxides via diverse reaction pathways several meters below the seafloor. Degree of pyritization calculations for both Sites U1537 and U1538 range from 0 to 0.5 (DOP maximum values are 1.0), which suggests sediment deposition under oxic conditions (Canfield et al., 1996; Raiswell et al., 1988). Calculated values for DOP are mostly near 0.3 for both Sites U1537 and U1538. At site 1538 at a depth 120 mbsf, sedimentary Fe concentrations decrease, and there is an associated peak in pore water Fe rising from 0.5µM at 42.3 mbsf to 6.69µM at 203.7 mbsf before decreasing again (Figure 1), suggesting reductive dissolution of Fe oxides (Figure 1). The consistent persistence of magnetite (Fe_{mag}) reflects the general lack of hydrogen sulfide availability (Canfield and Berner,

1987). Reactive iron (Fe_{HR}) is known to buffer sulfide in marine pore waters, and therefore buildup of dissolved sulfide suggests iron limitation. Conversely, sulfide-limited regions would have reactive Fe remaining in the absence of dissolved sulfide (Canfield, 1989a; Canfield and Berner, 1987; Raiswell et al., 2018). In this light, the depositional environments on Sites U1537 and U1538 are likely sulfide limited, consistent with TOC contents.

Pyrite abundance is primarily controlled by (1) the rate of microbial sulfate reduction, which depends on the amount and characteristics of buried organic matter and the upward flux of methane, and (2) the availability of reactive iron (Berner, 1970, 1984; Goldhaber and Kaplan, 1974; Jørgensen et al., 2019b; Lyons, 1997; Peckmann et al., 2001). In iron-dominated sedimentary systems, hydrogen sulfide is effectively scavenged by dissolved Fe^{2+} resulting first in the accumulation of metastable sulfur and iron sulfide phases, for instance as elemental sulfur, greigite, and mackinawite that can be altered into pyrite (Canfield, 1989a; Goldhaber and Kaplan, 1974; Kasten et al., 1998; Lan and Butler, 2014; Picard et al., 2018). In systems limited by hydrogen sulfide availability, intermediate sulfur phases such as thiosulfate and elemental sulfur can be microbially disproportionated into ^{34}S-enriched sulfate and ^{34}S-depleted hydrogen sulfide (Borowski et al., 2013; Bottrell and Raiswell, 2000; Jørgensen and Nelson, 2004; Thamdrup et al., 1993). This process further increases the offset between isotopically heavy sulfate and light sulfide (Canfield and Thamdrup, 1994; Habicht and Canfield, 2001).

The marine sedimentary sulfur cycle is regulated by the microbial reduction of sulfate (Bowles et al., 2014; Froelich et al., 1979; Jørgensen et al., 2019b; Wing and

Halevy, 2014). The two major pathways of catabolic microbial sulfate reduction, organoclastic sulfate reduction (OSR) and sulfate reduction coupled to anaerobic oxidation of methane (AOM), release hydrogen sulfide to the pore water (Boetius et al., 2000; Goldhaber and Kaplan, 1974; Hensen et al., 2003; Hoehler et al., 1994; Valentine and Reeburgh, 2000). Microbial sulfate reduction distinguishes against the heavier sulfur isotopes, leading to a depletion in ^{34}S in the produced hydrogen sulfide and a relative enrichment of ^{34}S in the remaining sulfate pool (Bottrell and Raiswell, 2000; Johnston et al., 2005; Riedinger et al., 2017; Sim et al., 2011). The sulfate pool becomes smaller with an increase of sediment depth, and the remaining sulfate becomes isotopically heavier (Paytan et al., 2002; Riedinger et al., 2006; Torres et al., 1996). The same trend is also reflected in the production of hydrogen sulfide. Therefore, sulfur phase resulting from sulfide oxidation or directly precipitated from iron sulfide will become enriched in ^{34}S with increasing sediment depth (Goldhaber and Kaplan, 1980; Jørgensen et al., 2004). Likewise, at the sulfate-methane transition (SMT) where sulfate is almost entirely consumed, iron sulfides are precipitated with the heaviest isotope composition compared to the upper sediments (Borowski et al., 2013; Jørgensen et al., 2019a; Jørgensen and Nelson, 2004; Lin et al., 2016).

Pyrite contents (CRS) at Site U1537 are elevated above and within the sulfidic zone, reaching values of up to 1.09 wt.%. In contrast, in the uppermost meter of the core and below the sulfidic zone, pyrite contents remain below 0.4 wt.% (Figure 4). The stable sulfur isotope composition of pyrite ($\delta^{34}S$-CRS) shows a trend similar to CRS profile, starting with −50.5‰ at the surface and showing the highest enrichment in ^{34}S of 1.8‰.

The lower availability of reactive iron phases at Site U1537 have resulted in higher sulfide accumulation rates and thus more complete pyritization of the reactive phases. In contrast, at Site U1538, there are two enrichments CRS, first in 42.4 mbsf to 51.8 mbsf interval (average values of 1.2wt%) and second at 613.6mbsf (2.95 wt%). The δ^{34}S-CRS data display a positive excursion in the sulfidic zone, reaching +31.1‰; however, it does not track the pyrite concentration profile. Below the sulfidic zone, δ^{34}S-CRS data decrease to an average of -32‰, followed by two major increases of 1.95‰ at 175 mbsf and -2.37 at 279.6 mbsf. The increase in δ^{34}S-CRS values at site U1537 from -50.5‰ to -1.8 ‰ within 1.5-84.5 mbsf and -50‰ to 31.1‰ within 5.9-70.8 mbsf at site U1538 (Figure 4) are associated with the present sulfate methane transition zone suggesting possible influence of the AOM on sulfate reduction. (Jørgensen et al., 2004). A high δ^{34}S-CRS value (31.13‰) (Figure 3) recorded at Site U1538 suggests AOM-induced sulfidization fueled by high methane flux at a paleo-sulfate methane transition zone (Borowski et al., 1996; Borowski et al., 2013; Jørgensen et al., 2004; Wehrmann et al., 2011). In spite of significantly lower methane concentrations, a higher contribution of AOM towards sulfate reduction is noticeable in both sites U1537 and U1538, which can be attributed to microbial ecology.

Site U1537 contains simultaneously decreasing TOC and sulfate consistent with sulfate reduction (Figure 3) (Canfield, 1989b; Westrich and Berner, 1984). Decreasing TOC abundance with depth is often seen in marine sediments as a consequence of progressive microbial degradation (Chanton et al., 1987; Martens and Klump, 1984; Westrich and Berner, 1984). Site U1538 TOC data are inconsistent with steady-state

behavior, with a rise in TOC of 3.42 wt. % at depth 501.8 mbsf. Such enrichment in organic matter can be linked to historical differences, such as enhanced inputs at times of higher primary production and greater preservation due to deposition under anoxic/euxinic settings (Canfield, 1989b). Further, increases in TOC can reflect times of lower clastic dilution. However, at Site 1538 there are no indications in the iron chemistry or the sediment fabric for anoxic conditions. The change in sedimentation rate, sedimentation rates of ~22 cm/kys between the seafloor and 432 mbsf (~1.75 Ma), ~2.5 cm/ky from 432 to 469 mbsf (~3.6 Ma), and ~12 cm/kys from 447 mbsf to the base (Weber et al., 2019) is observed at Site U1538 with minimal the bioturbation can justify the unique preservation of compounds that would otherwise degrade in the presence of oxygen (Canfield and Thamdrup, 1994; Ingall and Van Cappellen, 1990; Tyson, 2001).

High sedimentation rates can enhance preservation, but it also dilutes the TOC content (Sageman et al., 2003; Tyson, 2001) and leads to high microbial activity (Harvey et al., 1995; Meister et al., 2007). Under steady state conditions, i.e., when the rates of both organic and bulk sedimentation remain constant and the quality of the deposited organic matter is uniform over time, no expressive alteration occurs in the fluxes of dissolved methane and sulfate, and the SMT remains at a constant depth beneath the seafloor (Contreras et al., 2013; Hensen et al., 2003; Jørgensen et al., 2019a; Riedinger et al., 2005). Sedimentation and organic carbon flux, however, are rarely constant over time as it is shown at Site U1537 where the estimate sedimentation rates vary from of ~14.8 cm/ky between the seafloor and 180 mbsf and ~6.1 cm/ky from 180 mbsf to the base of Hole at 354 mbsf (Weber et al., 2019) and same applies to Site U1538 as mentioned above. The

high and variable sedimentation rate of our two sites support our argument that these sediments may be geochemically altered due to the anaerobic oxidation of methane (AOM) (Niewöhner et al., 1998; Hensen et al., 2003; Riedinger et al., 2005; Jørgensen and Kasten, 2006; Egger et al., 2017). Thus, the biogeochemical cycles of Fe, C, and S in marine sediments are closely linked (Berner, 1970).

CONCLUSION

The Dove Basin (Site U1537) and Pirie Basin (Site U1538), despite very similar average Fe_T and Fe speciation data, Fe availability down core and the associated Fe phases are very different. We suggest that this trend likely reflects differences in the local conditions of sediment deposition, such as sedimentation rate (Ingall and Van Cappellen, 1990; Jørgensen et al., 2019a), and Fe supply (e.g., via terrigenous input, iceberg and additional iron shuttling) (Anderson and Raiswell, 2004; Gomez et al., 2010; Lyons and Severmann, 2006; Tribovillard et al., 2015). The $\Delta(TA + Ca^{2+} + Mg^{2+})/ \Delta SO_4^2$ ratios and δ^{34}S-CRS suggest that sulfate consumption is a result of AOM caused by high sedimentation rate. The occurrence and distribution of our non-steady-state diagenetic signals, coupled with a quantitative understanding of the biogeochemical cycles of Fe, C, and S, endow foretelling insight into the role of microbial communities in global element and redox cycling.

REFERENCES

Anderson, J. B., and Andrews, J. T., 1999, Radiocarbon constraints on ice sheet advance and retreat in the Weddell Sea, Antarctica: Geology, v. 27, no. 2, p. 179-182.

Anderson, T. F., and Raiswell, R., 2004, Sources and mechanisms for the enrichment of highly reactive iron in euxinic Black Sea sediments: American Journal of Science, v. 304, no. 3, p. 203-233.

Barker, P., and Burrell, J., 1977, The opening of Drake passage: Marine geology, v. 25, no. 1-3, p. 15-34.

Barker, P., and Thomas, E., 2004, Origin, signature and palaeoclimatic influence of the Antarctic Circumpolar Current: Earth-Science Reviews, v. 66, no. 1-2, p. 143-162.

Beal, E. J., House, C. H., and Orphan, V. J., 2009, Manganese-and iron-dependent marine methane oxidation: Science, v. 325, no. 5937, p. 184-187.

Beck, M., Dellwig, O., Schnetger, B., and Brumsack, H.-J., 2008, Cycling of trace metals (Mn, Fe, Mo, U, V, Cr) in deep pore waters of intertidal flat sediments: Geochimica et Cosmochimica Acta, v. 72, no. 12, p. 2822-2840.

Berner, R. A., 1970, Sedimentary pyrite formation: American journal of science, v. 268, no. 1, p. 1-23.

Boetius, A., Ravenschlag, K., Schubert, C. J., Rickert, D., Widdel, F., Gieseke, A., Amann, R., Jørgensen, B. B., Witte, U., and Pfannkuche, O., 2000, A marine microbial consortium apparently mediating anaerobic oxidation of methane: Nature, v. 407, no. 6804, p. 623-626.

Borowski, W. S., Rodriguez, N. M., Paull, C. K., and Ussler III, W., 2013, Are 34S-enriched authigenic sulfide minerals a proxy for elevated methane flux and gas hydrates in the geologic record?: Marine and Petroleum Geology, v. 43, p. 381-395.

Bottrell, S., and Raiswell, R., 2000, Sulphur isotopes and microbial sulphur cycling in sediments, Microbial sediments, Springer, p. 96-104.

Bowles, M. W., Mogollón, J. M., Kasten, S., Zabel, M., and Hinrichs, K.-U., 2014, Global rates of marine sulfate reduction and implications for sub–sea-floor metabolic activities: Science, v. 344, no. 6186, p. 889-891.

Brunner, B., Arnold, G. L., Røy, H., Müller, I. A., and Jørgensen, B. B., 2016, Off limits: sulfate below the sulfate-methane transition: Frontiers in Earth Science, v. 4, p. 75.

Budge, J. S., and Long, D. G., 2018, A comprehensive database for Antarctic iceberg tracking using scatterometer data: IEEE Journal of Selected Topics in Applied Earth Observations and Remote Sensing, v. 11, no. 2, p. 434-442.

Cai, C., Leu, A. O., Xie, G.-J., Guo, J., Feng, Y., Zhao, J.-X., Tyson, G. W., Yuan, Z., and Hu, S., 2018, A methanotrophic archaeon couples anaerobic oxidation of methane to Fe (III) reduction: The ISME journal, v. 12, no. 8, p. 1929-1939.

Canfield, D. E., 1989a, Reactive iron in marine sediments: Geochimica et Cosmochimica Acta, v. 53, no. 3, p. 619-632.

Canfield, D. E., and Berner, R. A., 1987, Dissolution and pyritization of magnetite in anoxie marine sediments: Geochimica et Cosmochimica Acta, v. 51, no. 3, p. 645-659.

Canfield, D. E., Lyons, T. W., and Raiswell, R., 1996, A model for iron deposition to euxinic Black Sea sediments: American Journal of Science, v. 296, no. 7, p. 818-834.

Canfield, D. E., Raiswell, R., and Bottrell, S. H., 1992, The reactivity of sedimentary iron minerals toward sulfide: American Journal of Science, v. 292, no. 9, p. 659-683.

Canfield, D. E., and Thamdrup, B., 1994, The production of 34S-depleted sulfide during bacterial disproportionation of elemental sulfur: Science, v. 266, no. 5193, p. 1973-1975.

Canfield, D. E., Thamdrup, B., and Hansen, J. W., 1993, The anaerobic degradation of organic matter in Danish coastal sediments: iron reduction, manganese reduction, and sulfate reduction: Geochimica et Cosmochimica Acta, v. 57, no. 16, p. 3867-3883.

Chanton, J. P., Martens, C. S., and Goldhaber, M. B., 1987, Biogeochemical cycling in an organic-rich coastal marine basin. 8. A sulfur isotopic budget balanced by differential diffusion across the sediment-water interface: Geochimica et Cosmochimica Acta, v. 51, no. 5, p. 1201-1208.

Cline, J. D., 1969, Spectrophotometric determination of hydrogen sulfide in natural waters 1: Limnology and Oceanography, v. 14, no. 3, p. 454-458.

Collares, L. L., Mata, M. M., Kerr, R., Arigony-Neto, J., and Barbat, M. M., 2018, Iceberg drift and ocean circulation in the northwestern Weddell Sea, Antarctica: Deep Sea Research Part II: Topical Studies in Oceanography, v. 149, p. 10-24.

Cornell, R., and Schneider, W., 1989, Formation of goethite from ferrihydrite at physiological pH under the influence of cysteine: Polyhedron, v. 8, no. 2, p. 149-155.

Cornell, R. M., and Schwertmann, U., 2003, The iron oxides: structure, properties, reactions, occurrences and uses, John Wiley & Sons.

Cornwell, J. C., and Morse, J. W., 1987, The characterization of iron sulfide minerals in anoxic marine sediments: Marine Chemistry, v. 22, no. 2-4, p. 193-206.

Dalziel, I. W., Lawver, L. A., Norton, I. O., and Gahagan, L. M., 2013, The Scotia Arc: genesis, evolution, global significance: Annual Review of Earth and Planetary Sciences, v. 41.

DeConto, R. M., and Pollard, D., 2003, Rapid Cenozoic glaciation of Antarctica induced by declining atmospheric CO 2: Nature, v. 421, no. 6920, p. 245-249.

Deusner, C., Holler, T., Arnold, G. L., Bernasconi, S. M., Formolo, M. J., and Brunner, B., 2014, Sulfur and oxygen isotope fractionation during sulfate reduction coupled to anaerobic oxidation of methane is dependent on methane concentration: Earth and Planetary Science Letters, v. 399, p. 61-73.

Eagles, G., and Jokat, W., 2014, Tectonic reconstructions for paleobathymetry in Drake Passage: Tectonophysics, v. 611, p. 28-50.

Egger, M., Rasigraf, O., Sapart, C. l. J., Jilbert, T., Jetten, M. S., Röckmann, T., Van der Veen, C., Banda, N., Kartal, B., and Ettwig, K. F., 2015, Iron-mediated anaerobic oxidation of methane in brackish coastal sediments: Environmental Science & Technology, v. 49, no. 1, p. 277-283.

Elderfield, H., 1985, Element cycling in bottom sediments: Philosophical Transactions of the Royal Society of London. Series A, Mathematical and Physical Sciences, v. 315, no. 1531, p. 19-23.

Ettwig, K. F., Zhu, B., Speth, D., Keltjens, J. T., Jetten, M. S., and Kartal, B., 2016, Archaea catalyze iron-dependent anaerobic oxidation of methane: Proceedings of the National Academy of Sciences, v. 113, no. 45, p. 12792-12796.

Ferdelman, T. G., 1988, The distribution of sulfur, iron, manganese, copper and uranium in a salt marsh sediment core as determined by a sequential extraction method: University of Delaware.

Fossing, H., and Jorgensen, B., 1989, Chromium reduction method of bacterial sulfate reduction in sediments: measurement reduction of a single-step chromium method evaluation: Biogeochemistry, v. 8, no. 3, p. 205-222.

Froelich, P. N., Klinkhammer, G., Bender, M. L., Luedtke, N., Heath, G. R., Cullen, D., Dauphin, P., Hammond, D., Hartman, B., and Maynard, V., 1979, Early oxidation of organic matter in pelagic sediments of the eastern equatorial Atlantic: suboxic diagenesis: Geochimica et cosmochimica acta, v. 43, no. 7, p. 1075-1090.

Goldhaber, M., and Kaplan, I., 1974, The sulfur cycle. In 'The sea'. Vol. 5.(Ed. ED Goldberg) pp. 569–655, Wiley-Interscience: New York.

Gomez, N., Mitrovica, J. X., Huybers, P., and Clark, P. U., 2010, Sea level as a stabilizing factor for marine-ice-sheet grounding lines: Nature Geoscience, v. 3, no. 12, p. 850-853.

Habicht, K. S., and Canfield, D. E., 2001, Isotope fractionation by sulfate-reducing natural populations and the isotopic composition of sulfide in marine sediments: Geology, v. 29, no. 6, p. 555-558.

Hansel, C. M., Benner, S. G., Nico, P., and Fendorf, S., 2004, Structural constraints of ferric (hydr) oxides on dissimilatory iron reduction and the fate of Fe (II): Geochimica et Cosmochimica Acta, v. 68, no. 15, p. 3217-3229.

Hardie, L. A., 1991, On the significance of evaporites: Annual Review of Earth and Planetary Sciences, v. 19, no. 1, p. 131-168.

Hardisty, D. S., Lyons, T. W., Riedinger, N., Isson, T. T., Owens, J. D., Aller, R. C., Rye, D. M., Planavsky, N. J., Reinhard, C. T., and Gill, B. C., 2018, An evaluation of sedimentary molybdenum and iron as proxies for pore fluid paleoredox conditions: American Journal of Science, v. 318, no. 5, p. 527-556.

He, Z., Zhang, Q., Feng, Y., Luo, H., Pan, X., and Gadd, G. M., 2018, Microbiological and environmental significance of metal-dependent anaerobic oxidation of methane: Science of the Total Environment, v. 610, p. 759-768.

Henkel, S., Kasten, S., Hartmann, J. F., Silva-Busso, A., and Staubwasser, M., 2018, Iron cycling and stable Fe isotope fractionation in Antarctic shelf sediments, King George Island: Geochimica et Cosmochimica Acta, v. 237, p. 320-338.

Hensen, C., Zabel, M., Pfeifer, K., Schwenk, T., Kasten, S., Riedinger, N., Schulz, H. D., and Boetius, A., 2003, Control of sulfate pore-water profiles by sedimentary events and the significance of anaerobic oxidation of methane for the burial of sulfur in marine sediments: Geochimica et Cosmochimica Acta, v. 67, no. 14, p. 2631-2647.

Hoehler, T. M., Alperin, M. J., Albert, D. B., and Martens, C. S., 1994, Field and laboratory studies of methane oxidation in an anoxic marine sediment: Evidence for a methanogen-sulfate reducer consortium: Global biogeochemical cycles, v. 8, no. 4, p. 451-463.

Ingall, E. D., and Van Cappellen, P., 1990, Relation between sedimentation rate and burial of organic phosphorus and organic carbon in marine sediments: Geochimica et Cosmochimica Acta, v. 54, no. 2, p. 373-386.

Johnston, D. T., Farquhar, J., Wing, B. A., Kaufman, A. J., Canfield, D. E., and Habicht, K. S., 2005, Multiple sulfur isotope fractionations in biological systems: a case study with sulfate reducers and sulfur disproportionators: American Journal of Science, v. 305, no. 6-8, p. 645-660.

Jørgensen, B. B., 1982, Mineralization of organic matter in the sea bed—the role of sulphate reduction: Nature, v. 296, no. 5858, p. 643-645.

Jørgensen, B. B., Beulig, F., Egger, M., Petro, C., Scholze, C., and Røy, H., 2019a, Organoclastic sulfate reduction in the sulfate-methane transition of marine sediments: Geochimica et Cosmochimica Acta, v. 254, p. 231-245.

Jørgensen, B. B., Böttcher, M. E., Lüschen, H., Neretin, L. N., and Volkov, I. I., 2004, Anaerobic methane oxidation and a deep H2S sink generate isotopically heavy sulfides in Black Sea sediments: Geochimica et Cosmochimica Acta, v. 68, no. 9, p. 2095-2118.

Jørgensen, B. B., Findlay, A. J., and Pellerin, A., 2019b, The biogeochemical sulfur cycle of marine sediments: Frontiers in microbiology, v. 10, p. 849.

Jørgensen, B. B., and Kasten, S., 2006, Sulfur cycling and methane oxidation, Marine geochemistry, Springer, p. 271-309.

Jørgensen, B. B., and Nelson, D. C., 2004, Sulfide oxidation in marine sediments: geochemistry meets microbiology, Sulfur Biogeochemistry–Past and Present, Geological Society of America, p. 63-81.

Kappler, A., and Newman, D. K., 2004, Formation of Fe (III)-minerals by Fe (II)-oxidizing photoautotrophic bacteria: Geochimica et Cosmochimica Acta, v. 68, no. 6, p. 1217-1226.

Kasten, S., Freudenthal, T., Gingele, F. X., and Schulz, H. D., 1998, Simultaneous formation of iron-rich layers at different redox boundaries in sediments of the Amazon deep-sea fan: Geochimica et Cosmochimica Acta, v. 62, no. 13, p. 2253-2264.

Kendall, B., Anbar, A. D., Kappler, A., and Konhauser, K. O., 2012, The global iron cycle: Fundamentals of Geobiology, v. 1, p. 65-92.

Kennett, J. P., 1977, Cenozoic evolution of Antarctic glaciation, the circum-Antarctic Ocean, and their impact on global paleoceanography: Journal of geophysical research, v. 82, no. 27, p. 3843-3860.

Kostka, J. E., and Luther III, G. W., 1994, Partitioning and speciation of solid phase iron in saltmarsh sediments: Geochimica et Cosmochimica Acta, v. 58, no. 7, p. 1701-1710.

Krom, M. D., and Berner, R. A., 1980, Adsorption of phosphate in anoxic marine sediments 1: Limnology and oceanography, v. 25, no. 5, p. 797-806.

Lan, Y., and Butler, E. C., 2014, Monitoring the transformation of mackinawite to greigite and pyrite on polymer supports: Applied geochemistry, v. 50, p. 1-6.

Lin, Z., Sun, X., Peckmann, J., Lu, Y., Xu, L., Strauss, H., Zhou, H., Gong, J., Lu, H., and Teichert, B. M., 2016, How sulfate-driven anaerobic oxidation of methane affects the sulfur isotopic composition of pyrite: A SIMS study from the South China Sea: Chemical Geology, v. 440, p. 26-41.

Luther III, G. W., 1991, Pyrite synthesis via polysulfide compounds: Geochimica et Cosmochimica Acta, v. 55, no. 10, p. 2839-2849.

Lyons, T. W., 1997, Sulfur isotopic trends and pathways of iron sulfide formation in upper Holocene sediments of the anoxic Black Sea: Geochimica et Cosmochimica Acta, v. 61, no. 16, p. 3367-3382.

Lyons, T. W., and Severmann, S., 2006, A critical look at iron paleoredox proxies: New insights from modern euxinic marine basins: Geochimica et Cosmochimica Acta, v. 70, no. 23, p. 5698-5722.

Lyons, T. W., Werne, J. P., Hollander, D. J., and Murray, R., 2003, Contrasting sulfur geochemistry and Fe/Al and Mo/Al ratios across the last oxic-to-anoxic transition in the Cariaco Basin, Venezuela: Chemical Geology, v. 195, no. 1-4, p. 131-157.

Maldonado, A., Bohoyo, F., Galindo-Zaldívar, J., Hernández-Molina, J., Jabaloy, A., Lobo, F., Rodríguez-Fernández, J., Suriñach, E., and Vázquez, J., 2006, Ocean basins near the Scotia–Antarctic plate boundary: influence of tectonics and paleoceanography on the Cenozoic deposits: Marine Geophysical Researches, v. 27, no. 2, p. 83-107.

Martens, C. S., and Klump, J. V., 1984, Biogeochemical cycling in an organic-rich coastal marine basin 4. An organic carbon budget for sediments dominated by sulfate reduction and methanogenesis: Geochimica et Cosmochimica Acta, v. 48, no. 10, p. 1987-2004.

Martinson, D. G., 2012, Antarctic circumpolar current's role in the Antarctic ice system: An overview: Palaeogeography, Palaeoclimatology, Palaeoecology, v. 335, p. 71-74.

Meyer, K., Ridgwell, A., and Payne, J., 2016, The influence of the biological pump on ocean chemistry: implications for long-term trends in marine redox chemistry, the global carbon cycle, and marine animal ecosystems: Geobiology, v. 14, no. 3, p. 207-219.

Michel, F. M., Barrón, V., Torrent, J., Morales, M. P., Serna, C. J., Boily, J.-F., Liu, Q., Ambrosini, A., Cismasu, A. C., and Brown, G. E., 2010, Ordered ferrimagnetic form of ferrihydrite reveals links among structure, composition, and magnetism: Proceedings of the National Academy of Sciences, v. 107, no. 7, p. 2787-2792.

Michel, F. M., Ehm, L., Antao, S. M., Lee, P. L., Chupas, P. J., Liu, G., Strongin, D. R., Schoonen, M. A., Phillips, B. L., and Parise, J. B., 2007, The structure of ferrihydrite, a nanocrystalline material: Science, v. 316, no. 5832, p. 1726-1729.

Morford, J. L., Emerson, S. R., Breckel, E. J., and Kim, S. H., 2005, Diagenesis of oxyanions (V, U, Re, and Mo) in pore waters and sediments from a continental margin: Geochimica et Cosmochimica Acta, v. 69, no. 21, p. 5021-5032.

Morse, J. W., and Cornwell, J. C., 1987, Analysis and distribution of iron sulfide minerals in recent anoxic marine sediments: Marine Chemistry, v. 22, no. 1, p. 55-69.

Paytan, A., Mearon, S., Cobb, K., and Kastner, M., 2002, Origin of marine barite deposits: Sr and S isotope characterization: Geology, v. 30, no. 8, p. 747-750.

Peckmann, J., Reimer, A., Luth, U., Luth, C., Hansen, B., Heinicke, C., Hoefs, J., and Reitner, J., 2001, Methane-derived carbonates and authigenic pyrite from the northwestern Black Sea: Marine geology, v. 177, no. 1-2, p. 129-150.

Pérez, L. F., Maldonado, A., Bohoyo, F., Hernández-Molina, F. J., Vázquez, J. T., Lobo, F. J., and Martos, Y. M., 2014, Depositional processes and growth patterns of isolated oceanic basins: the Protector and Pirie basins of the Southern Scotia Sea (Antarctica): Marine Geology, v. 357, p. 163-181.

Pérez, L. F., Maldonado, A., Hernández-Molina, F. J., Lodolo, E., Bohoyo, F., and Galindo-Zaldívar, J., 2017, Tectonic and oceanographic control of sedimentary

patterns in a small oceanic basin: Dove Basin (Scotia Sea, Antarctica): Basin Research, v. 29, p. 255-276.

Pérez, L. F., Martos, Y. M., García, M., Weber, M. E., Raymo, M. E., Williams, T., Bohoyo, F., Armbrecht, L., Bailey, I., and Brachfeld, S., 2021, Miocene to present oceanographic variability in the Scotia Sea and Antarctic ice sheets dynamics: Insight from revised seismic-stratigraphy following IODP Expedition 382: Earth and Planetary Science Letters, v. 553, p. 116657.

Picard, A., Gartman, A., Clarke, D. R., and Girguis, P. R., 2018, Sulfate-reducing bacteria influence the nucleation and growth of mackinawite and greigite: Geochimica et Cosmochimica Acta, v. 220, p. 367-384.

Poulton, S. W., and Canfield, D. E., 2005, Development of a sequential extraction procedure for iron: implications for iron partitioning in continentally derived particulates: Chemical geology, v. 214, no. 3-4, p. 209-221.

Raiswell, R., 2011, Iron transport from the continents to the open ocean: The aging–rejuvenation cycle: Elements, v. 7, no. 2, p. 101-106.

Raiswell, R., Buckley, F., Berner, R. A., and Anderson, T., 1988, Degree of pyritization of iron as a paleoenvironmental indicator of bottom-water oxygenation: Journal of Sedimentary Research, v. 58, no. 5, p. 812-819.

Raiswell, R., and Canfield, D. E., 1998, Sources of iron for pyrite formation in marine sediments: American Journal of Science, v. 298, no. 3, p. 219-245.

Raiswell, R., Hardisty, D. S., Lyons, T. W., Canfield, D. E., Owens, J. D., Planavsky, N. J., Poulton, S. W., and Reinhard, C. T., 2018, The iron paleoredox proxies: A guide to the pitfalls, problems and proper practice: American Journal of Science, v. 318, no. 5, p. 491-526.

Rickard, D., 1997, Kinetics of pyrite formation by the H2S oxidation of iron (II) monosulfide in aqueous solutions between 25 and 125 C: The rate equation: Geochimica et Cosmochimica Acta, v. 61, no. 1, p. 115-134.

Rickard, D., and Morse, J. W., 2005, Acid volatile sulfide (AVS): Marine chemistry, v. 97, no. 3-4, p. 141-197.

Riedinger, N., Brunner, B., Krastel, S., Arnold, G. L., Wehrmann, L. M., Formolo, M. J., Beck, A., Bates, S. M., Henkel, S., and Kasten, S., 2017, Sulfur cycling in an iron oxide-dominated, dynamic marine depositional system: the Argentine continental margin: Frontiers in Earth Science, v. 5, p. 33.

Riedinger, N., Formolo, M. J., Lyons, T. W., Henkel, S., Beck, A., and Kasten, S., 2014, An inorganic geochemical argument for coupled anaerobic oxidation of methane and iron reduction in marine sediments: Geobiology, v. 12, no. 2, p. 172-181.

Riedinger, N., Kasten, S., Gröger, J., Franke, C., and Pfeifer, K., 2006, Active and buried authigenic barite fronts in sediments from the Eastern Cape Basin: Earth and Planetary Science Letters, v. 241, no. 3-4, p. 876-887.

Rooze, J., Egger, M., Tsandev, I., and Slomp, C. P., 2016, Iron-dependent anaerobic oxidation of methane in coastal surface sediments: Potential controls and impact: Limnology and Oceanography, v. 61, no. S1, p. S267-S282.

Scher, H. D., and Martin, E. E., 2006, Timing and climatic consequences of the opening of Drake Passage: science, v. 312, no. 5772, p. 428-430.

Scholz, F., Hensen, C., Schmidt, M., and Geersen, J., 2013, Submarine weathering of silicate minerals and the extent of pore water freshening at active continental margins: Geochimica et Cosmochimica Acta, v. 100, p. 200-216.

Schoonen, M., and Barnes, H., 1991, Reactions forming pyrite and marcasite from solution: II. Via FeS precursors below 100 C: Geochimica et Cosmochimica Acta, v. 55, no. 6, p. 1505-1514.

Shaw, T. J., Gieskes, J. M., and Jahnke, R. A., 1990, Early diagenesis in differing depositional environments: the response of transition metals in pore water: Geochimica et Cosmochimica Acta, v. 54, no. 5, p. 1233-1246.

Sim, M. S., Bosak, T., and Ono, S., 2011, Large sulfur isotope fractionation does not require disproportionation: Science, v. 333, no. 6038, p. 74-77.

Sivan, O., Adler, M., Pearson, A., Gelman, F., Bar-Or, I., John, S. G., and Eckert, W., 2011, Geochemical evidence for iron-mediated anaerobic oxidation of methane: Limnology and Oceanography, v. 56, no. 4, p. 1536-1544.

Sivan, O., Antler, G., Turchyn, A. V., Marlow, J. J., and Orphan, V. J., 2014, Iron oxides stimulate sulfate-driven anaerobic methane oxidation in seeps: Proceedings of the National Academy of Sciences, v. 111, no. 40, p. E4139-E4147.

Taylor, S. R., and McLennan, S. M., 1985, The continental crust: its composition and evolution.

Thamdrup, B., Finster, K., Hansen, J. W., and Bak, F., 1993, Bacterial disproportionation of elemental sulfur coupled to chemical reduction of iron or manganese: Applied and environmental microbiology, v. 59, no. 1, p. 101-108.

Torres, M., Brumsack, H., Bohrmann, G., and Emeis, K., 1996, Barite fronts in continental margin sediments: a new look at barium remobilization in the zone of sulfate reduction and formation of heavy barites in diagenetic fronts: Chemical Geology, v. 127, no. 1-3, p. 125-139.

Tribovillard, N., Hatem, E., Averbuch, O., Barbecot, F., Bout-Roumazeilles, V., and Trentesaux, A., 2015, Iron availability as a dominant control on the primary composition and diagenetic overprint of organic-matter-rich rocks: Chemical Geology, v. 401, p. 67-82.

Tyson, R., 2001, Sedimentation rate, dilution, preservation and total organic carbon: some results of a modelling study: Organic Geochemistry, v. 32, no. 2, p. 333-339.

Valentine, D. L., and Reeburgh, W. S., 2000, New perspectives on anaerobic methane oxidation: minireview: Environmental microbiology, v. 2, no. 5, p. 477-484.

van der Zee, C., Roberts, D. R., Rancourt, D. G., and Slomp, C. P., 2003, Nanogoethite is the dominant reactive oxyhydroxide phase in lake and marine sediments: Geology, v. 31, no. 11, p. 993-996.

van Grinsven, S., Sinninghe Damsté, J. S., and Villanueva, L., 2020, Assessing the effect of humic substances and Fe (III) as potential electron acceptors for anaerobic methane oxidation in a marine anoxic system: Microorganisms, v. 8, no. 9, p. 1288.

Vandieken, V., Nickel, M., and Jørgensen, B. B., 2006, Carbon mineralization in Arctic sediments northeast of Svalbard: Mn (IV) and Fe (III) reduction as principal anaerobic respiratory pathways: Marine Ecology Progress Series, v. 322, p. 15-27.

Weber, M., Raymo, M., Peck, V. L., and Williams, T., 2019, Expedition 382 Preliminary Report: Iceberg Alley and subAntarctic ice and ocean dynamics 20 March-20 May 2019.

Wehrmann, L. M., Riedinger, N., Brunner, B., Kamyshny Jr, A., Hubert, C. R., Herbert, L. C., Brüchert, V., Jørgensen, B. B., Ferdelman, T. G., and Formolo, M. J., 2017, Iron-controlled oxidative sulfur cycling recorded in the distribution and isotopic composition of sulfur species in glacially influenced fjord sediments of west Svalbard: Chemical Geology, v. 466, p. 678-695.

Werne, J. P., Lyons, T. W., Hollander, D. J., Formolo, M. J., and Damsté, J. S. S., 2003, Reduced sulfur in euxinic sediments of the Cariaco Basin: sulfur isotope constraints on organic sulfur formation: Chemical Geology, v. 195, no. 1-4, p. 159-179.

Westrich, J. T., and Berner, R. A., 1984, The role of sedimentary organic matter in bacterial sulfate reduction: The G model tested 1: Limnology and oceanography, v. 29, no. 2, p. 236-249.

Wilkin, R., and Barnes, H., 1996, Pyrite formation by reactions of iron monosulfides with dissolved inorganic and organic sulfur species: Geochimica et Cosmochimica Acta, v. 60, no. 21, p. 4167-4179.

Wing, B. A., and Halevy, I., 2014, Intracellular metabolite levels shape sulfur isotope fractionation during microbial sulfate respiration: Proceedings of the National Academy of Sciences, v. 111, no. 51, p. 18116-18125.

FIGURES

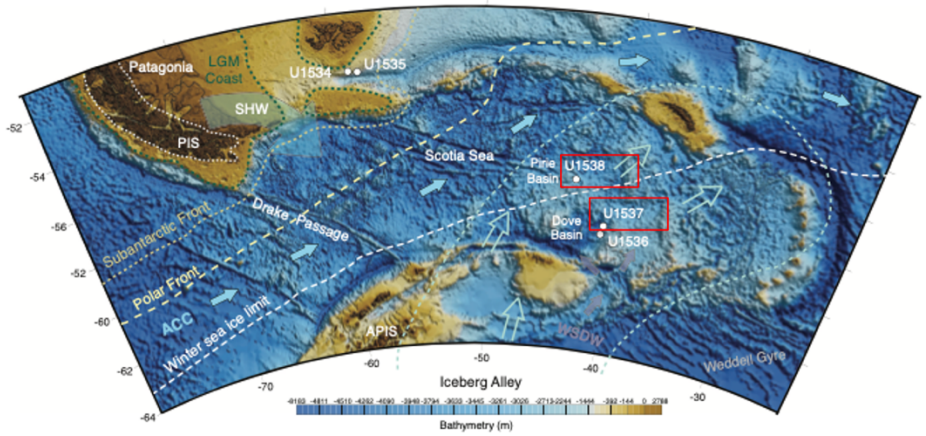

Figure 3.1: Map of studied area located at Scotia Sea sites in Dove Basin (U1537) and Pirie Basin (U1538). Light blue dotted line and open arrows = Iceberg Alley after Anderson and Andrews (1999), large curved gray arrow = main wind direction of South- ern Hemisphere westerlies (SHW), light blue solid arrows = Antarctic Circumpolar Current (ACC) flow direction, purple arrows = Weddell Sea Deep Water (WSDW) exit route (Maldonado et al., 2003), yellow dotted line = Subantarctic Front, yellow dashed line = polar front, green dotted line = Patagonian coastline during LGM (Iriondo, 2000), white dotted line = limit of Patagonian Ice Sheet (PIS) at LGM (Hein et al., 2010), white dashed line = winter sea ice limit. Satellite bathymetry is shown (Weatherall et al., 2015).

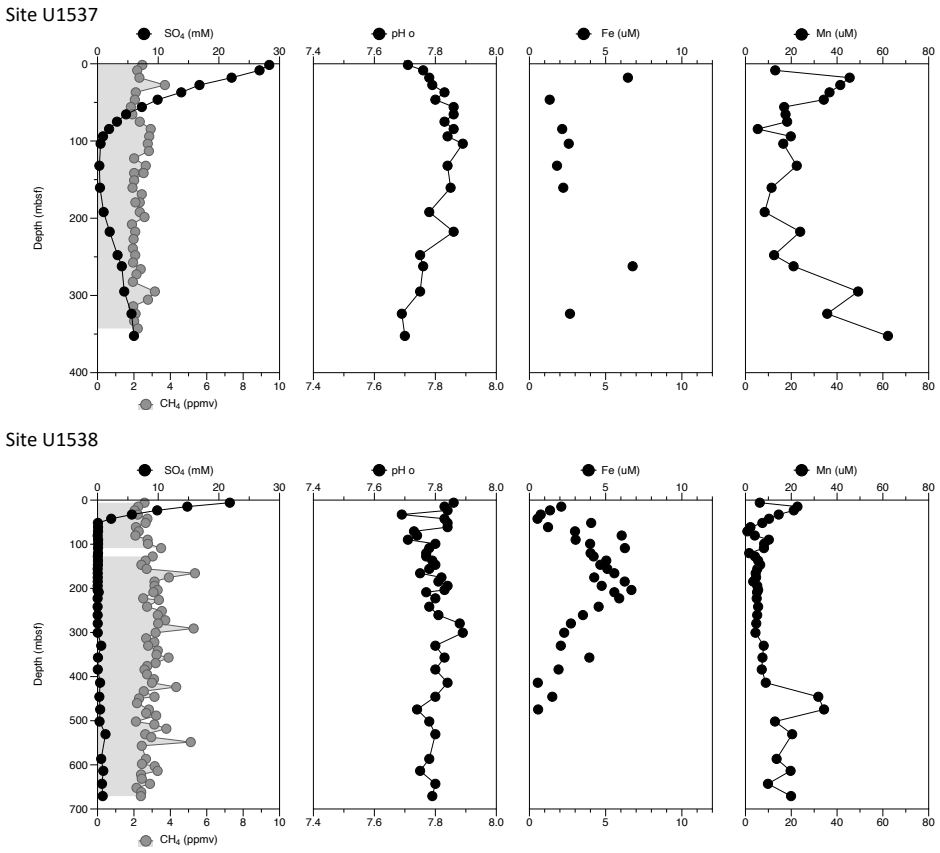

Figure 3.2: Pore water concentrations of sulfate (SO_4^{2-}), Methane (CH_4), pH, iron (Fe) and manganese (Mn) for Site U1537 and Site U1538 measured onboard the JOIDES Resolution by IODP Expedition 382 Scientists (Weber et al., 2019).

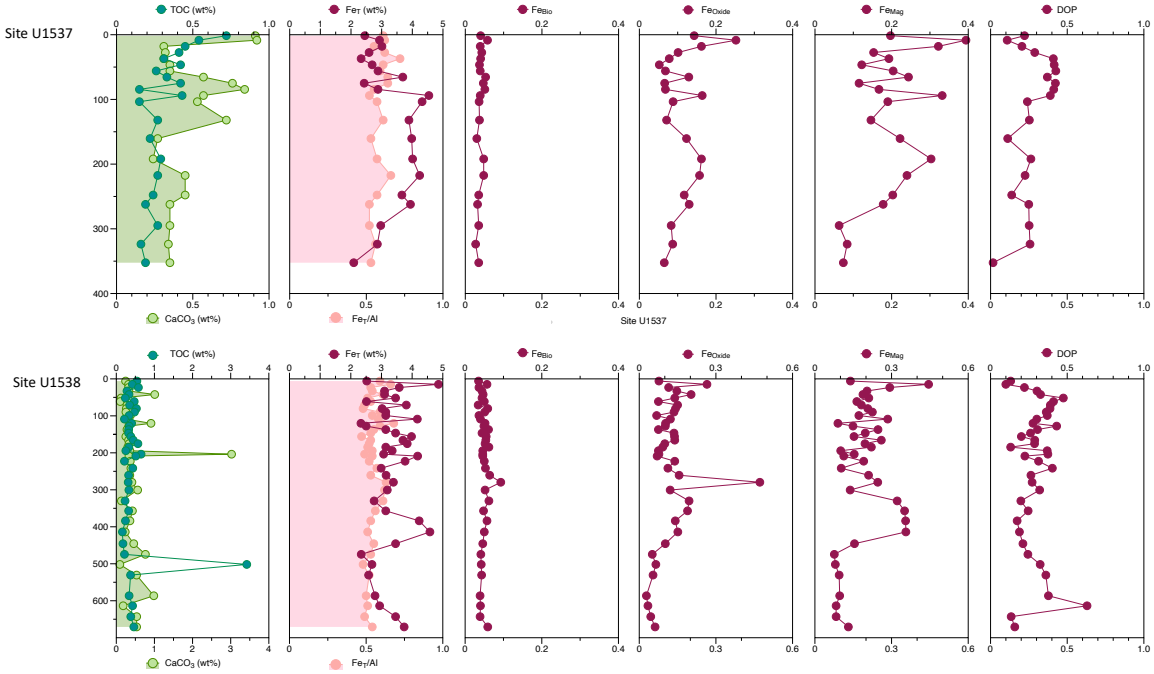

Figure 3.3: Solid phase concentration profiles of total organic carbon (TOC), calcium carbonate ($CaCO_3$), total Fe (Fe_T), Fe/Al ratio, Fe bioavailable ferric iron, Fe oxide phases (Fe_{oxide}, including labile and crystallized Fe-oxide), magnetite (Fe_{mag}) and degree of pyritization (DOP) determined on samples from sites U1537 and U1538.

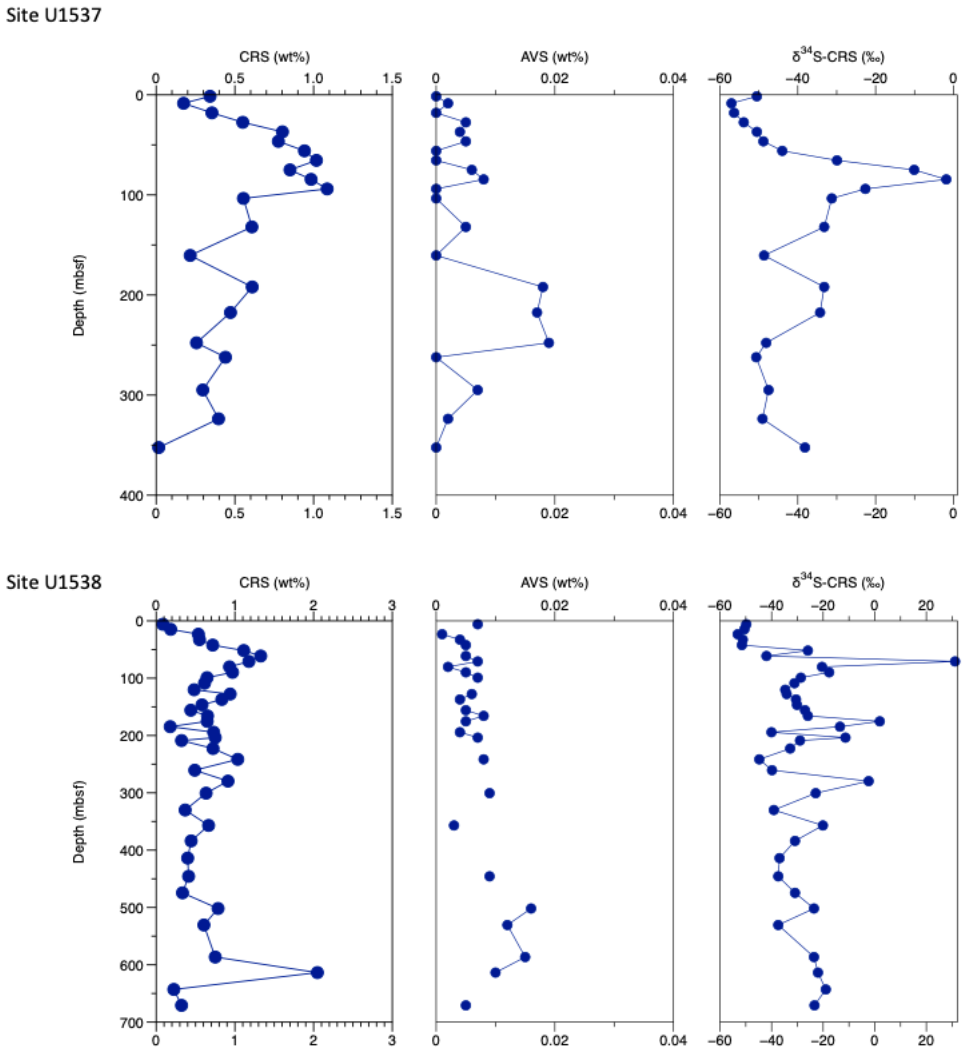

Figure 3.4: Concentration profiles of chromium reducible sulfur (CRS), acid volatile sulfide (AVS), elemental sulfur (S^0), and sulfur stable isotope profiles in addition to sulfate (δ^{34}S-CRS) from sites U1537 and U1538.

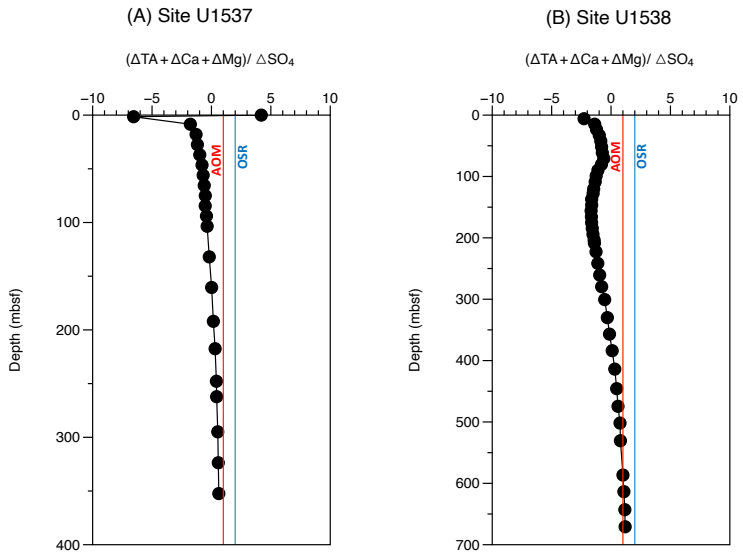

Figure 3.5: Vertical profile of pore water ($\Delta TA + \Delta Ca + \Delta Mg$)/ ΔSO_4^{2-} ratios of Site U1537 and Site U1538. Red and blue line indicates ratios of AOM and OSR respectively.

CHAPTER 4

Biogeochemical changes of the late Archean preceding the rise of oxygen

ABSTRACT

Oxygenation of the atmosphere and oceans had significant impacts on the evolution of the biosphere and the geochemical cycles of redox-sensitive elements. The details of how net accumulation of oxygen in the atmosphere occurred—that is, when oxygen production exceeded oxygen consumption—are still debated and lie at the center of many studies that use geochemical and mineralogical proxies applied to Archean and Paleoproterozoic sedimentary rocks. Here we present geochemical profiles from 2.8- to 2.5-billion-year-old black shales of the Batatal Formation, Minas Supergroup, Brazil. The Re enrichment without Mo, a negative correlation of Mn concentrations and $\delta^{98}Mo$, and $\delta^{13}C_{org}$ enrichment of the Batatal Formation reveals the shift from essentially anerobic settings to transiently oxic depositional conditions of the late-Archean before the rise of oxygen.

INTRODUCTION

Life and its environments have co-evolved through Earth history with changes in the environment occurring in parallel with origin and evolution of life (Catling and Claire, 2005). One of the most complex relationships is between life and oxygen. Almost half of Earth history is known to be reducing with only trace amounts of O_2, unlike the present-day oxidizing atmosphere (Kasting and Catling, 2003; Lyons et al., 2014). The oxygenation of the atmosphere and oceans is a milestone in the evolution of the biosphere and is linked to the expansion of complex life (Reinhard et al., 2016) and impacted metal redox cycling over wide spatial scales ranging from those within microbial mats to global geochemical cycles. The timing of ocean oxygenation is still debated, and the collective evidence suggests a substantial delay between the rise of atmospheric oxygen and deep ocean oxygenation (Holland, 2006; Scott et al., 2008). On the other hand, recent studies allude to the possible accumulation of oxygen in shallow marine environments millions of years before the 'Great Oxidation Event' (GOE) (Duan et al., 2010; Olson et al., 2013; Planavsky et al., 2014b).

The rise of atmospheric oxygen is dependent on the balance between oxygen sources and sinks. Sources of oxygen on early Earth included the burial of organic carbon originally sourced from oxygenic photosynthesis, burial of biogenic pyrite (Holland, 1973), and escape of $H_2(g)$ into space (Catling et al., 2001). Sinks of oxygen were comprised of weathering/oxidation of reduced minerals and reduced volcanic and metamorphic gases (Catling and Claire, 2005). Late Archean Eon cratons played a critical role in the early development of stable continental shelves and epicontinental seas and likely the rise of oxygen (Kump and Barley, 2007) as recorded in Earth's earliest

sedimentary successions (Barley et al., 2005). The large and stable cratons became the sites for stable-shelf sediment deposition during the Neoarchean (Eriksson, 1995), including the shallow-marine 'oxygen oases' where aerobic microbial communities thrived (Eigenbrode and Freeman, 2006; Olson et al., 2013). Thus, we focus this work on understanding the terminal Neoarchean world by contributing essential geochemical time series data across Archean-Proterozoic sedimentary successions, in this case through study of the Batatal Formation, Minas Supergroup from the São Francisco Craton located in the eastern portion of the Brazilian shield (Fig.1) (De Almeida et al., 1981).

The Batatal Formation marks the shift from the clastic deposition of the Caraça Group to the biochemical accumulation of the overlying Itabira Group (Dorr, 1969) (Fig. 2, Fig. S1) (Bekker et al., 2003; Rosière and Chemale Jr, 2017). The Batatal Formation is comprised of offshore sediments deposited on a gradually subsiding continental shelf consisting of three distinct facies: lower laminated shale, carbonate and carbonaceous shale, and uppermost black shale enriched in silica that transition into the overlying Cauê Iron Formation (Fig. 2). The lithological transitions of the Batatal Formation are similar to two those of other Archean-Paleoproterozoic successions, the Klein Naute and Kuruman Iron formations from South Africa and Mt. McRae Shale Formation and the Brockman Iron Formation from Western Australia (Fig. S2). The Batatal Formation, however, differs from other two successions insofar as the Brazilian succession was deposited directly on terrestrial or marginal marine clastic sediments (the Moeda Formation) (Bekker et al., 2003). This difference allows us to compare records of the GOE under different depositional conditions and thus assess the relative controls linked to local versus global

processes—or some combination of both. To effectively explore the evolution of ocean redox during the Archean-Paleoproterozoic transition, we generated high-resolution geochemical profiles for iron (Fe) speciation, redox-sensitive metal enrichments (molybdenum, Mo; rhenium, Re; and uranium, U), and Mo and organic carbon (C) isotope data from 2.5-Gyr-old Batatal Formation Shale.

MATERIAL AND METHODS

Study Site: Geological Setting and Stratigraphy

The sedimentary succession of Minas Supergroup comprises three groups: the Caraça, Itabira, and Piracicaba (Bekker and Eriksson, 2003). The Batatal Formation forms the upper part of the Caraça Group, which overlies the Moeda Formation with a generally sharp contact. The Batatal Formation is comprised of offshore sediments deposited on a slowly subsiding continental shelf along a passive margin (Spier et al., 2007). The shallow marine Batatal platform is composed of two shale-rich intervals above and below a stromatolitic carbonate (Dorr, 1969). The Itabira Group comprises itabirites (BIFs), also known as banded-quartz hematite and hematite schist, with minor dolomite of the Cauê Formation (Rosiere et al., 2008; Spier et al., 2003) and carbonates of the Gandarela Formation. Rocks in these three successions consist mostly of black shale, carbonate, and BIF, representing both deep and shallow water marine environments (Bekker and Eriksson, 2003; Cheney, 1996). These geographically and spatially discrete sedimentary units thus provides a unique opportunity to examine similarities and differences in sediment geochemistry across the terminal Neoarchean. Given available age constraints, it is

possible that the contact between the Batatal Formation and the overlying Cauê Iron Formation might be directly correlated with similarly aged contacts between shale and BIF in South Africa (between the Klein Naute and Kuruman Iron formations) and Western Australia (between the Mt. McRae Shale Formation and the Brockman Iron Formation).

Sampling

The Batatal Formation consists largely of sericitic phyllite, and lesser meta-chert, iron formation and graphitic phyllite with a thickness that can range from a few meters to more than 200m (Dorr, 1969). The Batatal Formation is extensive but is poorly preserved in outcrop, showing high degrees of weathering where it does occur on the surface. Our black shale samples were collected in drill core from Alegria Mine Minas Gerais, MG, Brazil, thus removing the effects of weathering. For this study, we collected seventy-three samples in total from the BT-AL-01core. In the BT-AL-01 core the Batatal Formation consists of upper and lower black laminated shale intervals, which we denote as S1 (from 582.1 to 625 m) and S2 (from 679.6 to 690 m), separated by the carbonate-rich black shale (Fig. 2). The contact between the lower black shale and the upper black shale is gradational. Samples often contain black graphitic phyllite indicating the low degree of reginal metamorphism resulted from two major tectonic events, the Transamazonian (ca. 2.2-2.0 Gyr) and Brasiliano (ca. 0.6-0.5Gyr) orogenies (Alkmim and Marshak, 1998; Caby et al., 1991; Rosière et al., 2019; Rosière and Chemale Jr, 2017).

Total sulfur, carbon, and inorganic carbon analysis

Total carbon (C), sulfur (S), and inorganic carbon (TIC) were measured using an ELTRA carbon and sulfur analyzer. Total C and S were determined through combustion of samples at 1,350°C, with quantification of evolved gasses by infrared absorption. Total inorganic carbon (TIC) was determined by acidification of a split of the sample. Total organic carbon (TOC) content was calculated as the difference between TC and TIC. The geostandards AR4007 and AR4011 were analyzed routinely, with values falling within reported ranges and deviating by less than <5%. Calcium carbonate concentrations ($CaCO_3$), as weight percent, were calculated from the measured IC content assuming that all evolved CO_2 was derived from dissolution of $CaCO_3$:

$$CaCO_3\ (wt\%) = IC \times 8.33(wt\%)$$

Standard $CaCO_3$ (>99.9% calcium carbonate, Fisher Scientific) was included during individual batches of analyses to confirm accuracy and instrument performance before, during, and after each run (with reproducibility better than 3%).

Iron speciation to determine highly reaction iron (Fe_{HR})

The speciation of highly reactive iron (Fe_{HR}), which is comprised of pyrite iron and other iron phases that can react with sulfide to form pyrite in the water column or during early diagenesis is in the sediments, was obtained via a calibrated sequential extraction protocol (Poulton and Canfield, 2005). Approximately 100 mg of sample powder were first treated with a buffered sodium acetate solution, which extracts carbonate-associated Fe (either siderite, ferroan calcite, and/or the dolomite-ankerite solid solution series). This

fraction is here referred to as Fe_{carb}. Samples were then treated with a sodium dithionite solution. Iron obtained from this extraction step, hereafter referred to as Fe_{ox}, consists of "reducible" iron oxide phases—that is, iron oxides such as goethite and hematite that are reactive to hydrogen sulfide (H_2S) on early diagenetic timescales. Magnetite, a mixed-valence iron oxide that does not react with dithionite, was extracted with an ammonium oxalate solution. Sequential extracts were analyzed on an Agilent 7500ce ICP-MS after 100-fold dilution in trace-metal grade 2% HNO_3 at University of California, Riverside. Pyrite iron was calculated (assuming a stoichiometry of FeS_2) based on wt% sulfur extracted during a two-hour hot chromous chloride distillation followed by iodometric titration (Canfield et al., 1986).

The total amount of highly reactive iron, or Fe_{HR}, is defined as:

$$Fe_{HR} = Fe_{carb} + Fe_{ox} + Fe_{mag} + Fe_{Py}$$

Data are reported as the ratio of a particular reactive Fe phase to the total amount of highly reactive Fe (e.g., Fe_{carb} / Fe_{HR}).

Elemental Analysis (Major and trace elements)

A multi-acid digest was performed to determine total solid-phase iron (Fe_T) and aluminum (Al) concentrations. Dried samples were ashed at 550°C, and a standard three-step digestion performed using trace metal grade HF, HNO_3, and HCl at 140°C. This way, the potential bioreactivity of the Fe can be expressed as a fraction of the total Fe pool. Final concentrations were determined using the Agilent 7900 ICP-MS. Reference standards

SDO-1 (Devonian Ohio Shale) and SCO-1 (Cody Shale) were digested and analyzed in parallel with the sample extractions and yielded errors of less than <4%.

δ^{98}Mo

Splits from the multi-acid digest was used to measure the Mo (δ^{98}Mo) isotope composition of the bulk sample. Using the measured Mo concentrations, a double spike will be added to each sample at a 1:1 sample:spike ratio. Molybdenum purification was completed through a two-stage column technique.

Aliquots of each digest solution were treated with a Mo^{97}/Mo^{100} double spike to achieve a sample/spike Mo ratio of 1:1. The Mo was then purified using a two-stage column chromatographic procedure (Asael et al., 2018). Isotopic compositions were measured on Thermo Neptune MC-ICP-MS (Multiple Collector-Inductively Coupled Plasma-Mass Spectrometer) at Yale University. Accuracy and precision were monitored through repeated measurements of processed USGS standard NOD-A-1. All Mo isotope data are reported relative to standard NIST-3134 using the following conventional delta notation:

$$\delta^{98}Mo_{‰} = \left[\frac{(^{98}Mo/^{95}Mo)sample)}{(^{98}Mo/^{95}Mo)NIST3134)}\right] - 1$$

$\delta^{13}C_{org}$

For organic carbon isotope analysis, 50-100 mg sample powders were acidified using 6N HCl in 50 mL centrifuge tubes. Magnetic stir bar was spun at 150 rpm during acidification, and vials were periodically vortexed to ensure complete decarbonation. Decarbonated and dried insoluble residue of samples were weighed into tin (Sn) capsules

for analysis. Organic carbon isotope ratios were measured using a Costech EA 4010 linked to a Thermo-Finnigan Delta V Advantage mass spectrometer via a Conflo IV open-split interface system at University of California, Riverside. Unknowns were corrected against USGS 40, USGS 41a, SDO-1, and UW-McRae. Analytical error was better than 0.1 ‰ for organic carbon (1σ).

Statistical Analysis

The t test was applied to determine the significance of differences between the upper and lower shales (S1 and S2, respectively) (Krzywinski and Altman, 2013). A *p*-value higher than 0.05 (> 0.05) is not statistically significant and is strong evidence for the null hypothesis. A *p*-value less than 0.05 (typically ≤ 0.05) is statistically significant. Such data are strong evidence against the null hypothesis, as there is less than a 5% probability the null is correct. In such cases, we reject the null hypothesis—i.e., that there is no relationship—and seek alternative hypothesis.

RESULTS AND DISCUSSION

Iron Speciation

Iron (Fe) has two thermodynamically stable phases, a reduced form in the ferrous (Fe^{2+}) state and an oxidized ferric state (Fe^{3+}). In ancient oceans, where deep ocean anoxia was predominant, Fe would occur in its ferrous state. Liable Fe—that is, highly reactive Fe (Fe_{HR}) that is reactive toward H_2S on diagenetic timescales—occurs under both ferruginous and euxinic conditions and is subdivided in four sub-pools: Fe-carbonates (Fe_{Carb}), Fe-

oxides (Fe_{Ox}), magnetite Fe (Fe_{Mag}), and pyrite Fe (Fe_{Py}). In modern oxic marine sediments, Fe_{HR} encompasses less than 38% of the total sedimentary Fe pool (i.e., $Fe_{HR}/Fe_T < 0.38$) (Poulton and Canfield, 2011). Appreciable enrichments beyond this limit ($Fe_{HR}/Fe_T > 0.38$) are an indication of an anoxic water column (Canfield et al., 2008; Lyons et al., 2009b). At sites where anoxia is inferred, we can further discriminate between ferruginous ($Fe^{2+} > H_2S$) and euxinic ($Fe^{2+} < H_2S$) conditions by determining the extent to which Fe_{HR} has reacted with H_2S to form pyrite (Fe_{Py}/Fe_{HR}). As such, when Fe_{Py} comprises at least 80% of the Fe_{HR} pool in a shale ($Fe_{Py}/Fe_{HR} \geq 0.8$), it is interpreted to indicate euxinic depositional conditions (Poulton and Canfield, 2011). The interpretations are more equivocal in samples with Fe_{HR}/Fe_T ratio between 0.22-0.38 and may reflect oxic deposition or an anoxic setting where Fe_{HR} enrichment are masked by high sedimentation rates and/or diagenetic transfer of Fe_{HR} into Fe silicate phases that may be weakly reactive with free sulfide to form pyrite (Poulton and Canfield, 2011; Raiswell et al., 2018a). Here, Fe speciation was employed with a calibrated sequential Fe extraction protocol (Materials; Poulton and Canfield, 2005).

The Fe speciation of the Batatal Formation shows variable inferred redox signatures. The fundamental water column redox conditions are captured in the Fe_{HR}/Fe_T profile, with data inferred as oxic ($Fe_{HR}/Fe_T < 0.22$), equivocal (Fe_{HR}/Fe_T 0.22-0.38), or anoxic ($Fe_{HR}/Fe_T > 0.38$). The sediments of the Batatal Formation show some evidence suggesting oxic depositional conditions, with majority of samples falling in the equivocal zone (Fig.3). In a few cases, Fe_{Py}/Fe_{HR} values verge on the threshold ($Fe_{Py}/Fe_{HR} \geq 0.8$) inferred to reflect euxinia when combined with evidence for anoxic deposition (Anderson

and Raiswell, 2004; Poulton et al., 2004). However, the average Fe_{Py}/Fe_{HR} for this formation (0.15±0.18) suggests a predominance of ferruginous conditions (Fig. 3). We also look at the Fe_T/Al ratio, since enrichments in total Fe can be an alternative indicator of water column anoxia (Lyons and Severmann, 2006), where ratios above the oxic Phanerozoic shale value (0.53±0.11wt%) are indicative of anoxic settings. Unlike the Fe speciation approach, total Fe data are not impacted by post-depositional transformations (Clarkson et al., 2014; Lyons and Severmann, 2006; Raiswell et al., 2008). Values of Fe_T/Al and Fe_{HR}/Fe_T are low and follow similar patterns throughout the sequence (Fig. 3 and S2). Previous studies have shown that during diagenesis and low-grade metamorphism, unsulfidized Fe-bearing highly reactive minerals can be transformed to poorly reactive Fe-silicates, lowering Fe_{HR}/Fe_T and increasing Fe_{Py}/Fe_{HR} ratios, particularly when the porewater sulfide concentrations are very low (Hardisty et al., 2018b; Poulton et al., 2010; Raiswell et al., 2018a). To address the potential alteration of primary Fe geochemical signals we compare the Fe_{Py}/Fe_{HR} with the degree of pyritization (DOP) (Cunningham and Reinhard, 2002; Lyons et al., 2009a). The DOP technique relies on a more aggressive leach of "reactive" Fe (boiling concentrated HCl). It can extract appreciable Fe silicate phases and thus overestimate the readily reactive pool (see Lyons and Severmann, 2006 and Lyons et al., 2009, for review) (Lyons et al., 2009a; Lyons and Severmann, 2006). Our data, however, demonstrate a good correlation between DOP and $Fe_{Py}/Fe_{HR,}$ confirming that Fe speciation values represent a primary water column signal.

Redox-sensitive element enrichments

The degree of enrichment in sediments is regulated by the rain rate of organic carbon through the water column, bottom water oxygen concentrations, or combination of both (McManus et al., 2005) and therefore can provide a detailed perspective on the ancient water-column redox state. Molybdenum (Mo) is the most abundant transition metal in today's ocean (Collier, 1985; Emerson and Huested, 1991). The concentration of dissolved Mo in the oceans is partially a product of the degree of oxidative weathering of continental crust. The Mo concentration of the oceans is also controlled by the extent of ocean oxygenation because molybdate (MoO_4^{-2}), which is stable and largely unreactive under oxic settings, is converted to oxythiomolybdates ($MoO_{(4-x)}S^{2-}_x$) by reaction with HS^- and co-precipitate with iron sulfides in anoxic (euxinic) conditions or scavenged by organic matter (Chappaz et al., 2012; Erickson and Helz, 2000; Tribovillard et al., 2004). Because Mo enrichments in shales are controlled by oxidative weathering, local redox conditions, and prevailing redox state of the global ocean, they can be used to track the global redox landscape (Scott et al., 2008).

Rhenium (Re) behavior resembles that of Mo in seawater and in reducing sediment (Anbar et al., 1992; Koide et al., 1986). Re occurs predominately as perrhenate (ReO_4^-) in oxygenated ocean waters with a residence time calculated to be as long as 130 k.y. (Miller et al., 2011) and is reduced to an Re(IV) oxide or sulfide in anoxic environments (Helz and Dolor, 2012). There are two important differences between Mo and Re. The Re removal to the sediment is entirely abiotic (Morford et al., 2009), and Re is indifferent to Mn-oxyhydroxide scavenging, unlike Mo (Helz and Dolor, 2012). The conservative behavior

of Re in oxygenated seawater allows Re to be removed efficiently to anoxic sediments at low dissolved H_2S when the bottom waters are weakly oxygenated or anoxic (Colodner et al., 1993; Morford and Emerson, 1999; Morford et al., 2005; Morford et al., 2009). The redox-sensitive behavior of Re is used to characterize the evolution of ancient marine redox conditions through geologic time by examining the sedimentary enrichment (Helz and Dolor, 2012; Kendall et al., 2010; Sheen et al., 2018) and the distinctive sensitivity of Re to differing conditions allows additional capacity to solve spatial and temporal patters in the ancient redox landscape (Sheen et al., 2018).

The degree of Uranium (U) enrichment on other hand takes the primary form U(VI) in oxic to suboxic waters where uranyl ions bind with carbonate ions to form uranyl carbonate complexes ($UO_2(CO_3)_3^{4-}$) and is largely unreactive. U, similarly to Mo, is adsorbed to Mn-Fe (oxyhydr)oxides in well-oxygenated marine settings associated with particulate matter in the water column (Dunk et al., 2002). In the sediments, U reduction occurs at the same redox boundary where Fe(III) reduces to Fe(II) and is often mediated by microbial reduction (i.e. bacterial sulfate reduction (BSR); (Algeo and Tribovillard, 2009). The degree of U enrichment is controlled by either bottom water oxygen concentrations, the rain rate of organic carbon through the water column, or both (McManus et al., 2005; Partin et al., 2013).

We focus on the two intervals containing black laminated shale, which we denote as S1 (from 582.1 to 625 m) and S2 (from 679.6 to 690 m). The shales in both intervals contain low weight % (wt%) total sulfur (S) (average = 0.12 ± 0.16) and total organic carbon (TOC) (average = 1.06 ± 0.20), and Mo concentrations are typically < 2 parts per

million (ppm) (Fig. 2, S table S5). Ratios of Mo to total organic carbon (TOC) (average Mo/TOC=1.97 ± 0.74) are lower than those found in sediments from the modern Black Sea (4.5 ppm/wt% (Algeo and Lyons, 2006)) and are typical of Archean shales because the bottom-water Mo concentrations were likely low in the absence of appreciable oxidative weathering on the continents (Scott et al., 2008). The most prominent feature of the data is the sizable enrichment of Re (Al-normalized enrichment factor (EF) = 6-33), with negligible enrichments in Mo (EF < 3) and U (EF <2) (Fig. 2). The disparity in Mo versus Re EF could be due to the different removal mechanism. The authigenic Mo accumulation rate varies depending on sulfide availability and takes place when MoO_4^{2-} reacts with sulfidic waters to form particle-reactive thiomolybdates ($MoO_{4-x}Sx^{2-}$), which are scavenged from solution (Algeo and Lyons, 2006; Erickson and Helz, 2000). On the other hand, the Re accumulation rate is regulated by slow kinetic chemical reduction of Re^{VII} to Re^{IV} (Helz and Dolor, 2012; Sundby et al., 2004). Under mildly reducing depositional conditions, Mo and Re do not accumulate simultaneously. Specially, when O_2 penetrates ~1 cm or less in the sediment-water interface, Re accumulates while Mo does not since it is limited by sulfide concentrations in the pore water and water column (Morford et al., 2005). The enrichment patterns for Re and Mo in the S1 unit of the Batatal Formation suggest mildly oxygenated surface ocean resembling modern environment where O_2 penetrates below the sediment-water interface (Algeo and Tribovillard, 2009; Crusius et al., 1996; Nameroff et al., 2002) as previously suggested for Archean sediments (Kendall et al., 2010). The Mo low abundance in Batatal Formation is due to the absence of sulfide as well as low oceanic inventory (Scott et al., 2008) as noted with low pyrite content

(Fe_{Py}/Fe_{HR}) (Fig. 2). The enrichment of Re is prominent since Re burial in sediments below anoxic waters does not depend on H_2S availability in the water column (Miller et al., 2011) and the similar ionic size and charge of Mo^{+4} and Re^{+4} facilitates sizable uptake of Re during crystallization of molybdenites resulting in an increase of Re concentration (Golden et al., 2013). Our results suggest a weakly reducing depositional conditions with Re enrichment without Mo in Batatal Formation.

Mo isotope records

The Mo isotope system can allow us to reconstruct global paleoredox conditions and uncover the evolution of ocean oxygenation through Earth's history (Anhar et al., 2005; Asael et al., 2018; Dickson et al., 2017; Kendall et al., 2017; Ostrander et al., 2020). In well-oxygenated modern seawater, Mo is removed via adsorption to Fe-Mn oxides and crusts (Barling and Anbar, 2004). Lighter Mo isotopes are removed with Mn-oxyhydroxides, making the modern seawater enriched with heavier Mo isotopes (2.34 ± 0.10‰) compared with rivers (average = 0.7‰) (Archer and Vance, 2008). Under mildly oxygenated bottom waters (O_2: 10-35 μM) of the modern continental margins, Mo adsorption to Fe-Mn oxyhydroxides yields a range of δ^{98}Mo values from –0.5‰ to 1.3‰ (Poulson Brucker et al., 2009). In a strongly euxinic environment ($H_2S_{(aq)} \geq 11$ μM) within a restricted marine basin such as the modern Black Sea, the soluble molybdate rapidly transforms to tetrathiomolybdate and is removed almost quantitatively from bottom waters to sediments, yielding δ^{98}Mo (2.0‰ to 2.4‰) similar to the open ocean (2.34 ± 0.10‰) in organic-rich sediments deposited under strongly euxinic waters (Neubert et al., 2008).

Previous studies show the Archean ocean δ^{98}Mo values with an average of 0.2‰ (Czaja et al., 2012; Wille et al., 2007).

The Batatal Formation δ^{98}Mo values are show an extensive range throughout the section from -1.4 to 1.15‰. (Fig. 3). Today, an incomplete transfer of Mo from marine bottom-waters to sediments in non-euxinic or weakly sulfidic euxinic marine settings results in highly variable sedimentary δ^{98}Mo that are often isotopically lighter than coeval seawater ($\delta^{98}Mo_{seawater\text{-}sediments}$ = 0-3‰) (Kendall et al., 2017). For example, the complexation of Mo with Fe oxide minerals (Goldberg et al., 2009), Mn oxide minerals (Wasylenki et al., 2008), the formation of intermediate thiomolybdate species in sediment pore fluids and the water column can result in varying sedimentary Mo isotope data (Neubert et al., 2008). The transient development of a Mn oxide 'shuttle' (Hardisty et al., 2016; Planavsky et al., 2014a) in the Batatal formation could help to explain the negative correlation of Mn concentrations and δ^{98}Mo (Fig. 2, Fig. 4 and Fig. S3). Previous studies in iron formations suggested that low δ^{98}Mo values reflect the local formation of Mn oxides followed by the preferential adsorption of isotopically light Mo resulting in Mn enriched samples with low δ^{98}Mo values (Planavsky et al., 2014a) and the delivery of Mn oxides to the seafloor would be consistent with an at least locally transient oxygenated water column (Planavsky et al., 2014a).

Organic Carbon

The $\delta^{13}C_{org}$ values from the Batatal Formation, averaging -18.44‰ (Figure 2), suggest the possibility of different environmental condition of formation relative to the Mt.

McRae Shale and Klein Naute Formation where $\delta^{13}C_{org}$ shows an average value of -35‰ (Fischer et al., 2009; Kaufman et al., 2007). The $\delta^{13}C_{org}$ enrichment is not likely the result of thermal effects since the metamorphic grade in Batatal Formation is low (Coplen et al., 2006). Instead, it could be explained by the decrease in the significance of anaerobic processes involving methane cycling since the shallow-water ecosystem dominated by methane assimilation of the late-Archean was highly sensitive to environmental changes (Eigenbrode and Freeman, 2006; Krissansen-Totton et al., 2015). Thus, it is fair to say that the $\delta^{13}C_{org}$ of the Batatal Formation is a reflection of a weakly reducing and transiently oxic depositional conditions that features the beginning of global carbon-cycle restructuring originated by the release of molecular oxygen into an otherwise anaerobic world.

CONCLUSIONS

In summary, this study adds to further evidence in the growing body of work that shows the evolution of atmospheric and marine O_2 was more complex than a simple punctuated rise (Anbar et al., 2007; Kendall et al., 2015; Kendall et al., 2010; Lyons et al., 2014; Ostrander et al., 2020; Reinhard et al., 2009). Specifically, the Re enrichment without Mo, a negative correlation of Mn concentrations and $\delta^{98}Mo$, and $\delta^{13}C_{org}$ enrichment of the Batatal Formation reveals the shift from purely anerobic communities (e.g. methane-assimilating) to transient episode of oxic conditions of the late-Archean. Our data support the conclusion that oxygenic photosynthesis was present before the GOE along with an oscillating of O_2 levels (Anbar et al., 2007; Kaufman et al., 2007; Olson et al., 2013; Planavsky et al., 2014a; Riding et al., 2014) and reveals a temporal and spatial patterns that

document profound biogeochemical changes of the late Archean preceding the rise of oxygen driven by complex biospheric feedbacks and tectonic processes (Barley et al., 2005; Catling and Zahnle, 2020; Kadoya et al., 2020; Kump et al., 2001; Lee et al., 2016; Olson et al., 2013; Ostrander et al., 2020; Ostrander et al., 2019).

REFERENCES

Algeo, T. J., and Lyons, T. W., 2006, Mo-total organic carbon covariation in modern anoxic marine environments: Implications for analysis of paleoredox and paleohydrographic conditions: Paleoceanography, v. 21, no. 1.

Algeo, T. J., and Tribovillard, N., 2009, Environmental analysis of paleoceanographic systems based on molybdenum–uranium covariation: Chemical Geology, v. 268, no. 3-4, p. 211-225.

Alkmim, F. F., and Marshak, S., 1998, Transamazonian orogeny in the Southern Sao Francisco craton region, Minas Gerais, Brazil: evidence for Paleoproterozoic collision and collapse in the Quadrilátero Ferrıfero: Precambrian Research, v. 90, no. 1-2, p. 29-58.

Anbar, A., Creaser, R., Papanastassiou, D., and Wasserburg, G., 1992, Rhenium in seawater: Confirmation of generally conservative behavior: Geochimica et Cosmochimica Acta, v. 56, no. 11, p. 4099-4103.

Anbar, A. D., Duan, Y., Lyons, T. W., Arnold, G. L., Kendall, B., Creaser, R. A., Kaufman, A. J., Gordon, G. W., Scott, C., and Garvin, J., 2007, A whiff of oxygen before the great oxidation event?: Science, v. 317, no. 5846, p. 1903-1906.

Anderson, T. F., and Raiswell, R., 2004, Sources and mechanisms for the enrichment of highly reactive iron in euxinic Black Sea sediments: American Journal of Science, v. 304, no. 3, p. 203-233.

Anhar, A. D., Williams, G. A., Marshall, L., Arnold, G. L., and Lyons, T. W., 2005, Tracking changes in ocean oxygenation with molybdenum isotopes.: Abstracts of Papers of the American Chemical Society, v. 229, p. U891-U891.

Archer, C., and Vance, D., 2008, The isotopic signature of the global riverine molybdenum flux and anoxia in the ancient oceans: Nature Geoscience, v. 1, no. 9, p. 597-600.

Asael, D., Rouxel, O., Poulton, S. W., Lyons, T. W., and Bekker, A., 2018, Molybdenum Record from Black Shales Indicates Oscillating Atmospheric Oxygen Levels in the Early Paleoproterozoic: American Journal of Science, v. 318, no. 3, p. 275-299.

Barley, M. E., Bekker, A., and Krapež, B., 2005, Late Archean to Early Paleoproterozoic global tectonics, environmental change and the rise of atmospheric oxygen: Earth and Planetary Science Letters, v. 238, no. 1-2, p. 156-171.

Barling, J., and Anbar, A., 2004, Molybdenum isotope fractionation during adsorption by manganese oxides: Earth and Planetary Science Letters, v. 217, no. 3-4, p. 315-329.

Bekker, A., and Eriksson, K. A., 2003, A Paleoproterozoic drowned carbonate platform on the southeastern margin of the Wyoming Craton: a record of the Kenorland breakup: Precambrian Research, v. 120, no. 3, p. 327-364.

Bekker, A., Holland, H., Wang, P.-L., Rumble, D., Stein, H., Hannah, J., Coetzee, L., and Beukes, N., 2004, Dating the rise of atmospheric oxygen: Nature, v. 427, no. 6970, p. 117-120.

Bekker, A., Sial, A., Karhu, J., Ferreira, V., Noce, C., Kaufman, A., Romano, A., and Pimentel, M., 2003, Chemostratigraphy of carbonates from the Minas Supergroup, Quadrilátero Ferryífero (Iron Quadrangle), Brazil: A stratigraphic record of early proterozoic atmospheric, biogeochemical and climactic change: American Journal of Science, v. 303, no. 10, p. 865-904.

Caby, R., Sial, A., Arthaud, M., and Vauchez, A., 1991, Crustal evolution and the Brasiliano orogeny in Northeast Brazil, The west African orogens and circum-Atlantic correlatives, Springer, p. 373-397.

Canfield, D. E., Poulton, S. W., Knoll, A. H., Narbonne, G. M., Ross, G., Goldberg, T., and Strauss, H., 2008, Ferruginous conditions dominated later Neoproterozoic deep-water chemistry: Science, v. 321, no. 5891, p. 949-952.

Canfield, D. E., Raiswell, R., Westrich, J. T., Reaves, C. M., and Berner, R. A., 1986, The Use of Chromium Reduction in the Analysis of Reduced Inorganic Sulfur in Sediments and Shales: Chemical Geology, v. 54, no. 1-2, p. 149-155.

Catling, D. C., and Claire, M. W., 2005, How Earth's atmosphere evolved to an oxic state: a status report: Earth and Planetary Science Letters, v. 237, no. 1-2, p. 1-20.

Catling, D. C., and Zahnle, K. J., 2020, The archean atmosphere: Science Advances, v. 6, no. 9, p. eaax1420.

Catling, D. C., Zahnle, K. J., and McKay, C. P., 2001, Biogenic methane, hydrogen escape, and the irreversible oxidation of early Earth: Science, v. 293, no. 5531, p. 839-843.

Chappaz, A., Lyons, T. W., Gordon, G. W., and Anbar, A. D., 2012, Isotopic Fingerprints of Anthropogenic Molybdenum in Lake Sediments: Environmental Science & Technology, v. 46, no. 20, p. 10934-10940.

Cheney, E., 1996, Sequence stratigraphy and plate tectonic significance of the Transvaal succession of southern Africa and its equivalent in Western Australia: Precambrian Research, v. 79, no. 1-2, p. 3-24.

Clarkson, M., Poulton, S., Guilbaud, R., and Wood, R., 2014, Assessing the utility of Fe/Al and Fe-speciation to record water column redox conditions in carbonate-rich sediments: Chemical Geology, v. 382, p. 111-122.

Collier, R. W., 1985, Molybdenum in the northeast Pacific Ocean: Limnology and Oceanography, v. 30, no. 6, p. 1351-1354.

Colodner, D., Sachs, J., Ravizza, G., Turekian, K., Edmond, J., and Boyle, E., 1993, The geochemical cycle of rhenium: a reconnaissance: Earth and Planetary Science Letters, v. 117, no. 1-2, p. 205-221.

Coplen, T. B., Brand, W. A., Gehre, M., Gröning, M., Meijer, H. A., Toman, B., and Verkouteren, R. M., 2006, New guidelines for δ 13C measurements: Analytical Chemistry, v. 78, no. 7, p. 2439-2441.

Crusius, J., Calvert, S., Pedersen, T., and Sage, D., 1996, Rhenium and molybdenum enrichments in sediments as indicators of oxic, suboxic and sulfidic conditions of deposition: Earth and Planetary Science Letters, v. 145, no. 1-4, p. 65-78.

Cunningham, J. A., and Reinhard, M., 2002, Injection-extraction treatment well pairs: An alternative to permeable reactive barriers: Ground Water, v. 40, no. 6, p. 599-607.

Czaja, A. D., Johnson, C. M., Roden, E. E., Beard, B. L., Voegelin, A. R., Nägler, T. F., Beukes, N. J., and Wille, M., 2012, Evidence for free oxygen in the Neoarchean ocean based on coupled iron–molybdenum isotope fractionation: Geochimica et Cosmochimica Acta, v. 86, p. 118-137.

De Almeida, F., Hasui, Y., de Brito Neves, B., and Fuck, R., 1981, Brazilian structural provinces: an introduction: Earth-Science Reviews, v. 17, no. 1-2, p. 1-29.

Dickson, A. J., Gill, B. C., Ruhl, M., Jenkyns, H. C., Porcelli, D., Idiz, E., Lyons, T. W., and van den Boorn, S. H. J. M., 2017, Molybdenum-isotope chemostratigraphy and paleoceanography of the Toarcian Oceanic Anoxic Event (Early Jurassic): Paleoceanography, v. 32, no. 8, p. 813-829.

Dorr, J. V. N., 1969, Physiographic, stratigraphic, and structural development of the Quadrilatero Ferrifero, Minas Gerais, Brazil: US Government Printing Office, 2330-7102.

Duan, Y., Anbar, A. D., Arnold, G. L., Lyons, T. W., Gordon, G. W., and Kendall, B., 2010, Molybdenum isotope evidence for mild environmental oxygenation before the Great Oxidation Event: Geochimica Et Cosmochimica Acta, v. 74, no. 23, p. 6655-6668.

Dunk, R., Mills, R., and Jenkins, W., 2002, A reevaluation of the oceanic uranium budget for the Holocene: Chemical Geology, v. 190, no. 1-4, p. 45-67.

Eigenbrode, J. L., and Freeman, K. H., 2006, Late Archean rise of aerobic microbial ecosystems: Proceedings of the National Academy of Sciences, v. 103, no. 43, p. 15759-15764.

Emerson, S. R., and Huested, S. S., 1991, Ocean anoxia and the concentrations of molybdenum and vanadium in seawater: Marine Chemistry, v. 34, no. 3-4, p. 177-196.

Erickson, B. E., and Helz, G. R., 2000, Molybdenum (VI) speciation in sulfidic waters:: stability and lability of thiomolybdates: Geochimica et Cosmochimica Acta, v. 64, no. 7, p. 1149-1158.

Eriksson, K. A., 1995, Crustal growth, surface processes, and atmospheric evolution on the early Earth: Geological Society, London, Special Publications, v. 95, no. 1, p. 11-25.

Fischer, W. W., Schroeder, S., Lacassie, J. P., Beukes, N. J., Goldberg, T., Strauss, H., Horstmann, U. E., Schrag, D. P., and Knoll, A., 2009, Isotopic constraints on the Late Archean carbon cycle from the Transvaal Supergroup along the western margin of the Kaapvaal Craton, South Africa: Precambrian Research, v. 169, no. 1-4, p. 15-27.

Goldberg, T., Archer, C., Vance, D., and Poulton, S. W., 2009, Mo isotope fractionation during adsorption to Fe (oxyhydr) oxides: Geochimica et Cosmochimica Acta, v. 73, no. 21, p. 6502-6516.

Golden, J., McMillan, M., Downs, R. T., Hystad, G., Goldstein, I., Stein, H. J., Zimmerman, A., Sverjensky, D. A., Armstrong, J. T., and Hazen, R. M., 2013, Rhenium variations in molybdenite (MoS2): Evidence for progressive subsurface oxidation: Earth and Planetary Science Letters, v. 366, p. 1-5.

Hardisty, D. S., Lyons, T. W., Riedinger, N., Isson, T. T., Owens, J. D., Aller, R. C., Rye, D. M., Planavsky, N. J., Reinhard, C. T., Gill, B. C., Masterson, A. L., Asael, D., and Johnston, D. T., 2018, An Evaluation of Sedimentary Molybdenum and Iron as Proxies for Pore Fluid Paleoredox Conditions: American Journal of Science, v. 318, no. 5, p. 527-556.

Hardisty, D. S., Riedinger, N., Planavsky, N. J., Asael, D., Andren, T., Jorgensen, B. B., and Lyons, T. W., 2016, A Holocene History of Dynamic Water Column Redox Conditions in the Landsort Deep, Baltic Sea: American Journal of Science, v. 316, no. 8, p. 713-745.

Helz, G. R., and Dolor, M. K., 2012, What regulates rhenium deposition in euxinic basins?: Chemical Geology, v. 304, p. 131-141.

Holland, H. D., 1973, Systematics of the isotopic composition of sulfur in the oceans during the Phanerozoic and its implications for atmospheric oxygen: Geochimica et Cosmochimica Acta, v. 37, no. 12, p. 2605-2616.

Kadoya, S., Catling, D. C., Nicklas, R. W., Puchtel, I. S., and Anbar, A. D., 2020, Mantle data imply a decline of oxidizable volcanic gases could have triggered the Great Oxidation: Nature communications, v. 11, no. 1, p. 1-9.

Kasting, J. F., and Catling, D., 2003, Evolution of a habitable planet: Annual Review of Astronomy and Astrophysics, v. 41, no. 1, p. 429-463.

Kaufman, A. J., Johnston, D. T., Farquhar, J., Masterson, A. L., Lyons, T. W., Bates, S., Anbar, A. D., Arnold, G. L., Garvin, J., and Buick, R., 2007, Late Archean biospheric oxygenation and atmospheric evolution: Science, v. 317, no. 5846, p. 1900-1903.

Kendall, B., Creaser, R. A., Reinhard, C. T., Lyons, T. W., and Anbar, A. D., 2015, Transient episodes of mild environmental oxygenation and oxidative continental weathering during the late Archean: Science Advances, v. 1, no. 10.

Kendall, B., Dahl, T. W., and Anbar, A. D., 2017, The stable isotope geochemistry of molybdenum: Reviews in Mineralogy and Geochemistry, v. 82, no. 1, p. 683-732.

Kendall, B., Reinhard, C. T., Lyons, T., Kaufman, A. J., Poulton, S. W., and Anbar, A. D., 2010, Pervasive oxygenation along late Archaean ocean margins: Nature Geoscience, v. 3, no. 9, p. 647-652.

Koide, M., Hodge, V., Yang, J., Stallard, M., Goldberg, E., Calhoun, J., and Bertine, K., 1986, Some comparative marine chemistries of rhenium, gold, silver and molybdenum: Applied Geochemistry, v. 1, no. 6, p. 705-714.

Krissansen-Totton, J., Buick, R., and Catling, D. C., 2015, A statistical analysis of the carbon isotope record from the Archean to Phanerozoic and implications for the rise of oxygen: American Journal of Science, v. 315, no. 4, p. 275-316.

Krzywinski, M., and Altman, N., 2013, Points of significance: error bars, Nature Publishing Group.

Kump, L. R., and Barley, M. E., 2007, Increased subaerial volcanism and the rise of atmospheric oxygen 2.5 billion years ago: Nature, v. 448, no. 7157, p. 1033-1036.

Kump, L. R., Kasting, J. F., and Barley, M. E., 2001, Rise of atmospheric oxygen and the "upside-down" Archean mantle: Geochemistry, Geophysics, Geosystems, v. 2, no. 1.

Lee, C.-T. A., Yeung, L. Y., McKenzie, N. R., Yokoyama, Y., Ozaki, K., and Lenardic, A., 2016, Two-step rise of atmospheric oxygen linked to the growth of continents: Nature Geoscience, v. 9, no. 6, p. 417-424.

Lyons, T. W., Anbar, A. D., Severmann, S., Scott, C., and Gill, B. C., 2009a, Tracking Euxinia in the Ancient Ocean: A Multiproxy Perspective and Proterozoic Case Study: Annual Review of Earth and Planetary Sciences, v. 37, p. 507-534.

Lyons, T. W., Reinhard, C. T., and Planavsky, N. J., 2014, The rise of oxygen in Earth's early ocean and atmosphere: Nature, v. 506, no. 7488, p. 307-315.

Lyons, T. W., Reinhard, C. T., and Scott, C., 2009b, Redox Redux: Geobiology, v. 7, no. 5, p. 489-494.

Lyons, T. W., and Severmann, S., 2006, A critical look at iron paleoredox proxies: New insights from modern euxinic marine basins: Geochimica Et Cosmochimica Acta, v. 70, no. 23, p. 5698-5722.

McManus, J., Berelson, W. M., Klinkhammer, G. P., Hammond, D. E., and Holm, C., 2005, Authigenic uranium: relationship to oxygen penetration depth and organic carbon rain: Geochimica et Cosmochimica Acta, v. 69, no. 1, p. 95-108.

Miller, C. A., Peucker-Ehrenbrink, B., Walker, B. D., and Marcantonio, F., 2011, Re-assessing the surface cycling of molybdenum and rhenium: Geochimica et Cosmochimica Acta, v. 75, no. 22, p. 7146-7179.

Morford, J. L., and Emerson, S., 1999, The geochemistry of redox sensitive trace metals in sediments: Geochimica et Cosmochimica Acta, v. 63, no. 11, p. 1735-1750.

Morford, J. L., Emerson, S. R., Breckel, E. J., and Kim, S. H., 2005, Diagenesis of oxyanions (V, U, Re, and Mo) in pore waters and sediments from a continental margin: Geochimica et Cosmochimica Acta, v. 69, no. 21, p. 5021-5032.

Morford, J. L., Martin, W. R., François, R., and Carney, C. M., 2009, A model for uranium, rhenium, and molybdenum diagenesis in marine sediments based on results from coastal locations: Geochimica et Cosmochimica Acta, v. 73, no. 10, p. 2938-2960.

Nameroff, T., Balistrieri, L., and Murray, J., 2002, Suboxic trace metal geochemistry in the eastern tropical North Pacific: Geochimica et Cosmochimica Acta, v. 66, no. 7, p. 1139-1158.

Neubert, N., Nägler, T. F., and Böttcher, M. E., 2008, Sulfidity controls molybdenum isotope fractionation into euxinic sediments: Evidence from the modern Black Sea: Geology, v. 36, no. 10, p. 775-778.

Olson, S. L., Kump, L. R., and Kasting, J. F., 2013, Quantifying the areal extent and dissolved oxygen concentrations of Archean oxygen oases: Chemical Geology, v. 362, p. 35-43.

Ostrander, C. M., Kendall, B., Olson, S. L., Lyons, T. W., Gordon, G. W., Romaniello, S. J., Zheng, W., Reinhard, C. T., Roy, M., and Anbar, A. D., 2020, An expanded shale delta Mo-98 record permits recurrent shallow marine oxygenation during the Neoarchean: Chemical Geology, v. 532.

Ostrander, C. M., Nielsen, S. G., Owens, J. D., Kendall, B., Gordon, G. W., Romaniello, S. J., and Anbar, A. D., 2019, Fully oxygenated water columns over continental shelves before the Great Oxidation Event: Nature geoscience, v. 12, no. 3, p. 186-191.

Partin, C., Bekker, A., Planavsky, N., Scott, C., Gill, B., Li, C., Podkovyrov, V., Maslov, A., Konhauser, K., and Lalonde, S., 2013, Large-scale fluctuations in Precambrian atmospheric and oceanic oxygen levels from the record of U in shales: Earth and Planetary Science Letters, v. 369, p. 284-293.

Planavsky, N. J., Asael, D., Hofman, A., Reinhard, C. T., Lalonde, S. V., Knudsen, A., Wang, X., Ossa, F. O., Pecoits, E., and Smith, A. J., 2014a, Evidence for oxygenic photosynthesis half a billion years before the Great Oxidation Event: Nature Geoscience, v. 7, no. 4, p. 283-286.

Planavsky, N. J., Asael, D., Hofmann, A., Reinhard, C. T., Lalonde, S. V., Knudsen, A., Wang, X. L., Ossa, F. O., Pecoits, E., Smith, A. J. B., Beukes, N. J., Bekker, A., Johnson, T. M., Konhauser, K. O., Lyons, T. W., and Rouxel, O. J., 2014b, Evidence for oxygenic photosynthesis half a billiion years before the Great Oxidation Event: Nature Geoscience, v. 7, no. 4, p. 283-286.

Poulson Brucker, R. L., McManus, J., Severmann, S., and Berelson, W. M., 2009, Molybdenum behavior during early diagenesis: Insights from Mo isotopes: Geochemistry, Geophysics, Geosystems, v. 10, no. 6.

Poulton, S. W., and Canfield, D. E., 2005, Development of a sequential extraction procedure for iron: implications for iron partitioning in continentally derived particulates: Chemical Geology, v. 214, no. 3-4, p. 209-221.

Poulton, S. W., and Canfield, D. E., 2011, Ferruginous conditions: a dominant feature of the ocean through Earth's history: Elements, v. 7, no. 2, p. 107-112.

Poulton, S. W., Fralick, P. W., and Canfield, D. E., 2004, The transition to a sulphidic ocean~ 1.84 billion years ago: Nature, v. 431, no. 7005, p. 173-177.

Raiswell, R., Hardisty, D. S., Lyons, T. W., Canfield, D. E., Owens, J. D., Planavsky, N. J., Poulton, S. W., and Reinhard, C. T., 2018, The Iron Paleoredox Proxies: A Guide to the Pitfalls, Problems and Proper Practice: American Journal of Science, v. 318, no. 5, p. 491-526.

Raiswell, R., Newton, R., Bottrell, S. H., Coburn, P. M., Briggs, D. E., Bond, D. P., and Poulton, S. W., 2008, Turbidite depositional influences on the diagenesis of Beecher's Trilobite Bed and the Hunsrück Slate; sites of soft tissue pyritization: American Journal of Science, v. 308, no. 2, p. 105-129.

Reinhard, C. T., Planavsky, N. J., Olson, S. L., Lyons, T. W., and Erwin, D. H., 2016, Earth's oxygen cycle and the evolution of animal life: Proceedings of the National Academy of Sciences of the United States of America, v. 113, no. 32, p. 8933-8938.

Reinhard, C. T., Raiswell, R., Scott, C., Anbar, A. D., and Lyons, T. W., 2009, A Late Archean Sulfidic Sea Stimulated by Early Oxidative Weathering of the Continents: Science, v. 326, no. 5953, p. 713-716.

Riding, R., Fralick, P., and Liang, L., 2014, Identification of an Archean marine oxygen oasis: Precambrian Research, v. 251, p. 232-237.

Rosière, C. A., Bekker, A., Rolim, V. K., and Santos, J. O. S., 2019, Post-Great Oxidation Event Orosirian–Statherian iron formations on the São Francisco craton: Geotectonic implications: Island Arc, v. 28, no. 4, p. e12300.

Rosière, C. A., and Chemale Jr, F., 2017, Brazilian iron formations and their geological setting: Revista Brasileira de Geociências, v. 30, no. 2, p. 274-278.

Rosiere, C. A., Spier, C. A., Rios, F. J., and Suckau, V. E., 2008, The itabirites of the Quadrilátero Ferrífero and related high-grade iron ore deposits: an overview: Reviews in Economic Geology, v. 15, p. 223-254.

Scott, C., Lyons, T., Bekker, A., Shen, Y.-a., Poulton, S., Chu, X.-l., and Anbar, A., 2008, Tracing the stepwise oxygenation of the Proterozoic ocean: Nature, v. 452, no. 7186, p. 456-459.

Sheen, A. I., Kendall, B., Reinhard, C. T., Creaser, R. A., Lyons, T. W., Bekker, A., Poulton, S. W., and Anbar, A. D., 2018, A model for the oceanic mass balance of rhenium and implications for the extent of Proterozoic ocean anoxia: Geochimica Et Cosmochimica Acta, v. 227, p. 75-95.

Spier, C., Deoliveira, S., Sial, A., and Rios, F., 2007, Geochemistry and genesis of the banded iron formations of the Cauê Formation, Quadrilátero Ferrífero, Minas Gerais, Brazil: Precambrian Research, v. 152, no. 3-4, p. 170-206.

Spier, C. A., de Oliveira, S. M. B., and Rosiere, C. A., 2003, Geology and geochemistry of the Águas Claras and Pico Iron Mines, Quadrilátero Ferrífero, Minas Gerais, Brazil: Mineralium Deposita, v. 38, no. 6, p. 751-774.

Sundby, B., Martinez, P., and Gobeil, C., 2004, Comparative geochemistry of cadmium, rhenium, uranium, and molybdenum in continental margin sediments: Geochimica et Cosmochimica Acta, v. 68, no. 11, p. 2485-2493.

Tribovillard, N., Riboulleau, A., Lyons, T., and Baudin, F., 2004, Enhanced trapping of molybdenum by sulfurized marine organic matter of marine origin in Mesozoic limestones and shales: Chemical Geology, v. 213, no. 4, p. 385-401.

Wasylenki, L. E., Rolfe, B. A., Weeks, C. L., Spiro, T. G., and Anbar, A. D., 2008, Experimental investigation of the effects of temperature and ionic strength on Mo isotope fractionation during adsorption to manganese oxides: Geochimica et Cosmochimica Acta, v. 72, no. 24, p. 5997-6005.

Wille, M., Kramers, J. D., Nägler, T. F., Beukes, N., Schröder, S., Meisel, T., Lacassie, J., and Voegelin, A., 2007, Evidence for a gradual rise of oxygen between 2.6 and 2.5 Ga from Mo isotopes and Re-PGE signatures in shales: Geochimica et Cosmochimica Acta, v. 71, no. 10, p. 2417-2435.

FIGURES

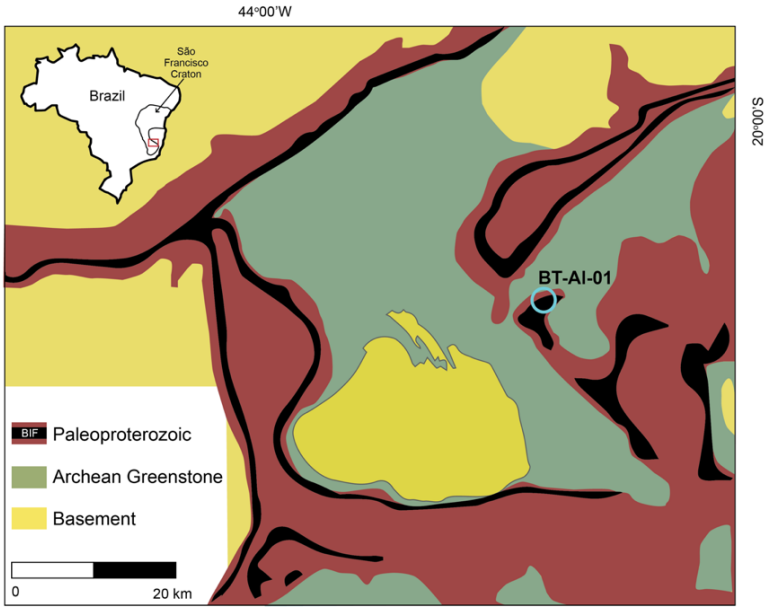

Figure 4.1: Simplified geological map of the Quadrilátero Ferrífero with the position of the BT-AL-01 core (modified after Dorr 1969).

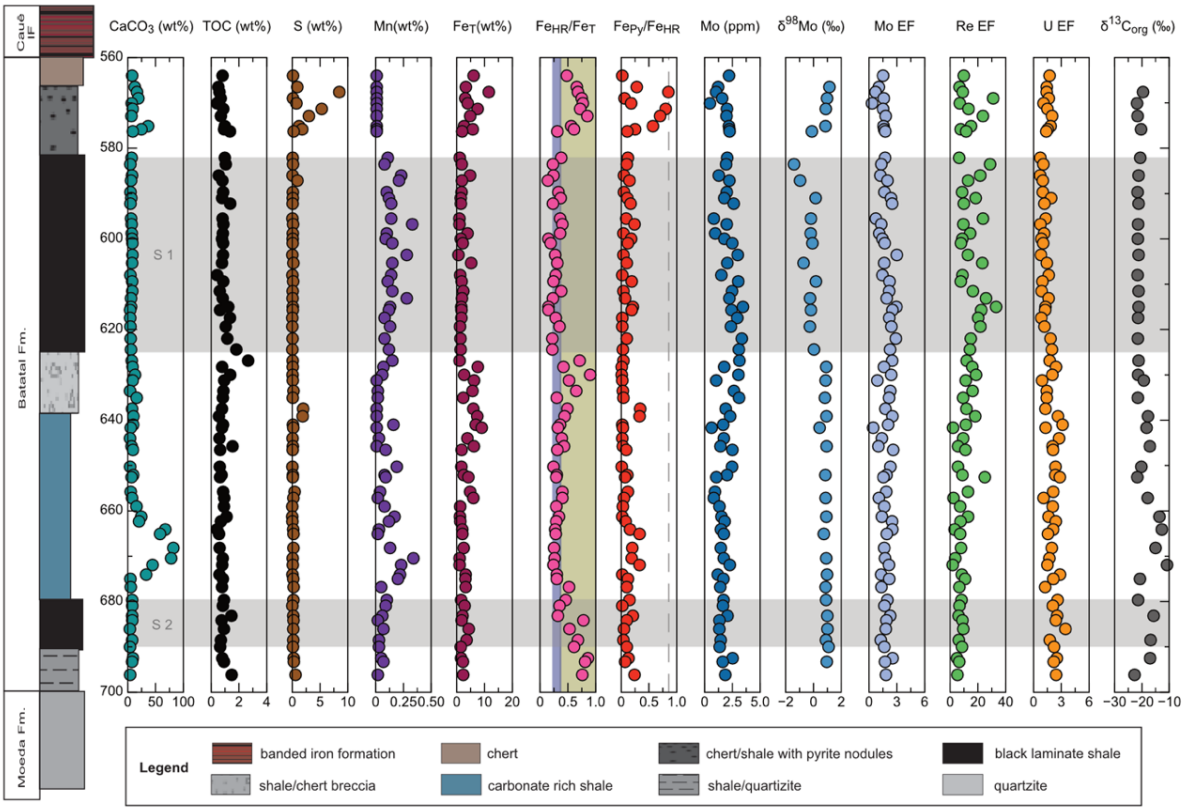

Figure 4.2: Geochemical profiles: Total Fe, highly reactive Fe and pyrite Fe are denoted by Fe_T, Fe_{HR} and Fe_{PY}, respectively. Fe_{HR} / Fe_T > 0.38 and < 0.22 typically represent anoxic and oxygenated bottom water conditions, respectively. When Fe_{HR} / Fe_T is over 0.38, Fe_{Py} / Fe_{HT} can further be used to identify euxinic (>0.8) or ferruginous (<0.8) conditions (Poulton and Canfield, 2011). Enrichment factor (EF)=$(metal/Al)_{sample}/(metal/Al)_{average\ upper\ crust}$.

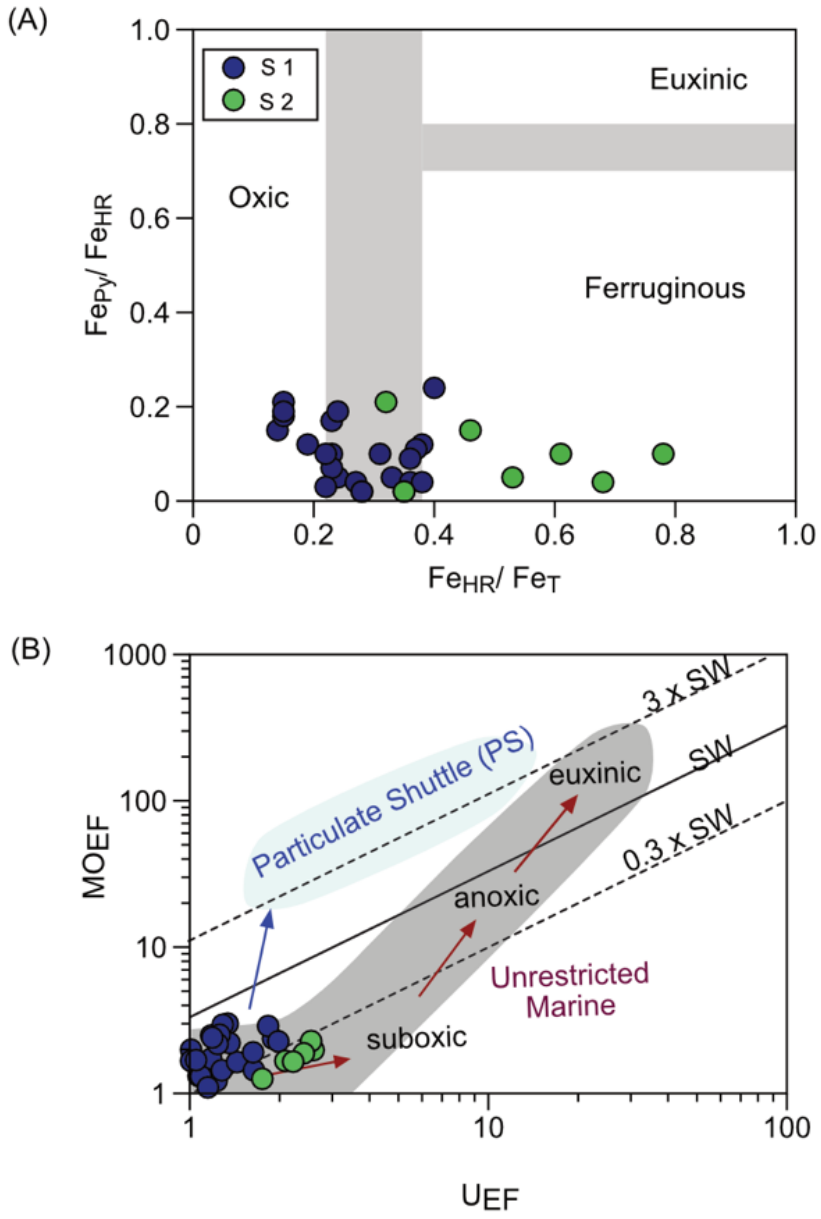

Figure 4.3: Geochemical diagrams showing (A) Fe_{py}/Fe_{HR} versus Fe_{HR}/Fe_T and (B) Mo_{EF} versus U_{EF}. Dashed lines in (A) are used to clarify different bottom water conditions (see details in text). Dashed lines in (B) present the molar Mo/U (Algeo and Tribovillard, 2009) ratios of modern seawater (SW) and their corresponding fractions of modern seawater (0.3 × SW, and 3 × SW). Enrichment patterns and corresponding controls in (B) are illustrated following Algeo and Tribovillard (2009).

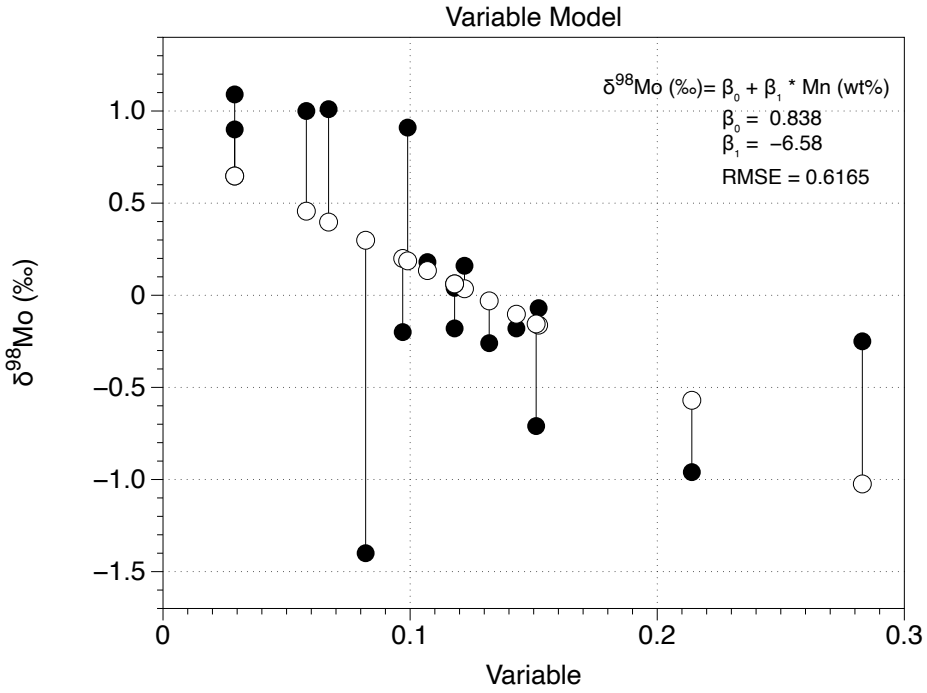

Figure 4.4:Variable Model for Mo isotope distribution based on Mn concentrations. Root Mean Square Error (RMSE) was used to indicate the absolute fit of the model to the data and how close the observed data points are to the model's predicted values. Black closed circle is the measured data from S1 and S2, and open circle is modeled data.

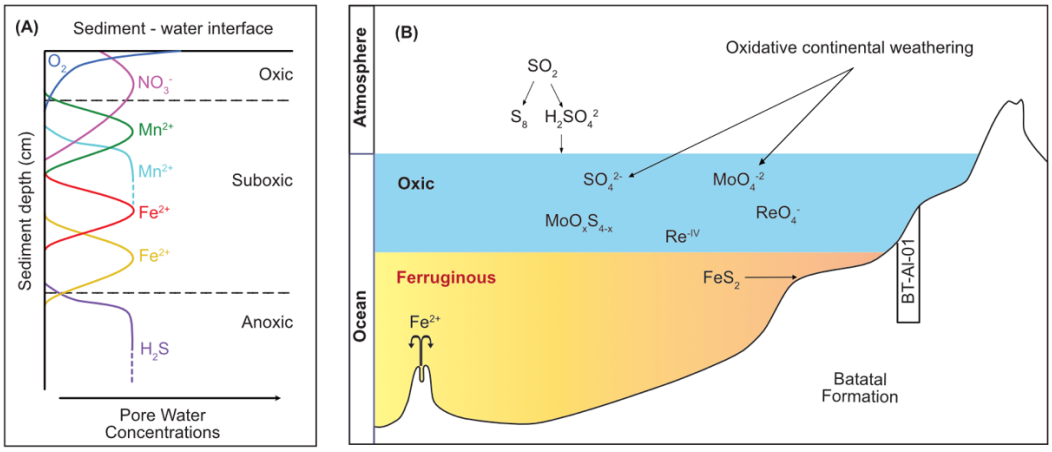

Figure 4.5: Schematic diagram of late Archaean redox conditions of the Batatal formation. (A) Redox ladder adapted from Froelich et al (1979) with simplified redox classification modified from Berner (1981). (B) The sufficient O_2 accumulation was limited in the shallow waters of the Batatal Formation. Otherwise, the deep ocean was ferruginous.

SUPPLEMENTARY MATERIALS

The sedimentary succession of Minas Supergroup comprises three groups: the Caraça, Itabira, and Piracicaba (Bekker et al., 2004) (Fig. S1). The Batatal Formation from Caraça group (2.6 Ga), and Cauê and Gandarela Formation from Itabira groups (2.4 Ga) will allow an evaluation of environmental changes spanning the Archean–Paleoproterozoic boundary. The Batatal Formation forms the upper part of the Caraça Group, which overlies the Moeda Formation with a generally sharp contact. The Batatal Formation is comprised of offshore sediments deposited on a slowly subsiding continental shelf along a passive margin (Spier et al., 2007). The shallow marine Batatal platform is composed of two shale-rich intervals above and below a stromatolitic carbonate (Dorr, 1969). These geographically and spatially discrete sedimentary unit thus provides a unique opportunity to examine similarities and differences in sediment geochemistry across the terminal Neoarchean (Fig 4). Given available age constraints, it is possible that the contact between the Batatal Formation and the overlying Cauê Iron Formation might be directly correlated with similarly aged contacts between shale and BIF in South Africa (between the Klein Naute and Kuruman Iron formations) and Western Australia (between the Mt. McRae Shale Formation and the Brockman Iron Formation) (Fig S1).

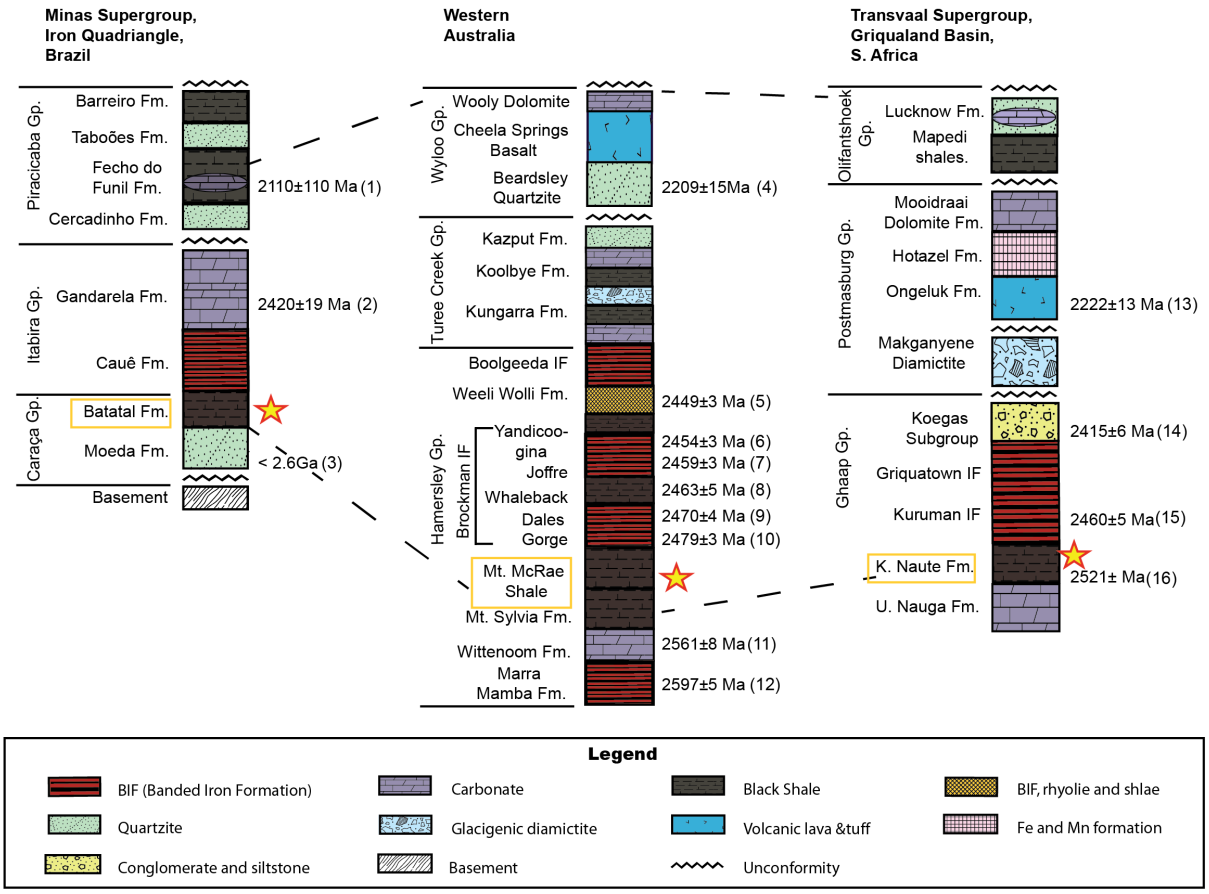

Figure 4. S1:. Simplified stratigraphic correlation between Minas Supergroup, Western Australia and Transvaal Supergroup. Stratigraphic correlation is based on: (Bekker et al., 2003; Dorland, 2004; Dorr, 1969; Lindsay and Brasier, 2002; Marshak and Alkmim, 1989; Martin, 1999; Tang and Chen, 2013). Age constrains are from: 1 and 2- (Babinski et al., 1995), 3- (Hartmann et al., 2006), 4-(Martin et al., 1998; Trendall, 1981), 5- (Barley et al., 1997), 6- (Anbar et al., 2007a), 7- (Pickard, 2002), 8- (Trendall et al., 2004), 9-(Tyler et al., 1998) 10- (Arndt et al., 1991; Nelson et al., 1999)11-(Trendall et al., 1998),12-(Trendall et al., 2004) ,13- (Cornell et al., 1996), 14- (Gutzmer and Beukes, 1998; Kirschvink et al., 2000), 15- (Pickard, 2003), 16- (Sumner and Bowring, 1996).

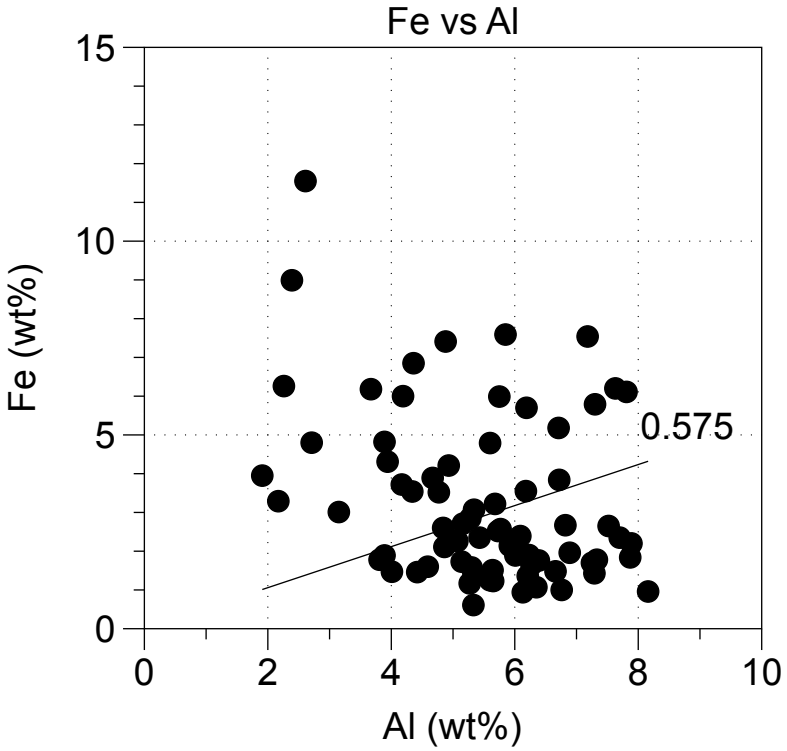

Figure 4. S2:Fe_T/Al ratio to detect the Fe enrichments as an alternative indicator of water column anoxia.

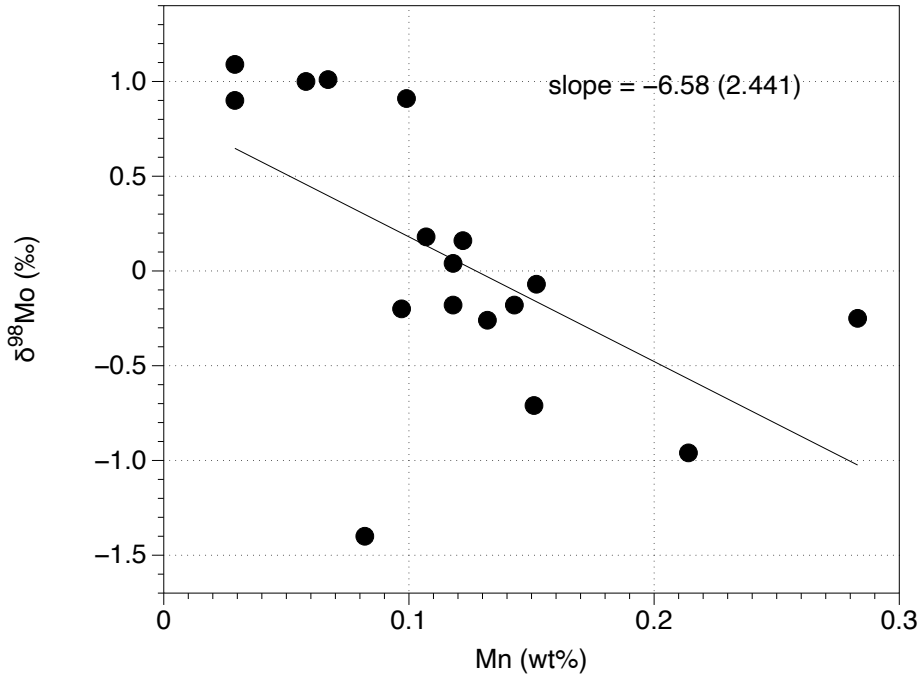

Figure 4. S3: Relationships between Mo isotope values and Mn from S1 and S2.

Statistical Analysis

The t test was applied to determine significant the differences between upper and lower shales (S1 and S2) (Krzywinski and Altman, 2013). A p-value higher than 0.05 (> 0.05) is not statistically significant and indicates strong evidence for the null hypothesis. A p-value less than 0.05 (typically ≤ 0.05) is statistically significant. It indicates strong evidence against the null hypothesis, as there is less than a 5% probability the null is correct (and the results are random). Therefore, we reject the null hypothesis, and accept the alternative hypothesis.

a. t-Test: FeHR / FeT
Statistically significant.

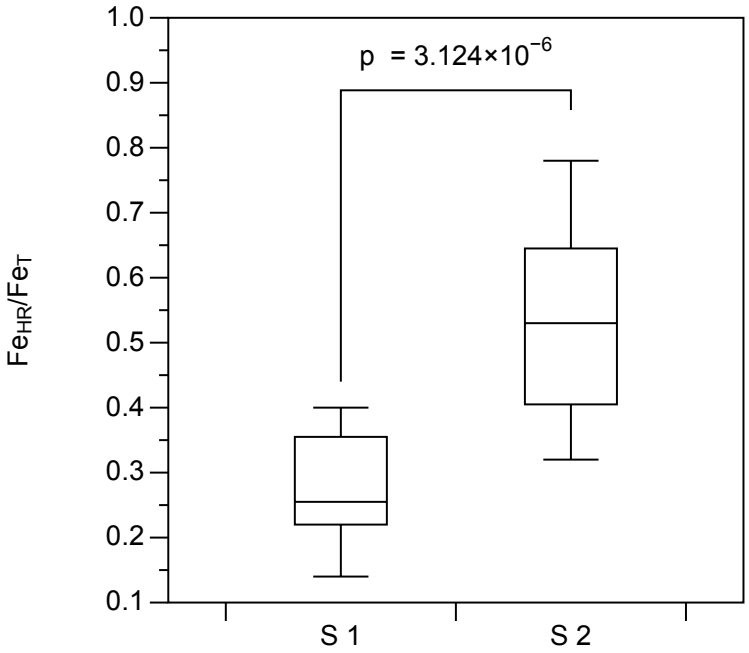

Figure 4. S4a: t-Test output.

Shale	# of samples	Min	1Q	Median	Mean	3Q	Max	Range
S 1	24	0.14	0.22	0.25	0.27	0.36	0.4	0.26
S 2	7	0.41	0.53	0.53	0.53	0.65	0.78	0.46

Table 4. S4a: t-Test data.

b. t-Test: $\delta^{98}Mo_{‰}$
Statistically significant.

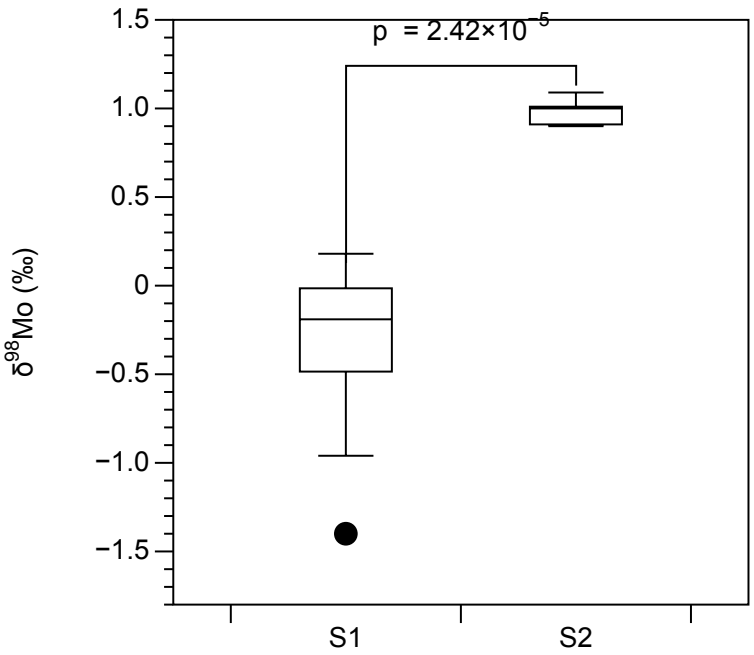

Figure 4. S4b: t-Test output.

Shale	# of samples	Min	1Q	Median	Mean	3Q	Max	Range
S 1	24	-1.4	-0.49	-0.19	-0.32	-0.02	0.18	1.58
S 2	7	0.9	0.91	1	0.98	1.01	1.09	0.19

Table 4. S4b: t-Test data.

c. t- test: Mo_{EF}
Statistically significant.

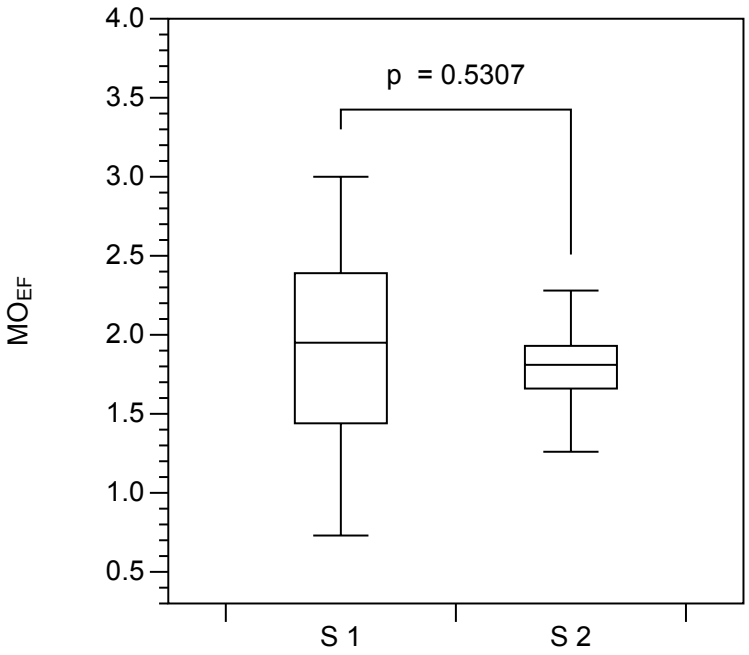

Figure 4. S4c: t-Test output.

Shale	# of samples	Min	1Q	Median	Mean	3Q	Max	Range
S 1	24	0.73	1.44	1.95	1.94	2.39	3	2.27
S 2	7	1.26	1.66	1.81	1.79	1.93	2.28	1.02

Table 4. S4c: t-Test data.

d. t-test: U_{EF}
Statistically significant.

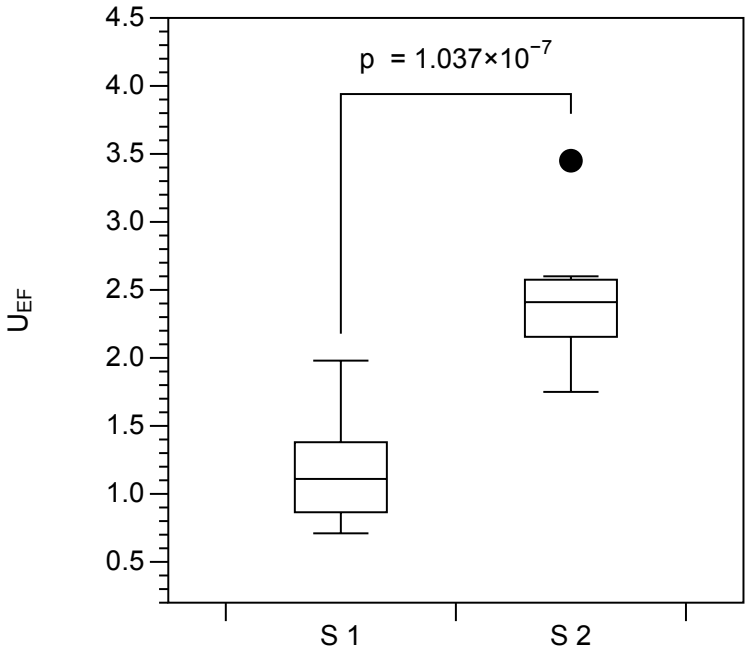

Figure 4. S4d: t-Test output.

Shale	# of samples	Min	1Q	Median	Mean	3Q	Max	Range
S 1	24	0.71	0.87	1.11	1.87	1.38	1.98	1.27
S 2	7	1.75	2.16	2.41	2.44	2.58	3.45	1.7

Table 4. S4d: t-Test data.

e. t-test: Re_{EF}
Statistically significant.

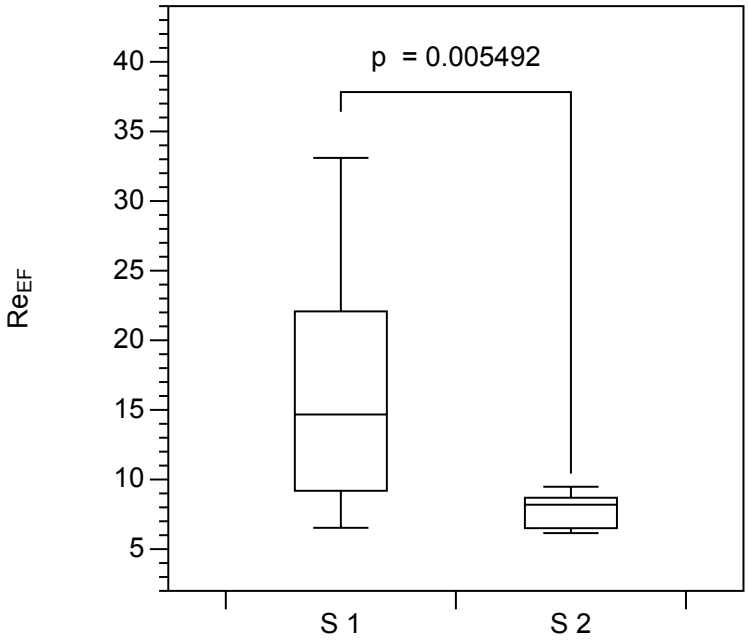

Figure 4. S4e: t-Test output.

Shale	# of samples	Min	1Q	Median	Mean	3Q	Max	Range
S 1	24	6.53	9.19	14.67	16.34	22.08	33.1	26.57
S 2	7	6.15	6.51	8.19	7.75	8.69	9.48	3.33

Table 4. S4e: t-Test data.

Reference

Bekker, A., Holland, H., Wang, P.-L., Rumble, D., Stein, H., Hannah, J., Coetzee, L., and Beukes, N., 2004, Dating the rise of atmospheric oxygen: Nature, v. 427, no. 6970, p. 117-120.

Dorr, J. V. N., 1969, Physiographic, stratigraphic, and structural development of the Quadrilatero Ferrifero, Minas Gerais, Brazil: US Government Printing Office, 2330-7102.

Krzywinski, M., and Altman, N., 2013, Points of significance: error bars, Nature Publishing Group.

Spier, C., Deoliveira, S., Sial, A., and Rios, F., 2007, Geochemistry and genesis of the banded iron formations of the Cauê Formation, Quadrilátero Ferrífero, Minas Gerais, Brazil: Precambrian Research, v. 152, no. 3-4, p. 170-206.

CHAPTER 5

The evolution of Banded Iron Formation (BIFs)
from Quadrilátero Ferrífero, Brazil

ABSTRACT

Iron formations (IF), iron-rich (15-40 wt.% Fe) and siliceous (40-60 wt.% SiO_2) chemical sedimentary rocks precipitated from seawater during the Precambrian Eon accumulated episodically on the seafloor for over two billion years of Earth's early history. These facies are among our greatest archives of environmental changes that took place on the evolving early Earth. Here, we present rare earth element and yttrium (REE+Y) compositions together with iron speciation data from two comprehensively sampled Neoarchean and Paleoproterozoic Banded Iron Formation (BIFs) from Quadrilátero Ferrífero (QF), located at the southeastern border of the São Francisco Craton in southeastern Brazil. The REE+Y data in both formations indicate hydrothermal iron contribution with positive europium (Eu) anomaly and light rare earth element (LREE) depletion. Oxygen was available at least intermittently and in the shallow portions of the water column during the Neoarchean and Paleoproterozoic. However, the main contrast for the two formations is the suggestion of the presence (Paleoproterozoic BIFs) versus absence (Neoarchean) of a water column with an Fe-Mn redoxcline. The combined data thus provide new insights into the depositional conditions of the QF region and broader geochemical evolution of the ocean.

INTRODUCTION

Life and its environments have coevolved through Earth history with changes in the environment occurring in parallel with evolutionary innovation often in cause-and-effect relationships. One of the most complex and least understood relationships is between life and oxygen. Oxygenation of the atmosphere and oceans is a milestone in the evolution of the biosphere and geochemical cycles of elements. There was likely a 300-Myr delay between the evolution of oxygenic photosynthesis at ~3.0 Ga (Buick, 2008; Planavsky et al., 2014) and global oxygenation at ~2.4 Ga, known as the Great Oxidation Event (GOE) (Lyons et al., 2014; Scott et al., 2008).

The precise nature of ocean redox conditions is among the most uncertain aspects of early Earth's surface. It is generally thought that Earth's atmosphere was anoxic until the GOE (Bekker et al., 2004; Fru et al., 2019), but there is less agreement about the timing and extent of the oxygenation of the oceans (Canfield et al., 2008; Heard and Dauphas, 2020; Ohmoto et al., 2006; Ostrander et al., 2019). The rise of atmospheric oxygen during the GOE should have similarly triggered oxygenation of the oceans—initially in the surface waters followed much later by ventilation of the deep oceans. The peak in worldwide deposition of BIFs prior to and around the GOE bear information on the redox state and chemical composition of seawater and suggest that these sediments were inherently linked to the production and accumulation of photosynthetically produced O_2 (Haqq-Misra et al., 2011; Konhauser et al., 2011) and concomitant precipitated via oxidation of the large oceanic Fe^{2+} reservoir (Fischer and Knoll, 2009).

Concentrations of Fe in seawater over Earth history depend on the ocean's redox state. The deposition of mixed-valence iron (Fe) minerals in banded iron formations (BIFs) can reflect the chemical signatures of seawater (Bau and Dulski, 1996; Bekker et al., 2014; Konhauser et al., 2017a), with low concentrations of crustal elements indicating an authigenic origin. These finely laminated, iron-rich (>15 wt.% Fe) sedimentary deposits likely track the evolution of both oxygenic and anoxygenic photosynthesis and dissolved O_2 concentrations in the oceans by association with the former. Further, their specific geochemical properties yield evidence for a broad range of biological activity (Fru et al., 2013; Olson, 2006) and environmental conditions (Canfield et al., 2008). The origin of banded iron formations (BIFs) reflects oxidation and precipitation of Fe(II) and Fe(III), respectively, in near-surface environments of the anoxic oceans of the Archean. Oxygenic photosynthesis is restricted to the photic zone, and accumulation of O_2 before the GOE must have been limited to the shallow parts of the oceans, creating local oxygen oases (Olson et al., 2013). Assuming oxygenic photosynthesis began well before the GOE (Lalonde and Konhauser, 2015; Planavsky et al., 2014) suggest that global O_2 levels did not increase in a strictly stepwise fashion but instead varied intermittently (Anbar et al., 2007) and likely locally well before the onset of the GOE.

We conducted a geochemical study of the Neoarchean Rio das Velhas Supergroup (2.7Ga) and early Paleoproterozoic Minas Supergroup sedimentary sequences (2.4Ga) of the Quadrilátero Ferrífero, Brazil, (Figure 1) with the goal of exploring the redox structure and the mechanisms behind the BIFs. Our study focuses on Rare Earth Element (REE) and yttrium (Y) concentrations and Fe-speciation studies in BIFs to constrain

environmental conditions during BIFs deposition. Our spatially discrete sedimentary units thus provide a unique opportunity to examine the geochemistry to gain insight about their depositional environment, the role that diagenesis played, and the significance and nature of hydrothermal inputs during deposition.

MATERIAL AND METHODS

Geologic Setting and Sampling

The Quadrilátero Ferrífero (QF) is situated on the southern margin of the São Francisco Craton, Brazil, and extends from Archean to Paleoproterozoic (Dorr, 1969). The QF encompasses an area of about 7000 km^2 and hosts one of the largest concentrations of lateritic iron-ore deposits in the world. The most important lithostratigraphic units of the Quadrilátero Ferrífero are: (1) the Archean crystalline basement, spanning the 3.2–2.7 Ga interval (Chemale Jr et al., 2012; Dopico et al., 2017; Lana et al., 2013; Nass et al., 2015; Teixeira et al., 2017); (2) the Rio das Velhas Supergroup, a typical Archean greenstone belt sequence of circa 2.7 Ga age (Baltazar and Zucchetti, 2007; Lobato et al., 2007); (3) the Paleoproterozoic Minas Supergroup, consisting mainly of a clastic metasedimentary package with chemical rock intercalations (BIFs and carbonates), deposited in the 2.7–2.0 Ga time interval (Babinski et al., 1995; Cabral et al., 2012; Machado et al., 1992); and (4) the Itacolomi Group. Post-Itacolomi mafic dykes and sills at circa 1.7 Ga (U-Pb in badelleyte) provide a minimum age for the sedimentation of the Proterozoic sequences in the region (Silva et al., 1995) (Figure 2).

Basement crystalline rocks include a gneiss/migmatite complex and two generations of voluminous Late Archean plutons: calk-alkaline and anorogenic granites (Alkmim and Marshak, 1998). The Rio das Velhas Supergroup consists of greenstone (basalt and komatiite), rhyolitic lava, and intercalated sedimentary rocks. Sedimentary units of the Rio das Velhas Supergroup include Algoma-type banded-iron formations (BIFs), carbonates, and siliciclastics. Alluvial conglomerate and sandstone make up the basal units of the Minas Supergroup. These units grade upward into shallow-water marine pelites of the Tamanduá and Caraça groups. The Lake Superior-type Cauê banded-iron Formation lies on Caraça metasediments. The Cauê Formation is a carbonate sequence of the Gandarela Formation. Lying locally unconformably on the Gandarela Formation, the Piracicaba Group comprises a thick pile of shallow-water and deltaic strata. Separated from the Piracicaba Group by an unconformity, the Sabará Group is a thick sequence of turbidites, tuffs, volcaniclastics, conglomerates, and diamictites derived from a source to the east–southeast. The Post Minas intrusives comprise thin, undated, pegmatite veins cutting Minas rock (Chemale Jr et al., 2012; Rosière and Chemale Jr, 2017). Finally, the Itacolomi Group consists of alluvial sandstones, conglomerates, and minor pelites (Bekker et al., 2003; Dorr, 1969) deposited in intramontane grabens (Alkmim and Martins-Neto, 2012) (Figure 2).

For our studies, samples were made available via IAMGOLD Ltda. and SAMARCO S.A. These consist of an exceptionally well-preserved deep drill core from the Pitangui project (QF-P) containing Neoarchean BIFs from Nova Lima Group of the Rio das Velhas Supergroup and Paleoproterozoic BIFs from Cauê Formation-Itabira Group of

the Minas Supergroup from Alegria mine (QF-AL-B) (Figure 1 and 2). These two drill cores were selected for their exceptional preservation from weathering and the apparent relative absence of post-depositional (hydrothermal and metamorphic) alteration. Only homogeneous intervals free from surface weathering effects and lacking veins were used for geochemical analysis.

Methods

Analytical methods optimized for these sample were applied with particular attention to the special requirements for metasedimentary rocks that span low- to medium-grade schist metamorphism. The banded iron-rich bodies of BIFs consist of Fe-oxide- and SiO_2-rich layers with dolomitic hematite phyllites and magnetite. Iron speciation is a bulk sequential chemical extraction technique used to quantify the proportions of different iron phases in a given sample for the purpose of determining the paleoredox state of the depositional environment: oxic, anoxic/ferruginous, or euxinic (anoxic and sulfide bearing) (Poulton and Canfield, 2005; Raiswell and Canfield, 2012).Iron speciation is a bulk sequential chemical extraction technique used to quantify the proportions of different iron phases in a given sample for the purpose of determining the paleoredox state of the depositional environment: oxic, anoxic/ferruginous or euxinic (anoxic and sulfide bearing) (Poulton and Canfield, 2005; Raiswell and Canfield, 2012). We adopted a three-step sequential extraction. First, sample powder was treated with a buffered sodium acetate solution for 48 hours to extract Fe bearing carbonate phases (e.g., siderite or ankerite) and it is referred as Fe_{carb}. Following this step, the samples were treated with a buffered sodium

dithionite solution for two hours to extract labile Fe-oxides (Fe_{ox}). The lastly, samples were buffered with ammonium oxalate solution for six hours to extract Fe present as mixed valence or highly crystalline oxides (e.g., magnetite), and is labeled Fe_{mag}. Multiple samples were replicated through all steps of the procedure. Among these replicates, average reproducibility of each was 8%. The fraction of the total extracted Fe is defined as 'highly-reactive' Fe and denoted Fe_{HR}. All reduced sulfur present in sulfide-bound species (predominantly pyrite) was extracted by a 2-hr hot chromium chloride/HCl distillation and quantitatively captured as $_{Ag2S}$ using a basic $AgNO_3$ trap solution (Canfield et al., 1986). Ag_2S was filtered, and the concentration of S present was determined gravimetrically. The concentration of Fe present in each sample as pyrite (Fe_{py}) was calculated assuming all chromium reducible sulfide was present as FeS_2.

Analysis of Fe via the sequential extraction, major and trace elements, and REEs+Y were performed on Agilent 7900 quadrupole inductively coupled plasma-mass spectrometer (ICP-MS) at the University of California, Riverside (UCR). All REE+Y data are normalized to Post-Archean Australian Shale (PAAS; (Taylor and McLennan, 1985). Although PAAS REE+Y values have been revisited (Pourmand et al., 2012), and there are more recent estimates for modern upper continental crustal REE+Y values (Kamber et al., 2005), we normalize our values to PAAS as calculated by Taylor & McLennan (1985) to maintain consistency with the large record of previous REE+Y studies. Analytical precision and the accuracy of our measurements and ratios were checked by multiple sample analysis of the geostandards BIR-1, BHVO-1, SDO-1, and SRM-692. The reproducibility at UCR was better than 7% for all chemical analysis.

RESULTS

Neoarchean BIFs – Nova Lima Group

Total of 39 samples were analyzed. Aluminum (Al) content varied from 0.03 to 1.67 wt%, with an average of 0.22 wt%, while Fe_T values ranged from 18.61 wt% to 43.85 wt%, with an average of 28.68 9 wt%. Iron speciation data from the Pitangui project drill cores yield $Fe_{HR}/Fe_T > 0.38$ and $Fe_{Py}/Fe_{HR} < 0.80$. We see a significant shale-normalized negative Ce anomaly (Figure) measured as $(Ce_{(SN)}/0.5Pr_{(SN)} + 0.5\ La_{(SN)})$. Praseodymium anomalies (Pr/Pr*), calculated by $(Pr_{(SN)}/(0.5Ce_{(SN)} + 0.5Nd_{(SN)})$ work with $Ce/Ce_{(SN)}$* to differentiate between positive La and true negative Ce anomalies (Figure 3 and 5) (Bau and Dulski, 1996; Planavsky et al., 2010). All the samples from the Nova Lima group contain positive shale-normalized (SN) Eu anomalies (Eu/Eu*) ranging from 1.29 to 3.70 (with an average of 2.1) calculated as $Eu_{(SN)}/0.66Sm_{(SN)}+0.33Tb_{(SN)}$, which considers the slight positive seawater Gd anomaly (Planavsky et al., 2010). The light-to-heavy fractionation calculated by the Pr_{SN}/Yb_{SN} ratio in Neoarchean BIFs have low Pr_{SN}/Yb_{SN} ratios, with an average Pr_{SN}/Yb_{SN} of 0.18 and a range from 0.09 to 0.43 (Table 1.b), meaning that these BIFs are vastly depleted in LREE. The average Y/Ho ratio for Archean sample set is 46.4, which is markedly higher than the shale composite ratio of approximately 27 (Bolhar et al., 2004).

Paleoproterozoic BIFs -Itabira Group

In total, 46 samples were analyzed from this formation for geochemical analysis. Samples show low Al and Mn concentrations with an average of 0.36 wt% and 0.08 wt%,

respectively. Total iron contents span from 17.17 wt% to 43.78 wt%. Calcium spans a large range from 0.06 wt% to 9.39 wt% (Figure 3). Iron speciation data from yield $Fe_{HR}/Fe_T > 0.38$ and $Fe_{Py}/Fe_{HR} < 0.80$, denoting ferruginous depositional conditions (Poulton and Canfield, 2011) with few instances where observe $Fe_{HR}/Fe_T < 0.38$. Rare earth element (REE) data normalized to average Post-Archean Australian Shale (PAAS; Taylor and McLennan, 1985) vary from 0.07 to 0.54 × PAAS and show relatively smooth patterns (Figure 4). The majority of samples display positive Eu anomalies (PAAS-normalized), with an average of 2.23 and a broad range of variance that extends from 0.77 to 7.97. True Ce anomalies, using Pr/Pr* values to identify La anomalies (Bau and Dulski, 1996; Planavsky et al., 2010), are limited. Three samples have significant positive Ce anomalies, ranging from 1.05 to 1.17; only six samples from the Itabira Group show a significant negative Ce anomaly (Figure 3 and 5). The Pr_{SN}/Yb_{SN} ratios range from 0.05 to 0.77, with an average $Pr_{SN}/Yb_{SN} = 0.24$, meaning that Paleoproterozoic BIFs are highly depleted in LREE. The Paleoproterozoic BIFs in our sample set present a wide range of Y/Ho ratios, ranging from 56.33 to 12.33 with an average Y/Ho ratio of 29.52.

DISCUSSION

Local redox proxies

Iron speciation was employed as a means of characterizing the depositional water column conditions (reviewed recently by Raiswell et al., 2018). The sequential extraction scheme (Poulton and Canfield, 2005) includes a range of highly reactive Fe phases (Fe bound in carbonate – Fe_{carb}, Fe bound in oxides – Fe_{ox}, and Fe in magnetite – Fe_{mag}) that

can react with sulfide to form pyrite on time scales relevant to early diagenesis (Canfield, 1989; Canfield, and others, 1992; Canfield and Raiswell, 1996), which, when summed with pyrite, define the 'highly reactive' Fe (Fe_{HR}) pool. The Fe_{HR} /Fe_T ratios are used as indicators of anoxic water column conditions (Fe_{HR} /Fe_T > 0.38), which, when combined with Fe_{Py} /Fe_{HR} > 0.80, can indicate euxinic conditions (Poulton and Canfield, 2011). Iron speciation data from drill cores of the Neoarchean BIFs of the Nova Lima Group and Paleoproterozoic BIFs of the Itabira Group yield Fe_{HR} /Fe_T > 0.38 and Fe_{Py} /Fe_{HR} < 0.80, suggesting a ferruginous depositional setting along with few instances where we see Fe_{HR} /Fe_T <0.38. Lower values can reflect oxygenation of the water column during deposition but can also reflect high sedimentation rates (Figure 3).

The behavior of REE+Y has been well-characterized in modern environments and plays an important role in efforts to describe the marine geochemistry. Relative concentrations between heavy REEs (HREEs) and light REEs (LREEs) and Y/Ho provide ocean redox constraints (Goldstein and Jacobsen, 1988) and elucidate palaeoceanographic processes. The cerium and europium anomalies relate to redox conditions and Fe sources, respectively (Holser, 1997; Planavsky et al., 2008) when compared to average crustal sediments (Elderfield and Greaves, 1982).

The light REE depletion arises in oxygenated waters due to preferential removal of light versus heavy REEs onto Mn-Fe-oxyhydroxides and other reactive phases. As a result, the ratio of light to heavy REE distinctively increases within the redox boundary due to reductive dissolution of Mn-Fe-oxyhydroxides (Byrne and Sholkovitz, 1996; Elderfield et al., 1990; German et al., 1991; Sholkovitz et al., 1994). The heavy REEs Ho and Y are

geochemically analogous but with unique complexion properties in marine systems whereby Ho is scavenged onto particulate matter two times faster than Y (Nozaki et al., 1997). Here, we observe differences in REE+Y behavior in our two formations. In early Archean BIFs formations, a light REE depletion and high Y/Ho ratios suggest a lack of redoxcline during its deposition (Planavsky et al., 2010). On the other hand, the Paleoproterozoic BIFs show a significant range in both Y/Ho and light-to-heavy REE (Pr_{SN}/Yb_{SN}) ratios (both below and above the shale composite values), indicating that the Paleoproterozoic BIFs were deposited under varying redox conditions triggered by the fluctuating inputs of REE+Y from precipitation and dissolution of Mn-Fe oxyhydroxides (Planavsky et al., 2010; Planavsky et al., 2009).

In the presence of free oxygen, the rare earth element (REE) cerium (Ce) can be oxidized from the soluble Ce^{3+} to the insoluble Ce^{4+}. This oxidation occurs when Ce^{3+} undergoes sorption onto Mn- and Fe-oxyhydroxide surfaces in depositional environments (Bau, 1999; Bau and Koschinsky, 2009). Subsequent removal of insoluble Ce^{4+} from seawater produces a negative Ce anomaly in seawater (Elderfield, 1988), which can then be incorporated into authigenic sediments (Bau and Dulski, 1996; De Baar et al., 1985; Tostevin et al., 2016). Cerium and manganese possess similar redox potentials and share a similar oxidation pathway (Ce^{3+}oxidation occurs on the surface of Mn^{4+} oxides and hydroxides) and as a result require a similar minimum oxygen concentration to be present in depositional environments to facilitate their oxidation (Moffett, 1994; Planavsky et al., 2010; Schippers et al., 2005; Tang et al., 2016; Tebo, 1991). We see a lack of positive Ce anomaly in both Neoarchean BIFs from Nova Lima Group and Paleoproterozoic BIFs from

Cauê Formation-Itabira Group suggesting that the basin in which these two formations were deposited were reducing with respect to Ce and Mn (Bekker et al., 2004; Planavsky et al., 2010), featuring the prevalence of anoxic water column conditions (Bau and Dulski, 1996; Frei et al., 2008; Konhauser et al., 2017a; Li et al., 2015; Planavsky et al., 2010).

True negative Ce anomalies, when present, are considered one of the most robust redox indicators of shallow marine oxidation (de Baar et al., 1988; German and Elderfield, 1990; Kamber et al., 2014; Liu et al., 2019). When oxidized, less soluble Ce^{4+} is preferentially scavenged by Mn particles, crusts, and nodules (Piper, 1974), as well as Fe-Mn oxides coating sediment particles, leaving a relative Ce deficiency in the oxic seawater host. By contrast, suboxic and anoxic waters do not contain noteworthy negative Ce anomalies because of reductive dissolution of settling Mn-Fe-rich sediments and can show positive anomalies marking the preferential transport and release of Ce from oxic to anoxic waters (Byrne and Sholkovitz, 1996; German et al., 1995; German et al., 1991; Planavsky et al., 2008). The true negative Ce anomaly is a rare feature in many Archean and early Paleoproterozoic IFs (Konhauser et al., 2017b; Planavsky et al., 2010). However, the absence of negative Ce anomalies can point to a more ambiguous situation, as it does not always preclude the presence of well-oxygenated surface waters (Tostevin et al., 2016). Negative Ce anomalies were observed in both Neoarchean BIFs from Nova Lima Group and Paleoproterozoic BIFs from Cauê Formation-Itabira Group supporting previous findings (Bosco-Santos et al., 2020; Cabral et al., 2016; Mendes et al., 2017; Sampaio et al., 2018; Soares et al., 2018; Soares et al., 2017; Spier et al., 2007; Teixeira et al., 2017)

implying towards a possibility of locally oxygenated environment in the otherwise oxygen-free ocean.

Hydrothermal sources of Fe

Archean IFs are enriched in Eu relative to the other REEs, which means Eu existed as Eu^{2+} in addition to Eu^{3+}. Modern seawater lacks this Eu enrichment (Danielson et al., 1992; Fryer, 1977) because hydrothermal vent fluids are a sink for seawater REEs, which co-precipitate with Fe oxides under oxic conditions (Brugger et al., 2000; Kamber and Webb, 2001; Kato et al., 1998). The reducing state of hydrothermal solutions (Bau, 1991; Bowers et al., 1985) and the stability fields of Eu species (Sverjensky, 1984) imply that divalent Eu is the stable form of Eu in reducing hydrothermal fluids until Eu is diluted by the seawater. The positive Eu anomalies throughout the Neoarchean BIFs of the Nova Lima Group are relatively constant (1.27-3.70) (Table 3), following the general trend of Eu anomalies of Archean oceans (Eu/Eu* = 1.2–4.5) (Fryer, 1977; Konhauser et al., 2017a; MacRae et al., 1992; Planavsky et al., 2010; Raiswell et al., 2011), caused by the erosion of Eu-enriched Archean continental crust (Bolhar et al., 2004) and hydrothermal fluid (Konhauser et al., 2017a). The BIFs of the Paleoproterozoic BIFs Group show a large range of Eu anomalies (0.77-7.97) that increases down core (Figure 3), reflecting the great variation in mixing ratios of hydrothermal fluids and ambient seawater over time.

Evidence for detrital contamination

Detrital input was monitored using cross plots of Yo/Ho, Ce anomalies ($Ce_{SN}/(0.5(Pr_{SN} + La_{SN})$, and light-to-heavy REE ratios (Pr_{SN}/Yb_{SN}) versus Al (Figure 6). No samples show a significant correlation, suggesting that the dominant REY signal is not detrital.

CONCLUSIONS

Our study provides evidence for redox evolution in the Archean to Paleoproterozoic ocean, which has important implications for the production of Fe formations. The positive Eu anomaly suggests that hydrothermal Fe was the dominant source of Fe. The Neoarchean BIFs from Nova Lima Group record signs of early oxygenation but without suggestions of deposition from a water column with a Fe-Mn redoxcline. In contrast, the Paleoproterozoic BIFs from Itabira Group display an apparent REE signature of ocean redox stratification and IF deposition under varying redox conditions where an oxic surface layer overlies anoxic bottom waters (Frei et al., 2016; Riding et al., 2014; Satkoski et al., 2015). A local accumulation of oxygen and redox conditions recorded in Neoarchean and Paleoproterozoic Banded Iron Formation (BIFs) from Quadrilátero Ferrífero capture the redox evolution of the Minas basin - São Francisco Craton and queries for further investigations concerning local controls in rise of atmospheric oxygen.

REFERENCES

Alkmim, F. F., and Marshak, S., 1998, Transamazonian orogeny in the Southern Sao Francisco craton region, Minas Gerais, Brazil: evidence for Paleoproterozoic collision and collapse in the Quadrilátero Ferrıfero: Precambrian Research, v. 90, no. 1-2, p. 29-58.

Alkmim, F. F., and Martins-Neto, M. A., 2012, Proterozoic first-order sedimentary sequences of the São Francisco craton, eastern Brazil: Marine and Petroleum Geology, v. 33, no. 1, p. 127-139.

Babinski, M., Chemale Jr, F., and Van Schmus, W. R., 1995, The PB/PB age of the minas supergroup carbonate rocks, quadrilatero FERRIFERO, BRAZIL: Precambrian Research, v. 72, no. 3-4, p. 235-245.

Baltazar, O., and Zucchetti, M., 2007, Lithofacies associations and structural evolution of the Archean Rio das Velhas greenstone belt, Quadrilátero Ferrífero, Brazil: A review of the setting of gold deposits: Ore Geology Reviews, v. 32, no. 3-4, p. 471-499.

Bau, M., 1991, Rare-earth element mobility during hydrothermal and metamorphic fluid-rock interaction and the significance of the oxidation state of europium: Chemical Geology, v. 93, no. 3-4, p. 219-230.

Bau, M., and Dulski, P., 1996, Distribution of yttrium and rare-earth elements in the Penge and Kuruman iron-formations, Transvaal Supergroup, South Africa: Precambrian Research, v. 79, no. 1-2, p. 37-55.

Bau, M., and Koschinsky, A., 2009, Oxidative scavenging of cerium on hydrous Fe oxide: evidence from the distribution of rare earth elements and yttrium between Fe oxides and Mn oxides in hydrogenetic ferromanganese crusts: Geochemical Journal, v. 43, no. 1, p. 37-47.

Bekker, A., Holland, H., Wang, P.-L., Rumble, D., Stein, H., Hannah, J., Coetzee, L., and Beukes, N., 2004, Dating the rise of atmospheric oxygen: Nature, v. 427, no. 6970, p. 117-120.

Bekker, A., Planavsky, N., Rasmussen, B., Krapez, B., Hofmann, A., Slack, J., Rouxel, O., and Konhauser, K., 2014, Iron formations: Their origins and implications for ancient seawater chemistry, Treatise on geochemistry, Volume 12, Elsevier, p. 561-628.

Bekker, A., Sial, A., Karhu, J., Ferreira, V., Noce, C., Kaufman, A., Romano, A., and Pimentel, M., 2003, Chemostratigraphy of carbonates from the Minas Supergroup, Quadrilátero Ferryífero (Iron Quadrangle), Brazil: A stratigraphic record of early

proterozoic atmospheric, biogeochemical and climactic change: American Journal of Science, v. 303, no. 10, p. 865-904.

Bolhar, R., Kamber, B. S., Moorbath, S., Fedo, C. M., and Whitehouse, M. J., 2004, Characterisation of early Archaean chemical sediments by trace element signatures: Earth and Planetary Science Letters, v. 222, no. 1, p. 43-60.

Bosco-Santos, A., Gilhooly III, W. P., Fouskas, F., Fabricio-Silva, W., and Oliveira, E. P., 2020, Euxinia in the Neoarchean: The starting point for early oxygenation in a Brazilian Craton: Precambrian Research, v. 341, p. 105655.

Bowers, T. S., Von Damm, K. L., and Edmond, J. M., 1985, Chemical evolution of mid-ocean ridge hot springs: Geochimica et Cosmochimica Acta, v. 49, no. 11, p. 2239-2252.

Brugger, J., Lahaye, Y., Costa, S., Lambert, D., and Bateman, R., 2000, Inhomogeneous distribution of REE in scheelite and dynamics of Archaean hydrothermal systems (Mt. Charlotte and Drysdale gold deposits, Western Australia): Contributions to Mineralogy and Petrology, v. 139, no. 3, p. 251-264.

Buick, R., 2008, When did oxygenic photosynthesis evolve?: Philosophical Transactions of the Royal Society B: Biological Sciences, v. 363, no. 1504, p. 2731-2743.

Byrne, R., and Sholkovitz, E., 1996, Marine chemistry and geochemistry of the lanthanides: Handbook on the physics and chemistry of rare earths, v. 23, p. 497-593.

Cabral, A. R., Lehmann, B., Gomes Jr, A. A. S., and Pašava, J., 2016, Episodic negative anomalies of cerium at the depositional onset of the 2.65-Ga Itabira iron formation, Quadrilátero Ferrífero of Minas Gerais, Brazil: Precambrian Research, v. 276, p. 101-109.

Cabral, A. R., Zeh, A., Koglin, N., Gomes Jr, A. A. S., Viana, D. J., and Lehmann, B., 2012, Dating the Itabira iron formation, Quadrilátero Ferrífero of Minas Gerais, Brazil, at 2.65 Ga: depositional U–Pb age of zircon from a metavolcanic layer: Precambrian Research, v. 204, p. 40-45.

Canfield, D. E., Poulton, S. W., Knoll, A. H., Narbonne, G. M., Ross, G., Goldberg, T., and Strauss, H., 2008, Ferruginous conditions dominated later Neoproterozoic deep-water chemistry: Science, v. 321, no. 5891, p. 949-952.

Canfield, D. E., Raiswell, R., Westrich, J. T., Reaves, C. M., and Berner, R. A., 1986, The use of chromium reduction in the analysis of reduced inorganic sulfur in sediments and shales: Chemical geology, v. 54, no. 1-2, p. 149-155.

Chemale Jr, F., Dussin, I. A., Alkmim, F. F., Martins, M. S., Queiroga, G., Armstrong, R., and Santos, M. N., 2012, Unravelling a Proterozoic basin history through detrital zircon geochronology: the case of the Espinhaço Supergroup, Minas Gerais, Brazil: Gondwana Research, v. 22, no. 1, p. 200-206.

Danielson, A., Möller, P., and Dulski, P., 1992, The europium anomalies in banded iron formations and the thermal history of the oceanic crust: Chemical Geology, v. 97, no. 1-2, p. 89-100.

De Baar, H. J., Bacon, M. P., Brewer, P. G., and Bruland, K. W., 1985, Rare earth elements in the Pacific and Atlantic Oceans: Geochimica et Cosmochimica Acta, v. 49, no. 9, p. 1943-1959.

de Baar, H. J., German, C. R., Elderfield, H., and Van Gaans, P., 1988, Rare earth element distributions in anoxic waters of the Cariaco Trench: Geochimica et Cosmochimica Acta, v. 52, no. 5, p. 1203-1219.

Dopico, C. I. M., Lana, C., Moreira, H. S., Cassino, L. F., and Alkmim, F. F., 2017, U–Pb ages and Hf-isotope data of detrital zircons from the late Neoarchean-Paleoproterozoic Minas Basin, SE Brazil: Precambrian Research, v. 291, p. 143-161.

Dorr, J. V. N., 1969, Physiographic, stratigraphic, and structural development of the Quadrilatero Ferrifero, Minas Gerais, Brazil: US Government Printing Office, 2330-7102.

Elderfield, H., 1988, The oceanic chemistry of the rare-earth elements: Philosophical Transactions of the Royal Society of London. Series A, Mathematical and Physical Sciences, v. 325, no. 1583, p. 105-126.

Elderfield, H., and Greaves, M. J., 1982, The rare earth elements in seawater: Nature, v. 296, no. 5854, p. 214-219.

Elderfield, H., Upstill-Goddard, R., and Sholkovitz, E., 1990, The rare earth elements in rivers, estuaries, and coastal seas and their significance to the composition of ocean waters: Geochimica et Cosmochimica Acta, v. 54, no. 4, p. 971-991.

Fischer, W. W., and Knoll, A. H., 2009, An iron shuttle for deepwater silica in Late Archean and early Paleoproterozoic iron formation: Geological Society of America Bulletin, v. 121, no. 1-2, p. 222-235.

Frei, R., Crowe, S. A., Bau, M., Polat, A., Fowle, D. A., and Døssing, L. N., 2016, Oxidative elemental cycling under the low O 2 Eoarchean atmosphere: Scientific reports, v. 6, no. 1, p. 1-9.

Frei, R., Dahl, P. S., Duke, E. F., Frei, K. M., Hansen, T. R., Frandsson, M. M., and Jensen, L. A., 2008, Trace element and isotopic characterization of Neoarchean and Paleoproterozoic iron formations in the Black Hills (South Dakota, USA): assessment of chemical change during 2.9–1.9 Ga deposition bracketing the 2.4–2.2 Ga first rise of atmospheric oxygen: Precambrian Research, v. 162, no. 3-4, p. 441-474.

Fru, E. C., Ivarsson, M., Kilias, S. P., Bengtson, S., Belivanova, V., Marone, F., Fortin, D., Broman, C., and Stampanoni, M., 2013, Fossilized iron bacteria reveal a pathway to the biological origin of banded iron formation: Nature communications, v. 4, no. 1, p. 1-7.

Fru, E. C., Somogyi, A., El Albani, A., Medjoubi, K., Aubineau, J., Robbins, L. J., Lalonde, S. V., and Konhauser, K. O., 2019, The rise of oxygen-driven arsenic cycling at ca. 2.48 Ga: Geology, v. 47, no. 3, p. 243-246.

Fryer, B., 1977, Rare earth evidence in iron-formations for changing Precambrian oxidation states: Geochimica et Cosmochimica Acta, v. 41, no. 3, p. 361-367.

German, C., Masuzawa, T., Greaves, M., Elderfield, H., and Edmond, J., 1995, Dissolved rare earth elements in the Southern Ocean: Cerium oxidation and the influence of hydrography: Geochimica et Cosmochimica Acta, v. 59, no. 8, p. 1551-1558.

German, C. R., and Elderfield, H., 1990, Application of the Ce anomaly as a paleoredox indicator: the ground rules: Paleoceanography, v. 5, no. 5, p. 823-833.

German, C. R., Holliday, B. P., and Elderfield, H., 1991, Redox cycling of rare earth elements in the suboxic zone of the Black Sea: Geochimica et Cosmochimica Acta, v. 55, no. 12, p. 3553-3558.

Goldstein, S. J., and Jacobsen, S. B., 1988, Rare earth elements in river waters: Earth and Planetary Science Letters, v. 89, no. 1, p. 35-47.

Haqq-Misra, J., Kasting, J. F., and Lee, S., 2011, Availability of O2 and H2O2 on pre-photosynthetic Earth: Astrobiology, v. 11, no. 4, p. 293-302.

Heard, A. W., and Dauphas, N., 2020, Constraints on the coevolution of oxic and sulfidic ocean iron sinks from Archean–Paleoproterozoic iron isotope records: Geology, v. 48, no. 4, p. 358-362.

Holser, W. T., 1997, Evaluation of the application of rare-earth elements to paleoceanography: Palaeogeography, Palaeoclimatology, Palaeoecology, v. 132, no. 1-4, p. 309-323.

Kamber, B. S., Greig, A., and Collerson, K. D., 2005, A new estimate for the composition of weathered young upper continental crust from alluvial sediments, Queensland, Australia: Geochimica et Cosmochimica Acta, v. 69, no. 4, p. 1041-1058.

Kamber, B. S., and Webb, G. E., 2001, The geochemistry of late Archaean microbial carbonate: implications for ocean chemistry and continental erosion history: Geochimica et Cosmochimica Acta, v. 65, no. 15, p. 2509-2525.

Kamber, B. S., Webb, G. E., and Gallagher, M., 2014, The rare earth element signal in Archaean microbial carbonate: information on ocean redox and biogenicity: Journal of the Geological Society, v. 171, no. 6, p. 745-763.

Kato, Y., Ohta, I., Tsunematsu, T., Watanabe, Y., Isozaki, Y., Maruyama, S., and Imai, N., 1998, Rare earth element variations in mid-Archean banded iron formations: Implications for the chemistry of ocean and continent and plate tectonics: Geochimica et Cosmochimica Acta, v. 62, no. 21-22, p. 3475-3497.

Konhauser, K., Planavsky, N., Hardisty, D., Robbins, L., Warchola, T., Haugaard, R., Lalonde, S., Partin, C., Oonk, P., and Tsikos, H., 2017a, Iron formations: A global record of Neoarchaean to Palaeoproterozoic environmental history: Earth-Science Reviews, v. 172, p. 140-177.

Konhauser, K. O., Kappler, A., and Roden, E. E., 2011, Iron in microbial metabolisms: Elements, v. 7, no. 2, p. 89-93.

Konhauser, K. O., Planaysky, N. J., Hardisty, D. S., Robbins, L. J., Warchola, T. J., Haugaard, R., Lalonde, S. V., Partin, C. A., Oonk, P. B. H., Tsikos, H., Lyons, T. W., Bekker, A., and Johnson, C. M., 2017b, Iron formations: A global record of Neoarchaean to Palaeoproterozoic environmental history: Earth-Science Reviews, v. 172, p. 140-177.

Lalonde, S. V., and Konhauser, K. O., 2015, Benthic perspective on Earth's oldest evidence for oxygenic photosynthesis: Proceedings of the National Academy of Sciences, v. 112, no. 4, p. 995-1000.

Lana, C., Alkmim, F. F., Armstrong, R., Scholz, R., Romano, R., and Nalini Jr, H. A., 2013, The ancestry and magmatic evolution of Archaean TTG rocks of the Quadrilátero Ferrífero province, southeast Brazil: Precambrian Research, v. 231, p. 157-173.

Li, C., Planavsky, N. J., Love, G. D., Reinhard, C. T., Hardisty, D., Feng, L. J., Bates, S. M., Huang, J., Zhang, Q. R., Chu, X. L., and Lyons, T. W., 2015, Marine redox conditions in the middle Proterozoic ocean and isotopic constraints on authigenic

carbonate formation: Insights from the Chuanlinggou Formation, Yanshan Basin, North China: Geochimica Et Cosmochimica Acta, v. 150, p. 90-105.

Liu, X.-M., Hardisty, D. S., Lyons, T. W., and Swart, P. K., 2019, Evaluating the fidelity of the cerium paleoredox tracer during variable carbonate diagenesis on the Great Bahamas Bank: Geochimica et Cosmochimica Acta, v. 248, p. 25-42.

Lobato, L., Santos, J., McNaughton, N., Fletcher, I., and Noce, C., 2007, U–Pb SHRIMP monazite ages of the giant Morro Velho and Cuiabá gold deposits, Rio das Velhas greenstone belt, Quadrilátero Ferrífero, Minas Gerais, Brazil: Ore Geology Reviews, v. 32, no. 3-4, p. 674-680.

Lyons, T. W., Reinhard, C. T., and Planavsky, N. J., 2014, The rise of oxygen in Earth's early ocean and atmosphere: Nature, v. 506, no. 7488, p. 307-315.

Machado, N., Noce, C., Ladeira, E., and De Oliveira, O. B., 1992, U-Pb geochronology of Archean magmatism and Proterozoic metamorphism in the Quadrilátero Ferrífero, southern São Francisco craton, Brazil: Geological Society of America Bulletin, v. 104, no. 9, p. 1221-1227.

MacRae, N., Nesbitt, H., and Kronberg, B., 1992, Development of a positive Eu anomaly during diagenesis: Earth and Planetary Science Letters, v. 109, no. 3-4, p. 585-591.

Mendes, M., Lobato, L. M., Kunzmann, M., Halverson, G. P., and Rosière, C. A., 2017, Iron isotope and REE+ Y composition of the Cauê banded iron formation and related iron ores of the Quadrilátero Ferrífero, Brazil: Mineralium Deposita, v. 52, no. 2, p. 159-180.

Moffett, J. W., 1994, A radiotracer study of cerium and manganese uptake onto suspended particles in Chesapeake Bay: Geochimica et Cosmochimica Acta, v. 58, no. 2, p. 695-703.

Nass, K., Foucar, L., Barends, T. R. M., Hartmann, E., Botha, S., Shoeman, R. L., Doak, R. B., Alonso-Mori, R., Aquila, A., Bajt, S., Barty, A., Bean, R., Beyerlein, K. R., Bublitz, M., Drachmann, N., Gregersen, J., Jonsson, H. O., Kabsch, W., Kassemeyer, S., Koglin, J. E., Krumrey, M., Mattle, D., Messerschmidt, M., Nissen, P., Reinhard, L., Sitsel, O., Sokaras, D., Williams, G. J., Hau-Riege, S., Timneanu, N., Caleman, C., Chapman, H. N., Boutet, S., and Schlichting, I., 2015, Indications of radiation damage in ferredoxin microcrystals using high-intensity X-FEL beams: Journal of Synchrotron Radiation, v. 22, p. 225-238.

Nozaki, Y., Zhang, J., and Amakawa, H., 1997, The fractionation between Y and Ho in the marine environment: Earth and Planetary Science Letters, v. 148, no. 1-2, p. 329-340.

Ohmoto, H., Watanabe, Y., Ikemi, H., Poulson, S. R., and Taylor, B. E., 2006, Sulphur isotope evidence for an oxic Archaean atmosphere: Nature, v. 442, no. 7105, p. 908-911.

Olson, J. M., 2006, Photosynthesis in the Archean era: Photosynthesis research, v. 88, no. 2, p. 109-117.

Olson, S. L., Kump, L. R., and Kasting, J. F., 2013, Quantifying the areal extent and dissolved oxygen concentrations of Archean oxygen oases: Chemical Geology, v. 362, p. 35-43.

Ostrander, C. M., Nielsen, S. G., Owens, J. D., Kendall, B., Gordon, G. W., Romaniello, S. J., and Anbar, A. D., 2019, Fully oxygenated water columns over continental shelves before the Great Oxidation Event: Nature geoscience, v. 12, no. 3, p. 186-191.

Piper, D. Z., 1974, Rare earth elements in ferromanganese nodules and other marine phases: Geochimica et Cosmochimica Acta, v. 38, no. 7, p. 1007-1022.

Planavsky, N., Bekker, A., Rouxel, O. J., Kamber, B., Hofmann, A., Knudsen, A., and Lyons, T. W., 2010, Rare Earth Element and yttrium compositions of Archean and Paleoproterozoic Fe formations revisited: New perspectives on the significance and mechanisms of deposition: Geochimica Et Cosmochimica Acta, v. 74, no. 22, p. 6387-6405.

Planavsky, N., Rouxel, O., Bekker, A., and Lyons, T., 2008, Rare Earth Element evidence for redox structure evolution: Geochimica Et Cosmochimica Acta, v. 72, no. 12, p. A753-A753.

Planavsky, N., Rouxel, O., Bekker, A., Shapiro, R., Fralick, P., and Knudsen, A., 2009, Iron-oxidizing microbial ecosystems thrived in late Paleoproterozoic redox-stratified oceans: Earth and Planetary Science Letters, v. 286, no. 1-2, p. 230-242.

Planavsky, N. J., Asael, D., Hofmann, A., Reinhard, C. T., Lalonde, S. V., Knudsen, A., Wang, X. L., Ossa, F. O., Pecoits, E., Smith, A. J. B., Beukes, N. J., Bekker, A., Johnson, T. M., Konhauser, K. O., Lyons, T. W., and Rouxel, O. J., 2014, Evidence for oxygenic photosynthesis half a billiion years before the Great Oxidation Event: Nature Geoscience, v. 7, no. 4, p. 283-286.

Poulton, S. W., and Canfield, D. E., 2005, Development of a sequential extraction procedure for iron: implications for iron partitioning in continentally derived particulates: Chemical geology, v. 214, no. 3-4, p. 209-221.

Pourmand, A., Dauphas, N., and Ireland, T. J., 2012, A novel extraction chromatography and MC-ICP-MS technique for rapid analysis of REE, Sc and Y: Revising CI-chondrite and Post-Archean Australian Shale (PAAS) abundances: Chemical Geology, v. 291, p. 38-54.

Raiswell, R., and Canfield, D. E., 2012, The iron biogeochemical cycle past and present: Geochemical perspectives, v. 1, no. 1, p. 1-2.

Raiswell, R., Reinhard, C. T., Derkowski, A., Owens, J., Bottrell, S. H., Anbar, A. D., and Lyons, T. W., 2011, Formation of syngenetic and early diagenetic iron minerals in the late Archean Mt. McRae Shale, Hamersley Basin, Australia: New insights on the patterns, controls and paleoenvironmental implications of authigenic mineral formation: Geochimica Et Cosmochimica Acta, v. 75, no. 4, p. 1072-1087.

Riding, R., Fralick, P., and Liang, L., 2014, Identification of an Archean marine oxygen oasis: Precambrian Research, v. 251, p. 232-237.

Rosière, C. A., and Chemale Jr, F., 2017, Brazilian iron formations and their geological setting: Revista Brasileira de Geociências, v. 30, no. 2, p. 274-278.

Sampaio, G., Pufahl, P., Raye, U., Kyser, K., Abreu, A., Alkmim, A., and Nalini Jr, H., 2018, Influence of weathering and hydrothermal alteration on the REE and δ56Fe composition of iron formation, Cauê Formation, Iron Quadrangle, Brazil: Chemical Geology, v. 497, p. 27-40.

Satkoski, A. M., Beukes, N. J., Li, W., Beard, B. L., and Johnson, C. M., 2015, A redox-stratified ocean 3.2 billion years ago: Earth and Planetary Science Letters, v. 430, p. 43-53.

Schippers, A., Neretin, L. N., Lavik, G., Leipe, T., and Pollehne, F., 2005, Manganese (II) oxidation driven by lateral oxygen intrusions in the western Black Sea: Geochimica et Cosmochimica Acta, v. 69, no. 9, p. 2241-2252.

Scott, C., Lyons, T., Bekker, A., Shen, Y.-a., Poulton, S., Chu, X.-l., and Anbar, A., 2008, Tracing the stepwise oxygenation of the Proterozoic ocean: Nature, v. 452, no. 7186, p. 456-459.

Sholkovitz, E. R., Landing, W. M., and Lewis, B. L., 1994, Ocean particle chemistry: the fractionation of rare earth elements between suspended particles and seawater: Geochimica et Cosmochimica Acta, v. 58, no. 6, p. 1567-1579.

Silva, A. M., Chemale Jr, F., Kuyumjian, R. M., and Heaman, L., 1995, Mafic dyke swarms of quadrilatero Ferrífero and southern Espinhaço, Minas Gerais, Brazil: Brazilian Journal of Geology, v. 25, no. 2, p. 124-137.

Soares, M. B., Neto, A. V. C., Bertolino, L. C., Alves, F. E. A., de Almeida, A. M., da Silva, P. H. M., de Araújo Mabub, R. O., Manduca, L. G., and de Pamplona Araújo, I. M. C., 2018, Multistage mineralization at the hypozonal São Sebastião gold deposit, Pitangui greenstone belt, Minas Gerais, Brazil: Ore Geology Reviews, v. 102, p. 618-638.

Soares, M. B., Neto, A. V. C., Zeh, A., Cabral, A. R., Pereira, L. F., do Prado, M. G. B., de Almeida, A. M., Manduca, L. G., da Silva, P. H. M., and de Araújo Mabub, R. O., 2017, Geology of the Pitangui greenstone belt, Minas Gerais, Brazil: stratigraphy, geochronology and BIF geochemistry: Precambrian Research, v. 291, p. 17-41.

Spier, C. A., de Oliveira, S. M., Sial, A. N., and Rios, F. J., 2007, Geochemistry and genesis of the banded iron formations of the Cauê Formation, Quadrilátero Ferrífero, Minas Gerais, Brazil: Precambrian Research, v. 152, no. 3-4, p. 170-206.

Sverjensky, D. A., 1984, Europium redox equilibria in aqueous solution: Earth and Planetary Science Letters, v. 67, no. 1, p. 70-78.

Tang, D., Shi, X., Wang, X., and Jiang, G., 2016, Extremely low oxygen concentration in mid-Proterozoic shallow seawaters: Precambrian Research, v. 276, p. 145-157.

Taylor, S. R., and McLennan, S. M., 1985, The continental crust: its composition and evolution.

Tebo, B. M., 1991, Manganese (II) oxidation in the suboxic zone of the Black Sea: Deep Sea Research Part A. Oceanographic Research Papers, v. 38, p. S883-S905.

Teixeira, N., Caxito, F., Rosière, C., Pecoits, E., Vieira, L., Frei, R., Sial, A., and Poitrasson, F., 2017, Trace elements and isotope geochemistry (C, O, Fe, Cr) of the Cauê iron formation, Quadrilátero Ferrífero, Brazil: Evidence for widespread microbial dissimilatory iron reduction at the Archean/Paleoproterozoic transition: Precambrian Research, v. 298, p. 39-55.

Tostevin, R., Shields, G. A., Tarbuck, G. M., He, T., Clarkson, M. O., and Wood, R. A., 2016, Effective use of cerium anomalies as a redox proxy in carbonate-dominated marine settings: Chemical Geology, v. 438, p. 146-162.

FIGURES

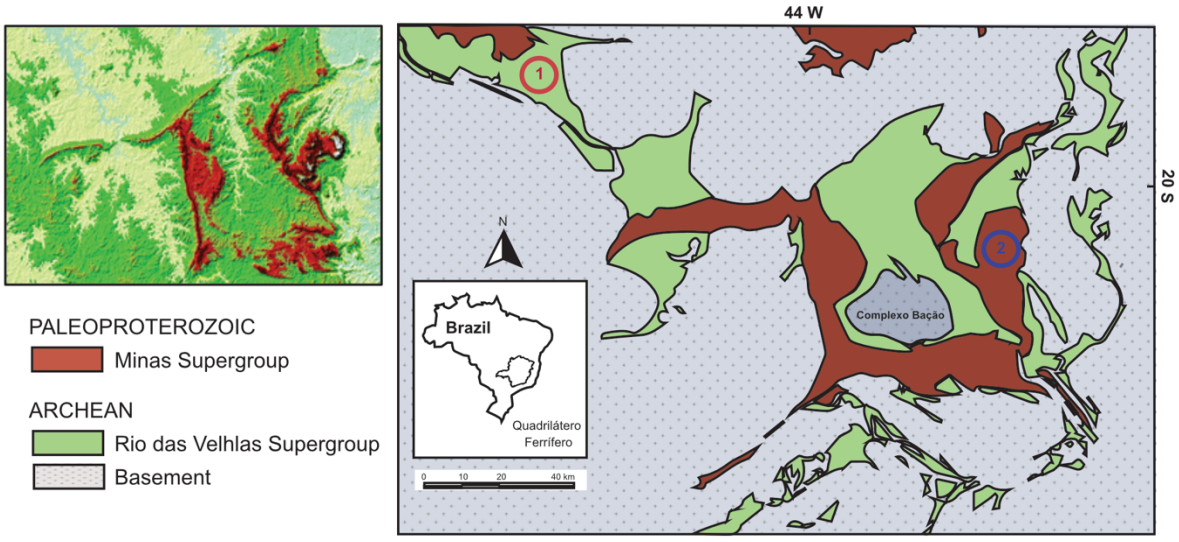

Figure 5.1: Regional Geological Setting of the Quadrilátero Ferrífero in the South Sector of the São Francisco Craton Source: Modified after Dorr (1969), Corrêa Neto et al. (2012), Pinto and Silva (2014) and Brando Soares et al. (2019). (1) Neoarchean BIFs from IAMGOLD mine and (2) Paleoproterozoic Alegria Mine sites.

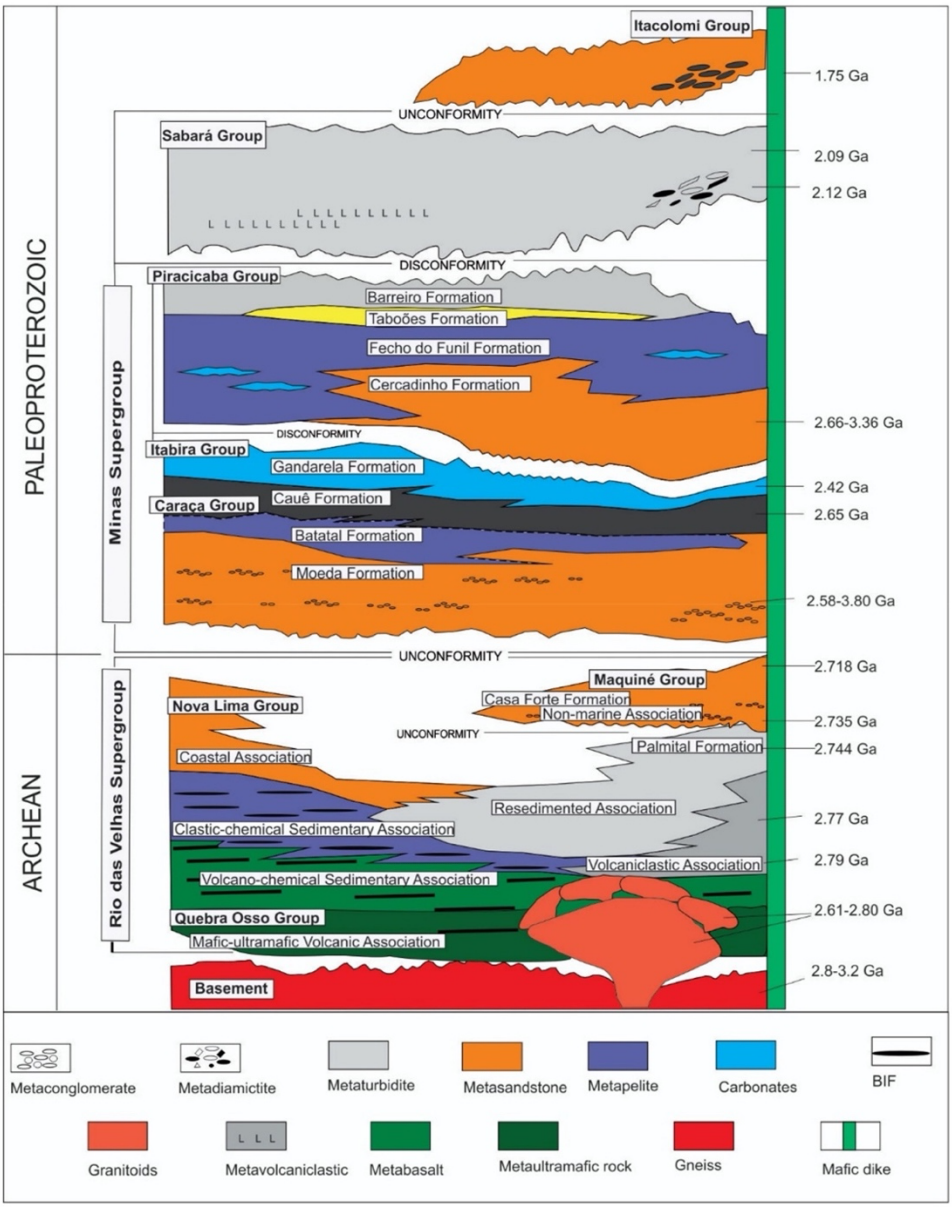

Figure 5.2: Stratigraphic column of the supracrustal sequences age model in the Quadrilátero Ferrífero (QF) region (based on (Alkmim and Marshak, 1998; Bekker et al., 2003; Brito-Neves, 1990; Carneiro et al., 1998; De Almeida et al., 1981; Dopico et al., 2017; Dorr, 1969; Farina et al., 2015; Heilbron et al., 2010; Lobato et al., 2007; Machado et al., 1992; Machado et al., 1989; Marshak and Alkmim, 1989; Mendes et al., 2014; Moreira et al., 2016; Noce et al., 1998; Teixeira et al., 1996; Teixeira et al., 1998). The lithostratigraphic outline of the QF is formed by (a) Archean granite-gneissic terranes; (b) Neoarchean-metavolcano-sedimentary sequences, including the Rio das Velhas Supergroup; and (c) Paleoproterozoic to Neoproterozoic metasedimentary sequences.

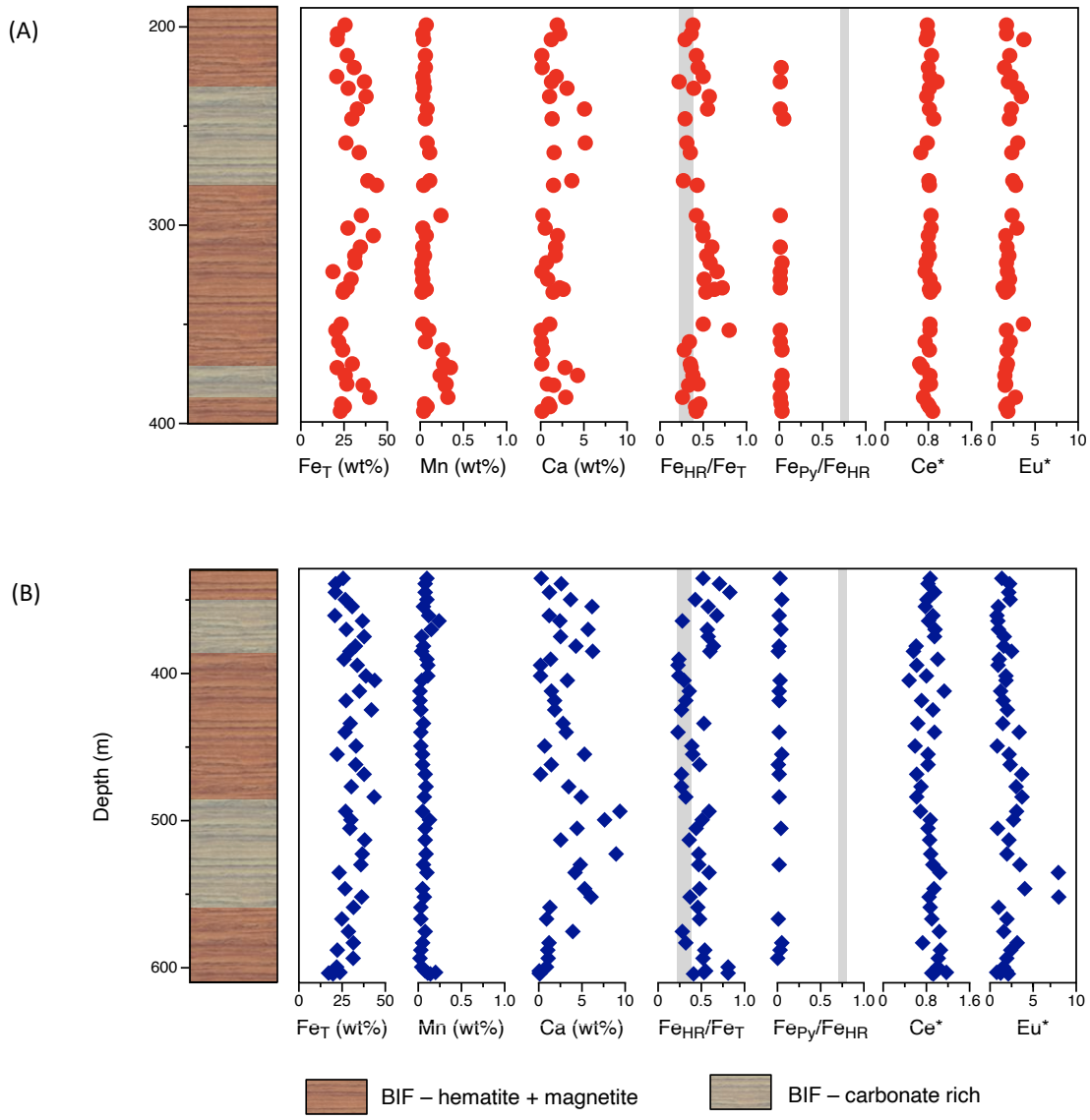

Figure 5.3: Chemostratigraphy of (A) Neoarchean BIFs-Nova Lima Group and (B) Paleoproterozoic BIFs-Itabira Group including iron speciation, Ce anomaly values and and Eu anomaly values. Highly reactive iron ratios (Fe_{HR}/Fe_T) > 0.38 are anoxic and pyrite iron (Fe_{Py}/Fe_{HR}) ratios > 0.7 are euxinic (Poulton and Canfield, 2011).

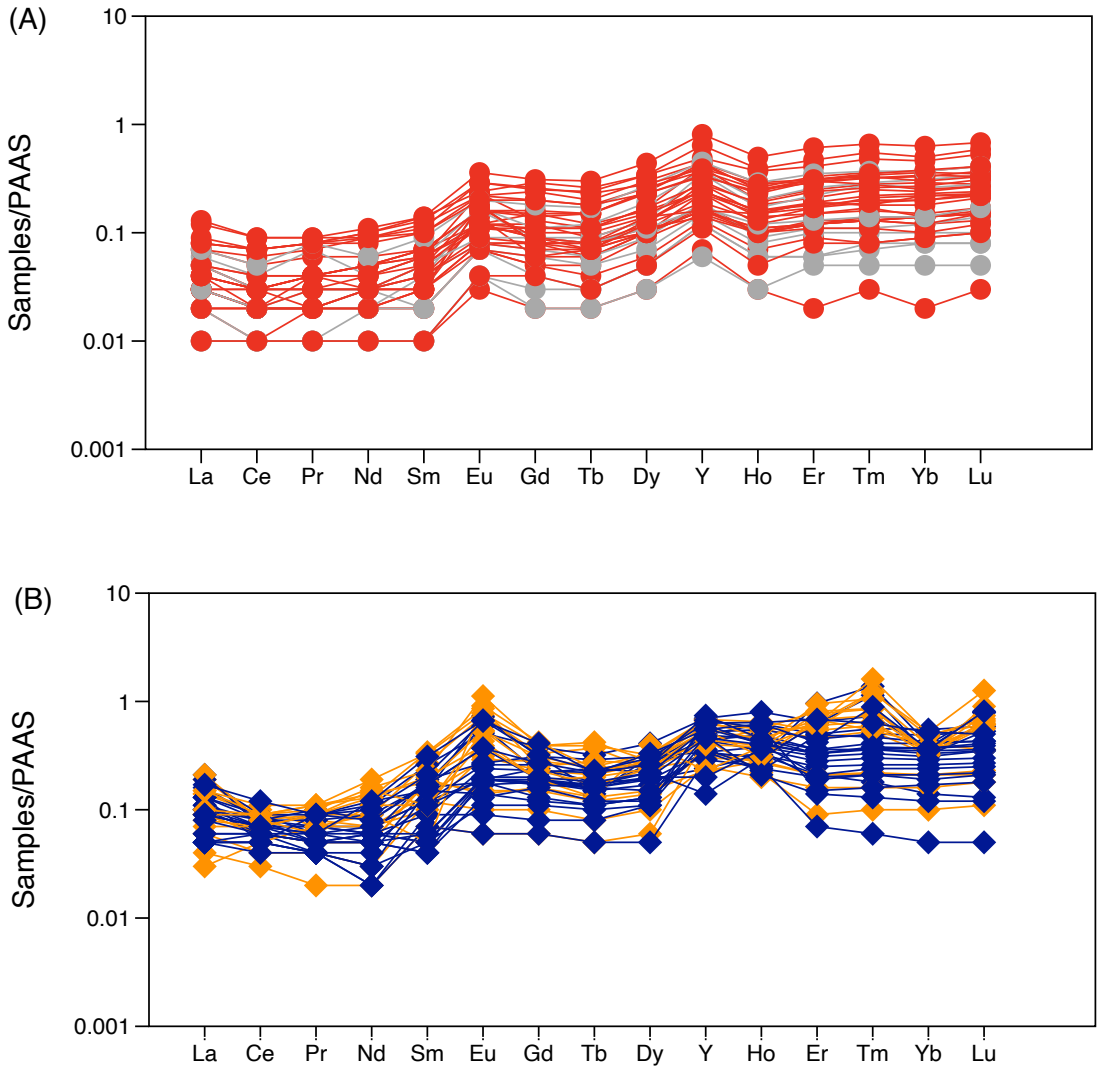

Figure 5.4: Shale-normalized (PAAS) REE patterns for the (A) Neoarchean BIFs – Nova Lima Group where the red circle indicates BIFs – Hematite and Magnetite and the gray circle denotes BIFs – Carbonate. (B) Paleoproterozoic BIFs -Itabira Group with blue and orange diamonds representing BIFs – Hematite and Magnetite and the gray circle BIFs – Carbonate.

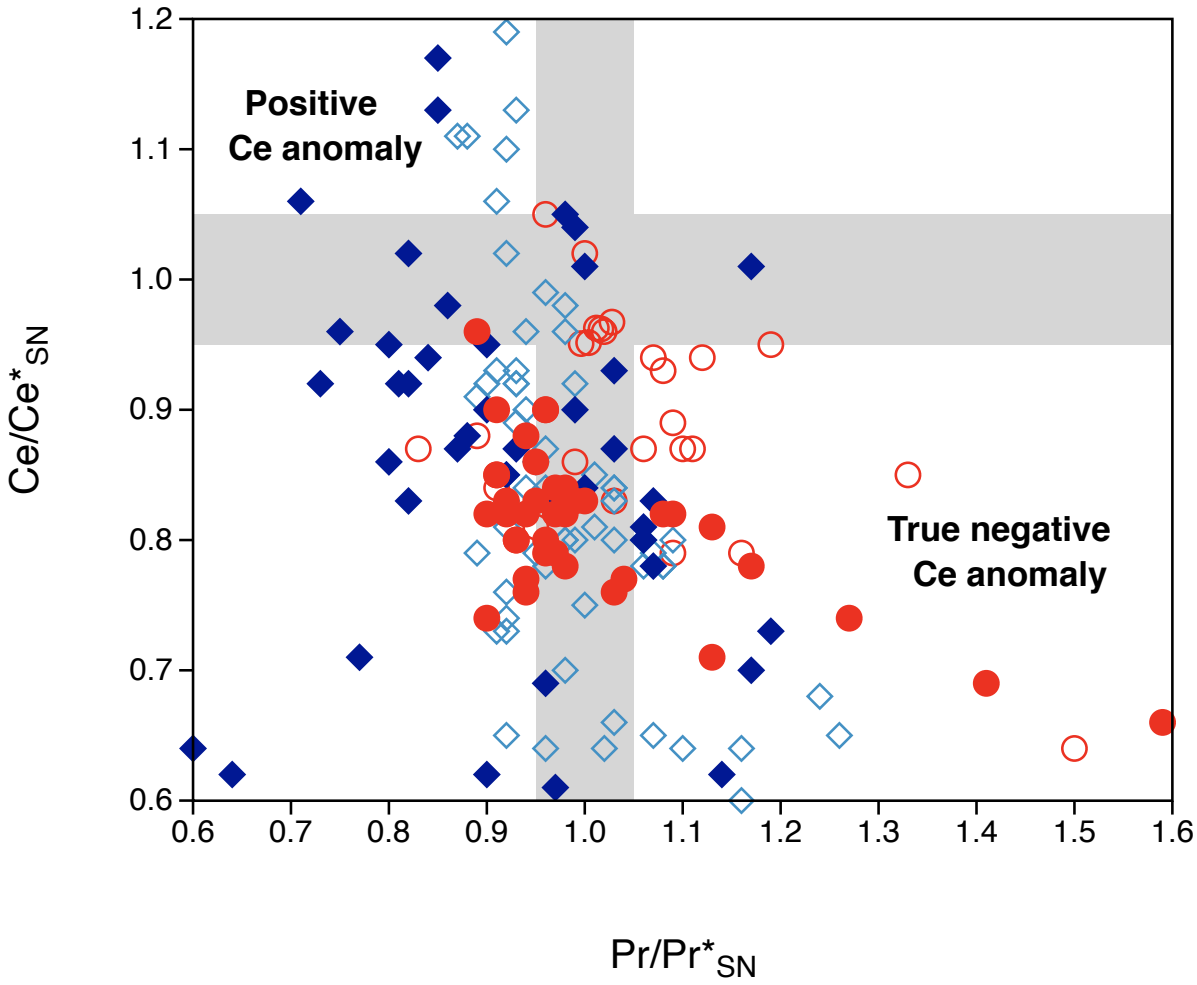

Figure 5.5: Crossplot identifying true negative Ce anomalies. True negative Ce anomalies are defined by Ce/Ce* ($Ce_{(SN)}/0.5Pr_{(SN)}$ + 0.5 $La_{(SN)}$) and ($Pr_{(SN)}$ /(0.5$Ce_{(SN)}$ + 0.5$Nd_{(SN)}$))), as explained by Bau and Dulski (1996) and Planavsky et al. (2010). Red filed circle indicates the Neoarchean BIFs – Nova Lima Group from this study and the red open circle are from previous studies (Bosco-Santos et al., 2020; Soares et al., 2018; Soares et al., 2017). Blue filed diamond represents Paleoproterozoic BIFs -Itabira Group from this study and the open diamond are from previous studies (Cabral et al., 2016; Mendes et al., 2017; Sampaio et al., 2018; Spier et al., 2007; Teixeira et al., 2017).

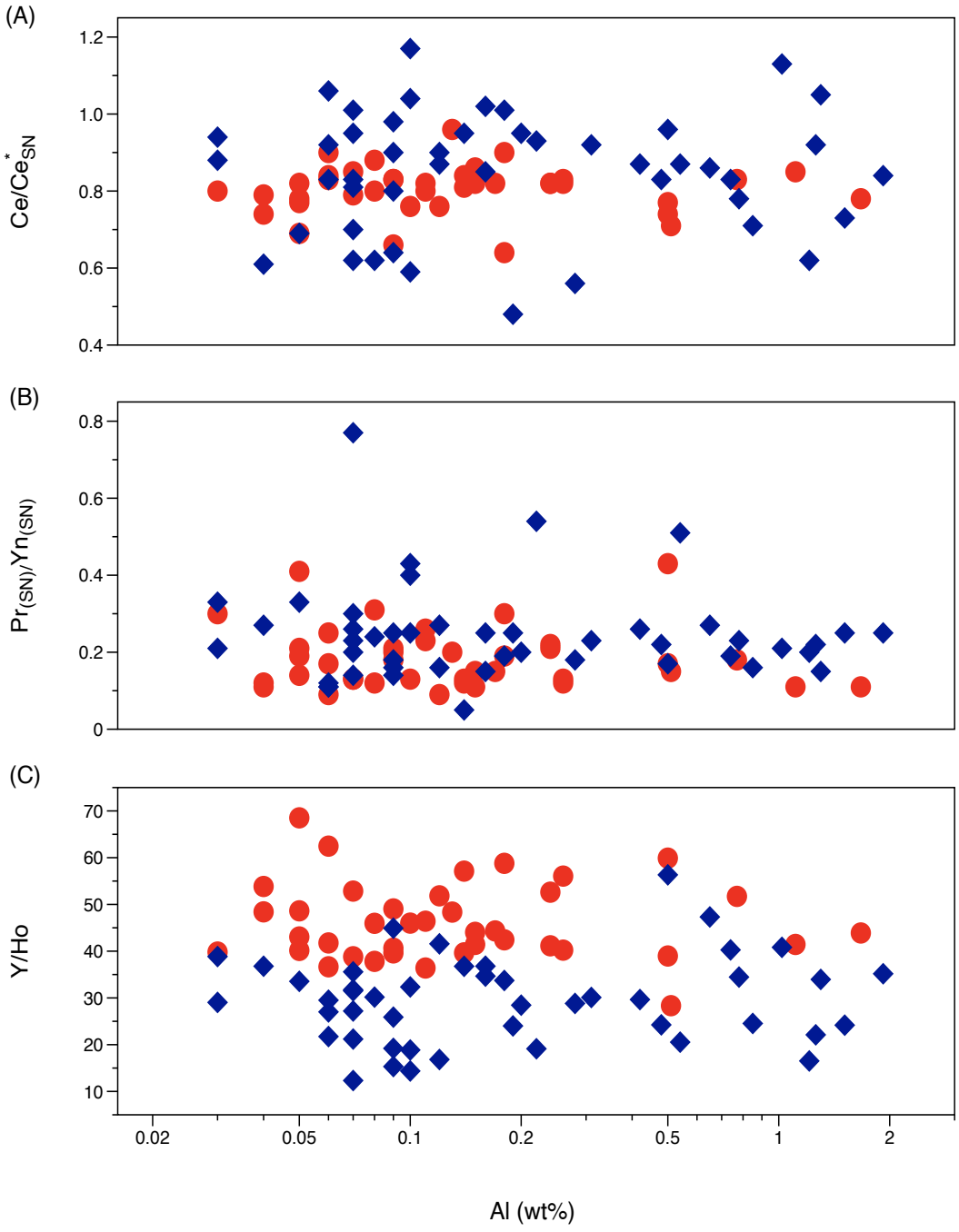

Figure 5.6: Cross-plots of REE+Y characteristics and Al (weight %) for Neorchean (red circle) and Paleoproterozoic (blue diamond) BIFs. (A) Ce anomalies (Ce_{SN}/(0.5(Pr_{SN} + La_{SN}) versus Al (wt %). (B) Light to heavy REE ratios (Pr_{SN}/Yb_{SN}) versus Al (wt %). (C) Y/Ho ratios versus Al (wt%). Variability in the REE+Y features does not resemble with degrees of detrital sediment input.

CHAPTER 6

Conclusion

The early evolution of life on Earth is closely linked with the geochemical history of the oceans. The evolution of oxygenic photosynthesis marks a crucial turning point in biology's evolutionary trajectory. Understanding the impacts of this remarkable innovation on the ocean-atmosphere system requires that we identify how biogeochemical cycles were structured before and after its inception. The biogeochemical iron (Fe) cycle has strongly influenced major cycles for carbon and other key biological elements throughout geologic time. Further, iron sulfide minerals may have provided energy and surfaces for the first pioneer organisms on Earth and even for the beginnings of life. Banded Iron Formations document the evolution of oxygenic photosynthesis and the associated changing redox state of the oceans. The distribution of bioavailable Fe drives primary productivity in today's oceans and is certain to have played a key role in the past.

This dissertation explores the wide range and complexity of Fe transformations in the environment and the co-occurring, often competing processes of Fe cycling in Earth's oceans and atmosphere from the Archean and Paleoproterozoic to the relatively recent geological history of the Cenozoic. As a consequence of this work, a variety of new data provide crucial insights into the precipitation, deposition, and diagenesis of Fe, along with the fidelity of signals recorded in Fe mineral archives. We are only beginning to appreciate the complexity of Fe transformations in the environment and their relationships to life—both cause and effect. Only through advances with geochemical proxies and models from these analogous studies spanning the geologic time scale will we understand the interwoven pathways of the Fe cycle and their relationships to the planetary co-evolution of life and global-scale climate.

APPENDIX -Table

Chapter 2 – data table

Site 658

Site 658	>43 µm	>43 µm	>43 µm	>43 µm	>43 µm	>43 µm	>43 µm	>43 µm
Age	FeT (wt%)	FeT/Al	Ti/Al	TOC (wt%)	Fe Na-ac(wt%)	Fe Dith (wt%)	Fe Ox (wt%)	CaCO3 (wt%)
3.84	0.95	0.68	0.06	0.73	0.03	0.21	0.11	75.92
8.71	0.99	0.63	0.07	0.8	0.03	0.27	0.14	54.42
20.89	2.24	0.6	0.07	0.83	0.07	0.54	0.29	60.6
26.98	1.78	0.58	0.07	0.8	0.05	0.4	0.22	63.8
33.07	1.72	0.6	0.07	0.7	0.04	0.36	0.19	60.84
39.16	1.28	0.72	0.09	0.77	0.05	0.41	0.22	61.6
45.25	1.94	0.57	0.07	0.91	0.07	0.58	0.31	70.12
51.34	1.37	0.49	0.06	0.81	0.03	0.27	0.14	54.24
57.43	2.44	0.63	0.07	0.68	0.07	0.6	0.32	41.43
63.52	3.16	0.58	0.07	0.7	0.07	0.55	0.3	61.52
69.61	1.91	0.51	0.06	0.64	0.04	0.31	0.17	69.68
75.7	1.55	0.47	0.05	0.47	0.04	0.29	0.16	68.31
81.79	2.29	0.64	0.05	0.39	0.04	0.3	0.16	70.59
87.88	1.41	0.54	0.06	0.52	0.03	0.23	0.12	77.45
93.97	1.17	0.63	0.06	0.5	0.03	0.22	0.12	62.02
100.06	2.03	0.47	0.05	0.36	0.06	0.49	0.26	56.86
112.24	1.26	0.53	0.06	0.73	0.03	0.23	0.12	54.16
118.33	1.56	0.57	0.06	0.6	0.04	0.35	0.19	62.97

Site 658	43 µm<x>20µm	43 µm<x>20µm	43 µm<x>20µm	43 µm<x>20µm	43 µm<x>20µm	43 µm<x>20µm	43 µm<x>20µm	43 µm<x>20µm
Age	FeT (wt%)	FeT/Al	Ti/Al	TOC (wt%)	Fe Na-ac (wt%)	Fe Dith (wt%)	Fe Ox (wt%)	CaCO3 (wt%)
3.84	0.88	0.68	0.06	0.7	0.03	0.21	0.14	76.15
8.71	1.08	0.63	0.06	0.78	0.03	0.45	0.27	54.56
20.89	2.25	0.6	0.07	0.81	0.03	0.86	0.57	60.76
26.98	1.8	0.58	0.07	0.72	0.03	0.67	0.4	64.46
33.07	1.74	0.6	0.08	0.63	0.03	0.57	0.37	61.43
39.16	1.26	0.72	0.09	0.71	0.03	0.6	0.4	62.11
45.25	1.92	0.57	0.06	0.91	0.03	0.59	0.57	70.08
51.34	1.39	0.49	0.06	0.82	0.03	0.38	0.26	54.13
57.43	2.42	0.63	0.06	0.69	0.03	0.8	0.58	41.37
63.52	3.16	0.58	0.07	0.7	0.03	0.81	0.55	61.55
69.61	1.9	0.51	0.06	0.61	0.03	0.45	0.3	69.93
75.7	1.54	0.47	0.05	0.5	0.03	0.48	0.29	68.08
81.79	2.33	0.64	0.05	0.3	0.03	0.44	0.3	71.37
87.88	1.4	0.54	0.06	0.38	0.03	0.38	0.23	78.65
93.97	1.16	0.63	0.06	0.44	0.03	0.36	0.21	62.5
100.06	2.02	0.47	0.05	0.37	0.03	0.63	0.48	56.42
112.24	1.24	0.53	0.06	0.73	0.03	0.37	0.22	54.87
118.33	1.56	0.57	0.06	0.57	0.03	0.5	0.34	63.91

Site 658	<20 µm	<20 µm	<20 µm	<20 µm	<20 µm	<20 µm	<20 µm	<20 µm
Age	FeT (wt%)	FeT/Al	Ti/Al	TOC (wt%)	Fe Na-ac (wt%)	Fe Dith (wt%)	Fe Ox (wt%)	CaCO3 (wt%)
3.84	0.89	0.68	0.06	0.71	0.02	0.23	0.13	76.04
8.71	1.09	0.63	0.06	0.77	0.03	0.27	0.14	54.63
20.89	2.28	0.6	0.07	0.81	0.07	0.58	0.3	60.71
26.98	1.83	0.58	0.07	0.73	0.05	0.41	0.21	64.41
33.07	1.74	0.6	0.07	0.65	0.05	0.37	0.19	61.23
39.16	1.28	0.72	0.09	0.72	0.05	0.41	0.22	61.97
45.25	2.07	0.57	0.07	0.94	0.07	0.58	0.3	69.88
51.34	1.39	0.49	0.06	0.81	0.03	0.27	0.14	54.22
57.43	2.41	0.63	0.07	0.69	0.07	0.59	0.31	41.43
63.52	3.21	0.58	0.07	0.75	0.07	0.55	0.29	61.15
69.61	1.9	0.51	0.05	0.63	0.04	0.31	0.16	69.76
75.7	1.56	0.47	0.05	0.43	0.04	0.29	0.15	68.68
81.79	2.33	0.64	0.06	0.32	0.04	0.3	0.16	71.18
87.88	1.47	0.54	0.06	0.38	0.03	0.23	0.12	78.61
93.97	1.18	0.63	0.06	0.42	0.03	0.22	0.11	62.7
100.06	1.77	0.47	0.05	0.33	0.06	0.48	0.25	56.38
112.24	1.24	0.53	0.06	0.73	0.03	0.22	0.12	54.46
118.33	1.58	0.57	0.06	0.57	0.04	0.35	0.18	63.8

Site 659

Site 659	>43 µm	>43 µm	>43 µm	>43 µm	>43 µm	>43 µm	>43 µm	>43 µm
Age	FeT (wt%)	FeT/Al	Ti/Al	TOC (wt%)	Fe Na-ac(wt%)	Fe Dith (wt%)	Fe Ox (wt%)	CaCO3 (wt%)
11.42	2.14	0.51	0.05	0.17	0.04	0.27	0.17	58.27
14.19	1.96	0.48	0.05	0.19	0.05	0.35	0.22	70.38
15.29	2.05	0.42	0.05	0.2	0.05	0.32	0.2	67.52
18.43	2.65	0.54	0.05	0.18	0.05	0.33	0.21	44.92
21.24	2.16	0.37	0.05	0.17	0.04	0.25	0.15	58.62
23.12	1.87	0.4	0.05	0.18	0.02	0.15	0.09	75.78
26.7	2.44	0.48	0.04	0.15	0.05	0.34	0.21	64.77
29.67	2.64	0.42	0.06	0.14	0.04	0.26	0.16	69.62
33.77	1.61	0.59	0.06	0.1	0.02	0.14	0.09	57.47
41.28	1.01	0.65	0.06	0.13	0.02	0.14	0.09	52.83
45.76	1.8	0.56	0.06	0.15	0.05	0.32	0.2	51.52
47.76	1.87	0.5	0.06	0.18	0.04	0.26	0.16	53.76
51.32	1.4	0.59	0.05	0.14	0.04	0.29	0.18	55.97
60.36	2.3	0.38	0.06	0.15	0.02	0.17	0.11	50.93
67.32	1.79	0.59	0.05	0.13	0.03	0.24	0.15	38.64
73.6	1.05	0.57	0.05	0.16	0.03	0.19	0.12	69.77
77	1.86	0.43	0.07	0.13	0.02	0.14	0.08	75.12
83.02	1.64	0.51	0.06	0.1	0.04	0.26	0.16	58.27
86	1.05	0.52	0.07	0.14	0.02	0.17	0.11	70.38
98.02	1.25	0.51	0.06	0.15	0.02	0.17	0.11	67.52
100.53	1.98	0.49	0.07	0.13	0.02	0.16	0.1	44.92
103.39	1.76	0.64	0.06	0.15	0.02	0.17	0.1	58.62

Site 659	43 µm<x>20µm	43 µm<x>20µm	43 µm<x>20µm	43 µm<x>20µm	43 µm<x>20µm	43 µm<x>20µm	43 µm<x>20µm	43 µm<x>20µm
Age	FeT (wt%)	FeT/Al	Ti/Al	TOC (wt%)	Fe Na-ac (wt%)	Fe Dith (wt%)	Fe Ox (wt%)	CaCO3 (wt%)
11.42	1.52	0.51	0.06	0.16	0.03	0.21	0.01	69.62
14.19	1.78	0.49	0.06	0.17	0.05	0.34	0.21	57.47
15.29	1.62	0.4	0.05	0.19	0.05	0.34	0.21	52.83
18.43	2.36	0.55	0.06	0.17	0.07	0.5	0.31	51.52
21.24	1.79	0.45	0.06	0.16	0.04	0.27	0.17	53.76
23.12	1.67	0.43	0.06	0.17	0.03	0.21	0.13	55.97
26.7	2.13	0.51	0.06	0.14	0.04	0.26	0.16	50.93
29.67	2.38	0.46	0.06	0.13	0.04	0.26	0.16	38.64
33.77	0.99	0.68	0.07	0.09	0.02	0.15	0.09	69.77
41.28	0.91	0.65	0.06	0.12	0.02	0.13	0.08	75.12
45.76	1.64	0.51	0.06	0.14	0.04	0.26	0.16	58.27
47.76	1.05	0.52	0.07	0.18	0.02	0.16	0.1	70.38
51.32	1.25	0.51	0.06	0.14	0.02	0.17	0.1	67.52
60.36	1.98	0.49	0.07	0.14	0.02	0.17	0.1	44.92
67.32	1.76	0.64	0.06	0.13	0.03	0.17	0.11	58.62
73.6	0.73	0.55	0.06	0.12	0.02	0.14	0.09	75.78
77	0.94	0.42	0.06	0.12	0.02	0.12	0.08	64.77
83.02	1.64	0.51	0.06	0.09	0.04	0.26	0.16	69.62
86	1.05	0.52	0.07	0.14	0.02	0.16	0.1	57.47
98.02	1.25	0.51	0.06	0.14	0.02	0.17	0.1	52.83
100.53	1.98	0.49	0.07	0.12	0.02	0.17	0.1	51.52
103.39	1.76	0.64	0.06	0.15	0.03	0.17	0.11	53.76

Site 659	<20 µm	<20 µm	<20 µm	<20 µm	<20 µm	<20 µm	<20 µm	<20 µm
Age	FeT (wt%)	FeT/Al	Ti/Al	TOC (wt%)	Fe Na-ac (wt%)	Fe Dith (wt%)	Fe Ox (wt%)	CaCO3 (wt%)
11.42	2.5	0.5	0.06	0.17	0.04	0.31	0.19	55.97
14.19	2.63	0.52	0.06	0.17	0.05	0.32	0.19	50.93
15.29	2.03	0.48	0.06	0.17	0.06	0.45	0.28	38.64
18.43	2.38	0.55	0.06	0.18	0.07	0.49	0.3	69.77
21.24	1.84	0.45	0.06	0.16	0.05	0.33	0.2	75.12
23.12	1.81	0.41	0.06	0.17	0.04	0.3	0.18	58.27
26.7	2.17	0.46	0.06	0.14	0.04	0.31	0.19	70.38
29.67	2.14	0.46	0.06	0.14	0.04	0.25	0.15	67.52
33.77	1.01	0.65	0.08	0.07	0.02	0.14	0.08	44.92
41.28	0.97	0.67	0.06	0.09	0.02	0.13	0.08	58.62
45.76	1.73	0.59	0.07	0.15	0.04	0.25	0.15	75.78
47.76	1.19	0.57	0.08	0.16	0.02	0.14	0.09	64.77
51.32	1.36	0.52	0.06	0.13	0.03	0.19	0.11	69.62
60.36	1.92	0.45	0.07	0.15	0.02	0.15	0.09	57.47
67.32	2.01	0.69	0.07	0.13	0.05	0.33	0.2	52.83
73.6	0.79	0.58	0.06	0.07	0.02	0.15	0.09	51.52
77	1.05	0.49	0.08	0.09	0.02	0.15	0.09	53.76
83.02	1.73	0.53	0.07	0.07	0.04	0.25	0.15	55.97
86	1.19	0.57	0.08	0.14	0.02	0.14	0.09	50.93
98.02	1.36	0.52	0.06	0.15	0.03	0.19	0.11	38.64
100.53	1.92	0.45	0.07	0.12	0.02	0.15	0.09	69.77
103.39	2.01	0.69	0.07	0.15	0.05	0.33	0.2	75.12

Site 1062

Site 1062	>43 µm	>43 µm	>43 µm	>43 µm	>43 µm	>43 µm	>43 µm	>43 µm
Age	FeT (wt%)	FeT/Al	Ti/Al	TOC (wt%)	Fe Na-ac(wt%)	Fe Dith (wt%)	Fe Ox (wt%)	CaCO3 (wt%)
15.9	2.65	0.51	0.07	0.46	0.02	0.22	0.14	38.4
17.19	3.09	0.52	0.07	0.49	0.02	0.27	0.17	28.12
18.24	2.91	0.56	0.07	0.61	0.02	0.22	0.14	15.79
20.37	4.19	0.46	0.07	0.49	0.03	0.36	0.23	5.2
21.11	3.34	0.58	0.06	0.51	0.02	0.26	0.17	9.68
26.53	4.23	0.6	0.06	0.65	0.03	0.39	0.25	6.09
34.34	4.26	0.58	0.06	0.6	0.03	0.32	0.2	9.41
36.85	3.93	0.52	0.06	0.4	0.03	0.39	0.25	16.08
40.73	3.89	0.53	0.06	0.48	0.03	0.38	0.24	13.93
42.41	3.62	0.61	0.07	0.34	0.03	0.38	0.25	19.03
43.39	2.98	0.59	0.07	0.45	0.02	0.2	0.13	15.92
45.66	5.27	0.42	0.08	0.6	0.03	0.4	0.25	11.34
47.5	3.64	0.58	0.07	0.55	0.02	0.3	0.19	14.06
49.18	4.13	0.53	0.07	0.5	0.03	0.37	0.23	21.25
50.32	2.9	0.48	0.07	0.24	0.01	0.17	0.11	24.51
54.66	5.14	0.43	0.07	0.29	0.03	0.42	0.27	12.15
57.64	3.1	0.59	0.05	0.37	0.02	0.2	0.13	16.63
60.21	4.35	0.41	0.05	0.25	0.02	0.29	0.19	22.4
62.21	3.06	0.52	0.06	0.41	0.01	0.16	0.1	6.95
65.34	3.35	0.61	0.06	0.41	0.02	0.27	0.17	3.07
67.73	3.32	0.42	0.07	0.43	0.02	0.19	0.12	5.79
69.01	4.21	0.54	0.07	0.42	0.02	0.22	0.14	13.5
70.15	4.18	0.56	0.07	0.02	0.02	0.28	0.18	13.73
73.43	4.01	0.43	0.08	0.35	0.01	0.18	0.12	41.78
76.61	3.96	0.58	0.07	0.58	0.01	0.18	0.12	28.11
79.77	3.97	0.52	0.07	0.41	0.02	0.2	0.13	15.78
82.76	3.62	0.6	0.06	0.4	0.02	0.19	0.12	5.19
85.76	5.44	0.6	0.05	0.42	0.03	0.34	0.22	9.67
88.25	4.12	0.5	0.05	0.24	0.01	0.18	0.12	6.08
94.92	4.64	0.54	0.06	0.35	0.02	0.28	0.18	9.4
100.28	3.87	0.62	0.06	0.16	0.03	0.38	0.24	16.07
104.09	4.16	0.65	0.07	0.58	0.01	0.15	0.09	13.92
109.69	3.53	0.61	0.07	0.25	0.02	0.2	0.13	19.02

Site 1062	43 µm<x>20µm	43 µm<x>20µm	43 µm<x>20µm	43 µm<x>20µm	43 µm<x>20µm	43 µm<x>20µm	43 µm<x>20µm	43 µm<x>20µm
Age	FeT (wt%)	FeT/Al	Ti/Al	TOC (wt%)	Fe Na-ac (wt%)	Fe Dith (wt%)	Fe Ox (wt%)	CaCO3 (wt%)
15.9	2.57	0.5	0.06	0.33	0.02	0.24	0.16	41.17
17.19	3.48	0.5	0.06	0.35	0.03	0.32	0.21	32.06
18.24	3.23	0.57	0.05	0.63	0.01	0.14	0.09	19.87
20.37	4.15	0.38	0.05	0.53	0.02	0.23	0.15	8.54
21.11	3.68	0.56	0.06	0.43	0.01	0.12	0.08	13.7
26.53	4.51	0.69	0.05	0.53	0.01	0.13	0.08	10.19
34.34	4.47	0.48	0.05	0.51	0.03	0.31	0.2	13.54
36.85	3.73	0.57	0.07	0.3	0.01	0.14	0.09	20.68
40.73	4.11	0.58	0.05	0.22	0.01	0.13	0.08	18.11
42.41	4.25	0.58	0.05	0.59	0.01	0.16	0.1	23.51
43.39	4.15	0.61	0.05	0.46	0.01	0.17	0.11	20.14
45.66	4.53	0.43	0.05	0.71	0.02	0.28	0.18	16
47.5	3.89	0.6	0.05	0.46	0.01	0.15	0.09	16.79
49.18	4.5	0.46	0.05	0.45	0.02	0.24	0.15	24.31
50.32	3.23	0.55	0.05	0.35	0.01	0.14	0.09	27.4
54.66	4.5	0.43	0.05	0.21	0.02	0.29	0.19	13.65
57.64	3.57	0.58	0.05	0.25	0.01	0.16	0.1	19.52
60.21	4.65	0.41	0.05	0.24	0.02	0.26	0.16	26.49
62.21	3.08	0.57	0.05	0.42	0.01	0.1	0.07	10.58
65.34	3.68	0.63	0.04	0.32	0.01	0.16	0.1	6.54
67.73	3.6	0.56	0.05	0.35	0.02	0.25	0.16	9.67
69.01	3.8	0.42	0.05	0.37	0.02	0.3	0.19	16.39
70.15	4.14	0.66	0.05	0.32	0.01	0.11	0.07	14.87
73.43	4	0.39	0.05	0.57	0.01	0.13	0.09	42.4
76.61	4.34	0.35	0.05	0.52	0.01	0.1	0.07	31.55
79.77	3.72	0.63	0.05	0.32	0.01	0.16	0.1	20.2
82.76	3.86	0.56	0.05	0.35	0.01	0.16	0.1	8.54
85.76	4.98	0.48	0.05	0.37	0.04	0.45	0.29	13
88.25	4.07	0.51	0.05	0.34	0.01	0.13	0.17	9.94
94.92	4.76	0.64	0.07	0.52	0.02	0.27	0.12	13.75
100.28	3.89	0.62	0.05	0.1	0.01	0.18	0.07	18.16
104.09	3.96	0.65	0.06	0.54	0.01	0.12	0.06	17.25
109.69	3.48	0.64	0.07	0.32	0.01	0.09	0.07	19.64

Site 1062	<20 µm	<20 µm	<20 µm	<20 µm	<20 µm	<20 µm	<20 µm	<20 µm
Age	FeT (wt%)	FeT/Al	Ti/Al	TOC (wt%)	Fe Na-ac (wt%)	Fe Dith (wt%)	Fe Ox (wt%)	CaCO3 (wt%)
15.9	2.63	0.53	0.06	0.33	0.02	0.24	0.15	38.06
17.19	3.37	0.51	0.06	0.47	0.03	0.33	0.21	28.41
18.24	3.89	0.58	0.05	0.49	0.02	0.19	0.12	15.09
20.37	4.04	0.5	0.07	0.4	0.02	0.19	0.12	4.59
21.11	3.25	0.55	0.07	0.48	0.02	0.2	0.13	9.75
26.53	4.22	0.7	0.06	0.49	0.01	0.16	0.1	5.53
34.34	3.65	0.46	0.06	0.5	0.02	0.28	0.18	9.09
36.85	3.26	0.56	0.07	0.55	0.01	0.15	0.09	17.21
40.73	3.39	0.58	0.05	0.5	0.01	0.15	0.1	14.76
42.41	3.07	0.57	0.06	0.54	0.01	0.12	0.08	19.43
43.39	4.34	0.58	0.06	0.51	0.01	0.18	0.12	16.23
45.66	4.69	0.55	0.06	0.56	0.02	0.21	0.14	10.81
47.5	3.56	0.59	0.06	0.33	0.01	0.13	0.09	13.07
49.18	4.08	0.47	0.05	0.37	0.01	0.14	0.09	20.65
50.32	2.6	0.55	0.06	0.35	0.01	0.17	0.11	24.8
54.66	4.86	0.41	0.06	0.18	0.02	0.21	0.14	11.75
57.64	2.58	0.56	0.05	0.35	0.01	0.17	0.11	16.83
60.21	4.44	0.46	0.05	0.49	0.02	0.2	0.13	23.76
62.21	3.51	0.55	0.05	0.44	0.01	0.1	0.06	7.06
65.34	3.72	0.64	0.05	0.42	0.01	0.1	0.07	3.35
67.73	3.46	0.57	0.05	0.47	0.01	0.17	0.11	6.21
69.01	4.09	0.45	0.06	0.35	0.02	0.21	0.14	13.23
70.15	4.47	0.71	0.05	0.08	0.02	0.21	0.13	11.81
73.43	3.79	0.42	0.07	0.41	0.02	0.26	0.17	41.23
76.61	4.13	0.39	0.05	0.53	0.02	0.21	0.13	27.84
79.77	4.18	0.67	0.05	0.4	0.02	0.23	0.15	15.68
82.76	3.96	0.57	0.05	0.4	0.01	0.09	0.06	5.39
85.76	4.75	0.46	0.04	0.46	0.02	0.27	0.17	9.82
88.25	4.12	0.51	0.05	0.25	0.01	0.13	0.09	6.46
94.92	4.34	0.59	0.05	0.4	0.02	0.26	0.16	9.68
100.28	3.86	0.65	0.06	0.08	0.02	0.23	0.15	15.85
104.09	3.98	0.67	0.05	0.53	0.01	0.1	0.07	13.73
109.69	3.42	0.65	0.06	0.28	0.01	0.1	0.07	18.71

Site 1063

Site 1063	43 µm<x>20µm	43 µm<x>20µm	43 µm<x>20µm	43 µm<x>20µm	43 µm<x>20µm	43 µm<x>20µm	43 µm<x>20µm	43 µm<x>20µm
Age	FeT (wt%)	FeT/Al	Ti/Al	TOC (wt%)	Fe Na-ac (wt%)	Fe Dith (wt%)	Fe Ox (wt%)	CaCO3 (wt%)
6.16	3.19	0.53	0.05	0.33	0.02	0.33	0.22	31.35
6.88	3.87	0.51	0.05	0.23	0.03	0.39	0.25	28.21
7.23	3.15	0.57	0.06	0.13	0.02	0.3	0.2	31.47
8.67	3.19	0.49	0.07	0.12	0.02	0.38	0.25	28.92
9.23	3.79	0.55	0.05	0.14	0.03	0.41	0.27	34.44
9.92	3.85	0.57	0.05	0.13	0.02	0.3	0.2	35.01
13.13	3.16	0.54	0.05	0.13	0.03	0.41	0.27	30.34
14.26	4.59	0.61	0.05	0.12	0.03	0.42	0.27	15.37
15.45	4.69	0.56	0.05	0.07	0.03	0.43	0.28	10.54
16.12	4.22	0.48	0.05	0.14	0.03	0.44	0.29	9.8
19.18	4.47	0.51	0.04	0.06	0.03	0.48	0.31	9.92
20.93	4.66	0.48	0.04	0.03	0.02	0.37	0.24	11.07
22.39	4.6	0.53	0.05	0.03	0.03	0.44	0.28	14
26.48	4.05	0.48	0.05	0.13	0.03	0.44	0.29	12.23
28.11	4.15	0.5	0.04	0.07	0.03	0.45	0.29	10.85
29.73	4.02	0.54	0.05	0.06	0.02	0.38	0.25	11.38
31.36	4.64	0.66	0.05	0.13	0.03	0.52	0.34	11.92
32.98	4.05	0.64	0.04	0.38	0.03	0.41	0.27	6.44
34.61	4.55	0.67	0.06	0.35	0.03	0.47	0.3	4.93
36.23	4.17	0.65	0.04	0.22	0.03	0.42	0.27	5.61
37.86	4.69	0.44	0.03	0.42	0.03	0.4	0.26	6.09
39.48	5.57	0.71	0.05	0.45	0.03	0.48	0.31	0.22
44.36	4.85	0.72	0.06	0.29	0.03	0.51	0.33	6.11
45.98	4.26	0.51	0.06	0.28	0.03	0.4	0.26	1.96
47.61	3.93	0.56	0.06	0.28	0.03	0.39	0.25	8.35
49.23	4.2	0.57	0.06	0.3	0.03	0.41	0.27	12.23
50.85	4.68	0.57	0.05	0.24	0.02	0.35	0.23	10.36
52.48	4.33	0.54	0.05	0.12	0.02	0.35	0.23	13.87
55.73	3.46	0.52	0.05	0.07	0.02	0.3	0.19	28.74
57.35	3.77	0.55	0.05	0.17	0.02	0.28	0.18	8.92
58.98	3.23	0.62	0.07	0.02	0.02	0.36	0.23	18.59
60.6	3.43	0.54	0.07	0.25	0.02	0.32	0.2	13.71
63.85	2.74	0.69	0.05	0.02	0.02	0.29	0.19	22.04
65.48	2.85	0.64	0.04	0.13	0.02	0.24	0.16	19.22
67.1	3.11	0.65	0.04	0.06	0.02	0.27	0.17	37.75
68.1	3.85	0.62	0.07	0.32	0.02	0.27	0.17	20.18
68.73	3.92	0.55	0.04	0.04	0.02	0.29	0.19	20.02
70.35	4.02	0.54	0.05	0.3	0.02	0.36	0.23	11.66
71.98	4.19	0.49	0.04	0.26	0.02	0.32	0.21	3.09
73.6	4.75	0.51	0.04	0.13	0.02	0.38	0.25	6.71
75.23	3.97	0.59	0.07	0.02	0.02	0.34	0.22	3.35
78.48	3.43	0.45	0.06	0.36	0.02	0.31	0.2	29.55
79.85	4.26	0.6	0.07	0.14	0.03	0.42	0.27	8.5
80.1	2.7	0.5	0.06	0.1	0.02	0.27	0.17	2.99
81.73	2.99	0.44	0.05	0.09	0.01	0.2	0.13	32.44
83.35	3.26	0.58	0.08	0.07	0.02	0.25	0.16	35.68
86.85	3.84	0.51	0.04	0.25	0.02	0.26	0.17	33.62
90.12	3.02	0.57	0.07	0.08	0.02	0.25	0.16	9.35
92.26	2.44	0.62	0.08	0.02	0.01	0.18	0.12	32.88
96.13	2.7	0.55	0.06	0.17	0.01	0.18	0.12	39.02
100.35	2.56	0.6	0.04	0.06	0.01	0.22	0.15	45.46
103.65	3.36	0.63	0.06	0.07	0.02	0.25	0.16	34.76

Site 1063	43 µm<x>20µm	43 µm<x>20µm	43 µm<x>20µm	43 µm<x>20µm	43 µm<x>20µm	43 µm<x>20µm	43 µm<x>20µm	43 µm<x>20µm
Age	FeT (wt%)	FeT/Al	Ti/Al	TOC (wt%)	Fe Na-ac (wt%)	Fe Dith (wt%)	Fe Ox (wt%)	CaCO3 (wt%)
6.16	3.19	0.53	0.05	0.33	0.02	0.33	0.22	31.35
6.88	3.87	0.51	0.05	0.23	0.03	0.39	0.25	28.21
7.23	3.15	0.57	0.06	0.13	0.02	0.3	0.2	31.47
8.67	3.19	0.49	0.07	0.12	0.02	0.38	0.25	28.92
9.23	3.79	0.55	0.05	0.14	0.03	0.41	0.27	34.44
9.92	3.85	0.57	0.05	0.13	0.02	0.3	0.2	35.01
13.13	3.16	0.54	0.05	0.13	0.03	0.41	0.27	30.34
14.26	4.59	0.61	0.05	0.12	0.03	0.42	0.27	15.37
15.45	4.69	0.56	0.05	0.07	0.03	0.43	0.28	10.54
16.12	4.22	0.48	0.05	0.14	0.03	0.44	0.29	9.8
19.18	4.47	0.51	0.04	0.06	0.03	0.48	0.31	9.92
20.93	4.66	0.48	0.04	0.03	0.02	0.37	0.24	11.07
22.39	4.6	0.53	0.05	0.03	0.03	0.44	0.28	14
26.48	4.05	0.48	0.05	0.13	0.03	0.44	0.29	12.23
28.11	4.15	0.5	0.04	0.07	0.03	0.45	0.29	10.85
29.73	4.02	0.54	0.05	0.06	0.02	0.38	0.25	11.38
31.36	4.64	0.66	0.05	0.13	0.03	0.52	0.34	11.92
32.98	4.05	0.64	0.04	0.38	0.03	0.41	0.27	6.44
34.61	4.55	0.67	0.06	0.35	0.03	0.47	0.3	4.93
36.23	4.17	0.65	0.04	0.22	0.03	0.42	0.27	5.61
37.86	4.69	0.44	0.03	0.42	0.03	0.4	0.26	6.09
39.48	5.57	0.71	0.05	0.45	0.03	0.48	0.31	0.22
44.36	4.85	0.72	0.06	0.29	0.03	0.51	0.33	6.11
45.98	4.26	0.51	0.06	0.28	0.03	0.4	0.26	1.96
47.61	3.93	0.56	0.06	0.28	0.03	0.39	0.25	8.35
49.23	4.2	0.57	0.06	0.3	0.03	0.41	0.27	12.23
50.85	4.68	0.57	0.05	0.24	0.02	0.35	0.23	10.36
52.48	4.33	0.54	0.05	0.12	0.02	0.35	0.23	13.87
55.73	3.46	0.52	0.05	0.07	0.02	0.3	0.19	28.74
57.35	3.77	0.55	0.05	0.17	0.02	0.28	0.18	8.92
58.98	3.23	0.62	0.07	0.02	0.02	0.36	0.23	18.59
60.6	3.43	0.54	0.07	0.25	0.02	0.32	0.2	13.71
63.85	2.74	0.69	0.05	0.02	0.02	0.29	0.19	22.04
65.48	2.85	0.64	0.04	0.13	0.02	0.24	0.16	19.22
67.1	3.11	0.65	0.04	0.06	0.02	0.27	0.17	37.75
68.1	3.85	0.62	0.07	0.32	0.02	0.27	0.17	20.18
68.73	3.92	0.55	0.04	0.04	0.02	0.29	0.19	20.02
70.35	4.02	0.54	0.05	0.3	0.02	0.36	0.23	11.66
71.98	4.19	0.49	0.04	0.26	0.02	0.32	0.21	3.09
73.6	4.75	0.51	0.04	0.13	0.02	0.38	0.25	6.71
75.23	3.97	0.59	0.07	0.02	0.02	0.34	0.22	3.35
78.48	3.43	0.45	0.06	0.36	0.02	0.31	0.2	29.55
79.85	4.26	0.6	0.07	0.14	0.03	0.42	0.27	8.5
80.1	2.7	0.5	0.06	0.1	0.02	0.27	0.17	2.99
81.73	2.99	0.44	0.05	0.09	0.01	0.2	0.13	32.44
83.35	3.26	0.58	0.08	0.07	0.02	0.25	0.16	35.68
86.85	3.84	0.51	0.04	0.25	0.02	0.26	0.17	33.62
90.12	3.02	0.57	0.07	0.08	0.02	0.25	0.16	9.35
92.26	2.44	0.62	0.08	0.02	0.01	0.18	0.12	32.88
96.13	2.7	0.55	0.06	0.17	0.01	0.18	0.12	39.02
100.35	2.56	0.6	0.04	0.06	0.01	0.22	0.15	45.46
103.65	3.36	0.63	0.06	0.07	0.02	0.25	0.16	34.76

Site 1063	<20 µm	<20 µm	<20 µm	<20 µm	<20 µm	<20 µm	<20 µm	<20 µm
Age	FeT (wt%)	FeT/Al	Ti/Al	TOC (wt%)	Fe Na-ac (wt%)	Fe Dith (wt%)	Fe Ox (wt%)	CaCO3 (wt%)
6.16	3.07	0.53	0.05	0.2	0.02	0.33	0.21	31.45
6.88	3.89	0.51	0.05	0.11	0.03	0.39	0.26	28.31
7.23	3.37	0.57	0.06	0.19	0.02	0.33	0.22	31.58
8.67	3.78	0.49	0.06	0.09	0.03	0.42	0.27	29.02
9.23	3.9	0.55	0.05	0.14	0.03	0.42	0.27	34.55
9.92	3.96	0.57	0.05	0.13	0.02	0.28	0.19	35.11
13.13	3.48	0.54	0.05	0.09	0.03	0.39	0.26	30.44
14.26	4.53	0.61	0.05	0.14	0.03	0.44	0.29	15.48
15.45	4.17	0.56	0.05	0.09	0.03	0.41	0.27	10.64
16.12	3.79	0.48	0.05	0.11	0.03	0.42	0.28	9.9
19.18	4.75	0.51	0.04	0.1	0.03	0.49	0.32	10.03
20.93	3.94	0.48	0.04	0.07	0.03	0.4	0.26	11.18
22.39	4.12	0.53	0.05	0.05	0.03	0.39	0.26	14.11
26.48	4.05	0.48	0.05	0.11	0.03	0.45	0.3	12.33
28.11	4.36	0.5	0.04	0.04	0.03	0.48	0.31	10.95
29.73	3.59	0.54	0.05	0.02	0.02	0.37	0.24	11.48
31.36	4.26	0.66	0.05	0.09	0.03	0.49	0.32	12.02
32.98	4.89	0.64	0.04	0.29	0.03	0.5	0.33	6.54
34.61	4.51	0.7	0.06	0.13	0.03	0.47	0.31	5.04
36.23	4.8	0.61	0.04	0.17	0.03	0.48	0.32	5.71
37.86	4.93	0.49	0.03	0.22	0.03	0.39	0.26	6.2
39.48	4.96	0.72	0.05	0.14	0.03	0.44	0.29	0.32
44.36	4.83	0.71	0.05	0.38	0.03	0.5	0.33	6.21
45.98	4.17	0.46	0.06	0.28	0.03	0.39	0.26	2.06
47.61	3.18	0.54	0.06	0.35	0.02	0.3	0.19	8.45
49.23	4.54	0.56	0.07	0.21	0.03	0.42	0.28	12.34
50.85	4.17	0.59	0.05	0.3	0.02	0.34	0.23	10.46
52.48	4.7	0.52	0.06	0.19	0.02	0.34	0.23	13.97
55.73	3.47	0.55	0.05	0.03	0.02	0.31	0.21	28.85
57.35	4.14	0.59	0.06	0.06	0.02	0.27	0.18	9.02
58.98	4.58	0.61	0.07	0.02	0.03	0.4	0.26	18.69
60.6	3.12	0.5	0.07	0.03	0.03	0.39	0.26	13.82
63.85	2.53	0.69	0.05	0.04	0.02	0.27	0.18	22.14
65.48	3.11	0.57	0.04	0.06	0.01	0.23	0.15	19.32
67.1	3.57	0.6	0.05	0.01	0.02	0.27	0.17	37.85
68.1	4.1	0.68	0.06	0.24	0.02	0.28	0.18	20.29
68.73	4.13	0.55	0.03	0.05	0.02	0.28	0.18	20.12
70.35	3.99	0.52	0.05	0.1	0.02	0.32	0.21	11.76
71.98	3.97	0.53	0.04	0.07	0.02	0.33	0.22	3.2
73.6	3.83	0.52	0.04	0.17	0.02	0.36	0.24	6.82
75.23	3.63	0.53	0.06	0.01	0.02	0.33	0.22	3.46
78.48	3.77	0.44	0.05	0.03	0.02	0.34	0.23	29.65
79.85	3.17	0.57	0.07	0.05	0.02	0.35	0.23	8.6
80.1	2.93	0.51	0.06	0.04	0.02	0.3	0.19	3.1
81.73	2.31	0.53	0.05	0.04	0.01	0.18	0.12	32.54
83.35	3.63	0.5	0.05	0	0.01	0.21	0.14	35.79
86.85	3.85	0.55	0.04	0.06	0.02	0.24	0.16	33.73
90.12	3.33	0.62	0.08	0.04	0.01	0.22	0.14	9.46
92.26	2.95	0.61	0.07	0.02	0.01	0.18	0.12	32.98
96.13	2.59	0.46	0.06	0.02	0.01	0.18	0.12	39.13
100.35	2.81	0.57	0.05	0.02	0.01	0.21	0.14	45.56
103.65	3.2	0.57	0.06	0.01	0.02	0.24	0.16	34.86

Chapter 3 – data table

Table 1. Site U1537 Fe data

U1537 (mbsf)	FeT (wt%)	Al l (wt%)	FeBio (wt%)	FeOx (wt%)	FeMag (wt%)	FeHCl (wt%)	DOP
1.5	2.45	4.02	0.04	0.14	0.20	0.60	0.22
8.5	2.93	4.73	0.06	0.25	0.39	0.72	0.11
18	3.01	5.47	0.04	0.16	0.32	0.69	0.20
27.5	2.59	4.18	0.04	0.10	0.15	0.68	0.29
37	2.33	3.24	0.04	0.08	0.19	0.58	0.41
46.5	2.69	4.41	0.04	0.05	0.12	0.55	0.41
56	2.88	4.88	0.04	0.07	0.20	0.64	0.43
65.5	3.69	5.77	0.05	0.13	0.24	0.87	0.37
75	2.43	3.8	0.05	0.07	0.12	0.58	0.42
84.5	2.88	5.24	0.05	0.07	0.17	0.70	0.41
94	4.54	8.73	0.04	0.16	0.33	0.85	0.39
103.5	4.32	7.58	0.04	0.09	0.19	0.88	0.24
132	3.89	6.38	0.04	0.07	0.15	0.90	0.25
160.5	3.98	7.51	0.03	0.12	0.22	0.86	0.11
192	4.01	7.04	0.05	0.16	0.30	0.85	0.26
217.5	4.24	6.42	0.05	0.16	0.24	0.81	0.22
247.8	3.66	6.43	0.04	0.12	0.20	0.80	0.14
262.2	3.94	7.58	0.03	0.13	0.18	0.66	0.25
294.9	2.97	5.7	0.04	0.08	0.06	0.44	0.25
323.7	2.86	5.11	0.03	0.09	0.08	0.57	0.26
352.4	2.09	3.94	0.04	0.07	0.07	0.49	0.02

Table 2: Site U1537 Sulfur data

U1537 (mbsf)	CRS (wt%)	AVS (wt%)	d 34S/ 32S (‰)
1.5	0.34	0	-50.53
8.5	0.17	0.002	-57.05
18	0.35	0	-56.38
27.5	0.55	0.005	-53.89
37	0.80	0.004	-50.52
46.5	0.78	0.005	-48.85
56	0.94	0	-43.99
65.5	1.02	0	-29.92
75	0.85	0.006	-10.08
84.5	0.98	0.008	-1.83
94	1.09	0	-22.63
103.5	0.55	0	-31.27
132	0.61	0.005	-33.21
160.5	0.22	0	-48.67
192	0.61	0.018	-33.21
217.5	0.47	0.017	-34.27
247.8	0.26	0.019	-48.13
262.2	0.44	0	-50.69
294.9	0.30	0.007	-47.52

323.7	0.40	0.002	-49.08
352.4	0.02	0	-38.16

Table 3: Site U1537 carbon data

U1537 (mbsf)	CaCO3 (wt%)	TOC (wt%)
1.5	0.91	0.72
8.5	0.92	0.54
18	0.31	0.45
27.5	0.32	0.41
37	0.31	0.31
46.5	0.35	0.42
56	0.35	0.26
65.5	0.57	0.33
75	0.76	0.42
84.5	0.84	0.15
94	0.57	0.43
103.5	0.53	0.15
132	0.72	0.27
160.5	0.27	0.22
192	0.24	0.29

217.5	0.45	0.27
247.8	0.45	0.24
262.2	0.35	0.19
294.9	0.35	0.27
323.7	0.34	0.16
352.4	0.35	0.19

Table 4: Site U1538 Fe data

U1538 (mbsf)	FeT (wt%)	Al l (wt%)	FeBio (wt%)	FeOx (wt%)	FeMag (wt%)	FeHCl (wt%)	DOP
5.9	2.52	4.27	0.04	0.08	0.14	0.28	0.13
14.8	4.86	7.36	0.06	0.27	0.45	0.83	0.10
23.3	3.58	6.75	0.04	0.12	0.29	0.95	0.22
32.8	3.1	5.74	0.04	0.15	0.20	0.63	0.30
42.3	3.1	5.08	0.05	0.20	0.19	0.74	0.33
51.8	3.46	6.78	0.04	0.14	0.21	0.62	0.47
61.3	2.51	4.74	0.05	0.08	0.16	0.95	0.41
70.8	3.81	7.78	0.03	0.15	0.18	0.92	0.39
80.3	3.02	6.29	0.06	0.14	0.21	0.74	0.39
89.8	3.14	5.32	0.05	0.14	0.23	0.85	0.36
99.1	3.14	5.82	0.04	0.07	0.17	0.55	0.37
108.8	4.17	7.19	0.04	0.12	0.29	0.71	0.30
120.2	2.33	3.43	0.05	0.10	0.09	0.63	0.28
127.7	2.5	4.24	0.05	0.10	0.15	0.62	0.43
137.1	3.14	5.71	0.06	0.08	0.25	0.94	0.31
146.6	3.46	6.53	0.04	0.14	0.20	0.83	0.26
155.9	3.98	8.47	0.06	0.14	0.15	0.88	0.20
165.8	3.7	6.98	0.05	0.14	0.26	0.81	0.29
175.3	3.84	7.38	0.05	0.10	0.20	0.81	0.29
184.6	3.14	6.16	0.06	0.09	0.22	0.59	0.13
194.3	3.35	6.21	0.05	0.08	0.10	0.62	0.37
203.7	3.07	6.27	0.05	0.08	0.15	0.63	0.37
208.8	4.18	7.74	0.05	0.07	0.11	0.56	0.22
222.7	3.77	7.25	0.05	0.14	0.19	0.79	0.31
241.6	2.99	5.25	0.05	0.11	0.10	0.77	0.40
260.6	3.15	5.94	0.06	0.16	0.21	0.69	0.26
279.6	3.39	5.38	0.09	0.47	0.25	1.23	0.27
300.6	3.19	5.15	0.05	0.12	0.14	0.67	0.32
330	2.76	4.52	0.06	0.20	0.32	0.75	0.20
356.9	3.14	5.61	0.05	0.19	0.35	1.02	0.25
383.9	4.23	7.98	0.06	0.14	0.36	1.06	0.17
413.9	4.58	8.98	0.05	0.15	0.36	0.86	0.19
445.7	3.46	6.29	0.05	0.10	0.16	0.77	0.21
474.5	2.34	4.42	0.04	0.05	0.08	0.52	0.24
501.8	2.69	5.6	0.04	0.07	0.08	0.82	0.32
530.6	2.58	4.96	0.04	0.05	0.10	0.54	0.36
586.5	2.79	5.58	0.04	0.03	0.10	0.62	0.38
613.6	2.94	5.76	0.04	0.03	0.08	0.60	0.63
643	3.46	7.06	0.04	0.05	0.08	0.72	0.13
670.8	3.74	6.93	0.06	0.06	0.13	0.86	0.16

Table 5: Site U1538 S data

U1538 (mbsf)	CRS (wt%)	AVS (wt%)	d 34S/ 32S (‰)
5.9	0.08	0.007	-49.80
14.8	0.18	b.d.	-50.54
23.3	0.54	0.001	-53.14
32.8	0.55	0.004	-51.16
42.3	0.72	0.005	-51.52
51.8	1.11	b.d.	-25.93
61.3	1.33	0.005	-42.00
70.8	1.18	0.007	31.13
80.3	0.93	0.002	-20.44
89.8	0.97	0.005	-17.68
99.1	0.65	0.007	-28.65
108.8	0.61	b.d.	-31.14
120.2	0.48	b.d.	-34.70
127.7	0.94	0.006	-34.16
137.1	0.83	0.004	-30.54
146.6	0.58	b.d.	-30.15
155.9	0.44	0.005	-27.05
165.8	0.65	0.008	-25.94
175.3	0.65	0.005	1.95

184.6	0.18	b.d.	-13.48
194.3	0.73	0.004	-40.05
203.7	0.75	0.007	-11.36
208.8	0.32	b.d.	-28.98
222.7	0.72	b.d.	-32.80
241.6	1.04	0.008	-44.76
260.6	0.49	b.d.	-39.83
279.6	0.91	b.d.	-2.37
300.6	0.63	0.009	-22.88
330	0.37	b.d.	-39.12
356.9	0.67	0.003	-20.10
383.9	0.44	b.d.	-30.92
413.9	0.40	b.d.	-36.91
445.7	0.41	0.009	-37.41
474.5	0.33	b.d.	-30.92
501.8	0.79	0.016	-23.56
530.6	0.61	0.012	-37.41
586.5	0.75	0.015	-23.56
613.6	2.05	0.01	-22.01
643	0.22	b.d.	-18.98
670.8	0.32	0.005	-23.37

Table 6: Site U 1538 C data

U1538 (mbsf)	CaCO3 (wt%)	TOC (wt%)
5.9	0.24	0.54
14.8	0.32	0.42
23.3	0.32	0.58
32.8	0.33	0.28
42.3	1.01	0.33
51.8	0.12	0.24
61.3	0.10	0.47
70.8	0.28	0.35
80.3	0.26	0.53
89.8	0.25	0.48
99.1	0.37	0.34
108.8	0.25	0.21
120.2	0.91	0.40
127.7	0.33	0.34
137.1	0.28	0.32
146.6	0.31	0.32
155.9	0.25	0.38
165.8	0.32	0.45
175.3	0.33	0.57

184.6	0.30	0.33
194.3	0.36	0.25
203.7	3.02	0.65
208.8	0.33	0.51
222.7	0.37	0.21
241.6	0.38	0.43
260.6	0.35	0.32
279.6	0.41	0.31
300.6	0.56	0.33
330	0.13	0.23
356.9	0.42	0.32
383.9	0.36	0.24
413.9	0.24	0.16
445.7	0.46	0.18
474.5	0.76	0.21
501.8	0.09	3.42
530.6	0.53	0.37
586.5	0.98	0.34
613.6	0.18	0.43
643	0.53	0.38
670.8	0.53	0.46

Chapter 4 – data table

Mo isotope

	Individual analysis		Grand average	
Depth	**$\delta^{98/95}$Mo**	**2σ**	**$\delta^{98/95}$Mo**	**2σ**
566.5	1.15	0.09	1.15	0.09
569	1.04	0.10	0.98	0.09
	0.92	0.08		
571.34	0.87	0.09	0.89	0.09
	0.90	0.09		
575.13	0.89	0.06	0.87	0.07
	0.84	0.07		
576.3	-0.06	0.09	-0.11	0.09
	-0.17	0.09		
	-0.10	0.09		
583.54	-1.38	0.10	-1.40	0.08
	-1.37	0.08		
	-1.46	0.07		
587.15	-1.01	0.10	-0.96	0.09
	-0.90	0.08		
591	0.25	0.09	0.16	0.09
	0.07	0.08		
595.53	-0.17	0.09	-0.18	0.09
	-0.18	0.09		
598.8	-0.32	0.12	-0.20	0.12
	-0.09	0.13		

600.96	0.02	0.12	-0.07	0.13
	-0.16	0.15		
605.34	-0.69	0.09	-0.71	0.08
	-0.73	0.07		
609.39	0.18	0.14	0.18	0.14
613.12	-0.26	0.10	-0.25	0.09
	-0.25	0.08		
615.7	-0.17	0.09	-0.18	0.08
	-0.19	0.07		
619.36	-0.26	0.07	-0.26	0.07
624.41	0.04	0.10	0.04	0.10
628.24	0.88	0.09	0.92	0.08
	0.96	0.07		
631.23	0.96	0.08	0.88	0.08
	0.80	0.07		
635.06	0.77	0.09	0.83	0.09
	0.89	0.08		
639.13	0.98	0.10	0.94	0.09
	0.90	0.08		
641.66	0.41	0.16	0.44	0.14
	0.46	0.13		
645.76	0.98	0.08	0.95	0.08
	0.93	0.07		

652.09	0.87	0.10	0.86	0.08
	0.86	0.07		
657.16	0.95	0.09	0.88	0.09
	0.80	0.08		
661.28	0.95	0.08	0.93	0.08
	0.91	0.08		
665.09	0.74	0.09	0.75	0.09
	0.76	0.08		
670.46	0.91	0.09	0.92	0.08
	0.93	0.08		
674.05	0.97	0.08	0.98	0.08
	0.99	0.08		
676.8	0.93	0.11	0.88	0.09
	0.82	0.08		
679.64	0.93	0.09	0.91	0.09
	0.88	0.09		
683.15	1.02	0.09	1.00	0.08
	0.98	0.07		
686.05	0.98	0.08	1.01	0.08
	1.01	0.08		
	1.03	0.07		
688.5	1.01	0.23	0.90	0.22
	0.78	0.25		
	0.91	0.19		
690	1.09	0.09	1.09	0.09

693.28	0.96	0.10	0.96	0.09
	0.96	0.08		

Fe-data

Depth (m)	Fe	Fe_{Carb}	Fe_{Ox}	Fe_{Mag}	Fe_{PY}	Fe_{HR}*	Fe_{HR}/Fe_{T}	Fe_{PY}/Fe_{HR}
	(wt %)	(wt %)	(wt %)	(wt %)	(wt %)	(wt %)		
564	6.11	0.63	0.1	2.13	0.05	2.91	0.48	0.02
566.5	3.29	0.64	0.03	0.89	0.61	2.17	0.66	0.28
567.62	11.55	0.51	0.01	0.69	6.63	7.84	0.68	0.85
569	3.07	1.37	0.01	0.78	0.15	2.31	0.75	0.06
570.1	3.95	1.6	0.14	0.76	0.55	3.05	0.77	0.18
571.34	7.54	0.78	0.03	0.25	4.36	5.42	0.72	0.8
572.91	4.82	0.34	0.07	0.81	2.86	4.08	0.85	0.7
575.13	2.65	0.16	0.07	0.41	0.85	1.49	0.56	0.57
575.84	5.79	1.49	0.05	1.1	0.89	3.53	0.61	0.25
576.3	1.96	0.24	0.01	0.29	0.07	0.61	0.31	0.11
582.12	1.07	0.15	0.05	0.16	0.05	0.41	0.38	0.12
583.54	1.84	0.08	0.06	0.24	0.04	0.42	0.23	0.1
586.02	4.79	0.52	0.09	0.49	0.06	1.16	0.24	0.05
587.15	1.89	0.08	0.05	0.09	0.04	0.62	0.14	0.15
589.7	1.76	0.39	0.02	0.14	0.03	0.58	0.33	0.05
591	1.47	0.19	0.02	0.27	0.06	0.54	0.37	0.11
592.24	1.51	0.13	0.02	0.14	0.06	0.35	0.23	0.17
595.53	0.94	0.19	0.03	0.09	0.03	0.34	0.36	0.09
596.78	0.96	0.16	0.04	0.09	0.09	0.38	0.4	0.24
598.8	3.89	0.27	0.08	0.99	0.05	1.39	0.36	0.04
600	1.48	0.06	0.04	0.08	0.04	0.22	0.15	0.18
600.96	2.2	0.15	0.09	0.13	0.05	0.42	0.19	0.12
603.55	0.61	0.07	0.02	0.07	0.01	0.17	0.27	0.04
605.34	5.18	0.61	0.08	0.74	0.16	1.59	0.31	0.1
608	1.25	0.14	0.02	0.19	0.01	0.36	0.28	0.02
609.39	1.78	0.21	0.02	0.12	0.08	0.43	0.24	0.19
611.53	2.39	0.61	0.02	0.23	0.04	0.9	0.38	0.04

613.12	1.9	0.21	0.09	0.1	0.03	0.43	0.23	0.07
615	1.65	0.08	0.03	0.08	0.05	0.24	0.15	0.21
615.7	1.73	0.1	0.03	0.08	0.05	0.26	0.15	0.19
617.43	1.7	0.27	0.02	0.18	0.01	0.48	0.28	0.02
619.36	1.17	0.19	0.04	0.17	0.01	0.41	0.35	0.02
622	1.36	0.1	0.03	0.14	0.03	0.3	0.22	0.1
624.41	1.43	0.13	0.03	0.15	0.01	0.32	0.22	0.03
626.87	1.02	0.04	0.01	0.64	0.03	0.72	0.71	0.04
628.24	7.59	1.18	0.02	1.91	0.04	3.15	0.42	0.01
630	2.67	1.29	0.03	1.04	0.03	2.39	0.9	0.01
631.23	6.26	1.38	0.06	1.76	0.05	3.25	0.52	0.02
633.54	5.7	1.7	0.08	1.82	0.13	3.73	0.65	0.03
635.06	2.35	0.28	0.04	0.36	0.03	0.71	0.3	0.04
637.49	5.99	0.14	0.13	1.67	0.99	2.93	0.49	0.34
639.13	7.41	1.06	0.03	1.09	1.05	3.23	0.44	0.33
641	6.85	1.23	0.03	1.14	0.06	2.46	0.36	0.02
641.66	8.99	1.06	0.12	1.59	0.1	2.87	0.32	0.03
644	3.84	0.9	0.04	0.54	0.03	1.51	0.39	0.02
645.76	6.2	0.61	0.06	1.89	0.08	2.64	0.43	0.03
646.55	1.78	0.33	0.03	0.14	0.05	0.55	0.31	0.09
650.27	1.68	0.22	0.04	0.14	0.01	0.41	0.24	0.01
652.09	2.52	0.25	0.03	0.4	0.08	0.76	0.3	0.11
652.56	4.18	0.44	0.04	0.66	0.08	1.22	0.29	0.07
655.78	4.8	0.92	0.05	0.71	0.22	1.9	0.4	0.12
657.16	6	1.33	0.04	0.92	0.13	2.42	0.4	0.05
659.03	1.24	0.11	0.06	0.18	0.01	0.36	0.29	0.03
661.28	1.14	0.14	0.04	0.2	0.01	0.39	0.34	0.02
662.32	1.29	0.13	0.04	0.17	0.03	0.37	0.29	0.08
664.1	2.01	0.28	0.04	0.14	0.09	0.55	0.27	0.16
665.09	2.06	0.15	0.04	0.2	0.19	0.58	0.28	0.33
668.18	2.52	0.03	0.05	0.43	0.13	0.64	0.25	0.2
670.46	1.01	0.05	0.03	0.13	0.05	0.26	0.26	0.19
671.92	1.01	0.07	0.01	0.08	0.08	0.24	0.24	0.33
674.05	3.21	0.57	0.05	0.32	0.02	0.96	0.3	0.02
675	3.13	0.43	0.05	0.36	0.11	0.95	0.3	0.12
676.8	3.22	1.04	0.1	0.37	0.17	1.68	0.52	0.1
679.64	1.6	0.22	0.03	0.38	0.11	0.74	0.46	0.15
680.94	2.85	0.13	0.03	0.81	0.02	0.99	0.35	0.02
683.15	2.11	0.13	0.04	0.36	0.14	0.67	0.32	0.21

684.15	1.78	0.64	0.02	0.58	0.14	1.38	0.78	0.1
686.05	4.31	1.19	0.07	0.92	0.12	2.3	0.53	0.05
688.5	3.55	1.39	0.06	0.88	0.1	2.43	0.68	0.04
690	1.46	0.22	0.03	0.55	0.09	0.89	0.61	0.1
692.5	1.58	0.26	0.04	0.88	0.18	1.36	0.86	0.13
693.28	2.26	0.73	0.04	0.95	0.12	1.84	0.81	0.07
696.16	2.35	0.57	0.03	0.75	0.43	1.78	0.76	0.24
* Fe_{HR} = $Fe_{Carbonate}$ (Fe_{Carb}) + Fe_{Oxide} (Fe_{Ox}) + $Fe_{Magnetite}$ (Fe_{Mag}) + Fe_{Pyrite} (Fe_{PY})								

Other geochemical data

Depth	δ13C org	Carbonate	TOC	S	Al	Mn	Fe	Mo	Re	U	Mo/Al	Re/Al	U/Al
(m)	(‰)	(wt %)	(wt %)	(wt %)	(wt %)	(wt %)	(wt %)	(ppm)	(ppb)	(ppm)	(ppm/wt %)	(ppb/wt %)	(ppm/wt %)
average upper crust*					8.04	0.06	3.5	1.5	1.00**	2.8	0.19	0.12	0.35
											EF**	EF**	EF**
564		7.73	0.82	0.15	7.81	0.01	6.11	2.2	9.53	4.71	1.51	9.8	1.73
566.5		12.74	0.52	0.91	6.17	0.01	3.29	1.22	5.19	3.07	1.06	6.76	1.43
567.62	-19.6	16.65	0.6	8.47	7.96	0.01	11.55	1.04	8.97	3.93	0.7	9.06	1.42
569		19	0.69	0.14	5.34	0.01	3.07	1.58	20.59	3.06	1.59	31	1.65
570.1	-21.8	7	0.43	0.75	7.91	0.01	3.95	0.48	6.84	3.01	0.33	6.96	1.09
571.34		8.79	0.87	5.3	7.18	0.01	7.54	2.02	11.82	3.75	1.51	13.23	1.5
572.91	-21.6	6.52	0.7	3	5.89	0.01	4.82	1.98	17.29	4.11	1.8	23.62	2
575.13		36.61	0.98	1.23	7.52	0.01	2.65	2.19	14.08	4.82	1.56	15.07	1.84
575.84	-20.3	24.53	0.93	1.78	7.3	0.01	5.79	2.23	6.92	3.9	1.64	7.62	1.53
576.3		9	1.35	0.26	6.89	0.01	1.96	2.25	9.87	3.31	1.75	11.52	1.38
582.12	-20.6	6.81	0.98	0.09	6.35	0.11	1.07	2.04	5.15	1.61	1.73	6.53	0.73
583.54		4.53	1.05	0.15	7.87	0.08	1.84	1.94	28.12	2.93	1.32	28.72	1.07
586.02	-21.2	7.51	0.55	0.07	5.6	0.23	4.79	1.28	15.07	1.39	1.22	21.64	0.71
587.15		5.82	0.81	0.93	6.01	0.21	1.89	2.23	9.68	2.11	1.99	12.95	1.01
589.7	-21.6	4.8	0.86	0.12	6.39	0.10	1.76	2	6.84	2.26	1.67	8.61	1.01
591		6.15	0.79	0.11	4.01	0.12	1.47	1.77	9.17	2.65	2.37	18.39	1.9
592.24	-21.2	4.76	1.37	0.08	5.64	0.14	1.51	2.62	6.9	2.32	2.49	9.83	1.18
595.53		5.85	0.82	0.04	6.13	0.14	0.94	0.83	18.03	2.83	0.73	23.66	1.32

596.78	-21.4	6.81	0.88	0.16	8.16	0.33	0.96	2	9.66	2.1	1.31	9.51	0.74
598.8		7.07	0.84	0.11	4.67	0.10	3.89	0.96	8.4	1.87	1.1	14.45	1.15
600	-21.5	7.51	0.78	0.09	6.66	0.09	1.48	1.78	7.24	1.96	1.44	8.74	0.85
600.96		8.22	0.86	0.09	7.89	0.15	2.2	2.49	7.65	2.88	1.69	7.79	1.05
603.55	-21.2	8.33	0.85	0.03	5.33	0.28	0.61	2.98	8.48	1.49	3	12.79	0.8
605.34		7.7	0.78	0.21	6.71	0.15	5.18	2.05	19.37	3.36	1.64	23.19	1.44
608	-21.6	4.62	0.43	0.04	5.6	0.14	1.25	1.51	6.18	3.2	1.44	8.87	1.64
609.39		7.72	0.87	0.17	7.33	0.11	1.78	3.03	6.98	2.47	2.21	7.66	0.97
611.53	-21.2	7.98	0.62	0.09	6.09	0.15	2.39	2.47	12.41	1.86	2.17	16.38	0.88
613.12		5.74	0.83	0.07	6.23	0.28	1.9	2.23	20.04	3.54	1.91	25.84	1.63
615	-21.2	5.77	1.23	0.11	6.27	0.13	1.65	3.45	25.82	2.81	2.95	33.1	1.29
615.7		4.17	0.64	0.11	5.14	0.12	1.73	2.42	14.31	2.25	2.52	22.4	1.26
617.43	-21.4	4.28	1.35	0.02	7.25	0.08	1.7	2.94	18.16	2.12	2.18	20.13	0.84
619.36		4.7	1.05	0.03	5.27	0.13	1.17	2.37	14.27	2.19	2.41	21.75	1.19
622	-21.5	5.09	1.16	0.07	6.21	0.08	1.36	3.35	11.51	3.96	2.89	14.89	1.83
624.41		5.7	1.81	0.03	7.29	0.12	1.43	3.09	12.96	5.03	2.27	14.3	1.98
626.87	-21.2	7.08	2.66	0.09	6.76	0.15	1.02	3.14	10	4.08	2.49	11.89	1.74
628.24		8.56	0.79	0.1	5.85	0.07	7.59	1.76	11.62	4.95	1.61	15.96	2.43
630	-21.4	13.13	1.37	0.07	6.82	0.06	2.67	3.05	15.83	4.83	2.39	18.65	2.03
631.23	-19.3	8.78	0.94	0.11	6.26	0.01	6.26	1.05	8.73	2.02	0.9	11.21	0.93
633.54		3.98	0.88	0.23	6.19	0.02	5.7	2.64	12.45	3.08	2.29	16.17	1.43
635.06	-21.5	16.11	0.84	0.1	7.7	0.02	2.35	3.11	8.93	3.82	2.16	9.33	1.43
637.49		7.64	0.78	1.97	5.75	0.01	5.99	1.9	8.37	2.58	1.77	11.7	1.29
639.13	-17.8	10.28	0.56	1.88	4.88	0.01	7.41	2.3	10.98	4.48	2.52	18.08	2.64
641		9.73	0.85	0.13	4.36	0.16	6.85	1.67	6.13	4.75	2.06	11.31	3.13
641.66	-18.3	5.3	0.78	0.19	7.39	0.01	8.99	0.63	1.91	3.38	0.45	2.08	1.31
644		4	0.6	0.07	6.72	0.03	3.84	1.73	7.83	6.45	1.38	9.38	2.76
645.76	-17.1	6.81	1.54	0.12	7.63	0.01	6.2	1.43	5.45	5.44	1.01	5.74	2.05
646.55		9.26	0.65	0.09	5.16	0.09	1.78	2.5	7.06	3.8	2.6	11	2.11
650.27	-20.2	4.18	0.62	0.04	5.77	0.19	1.68	2.47	4.07	4.79	2.3	5.68	2.38
652.09		9.82	0.75	0.12	5.73	0.08	2.52	2.02	6.31	4.69	1.89	8.85	2.35
652.56	-21.7	6.8	0.64	0.11	3.67	0.09	4.18	1.06	11.4	3.63	1.55	24.97	2.84
655.78		5.2	0.86	0.43	2.71	0.04	4.8	0.94	4.31	2.01	1.86	12.82	2.13
657.16	-17.9	7.56	0.94	0.21	4.19	0.02	6	0.83	1.26	1.59	1.06	2.41	1.09
659.03		15.77	0.92	0.02	4.34	0.08	1.24	1.34	3.92	3.13	1.65	7.25	2.07
661.28	-13.6	24.17	1.11	0.01	5.92	0.17	1.14	1.52	9.49	3.35	1.38	12.88	1.62

662.32		20.28	0.7	0.04	3.89	0.12	1.29	1.8	3.63	3.27	2.48	7.51	2.41
664.1	-12.7	67.47	0.42	0.18	3.15	0.03	2.01	1.47	1.25	2.32	2.51	3.19	2.12
665.09		58.16	0.57	0.23	4.84	0.02	2.06	1.73	4.35	2.63	1.92	7.23	1.56
668.18	-15	81.96	0.61	0.22	4.77	0.13	2.52	1.46	4.65	3.27	1.64	7.83	1.97
670.46		78.08	0.83	0.09	5.33	0.34	1.01	1.72	2.44	3.17	1.73	3.68	1.71
671.92	-10.8	44.56	0.8	0.11	5.65	0.23	1.01	2.27	1.3	2.96	2.15	1.85	1.5
674.05		33.13	0.6	0.05	4.93	0.22	3.21	1.19	5.17	4.91	1.3	8.44	2.86
675	-20.7	4.59	0.84	0.19	4.17	0.20	3.13	1.69	5.58	3.1	2.18	10.76	2.14
676.8		5.3	0.78	0.25	5.68	0.05	3.22	1.41	4.71	2.5	1.33	6.66	1.26
679.64	-21.4	7.7	0.92	0.21	4.59	0.10	1.6	1.7	4.68	4.17	1.98	8.19	2.6
680.94		7.94	0.84	0.03	5.28	0.09	2.85	1.65	4.43	3.84	1.67	6.74	2.09
683.15	-15.7	7.72	1.46	0.19	4.86	0.06	2.11	2.07	3.72	4.31	2.28	6.15	2.55
684.15		7.98	0.75	0.23	3.81	0.02	1.78	1.34	4.19	3.2	1.88	8.84	2.41
686.05		3.74	0.92	0.19	3.94	0.07	4.31	1.33	4.64	4.73	1.81	9.48	3.45
688.5	-16.8	7.73	0.7	0.19	6.18	0.03	3.55	1.45	4.82	3.78	1.26	6.27	1.75
690		3.98	0.65	0.14	4.42	0.03	1.46	1.36	4.69	3.42	1.65	8.54	2.22
692.5	-17	9.11	0.8	0.27	5.3	0.05	1.58	2.52	3.33	4.65	2.54	5.04	2.52
693.28		7.64	0.92	0.29	5.07	0.07	2.26	1.63	4.14	3.87	1.73	6.57	2.19
696.16	-22.7	4.24	1.48	0.59	5.43	0.02	2.35	1.86	3.58	4.62	1.83	5.3	2.44

*Average upper crust data from Taylor and McClennan (1985); **average [Re] from Selby et al., (2007).

Chapter 5 – data table

1.a Neoarchean BIFs-Nova Lima Group major elements

Depth	Al (wt%)	Fe (wt%)	Mn (wt%)	Ca (wt%)
198.7	1.67	25.60	0.07	1.91
203.2	0.04	21.22	0.03	2.21
206.1	0.10	21.07	0.04	1.23
214.2	0.15	26.88	0.06	0.13
220.3	0.03	30.85	0.06	0.17
224.85	0.77	20.81	0.03	1.80
227.5	0.13	36.79	0.04	1.25
230.8	0.26	27.40	0.05	3.04
234.98	0.50	37.75	0.03	1.03
241.32	0.24	32.69	0.08	5.07
246.27	0.18	29.53	0.06	1.32
258.5	0.05	26.11	0.08	5.16
263.4	0.09	33.78	0.11	1.55
277.67	0.14	38.77	0.11	3.60
280	0.05	43.85	0.04	1.48
295.3	1.11	35.03	0.24	0.26
301.7	0.07	27.26	0.03	0.52
305.53	0.11	41.94	0.07	1.95
311.3	0.08	34.46	0.03	1.72
315.67	0.15	31.19	0.05	1.70
319.31	0.12	31.41	0.02	0.67
323.78	0.04	18.61	0.02	0.14
327.63	0.06	29.11	0.03	0.81
332	0.06	26.79	0.05	2.19
332.76	0.17	24.99	0.07	2.61
334.2	0.06	24.45	0.02	1.43
350.4	0.09	23.27	0.03	1.05
353.5	0.26	20.27	0.10	0.05
359.36	0.50	21.90	0.06	0.07
363.5	0.24	24.24	0.26	0.24
370.55	0.18	29.77	0.27	0.12
372.46	0.05	21.01	0.35	2.82
376.43	0.09	25.70	0.23	4.27
380.8	0.14	26.63	0.30	0.77
381.4	0.05	36.04	0.29	1.50
387.5	0.51	39.79	0.32	2.90
390.85	0.07	23.60	0.05	0.91
392.24	0.11	25.18	0.08	1.07
394.6	0.08	22.88	0.04	0.16

1.b Neoarchean BIFs-Nova Lima Group REE+Y

Depth	Y (ppm)	La (ppm)	Ce (ppm)	Pr (ppm)	Nd (ppm)	Sm (ppm)	Eu (ppm)	Gd (ppm)	Tb (ppm)	Dy (ppm)	Ho (ppm)	Er (ppm)	Tm (ppm)	Yb (ppm)	Lu (ppm)
198.7	11.35	1.82	2.70	0.35	1.60	0.38	0.18	0.70	0.12	1.14	0.26	0.93	0.14	1.05	0.18
203.2	11.96	1.59	2.51	0.34	1.63	0.38	0.17	0.74	0.12	1.10	0.25	0.89	0.14	1.01	0.15
206.1	4.53	0.90	1.27	0.16	0.67	0.16	0.15	0.29	0.04	0.46	0.10	0.35	0.06	0.40	0.07
214.2	4.14	0.60	1.06	0.13	0.64	0.14	0.08	0.26	0.04	0.41	0.10	0.36	0.05	0.41	0.06
220.3	6.48	2.80	4.10	0.49	2.13	0.38	0.13	0.71	0.09	0.75	0.16	0.53	0.07	0.52	0.09
224.85	3.52	0.76	1.20	0.14	0.63	0.14	0.07	0.23	0.03	0.30	0.07	0.25	0.03	0.26	0.05
227.5	4.92	1.13	2.04	0.21	0.96	0.19	0.09	0.38	0.05	0.48	0.10	0.34	0.05	0.34	0.06
230.8	9.46	1.75	2.51	0.27	1.18	0.20	0.17	0.40	0.07	0.61	0.17	0.63	0.11	0.72	0.12
234.98	3.30	0.76	1.01	0.11	0.51	0.09	0.07	0.20	0.02	0.24	0.06	0.18	0.03	0.22	0.03
241.32	4.12	1.06	1.57	0.18	0.85	0.12	0.08	0.29	0.04	0.35	0.08	0.27	0.04	0.27	0.04
246.27	5.16	1.20	1.96	0.21	0.83	0.20	0.09	0.30	0.04	0.42	0.09	0.31	0.04	0.34	0.06
258.5	1.58	0.29	0.46	0.06	0.22	0.05	0.04	0.09	0.01	0.13	0.03	0.13	0.02	0.14	0.02
263.4	9.89	2.30	3.27	0.58	1.38	0.32	0.19	0.53	0.09	0.89	0.20	0.73	0.12	0.86	0.15
277.67	3.18	0.53	0.78	0.09	0.30	0.06	0.04	0.12	0.02	0.24	0.06	0.18	0.03	0.22	0.04
280	1.90	0.43	0.68	0.08	0.30	0.05	0.03	0.11	0.01	0.12	0.03	0.07	0.01	0.07	0.01
295.3	6.14	1.23	1.90	0.21	0.96	0.21	0.12	0.41	0.06	0.61	0.15	0.53	0.07	0.62	0.10
301.7	10.68	2.01	3.11	0.34	1.58	0.35	0.25	0.63	0.09	0.80	0.20	0.73	0.11	0.81	0.12
305.53	6.63	1.81	2.72	0.33	1.57	0.35	0.12	0.57	0.07	0.62	0.14	0.43	0.07	0.40	0.07
311.3	8.10	1.46	2.13	0.25	1.18	0.26	0.12	0.49	0.08	0.67	0.18	0.60	0.10	0.68	0.12
315.67	17.19	3.48	5.46	0.67	2.95	0.60	0.32	1.18	0.18	1.57	0.39	1.33	0.22	1.42	0.26
319.31	7.67	1.12	1.51	0.18	0.83	0.18	0.09	0.36	0.06	0.56	0.15	0.55	0.09	0.64	0.10
323.78	6.22	1.08	1.35	0.16	0.75	0.15	0.08	0.29	0.05	0.47	0.12	0.42	0.07	0.43	0.07
327.63	3.02	0.37	0.58	0.07	0.32	0.08	0.04	0.16	0.02	0.23	0.05	0.22	0.03	0.24	0.04
332	13.32	2.89	5.56	0.70	3.55	0.80	0.25	1.34	0.20	1.58	0.36	1.17	0.19	1.30	0.23
332.76	21.84	4.72	7.10	0.83	3.76	0.75	0.38	1.43	0.23	2.06	0.49	1.73	0.27	1.77	0.29
334.2	11.91	2.75	4.86	0.65	2.97	0.64	0.24	1.12	0.16	1.39	0.29	0.88	0.13	0.84	0.14
350.4	4.40	1.07	1.74	0.22	0.95	0.19	0.19	0.37	0.06	0.48	0.11	0.35	0.05	0.39	0.06
353.5	9.28	2.10	3.24	0.38	1.69	0.39	0.17	0.67	0.11	1.07	0.23	0.85	0.13	0.92	0.16
359.36	3.76	1.22	2.15	0.36	1.27	0.27	0.13	0.43	0.06	0.51	0.10	0.31	0.05	0.27	0.05
363.5	10.10	3.13	5.18	0.67	2.59	0.55	0.24	0.93	0.14	1.21	0.25	0.84	0.13	0.97	0.14
370.55	4.21	0.87	1.53	0.33	0.85	0.21	0.09	0.31	0.05	0.48	0.10	0.35	0.05	0.35	0.07
372.46	12.22	2.58	4.07	0.71	2.12	0.51	0.21	0.84	0.13	1.28	0.28	1.00	0.15	1.06	0.18
376.43	4.58	1.07	1.80	0.24	1.07	0.28	0.10	0.42	0.06	0.52	0.12	0.38	0.06	0.38	0.07
380.8	7.45	1.36	2.26	0.28	1.26	0.33	0.13	0.51	0.08	0.78	0.19	0.67	0.10	0.76	0.14
381.4	6.44	1.56	2.40	0.33	1.41	0.31	0.12	0.53	0.08	0.69	0.16	0.51	0.08	0.56	0.09
387.5	4.27	1.46	2.00	0.28	1.06	0.29	0.18	0.41	0.06	0.65	0.15	0.48	0.09	0.62	0.09
390.85	5.02	1.36	1.92	0.22	0.97	0.21	0.10	0.39	0.06	0.55	0.13	0.48	0.08	0.56	0.10
392.24	8.79	5.13	7.16	0.76	2.91	0.55	0.21	0.93	0.14	1.08	0.24	0.90	0.14	1.06	0.18
394.6	10.45	2.90	5.35	0.68	3.28	0.70	0.32	1.22	0.18	1.32	0.28	0.87	0.11	0.71	0.12

1.c Neoarchean BIFs-Nova Lima Group Fe-Ext

Depth	Fe-carb (wt%)	Fe-ox (wt%)	Fe-Mag (wt%)	Fe-Py (wt%)
198.7	0.89	2.86	6.01	
203.2	1.33	1.14	5.23	
206.1	1.20	1.50	3.40	
214.2	2.01	2.48	6.68	
220.3	1.88	3.22	8.17	0.27
224.85	1.35	2.16	6.92	
227.5	3.08	1.83	3.20	0.06
230.8	3.82	4.45	2.29	
234.98	2.74	4.50	14.09	
241.32	1.20	4.99	11.75	0.15
246.27	1.90	3.22	3.08	0.43
258.5	2.18	2.04	3.74	
263.4	1.37	6.62	3.86	
277.67	1.05	3.09	6.40	
280	0.90	4.05	13.85	
295.3	1.16	3.24	10.14	0.19
301.7	1.80	6.48	4.96	
305.53	2.26	5.95	12.92	
311.3	1.03	5.36	14.31	0.12
315.67	1.80	6.77	8.41	
319.31	1.77	4.62	11.27	0.49
323.78	1.71	4.97	5.43	0.15
327.63	2.25	3.05	9.34	0.17
332	0.60	6.91	11.62	0.13
332.76	1.08	4.92	9.69	
334.2	1.57	5.09	6.36	
350.4	1.21	3.07	7.37	
353.5	2.74	4.67	8.49	0.24
359.36	1.00	1.78	4.50	0.10
363.5	1.43	1.93	3.17	0.20
370.55	0.70	3.26	6.50	
372.46	1.01	2.45	4.09	
376.43	1.57	2.05	5.92	0.30
380.8	1.77	2.93	6.70	0.30
381.4	1.79	3.65	6.42	0.13
387.5	1.58	2.45	6.23	0.13
390.85	3.13	1.23	6.37	0.17
392.24	1.67	3.51	5.14	
394.6	1.66	3.22	4.37	0.30

2.a Paleoproterozoic BIFs-Itabira Group major elements

Depth	Al (wt%)	Fe (wt%)	Mn (wt%)	Ca (wt%)
336.55	0.54	25.60	0.10	0.29
340.2	0.48	21.22	0.08	2.60
346	0.07	21.07	0.08	1.23
350.9	0.07	26.88	0.10	3.68
355.65	0.78	30.85	0.06	6.17
361.7	1.26	20.81	0.12	1.21
365.35	1.92	36.79	0.24	2.44
371.1	0.50	27.40	0.15	5.71
375.95	0.20	37.75	0.04	2.52
382.35	0.04	32.69	0.06	4.30
385.9	0.28	29.53	0.04	6.24
391.25	0.18	26.11	0.10	1.37
395.3	0.07	33.78	0.11	0.21
402.5	0.09	38.77	0.11	0.21
405.55	0.19	43.85	0.04	3.31
412.8	1.02	35.03	0.02	1.46
419.2	0.85	27.26	0.02	1.83
425.5	0.06	41.94	0.03	1.85
434.65	0.09	29.72	0.06	2.81
440.6	0.14	26.73	0.03	3.17
449.9	0.10	33.06	0.03	0.68
455.5	0.74	22.13	0.05	5.29
462.5	0.06	32.88	0.05	1.45
469	0.08	37.73	0.08	0.21
477.4	0.07	30.34	0.09	3.46
484.35	1.21	43.53	0.07	4.91
494.1	0.05	27.02	0.05	9.39
499.85	0.42	30.09	0.13	7.62
505.6	0.07	29.53	0.08	4.43
513.45	0.65	38.07	0.08	2.54
522.9	0.03	36.68	0.09	8.95
530.15	0.31	35.88	0.06	4.81
535.5	1.30	23.31	0.10	4.20
546.4	0.03	26.71	0.05	5.31
552	0.16	36.33	0.07	6.06
559	0.12	31.58	0.03	1.29
566.85	0.09	24.86	0.03	0.90
575.35	0.10	28.66	0.08	3.94
583	1.51	31.51	0.05	1.19
587.9	0.06	22.23	0.03	1.04
593.45	0.16	31.40	0.02	1.09
599.35	0.07	21.85	0.04	0.89
602	0.09	19.92	0.08	0.06
602.98	0.10	23.77	0.20	0.17
603.46	0.12	17.17	0.11	0.07
604	0.22	19.73	0.14	0.11

2.b Paleoproterozoic BIFs-Itabira Group Alegria REE+Y

Depth	Y (ppm)	La (ppm)	Ce (ppm)	Pr (ppm)	Nd (ppm)	Sm (ppm)	Eu (ppm)	Gd (ppm)	Tb (ppm)	Dy (ppm)	Ho (ppm)	Er (ppm)	Tm (ppm)	Yb (ppm)	Lu (ppm)
336.55	6.54	3.99	6.01	0.61	2.48	0.65	0.20	1.11	0.14	0.89	0.32	0.60	0.07	0.38	0.06
340.2	9.06	4.02	5.78	0.61	1.93	0.28	0.21	0.86	0.12	0.90	0.37	0.87	0.13	0.89	0.15
346	8.73	3.58	5.77	0.52	1.94	0.26	0.19	0.85	0.11	0.81	0.32	0.72	0.11	0.72	0.12
350.9	11.49	5.54	7.37	0.74	2.24	0.54	0.33	1.08	0.16	1.24	0.54	1.30	0.22	0.91	0.25
355.65	6.84	2.46	3.18	0.33	1.03	0.68	0.11	0.45	0.06	0.48	0.20	0.45	0.07	0.45	0.08
361.7	6.15	3.42	4.96	0.41	1.71	1.06	0.15	0.75	0.10	0.69	0.28	0.60	0.09	0.58	0.09
365.35	9.24	3.43	4.76	0.47	1.57	1.01	0.16	0.69	0.09	0.66	0.26	0.60	0.09	0.59	0.10
371.1	12.10	1.50	2.17	0.16	0.68	0.41	0.07	0.29	0.04	0.29	0.21	0.27	0.04	0.28	0.05
375.95	18.30	5.38	7.98	0.62	2.51	0.77	0.31	1.29	0.19	1.54	0.64	1.54	0.24	1.00	0.27
382.35	11.58	7.95	7.16	0.76	2.97	0.93	0.34	1.44	0.21	1.64	0.31	1.64	0.27	0.92	0.30
385.9	8.22	7.40	6.42	0.82	2.98	1.47	0.80	1.52	0.29	1.13	0.29	1.83	0.49	1.46	0.55
391.25	11.81	2.00	3.75	0.36	0.79	0.51	0.10	0.39	0.06	0.50	0.35	0.53	0.08	0.60	0.10
395.3	7.89	4.94	4.18	0.36	0.64	0.38	0.06	0.29	0.04	0.25	0.25	0.19	0.02	0.15	0.02
402.5	14.08	3.81	5.35	0.61	2.12	0.52	0.26	1.06	0.17	1.27	0.54	1.27	0.20	1.39	0.23
405.55	18.99	7.95	5.74	0.80	3.66	1.42	0.55	1.76	0.25	1.91	0.79	1.86	0.30	1.03	0.34
412.8	9.80	2.47	4.75	0.37	1.29	0.91	0.19	0.61	0.09	0.61	0.24	0.56	0.08	0.55	0.09
419.2	11.81	6.14	6.02	0.45	1.97	1.06	0.29	1.44	0.11	1.26	0.48	1.02	0.15	0.93	0.15
425.5	13.36	5.09	7.06	0.52	2.43	0.68	0.28	1.23	0.11	1.44	0.61	1.43	0.23	1.56	0.25
434.65	5.40	7.41	6.87	0.67	5.68	2.89	0.66	1.67	0.16	3.14	0.28	1.77	0.46	1.33	0.50
440.6	19.79	3.86	4.88	0.24	1.76	0.30	0.22	0.97	0.06	1.22	0.54	1.29	0.20	1.41	0.24
449.9	4.12	4.44	4.33	0.59	1.30	0.87	0.12	0.62	0.08	0.58	0.29	0.49	0.07	0.48	0.08
455.5	9.26	4.02	6.17	0.71	2.95	0.97	0.40	0.90	0.12	0.72	0.23	1.41	0.19	1.19	0.18
462.5	13.21	3.97	4.98	0.41	1.72	0.21	0.21	0.85	0.13	1.04	0.45	1.03	0.16	1.14	0.19
469	9.12	7.14	6.95	0.84	4.22	0.85	0.78	1.46	0.22	1.46	0.30	2.75	0.56	1.12	0.34
477.4	3.71	5.05	6.31	0.85	2.84	0.98	0.64	1.05	0.18	1.05	0.30	1.77	0.46	0.91	0.23
484.35	6.22	7.95	6.65	0.55	3.71	0.62	0.46	0.88	0.10	1.86	0.38	1.70	0.26	0.89	0.29
494.1	14.96	5.63	7.06	0.97	4.76	1.00	0.58	1.09	0.13	1.12	0.45	1.93	0.30	0.93	0.27
499.85	16.54	2.94	5.66	0.77	4.37	1.88	0.92	1.17	0.21	1.24	0.56	2.30	0.35	0.95	0.32
505.6	17.40	1.87	2.27	0.18	0.45	0.32	0.05	0.20	0.03	0.21	0.49	0.20	0.04	0.28	0.05
513.45	14.49	3.84	7.22	0.98	6.27	1.83	0.84	1.83	0.32	1.31	0.31	1.94	0.22	1.14	0.16
522.9	10.84	5.75	8.99	0.93	4.34	1.12	0.42	0.88	0.15	1.14	0.37	2.18	0.35	0.90	0.39
530.15	11.76	2.68	5.89	0.80	5.03	0.63	0.57	1.47	0.19	1.19	0.39	2.69	0.43	1.11	0.24
535.5	18.42	1.23	4.37	0.64	3.18	0.29	0.98	1.94	0.19	1.26	0.54	1.64	0.49	1.37	0.30
546.4	17.84	3.28	7.05	0.91	5.36	1.26	1.20	1.83	0.30	1.49	0.46	1.81	0.65	1.42	0.26
552	14.34	3.63	6.53	0.87	4.45	0.13	0.78	1.40	0.17	1.38	0.41	1.63	0.40	1.13	0.41
559	16.46	2.08	3.23	0.34	1.17	0.86	0.15	0.57	0.08	0.62	0.40	0.59	0.10	0.67	0.11
566.85	19.97	6.38	9.19	0.78	2.79	0.95	0.40	1.25	0.17	1.19	0.44	0.95	0.15	0.99	0.15
575.35	18.17	2.06	3.93	0.36	1.16	0.30	0.12	0.53	0.07	0.52	0.56	0.44	0.07	0.47	0.08
583	14.88	1.80	4.02	0.81	3.50	1.17	0.72	1.90	0.17	1.54	0.62	1.19	0.36	1.01	0.35
587.9	17.14	1.79	4.61	0.55	4.03	1.71	0.72	1.49	0.17	1.39	0.63	1.93	0.25	1.47	0.22
593.45	15.10	3.52	5.97	0.48	1.94	0.35	0.21	0.92	0.14	1.02	0.41	0.93	0.15	1.05	0.17
599.35	12.38	2.29	4.48	0.46	1.61	0.59	0.21	0.78	0.12	0.92	0.39	0.93	0.15	1.05	0.18
602	5.46	2.97	5.01	0.44	1.84	0.35	0.20	0.91	0.13	0.94	0.36	0.79	0.12	0.81	0.13
602.98	5.00	2.15	4.32	0.32	1.09	0.70	0.09	0.44	0.05	0.34	0.27	0.27	0.04	0.24	0.04
603.46	4.35	2.78	4.46	0.45	1.58	0.58	0.15	0.71	0.10	0.69	0.26	0.55	0.08	0.53	0.08
604	3.91	3.40	5.70	0.57	1.82	0.20	0.14	0.75	0.09	0.57	0.20	0.39	0.05	0.34	0.05

2.c Paleoproterozoic BIFs-Itabira Group Fe-Ext

Depth	Fe-carb (wt%)	Fe-ox (wt%)	Fe-Mag (wt%)	Fe-Py (wt%)
336.55	4.21	2.43	6.32	0.35
340.2	3.09	2.34	9.69	
346	5.50	2.93	9.04	
350.9	3.48	2.35	5.08	0.62
355.65	4.48	3.55	9.79	
361.7	3.17	1.76	8.86	0.27
365.35	3.15	1.94	5.13	
371.1	5.17	1.63	8.10	0.59
375.95	4.11	1.96	15.93	
382.35	7.34	1.71	11.45	0.44
385.9	9.70	2.60	5.24	0.15
391.25	1.00	0.77	4.38	
395.3	3.73	1.15	3.04	
402.5	0.72	1.18	7.41	
405.55	4.64	1.41	6.61	0.35
412.8	2.42	0.66	9.25	0.22
419.2	2.88	1.28	4.24	0.19
425.5	4.01	1.14	6.31	
434.65	5.83	1.32	8.46	
440.6	2.51	0.81	2.79	0.12
449.9	2.62	1.28	8.93	
455.5	1.83	3.42	3.20	0.49
462.5	9.90	2.96	2.72	0.15
469	5.14	0.78	4.25	0.17
477.4	1.29	1.54	5.48	
484.35	3.04	1.86	8.95	0.22
494.1	5.79	0.70	9.40	
499.85	3.71	1.05	10.65	
505.6	1.06	2.00	9.41	0.46
513.45	2.53	1.06	10.04	
522.9	6.23	1.61	9.41	
530.15	1.21	2.06	13.11	0.32
535.5	1.52	1.50	10.65	
546.4	4.22	0.82	7.74	
552	3.18	1.20	8.97	
559	1.13	0.98	12.41	
566.85	2.48	1.11	8.32	0.13
575.35	1.48	0.86	5.60	
583	1.82	1.75	6.02	0.53
587.9	3.30	1.47	6.95	0.30
593.45	2.54	1.62	12.05	0.03
599.35	2.83	1.64	13.29	
602	1.50	1.24	8.23	
602.98	0.63	3.59	8.28	
603.46	2.63	3.64	7.55	
604	2.34	1.61	4.12	